Three-dimensional Radiation Hydrodynamics Simulations of Wandering Black Holes: Effects of Anisotropic Radiation Feedback in Dusty-Gas

Erika Ogata

July 2024

Three-dimensional Radiation Hydrodynamics Simulations of Wandering Black Holes: Effects of Anisotropic Radiation Feedback in Dusty-Gas

Erika Ogata
Doctoral Program in Physics

Submitted to the
Degree Programs in Pure and Applied Sciences of the
Graduate School of Science and Technology,
in Partial Fulfillment of the Requirements
for the Degree of Doctor of Philosophy in
Science

at the
University of Tsukuba

Graduate School of Science and Technology,
Degree Programs in Pure and Applied Sciences

Three-dimensional Radiation Hydrodynamics Simulations of Wandering Black Holes: Effects of Anisotropic Radiation Feedback in Dusty-Gas
（浮遊ブラックホールの三次元輻射流体力学シミュレーション: Dusty-gas 中の非等方輻射フィードバック）

Erika Ogata

Doctoral Program in Physics
Student ID Number: 202230054
Doctor of Philosophy in Science
Advised by Ken Ohsuga

Abstract

How have stars, planets, and the materials that make up our life evolved in the Universe? A clue to this mystery is supermassive black holes (BHs) which are several billion times as massive as the sun. This is because the powerful radiation produced in the vicinity of supermassive BHs induces enormous changes in interstellar matter such as atoms, molecules, and solid particles. However, the formation process of supermassive BHs is still unknown, and understanding this process is one of the most important issues in modern astronomy.

There is a proposal that supermassive BHs are formed via a process in which the low-mass BHs (seed BHs) wandering in galaxies grow into supermassive BHs by swallowing the surrounding gas. However, the growth rate of the seed BHs, which determines whether this idea is true or not, is not precisely known. This is because the interaction between radiation and matter, as well as gravity, must be investigated. When the seed BHs attract surrounding matter, a rotating disk is formed, generating strong and anisotropic radiation due to the release of gravitational energy. This causes ionization of the surrounding gas, dissociation of molecules, and sublimation of solid particles, and the force acting when photons are absorbed by matter induces the mixing of interstellar matter. Therefore, to understand the formation process of supermassive BHs, it is necessary to investigate how wandering seed BHs swallow matter by solving the forces due to gravity and radiation with consideration of the chemical evolution of interstellar matter caused by radiation.

To clarify the formation process of supermassive BHs, we perform three-dimensional radiation hydrodynamics simulations, solving gravity, radiation, hydrodynamics, and non-equilibrium chemical reactions together. This is the first simulation in the world that takes into account the anisotropic radiation produced by the accretion disks around wandering BHs and the sublimation process of solid particles. Our results show that near the rotation axis of the accretion disk, interstellar matter moves away from the BH, while matter is efficiently swallowed into the BH along the disk surface. Around the rotation axis, the plasma regions appear. Interstellar matter, originally composed of neutral atoms and molecules, is photoionized by the strong ultraviolet radiation from the disk. The strong radiation force acting on the solid particles in the interstellar matter (1000 times larger than that of gas) induces flows away from the

BH. When solid particles sublimate, plasma gas is swallowed by the BH even near the rotation axis of the disk. This is because the luminosity of the accretion disk is smaller than the Eddington luminosity for electron scattering, and plasma gas is almost unaffected by the radiation force. The amount of plasma gas accreted from the sublimation region near the rotation axis is roughly one-tenth of the amount accreted from near the disk surface. In the region along the disk plane, the effect of radiation is weak, and the matter is efficiently swallowed by the BH due to gravity. As a result, the amount of matter swallowed by the BH is about one-hundredth of the previous theoretical prediction that does not consider radiation feedback. This result is obtained by assuming the typical density of the molecular cloud (10^4 cm^{-3}). We also found that in high-density conditions ($\gtrsim 10^6$ cm^{-3}), where the effect of radiation is diminished due to the self-shielding effect of radiation by interstellar matter, the seed BHs could swallow a large amount of matter and grow rapidly.

As described above, we have succeeded in quantitatively clarifying for the first time in the world the effect of wandering seed BHs on the evolution of the surrounding interstellar medium and growth rate of BHs under more realistic conditions that take anisotropic radiation and dust sublimation into account.

Contents

Chapter 1

Supermassive Black Holes

Supermassive black holes (BHs) are known to be ubiquitous in the center of galaxies. These are considered the important objects that have had significant impacts on the evolution history of objects and matter via radiation and gas ejections that bring energy and momentum (feedback). However, the standard formation scenario has not yet been established. The formation history of supermassive BHs remains a bottleneck in understanding the evolution history of astronomical objects and matter.

1.1 Compact objects

The compact object is the generic term for neutron stars (NSs) and black holes (BHs). [1] These are born at the final phase of stellar evolution. Their size per mass is smaller than that of normal objects, and they have a strong gravitational field.

The NSs are thought to be formed via the core-collapse of relatively small objects with a mass of $8 - 30 M_\odot$. The NSs are sustained by the degeneracy pressure of neutrons and typically have a mass of $1 - 2 M_\odot$. The upper limit of the NS mass is determined by the force balance between gravity and the degenerate pressure (Tolman-Oppenheimer-Volkoff limit). If the NSs gain mass via mass accretion from the donor star and their mass exceeds this, the NSs would collapse into the BHs. The typical radius of the NSs is 10 km, which is larger than r_s of the NSs, $3 - 6$ km.

Stellar-mass BHs are thought to be formed when a progenitor with a mass of $\gtrsim 30 M_\odot$ goes through a supernova explosion. One of the most important characteristic radii of the BHs is the event horizon radius. If the BHs do not rotate, it is called the Schwarzschild radius and is defined as follows:

$$r_\mathrm{s} = \frac{2GM}{c^2}, \tag{1.1}$$

where, c, G, and M are the speed of light, the gravitational constant, and the mass of BHs, respectively. This radius can be roughly understood as the position where photons are bound by the gravity of the BHs and cannot escape. In addition to the stellar-mass BHs, different types of BHs exist in the Universe (see Table 1.1). Supermassive BHs and intermediate-mass BHs are more massive than the stellar-mass BHs. The supermassive BHs have a mass of $\gtrsim 10^6 M_\odot$, and the intermediate-mass BHs have a mass in the middle range, $100 M_\odot \lesssim M \lesssim 10^6 M_\odot$. The definitions of this mass range vary slightly in the literature, as no strict definition exists.

[1] In general, this definition also includes white dwarfs, but we omit them in this paper.

Table 1.1: Types of black holes

Name	Mass	Location	Formation mechanism
stellar-mass BHs	$\sim 10 M_\odot$	anywhere	gravitational collapse of stars
intermediate-mass BHs	$10^{2-6} M_\odot$	anywhere?	gravitational collapse of massive stars
			runaway collision in star cluster
			merging with other BHs
supermassive BHs	$\gtrsim 10^6 M_\odot$	center of galaxies	accretion onto IMBHs
			merging with other IMBHs

1.2 Supermassive black holes

Supermassive BHs, whose mass is estimated to be several billion times larger than that of the sun, are universally located at the center of galaxies. Observations suggest a strong correlation between the mass of the supermassive BHs, $M_{\rm BH}$, and the mass of the galactic bulge, $M_{\rm buldge}$, as shown below (Marconi & Hunt, 2003):

$$\frac{M_{\rm BH}}{M_{\rm buldge}} \sim 0.001. \tag{1.2}$$

This means that supermassive BHs and galaxies are co-evolving interacting with each other. Therefore, understanding the formation process of supermassive BHs is also important for understanding galaxy formation. However, the formation process of supermassive BHs is still not well understood.

Recent observations suggest that even in the early universe (redshift; $z \gtrsim 6$), the supermassive BHs exist. About 20 years ago, quasar observation project by SDSS (Sloan Digital Sky Survey) first confirmed the existence of supermassive BHs in the universe about a billion years after the Big Bang ($z \sim 6$). Since then, observations have progressed, and recently, HSC (Hyper Suprime-Cam) detected more than 100 quasars at redshifts of 6 or more. Figure 1.1 summarizes 196 observed bright quasars in the early Universe with redshift $z \geq 6$ (Inayoshi et al., 2020, as a recent review). The presence of supermassive BHs with a mass exceeding $\gtrsim 10^7 M_\odot$ before the universe was a few hundred million years old represents an intriguing puzzle.

In summary, there are three observational factors that are important for building a theoretical model of the formation process of a supermassive black hole: (1) its location at the center of a galaxy, (2) its mass correlation with the bulge mass of the host galaxy, and (3) its formation time in a few hundred million years.

1.3 Formation process of supermassive black holes

Supermassive BHs may be formed via either the gas accretion process onto low-mass BHs (seed BHs) or the BH-BH merger process, or both processes (see Figure 1.2). As discussed in the previous section, the observational results require a theoretical model in which supermassive BHs form in a few Gyr, but it takes time for the mass to increase by many orders of magnitude. For example, if the initial BH mass is $10 M_\odot$, the seed BHs cannot grow into a supermassive BHs in a few Gyr, even if it grows by gas accretion at the Eddington rate (see black solid lines in Figure 1.1). Therefore, many researchers suggest that supermassive BHs grow up from the heavier seed BHs. In the next subsection, we present the formation scenarios of seed BHs that are currently considered as the most likely scenarios: the first star scenario and the supermassive star scenario.

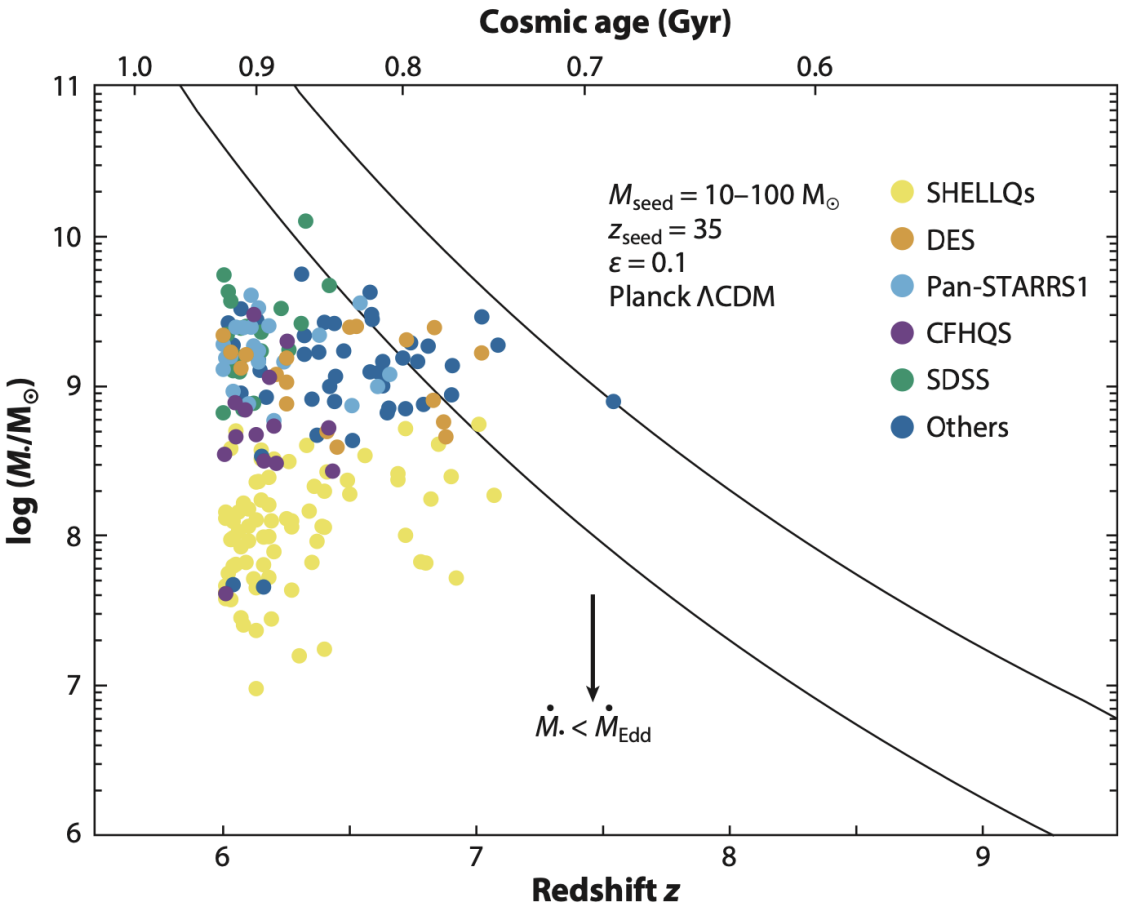

Figure 1.1: Summary of observed supermassive BHs at $z \gtrsim 6$ with different quasar surveys. Black curves show the Eddington limited growth curves of seed BHs with initial masses of $10M_{\odot}$ (lower-curve) and $100M_{\odot}$ (upper-curve) at $z = 35$, where the radiation efficiency is set to 0.1. Cited from Inayoshi et al. (2020).

1.3.1 Formation process of seed BHs

The first star scenario for the formation process of supermassive BHs is that the seed BHs formed by the gravitational collapse of the first star evolve into the supermassive BHs. Hydrodynamic simulations based on cosmological initial conditions revealed the formation process of the first star which originated in primordial density fluctuations, and the typical mass of the first star is estimated to be $\sim 10^2 M_{\odot}$ with an upper limit of $\sim 10^3 M_{\odot}$. The initial growth of the seed BHs originating from the first stars is expected to proceed mainly by gas accretion. This is because the merging of the seed BHs would cause the BHs to escape from the mini halo of the early universe, where the escape velocity is $\lesssim 10$ km/s, into intergalactic space so that further growth cannot be expected.

It has been proposed that primordial (metal-free) gas clouds exposed to strong ultraviolet radiation from nearby galaxies in the early universe could produce supermassive stars with masses as high as $10^5 M_{\odot}$. Supermassive stars are supposed to form when hydrogen molecules are completely photodissociated by strong ultraviolet radiation and Lyα cooling becomes effective. In the supermassive star scenario, the BHs with a mass of $10^5 M_{\odot}$ formed by the gravitational collapse of a supermassive star (Direct Collapse BH) are seed ones and grow into the supermassive BHs via gas accretion or/and BH-BH merger. The timescale in this mechanism is relatively short since the seed is very heavy. However,

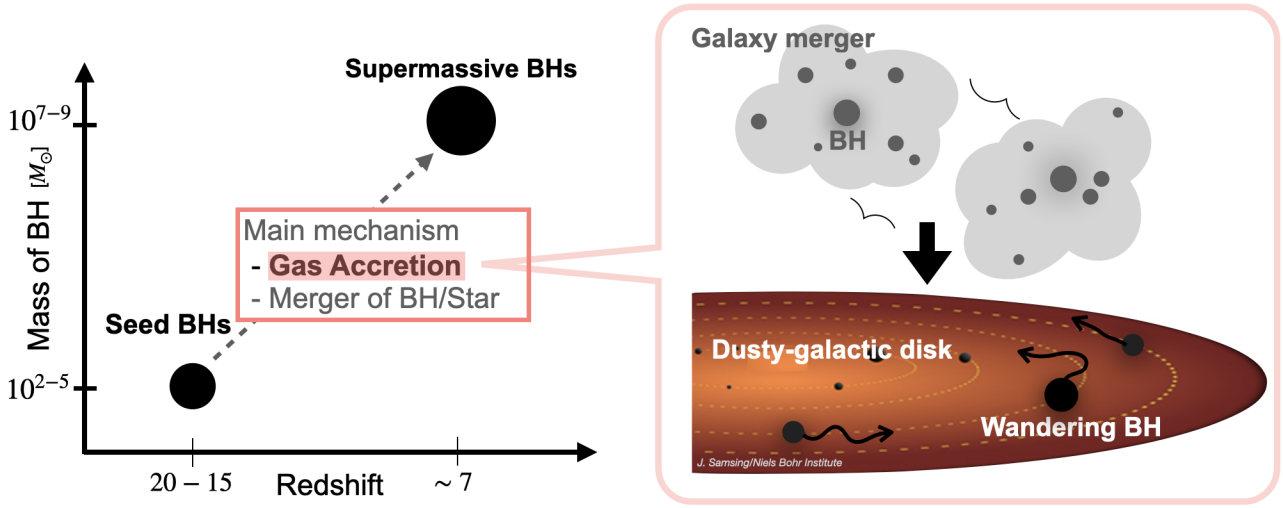

Figure 1.2: Image of the formation process of a supermassive BHs.

it is unclear how much of the environment exposed to powerful ultraviolet radiation can be realized.

1.3.2 Growth process of seed BHs

How do the seed BHs, which are born via the scenario introduced above, subsequently grow into the supermassive BHs? As shown on the right side of Figure 1.2, during the formation of the hierarchical structure of the Universe, the seed BHs are expected to swallow the surrounding gas while wandering in the interstellar medium (see Section 1.3.2). The seed BHs are inferred to be wandering in the interstellar medium mainly because of four reasons: the anisotropic supernova explosion, the galactic merger, the gravitational recoil, and the three-body slingshots. [2] We will explain this below.

Wandering BHs driven in the supernova explosion

As described in Section 1.1, stellar-mass BHs and NSs are formed by supernova explosions that occur at the end of the life of stars. Thus, these compact objects are widespread where stars exist. However, they do not stay where the supernova explosion occurred all the time. This is because when the supernova explosions occur asymmetrically, the compact objects start to float in the interstellar medium due to its recoil. In fact, observational results suggest that the NSs are floating in the interstellar medium at speeds as high as 100 km/s. Figure 1.3 shows an X-ray image of the Puppis A supernova remnant, created using data from the ROentgen SATellite (ROSAT). [3] The two insets imaged by Chandra in Figure 1.3 show the bright X-ray structures, whose origin is ejecta. The white and yellow arrows represent the ejecta found in visible and the intrinsic motion vectors of the NSs measured in X-rays. The yellow elliptical region is the center of the explosion estimated from the eigenmotion vector. The observational results indicate that the ejecta and NSs are recoiling by the hydrodynamic kick. This can be inferred from the observational results that the positions of the NS and the ejecta are symmetrical across the position of

[2] **Where is the compact objects?**
Considering that compact objects form in supernova explosions, we can suppose that they exist in any region where star formation occurs. So, do compact objects exist only in star-forming regions? The answer is no. This is because a compact objects does not continue to stay in the location where it was born. In this chapter, we introduce some of the mechanisms that drive compact objects to start wandering.

[3] The ROSAT was launched on June 1, 1990. This enabled us to conduct survey observations of X-ray sources by imaging telescopes for the first time.

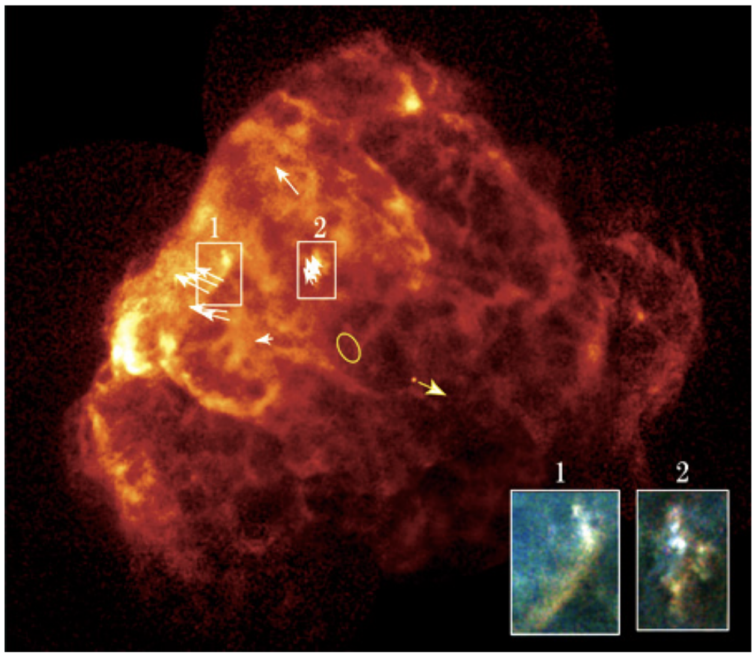

Figure 1.3: X-ray image of the Puppis A supernova remnant. This is created using data from the ROSAT High Resolution Image. The two insets imaged by Chandra X-ray Observatory show the bright X-ray structures, whose origin is ejecta. The white and yellow arrows represent the ejecta found in visible and the intrinsic motion vectors of the neutron star measured in X-rays, respectively. The yellow elliptical region is the explosion center estimated from the eigenmotion vector. Cited from JAXA arxiv first half of 2012.

the supernova explosion and their directions of motion are opposite (yellow and white arrows pointing in opposite directions in Figure 1.3). The left panel of Figure 1.4 shows the kick velocities of NSs (filled circles) and velocities of the center of ejecta mass (open boxes) obtained by analysis of observational data (cited by Katsuda et al., 2018), and the right panel shows the relative position for the sites that occurred supernova explosion. These figures reveal that the NSs float by the hydrodynamic kick due to the supernova explosions, with speeds of more than 100 km/s. We note that the hydrodynamic kicks occur only when the supernova explosions occur asymmetrically.

Figure 1.5 illustrates the momentum balance between the NS and the ejecta and indicates how the hydrodynamic kicks occur (cited by Scheck et al., 2006). The orange rings indicate the dense shells behind the shocks. In the case of a spherical explosion (left panel), the momentum of the NSs and the ejecta are zero, and the NSs remain where they were originally born. On the other hand, if one hemisphere expands later than the other (right panel), the gas has net momentum in the direction of the faster-expanding hemisphere. Based on the momentum conservation law, this also means that the NSs are in motion. The BHs formed via supernova explosions could float by the same mechanism as described so far.

Wandering BHs driven by galactic merger

The galactic merger is also thought to induce the wandering BHs (see recent reviews, e.g. Untzaga et al., 2024). Figure 1.6 shows schematic diagram of the three different formation mechanisms of wandering BHs caused by galactic merger. First, we introduce "disrupted wandering BHs" (see top line). The small satellite galaxies containing BHs begin to infall into more massive dark matter halos (light yellow region) at some period in their lifetimes. In this process, the satellite galaxies cannot withstand the tidal

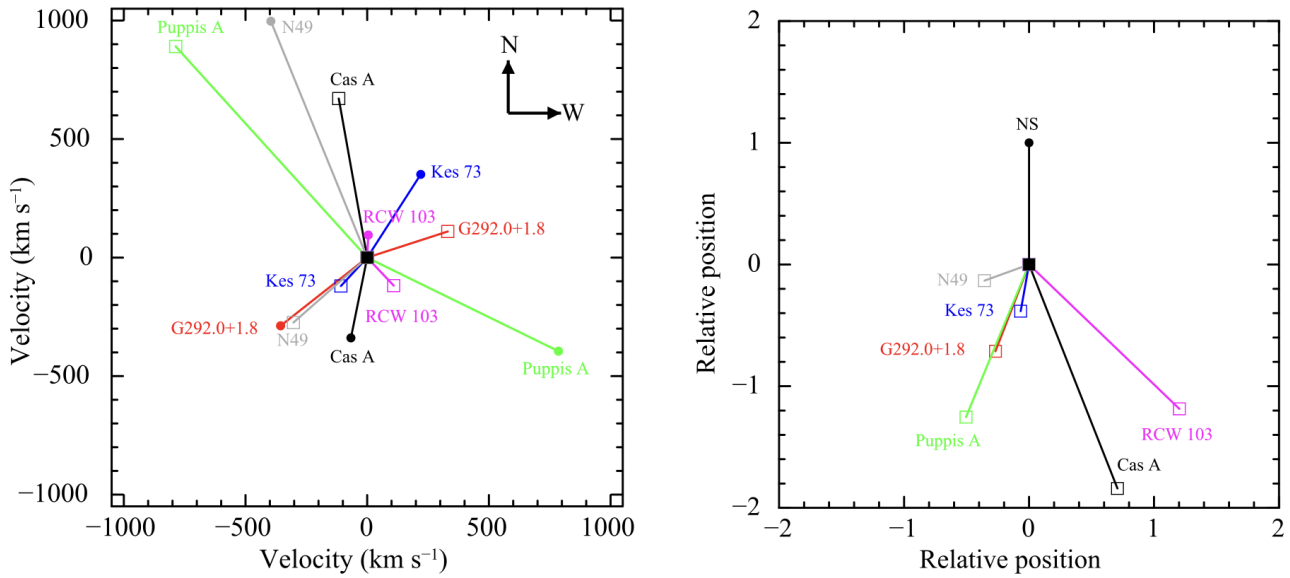

Figure 1.4: Left panel shows that kick velocity of NSs (filled circles) and velocities of center of ejecta mass (open boxes) obtained by analysis of observation data, and right panel shows the relative position for explosion sites. Cited from Katsuda et al. (2018).

force exerted by the massive dark matter halos, and then the cold gas (stellar) component is stripped away and accumulates in the hot atmosphere (interstellar medium) surrounding the main galaxy. Then, the BHs of the satellite galaxies (including central BHs and wandering BHs) are left in the massive dark matter halos as wandering BHs. This is called "Disrupted wandering BHs". Once the "disrupted" BHs are wandering in massive galaxies, it is expected to fall into the center of massive galaxies due to dynamical friction caused by the interstellar components: the dark matter, the stars, the hot gas, etc. (see Equation 32 in Izquierdo-Villalba et al. (2020)). We note, however, that there is a possibility that the wandering BHs could accelerate rather than decelerate (Toyouchi et al., 2020; Ogata et al., 2024). Second, we introduce "paring BHs" (see middle line). Similar to the disrupted wandering BHs, the pairing wandering BHs are originally hosted in the satellite galaxies. However, unlike the disrupted wandering BHs, the satellite galaxies withstand the tidal force exerted by the massive galaxies and merge with it. In this process, the BHs of satellite galaxies are deposited in the galactic remnant disk which is newly formed by the merging of satellite galaxies and massive galaxies. The differences between the model of disrupted wandering BHs and paring wandering BHs would appear in such things as the falling time to the galactic center (because of the different places to start wandering: the dark matter halos and the remnant galactic disks).

Wandering BHs driven by gravitational recoil

The next wandering model is a gravitational recoil type of wandering BHs (Recoiled wandering BHs). A schematic view of the formation of such wandering BHs is shown in the last line in Figure 1.6. Here we explain in the context of galactic mergers, but this model can be realized for any system in which two BHs in the binary system merge. In the context of galactic mergers, the wandering BHs of this type follow the same formation path as the pairing wandering BHs. After the satellite galaxies overcome the tidal force exerted by the dark matter halos, they merge with the massive galaxies and the BHs originating from the satellite ones wander as the pairing wandering BHs. Subsequently, the two BHs merge. If the merging two BHs have different masses, the binary BHs receive the recoil due

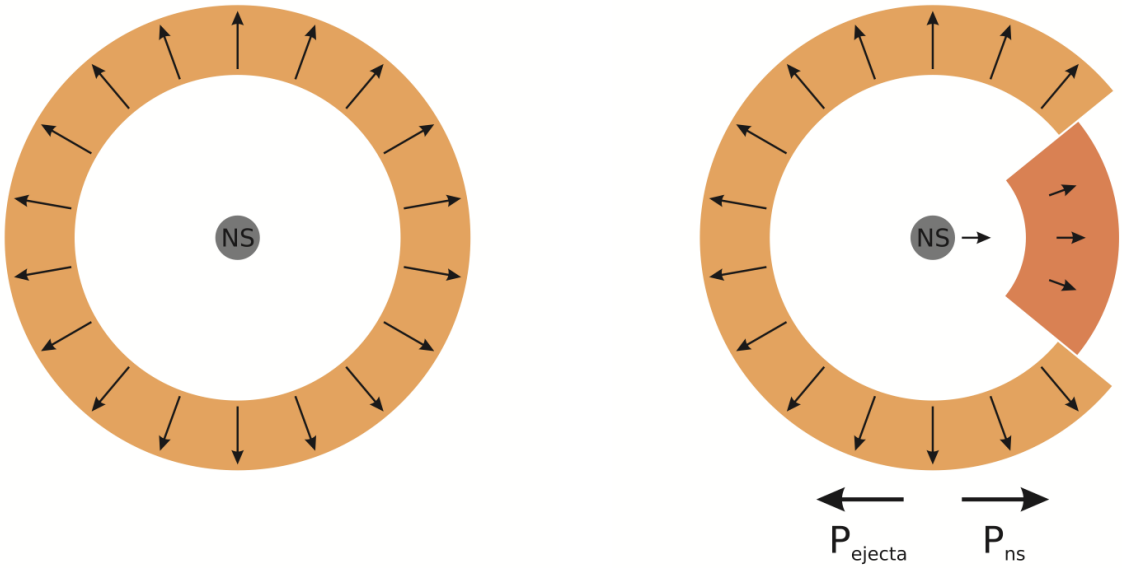

Figure 1.5: Schematic figure of the momentum balance between the NS and the ejecta. Most of the mass of the ejecta is concentrated in a dense shell (light-colored ring) behind the shock wave. In the case of a spherical explosion (left panel), the momentum of the NSs and the ejecta is zero. If one hemisphere expands later than the other, the gas has net momentum in the direction of the hemisphere that expands faster. The NSs are always accelerated in the opposite direction, i.e., the slow one (right panel). Cited from Scheck et al. (2006).

to the asymmetric emission of gravitational waves during the merger. The studies of gravitational wave emission indicate that the kick velocities of the binary BHs resulting from gravitational recoil can be larger than the escape velocity of the host galaxies, and when this happens, the binary BHs would be ejected from the center of the galaxies and deposited in the dark matter halo (again) enveloping the galaxies.

Wandering BHs driven by three-body slingshots

Finally, we introduce the wandering mechanism, the scattering process due to three-body interactions (ex. the two BHs in the binary system and the other intruder BH). When BHs or galaxies containing BHs merge, the BHs do not collide head-on with each other. They rather approach and pass through each other repeatedly. This is called "two-body scattering". If another object approaches while two-body scattering is occurring, the object receives kinetic energy from the two BHs and is kicked away, and the two BHs lose potential energy and get closer to each other. This is called the "slingshot". Such ejection phenomena of BHs due to three-body (two BHs + approching BH system) interactions investigated by numerical simulations (e.g. Samsing et al., 2022). They revealed that a gravitational wave event with a high eccentric orbit, named `GW190521`, can be explained by the three-body interaction of BHs in the flat gas disk (see Figure 1.7). Moreover, recent observations have suggested the existence of supermassive BHs wandering in the intergalactic gas, driven by the three-body interaction (van Dokkum et al., 2023). Their analysis indicates that the BH is floating at speeds as fast as 1600km/s. We note, however, that this scenario is predicted from the observational data of the gas filaments and not from directly observed BHs.

The accretion phenomenon of the wandering BHs that are born via the mechanism explained above is commonly referred to as Bondi-Hoyle-Lyttleton accretion (more details in Section 2). The growth process of the wandering BHs into the supermassive BHs via Bondi-Hoyle-Lyttleton accretion is not

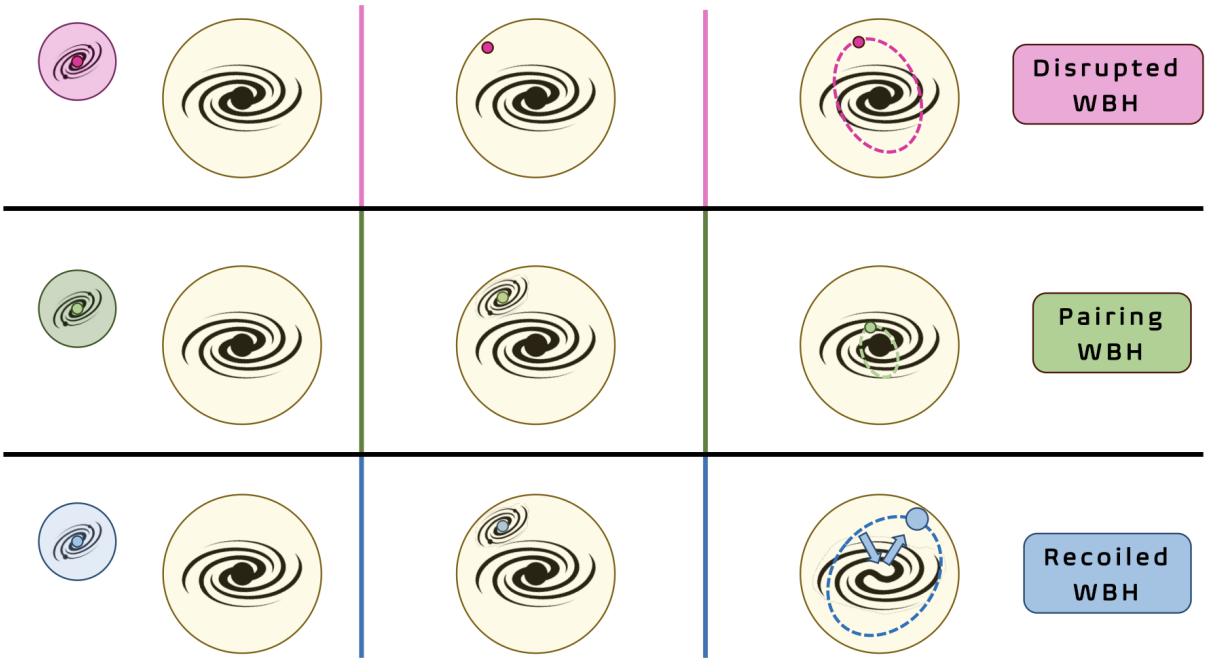

Figure 1.6: Schematic diagram of the three different formation scenario of the wandering BHs obtained by `L-galaxies`. Each row represents types of wandering BHs, and the columns show, from left to right, the steps show the steps BHs go through until wandering. Cited from Untzaga et al. (2024).

well understood. This is because the radiation emitted from the accretion disk around the seed BHs (see Section 1.3.3) induces changes in the composition and spatial distribution of the surrounding matter, which complicates the problem.

1.3.3 Accretion disks around compact objects

Accretion disks are disk-like accretion flows that form around gravitational objects such as the BHs, protostars, NSs, and white dwarfs as shown in Figure 1.8. When the gas having angular momentum is attracted to the seed BHs by gravity, disk-like structures, i.e. accretion disks, are formed around it. The accretion disks brightly illuminate due to the energy conversion from gas heated up via friction to radiation. The seed BHs are also expected to have the accretion disks. Therefore, to clarify the formation process of the supermassive BHs via Bondi-Hoyle-Lyttleton accretion onto the seed BHs, it is necessary to quantitatively understand how gas accretion proceeds under the radiation feedback as well as gravity. Here, we explain the fundamental physics of the accretion disks.

The accretion disks can be classified into three types with different disk thicknesses, H, and optical depths depending on the mass accretion rate onto disk ($\dot{M}_{\rm disk}$) normalized by the Eddington value, $\dot{M}_{\rm E}$ (see figure 1.9). Shakura et al. (1973) proposed a basic model of the accretion disks called the alpha disk model or standard accretion disk model. In their model, the radiative cooling and viscous heating are balanced, resulting in a geometrically thin disk. The standard disk is thought to be formed when $\dot{M}_{\rm disk} \sim \dot{M}_{\rm E}$. [4] Advection energy transport in the accretion disks has been studied since the late 1980s (see, e.g., Ichimaru et al., 1977; Abramowicz et al., 1988; Narayan et al., 1994; Abramowicz et al., 1994). The situation in which the advective cooling dominates over the radiative cooling in the accretion disks is called Advective Dominated Accretion Flows (ADAFs). Consideration of such cooling is essential

[4]We note that the standard accretion disk model was soon extended to the relativistic version by Novikov & Thorne (1973).

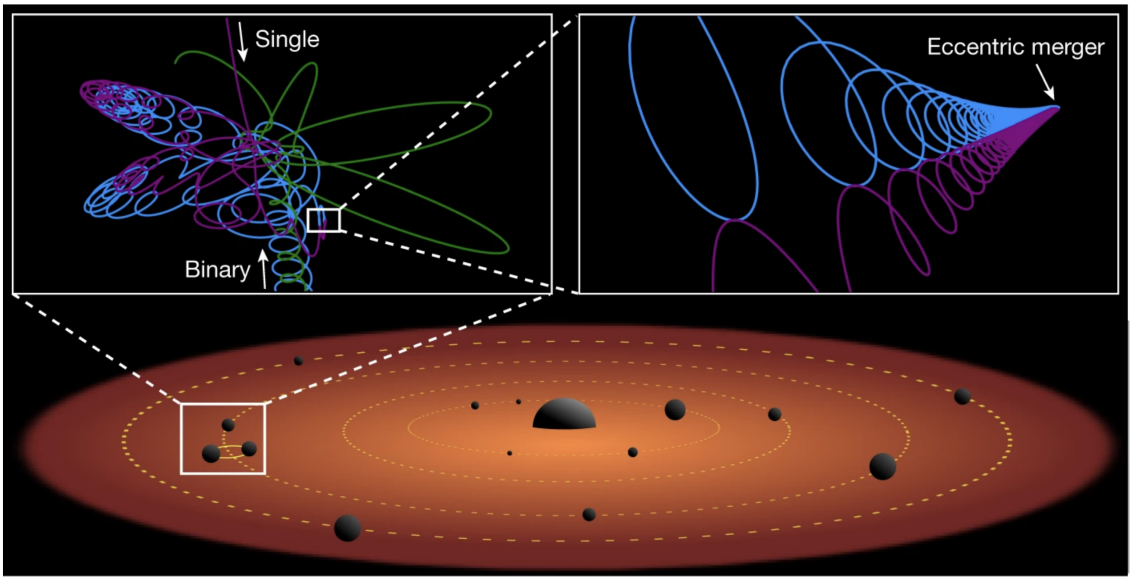

Figure 1.7: Schematic figure of the merger of BHs caused by three-body gravitational slingshots in a gas disk around a supermassive BHs. Cited from Samsing et al. (2022).

to understand the accretion disks with very high mass accretion rates and with extremely low mass accretion rates. The ADAFs that are optically thick are called slim disk and appear when the mass accretion rate exceeds the Eddington rate, $\dot{M}_{\rm disk} \gg \dot{M}_{\rm E}$ (Abramowicz et al., 1988; Watarai et al., 2000). The reason advective cooling dominates over radiative cooling is that the optical depth inside the accretion disks is too large for the photon to escape from the disks before it is swallowed by the BHs, which is called photon trapping (e.g., Katz, 1977; Begelman, 1978; Ohsuga et al., 2002). The gradient force of the radiation pressure in the vertical direction increases because the photon trapping leads to the accumulation of photons, resulting in the enhancement of radiation energy (pressure) within the disk; thus the geometrically thick disk is formed. In contrast, optically thin accretion flows are known as Radiatively Inefficient Accretion Flows (RIAFs), which are formed when the condition, $\dot{M}_{\rm disk} \ll \dot{M}_{\rm E}$, is satisfied (Ichimaru et al., 1977; Narayan et al., 1994; Abramowicz et al., 1994). In this model, the gas temperature in the disk is high because the radiative cooling does not work efficiently due to the low gas density of the disk. Thus, the RIAFs can reproduce high-energy emissions such as observed in the hard state of the galactic X-ray binary system. The scale height of the disks is determined by the force balance between vertical gravity and vertical gradient force of gas pressure, resulting in a geometrically thin disk. The numerical simulations confirm the presence of these three types of accretion disks (see Figure 1.8).

In the following, we briefly introduce the properties of the three models of accretion disks, focusing on the standard disk model that we will treat in this study.

Standard accretion disk model

The standard disk model was proposed by Shakura et al. (1973). In this model, there are three characteristics: optically thick, geometrically thin, and bright (but not exceeding the Eddington luminosity). First, we explain the basic equations (continuity equation, momentum equation, energy equation, and equation of state). Cylindrical coordinates (r, φ, z) with the z-axis perpendicular to the plane of the accretion disks are adopted. The following assumptions are used to establish the basic equations:

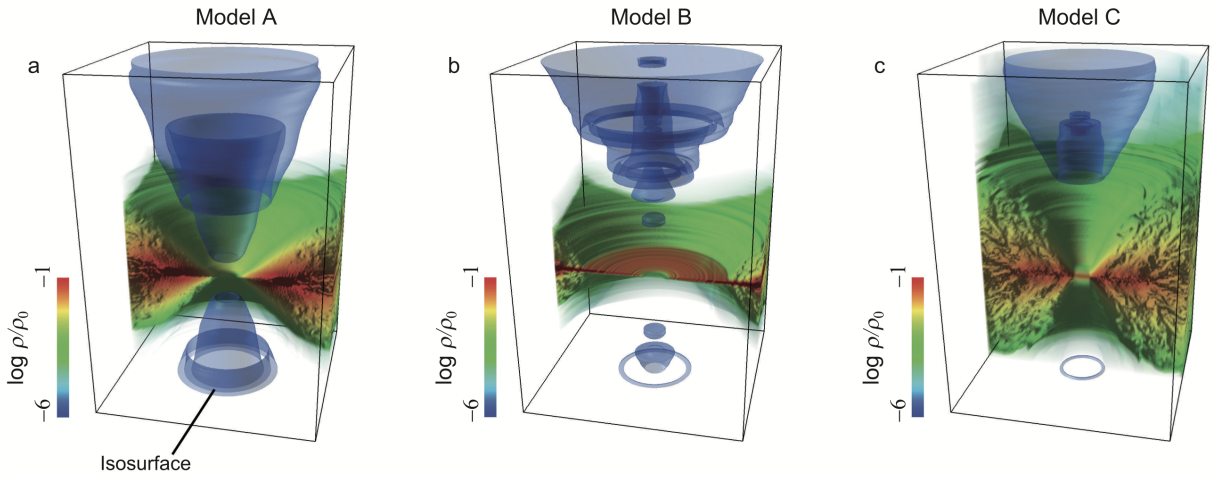

Figure 1.8: Three states of the accretion disk. Models A, B, and C represent the simulation results of slim disk, standard disk, and RIAF. The accretion disk is colored by normalized gas density. BH is located in the center of the accretion disk.

Cited from Ohsuga et al. (2009).

- The disks are steady, $\partial/\partial t \to 0$.
- The disks are axisymmetrical, $\partial/\partial \varphi \to 0$.
- The disks are geometrically thin, $H \ll r$. Here, H denotes the scale height of the disks.
- The gravitational field consists of a BH, and the self-gravity of the disk is ignored.
- The gas in the disks does a Keplerian rotation.
- Hydrostatic equilibrium holds in the vertical direction of the disks.
- The disks are optically thick in the vertical direction of the disks.
- The angular momentum of the gas is transported outward via the α-viscosity, at which the viscous stress tensor is adopted as $T_{r\varphi} = \alpha p$. Here, p is the total pressure, and α is in $0 \leq \alpha \leq 1$.
- The gas in the disks emits blackbody radiation.
- The viscous heating rate and radiative cooling rate are balanced.

Mass conservation law

Now consider a ring of width Δr at radius r (see Figure 1.10). The density integrated in the direction perpendicular to the ring surface is defined as surface density Σ,

$$\Sigma \equiv \int_{-H}^{H} \rho dz = 2\rho H. \tag{1.3}$$

Using surface density, the mass of the each ring is expressed as $2\pi r \Delta r \Sigma$. The time variation of the mass of the ring can be calculated by subtracting the mass leaving the ring from the mass entering the ring

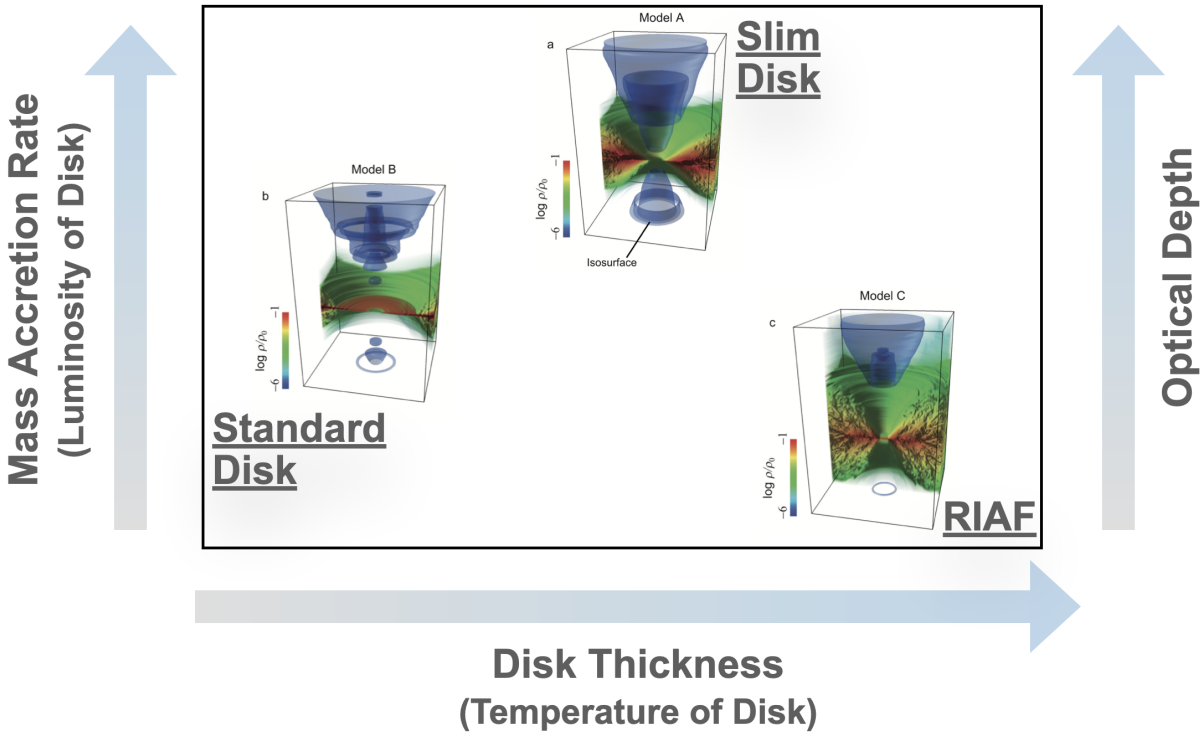

Figure 1.9: Summary of three accretion disk models. Cited from Ohsuga et al. (2009) with some modification.

in unit time,

$$\frac{\partial}{\partial t}\left(2\pi r\Delta r\Sigma\right) = \left(-v_r 2\pi r\Sigma\right)_{r+\Delta r} - \left(-v_r 2\pi r\Sigma\right)_r \approx \Delta r\frac{\partial \dot{M}}{\partial r}$$
$$\frac{\partial \Sigma}{\partial t} = \frac{1}{2\pi r}\frac{\partial \dot{M}}{\partial r}, \tag{1.4}$$

where v_r is the radial component of the gas velocity and $\dot{M} \equiv -2\pi r\Sigma v_r$ is mass accretion rate. Here, a minus sign means that the gas is moving in the direction of the origin. In this model, $\partial/\partial t \to 0$ is assumed, thus above equation is described as below,

$$\dot{M} = -2\pi r\Sigma v_r = \text{constant}. \tag{1.5}$$

This equation means that, in this model, the mass accretion rate is always constant at each radius r.

Equation of motion in r direction: Keplerian rotation

The equation of motion in r direction can be written as shown below: [5]

$$\frac{v_\varphi^2}{r} = \frac{GM}{r^2}, \tag{1.6}$$

where v_φ is rotational component of the velocity. Solving this equation for v_φ, we get,

$$v_\varphi = \sqrt{\frac{GM}{r}}. \tag{1.7}$$

[5]In the standard disk model, the pressure gradient force in the radial direction is assumed to be sufficiently smaller than gravity in the radial direction ($dP/\rho dr \ll GM/r^2$). Furthermore, we suppose that the radial component of the velocity, v_r, is sufficiently smaller than the velocity in the rotational direction, v_φ. With these two assumptions, the gravity due to the central celestial object and the centrifugal force due to the rotational motion of the gas are balanced at each radius in the radial direction (Keplerian motion).

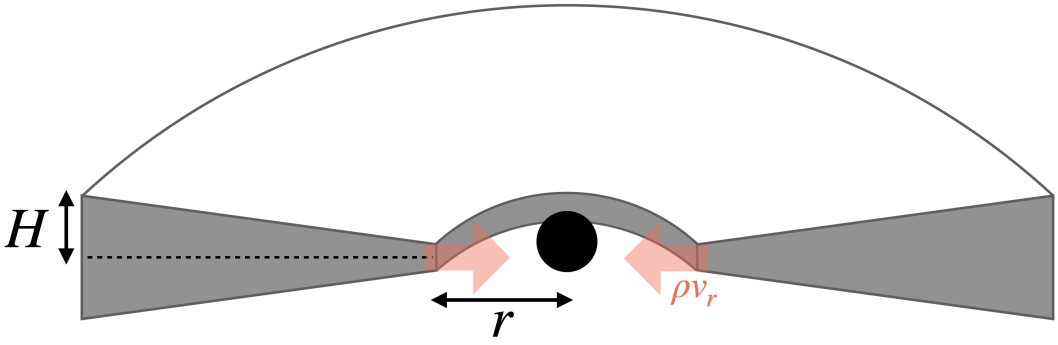

Figure 1.10: Imaged figure of a standard disk cross section. Red arrows indicate mass flux.

We can see that this is proportional to $r^{-1/2}$. Thus, the gas at the inner edge of the disk has a higher speed than the gas at the outer edge. This difference in rotational speed at each radius r generates viscous stress.

Equation of motion in z direction: hydrostatic equilibrium

The equation of motion in z direction can be written under the assumption as mentioned above:

$$\frac{1}{\rho}\frac{dP}{dz} = \frac{GMz}{(r^2+z^2)^{3/2}}. \tag{1.8}$$

Here, P denotes the total pressure, which consists of gas pressure and radiation pressure. Considering the geometrically thin nature ($r \gg z$), we can approximate Equation 1.8 as shown below,

$$\frac{1}{\rho}\frac{dP}{dz} \sim \frac{GMz}{r^3}. \tag{1.9}$$

Replacing dP/dz on the left hand side by P/H, [6] and transforming using $P = \rho c_s^2$ and $\Omega = v_\varphi/r = GM/r^3$, we obtain the scale height:

$$H = c_s/\Omega. \tag{1.10}$$

Equation of motion in φ direction: angular momentum conservation

The equation of motion in φ direction is as follows:

$$\rho\frac{v_r}{r}\frac{d}{dr}\left(\rho v_\varphi\right) = \frac{1}{r^2}\frac{\partial}{\partial r}\left(r^2 t_{r\varphi}\right). \tag{1.11}$$

Here, $t_{r\varphi}$ is the $r\varphi$ component of the viscous stress tensor, which means the φ component of the viscous stress per unit area acting on a plane perpendicular to the r direction, and proportional to the velocity gradient in the r direction:

$$\begin{aligned} t_{r\varphi} &= \eta\left(\frac{\partial v_\varphi}{\partial r} - \frac{v_\varphi}{r}\right) \\ &= \eta r\frac{d\Omega}{dr}. \end{aligned} \tag{1.12}$$

[6] $dP/dz \sim$ [P(equatorialplane) − P(disksurface)]/H ∼ P/H. Here, we assume that the pressure at the disk surface ($z = H$) is zero, P(disksurface) = 0.

Here, η is the kinetic viscosity, which is the coefficient imposed only by the density dependence. [7] Multiplying both sides of the momentum equation in the φ direction (Equation 1.11) by r^2 and integrating in the vertical direction yields,

$$\begin{aligned} r\Sigma v_r \frac{d}{dr}\left(r v_\varphi\right) &= \frac{d}{dr}\left(\tilde{\eta} r^3 \frac{d\Omega}{dr}\right) \\ &= \frac{d}{dr}\left(r^2 T_{r\varphi}\right), \end{aligned} \tag{1.13}$$

where $T_{r\varphi}\,(=\int t_{r\varphi} dz)$ is the viscous stress tensor integrated into the vertical direction and $\tilde{\eta}\,(=\int \eta dz)$ is the kinematic viscosity integrated into the vertical direction. Equation 1.13 can be easily integrated in the radial direction since $r\Sigma v_r$ on the left side of Equation 1.13 is constant based on Equation 1.3,

$$-\frac{\dot{M}}{2\pi} r v_\varphi = r^2 T_{r\varphi} + C,, \tag{1.14}$$

where C is the integration constant.

In this model, the viscous stresses does not act at the inner edge side of the accretion disk $r_{\rm in}$. Applying this condition to Equation 1.14, we obtain $C = -(\dot{M}/2\pi) r_{\rm in} v_\varphi(r_{\rm in})$. Substituting this into Equation 1.14, we obtain below equation,

$$-\frac{\dot{M}}{2\pi}\left(r v_\varphi - r_{\rm in} v_\varphi\left(r_{\rm in}\right)\right) = r^2 T_{r\varphi}. \tag{1.15}$$

Since $r v_\varphi$ is angular momentum at each radius, thus this equation means the transport of angular momentum. The negative sign indicates that angular momentum is transported from the inner edge side of the disk toward the outside (in the opposite direction of the gas flow).

Furthermore, considering the Keplerian rotation of the gas in the disk, Equation 1.15 can finally be expressed as follows:

$$\nu\Sigma = \frac{\dot{M}}{3\pi}\left(1 - \sqrt{\frac{r_{\rm in}}{r}}\right) \tag{1.16}$$

For $r_{\rm in}$, it is common to apply the radius of the innermost stable circular orbit. Assuming a Shwartzschild BHs, $r_{\rm in} = 3r_{\rm s}$. In the case of the Kerr BHs, the effect of the spinning of the BHs causes the inner edge radius to be smaller (when the direction of BH spinning coincides with the direction of disk rotation) or larger (when the direction of BH spinning and the direction of disk rotation are opposite).

Energy equation

In the standard disk model, radiative cooling (cooling rate $Q^-_{\rm rad}$) and viscous heating (heating rate $Q^+_{\rm rad}$) are assumed to be balanced at each radius of the disk.

$$Q^+_{\rm vis} = Q^-_{\rm rad}. \tag{1.17}$$

The heating rate per unit area $Q^+_{\rm vis}$ is given as a function of the viscous stress tensor integrated in the vertical direction $T_{r\varphi}$ and the gradient of the angular velocity Ω,

$$\begin{aligned} Q^+_{\rm vis} &= \int_{-\rm H}^{H} \eta r^2 \left(\frac{d\Omega}{dr}\right)^2 dz \\ &= \frac{9}{4}\nu\Sigma\Omega^2 = -\frac{3}{2} T_{r\varphi}\Omega. \end{aligned} \tag{1.18}$$

[7] viscous stress increases with density and velocity gradient

Substituting $\Omega = v_\varphi / r = \sqrt{GM/r^3}$ and Equation 1.16, we obtain $Q^+_{\rm vis}$ as a function of r,

$$Q^+_{\rm vis} = \frac{3GM\dot{M}}{4\pi r^3}\left(1 - \sqrt{\frac{r_{\rm in}}{r}}\right). \tag{1.19}$$

Assuming that the accretion disk is optically thick, a temperature gradient is induced from the disk equatorial plane to the disk surface, and the radiation diffuses in response to the temperature gradient. Thus, $Q^-_{\rm rad}$ is expressed as follows,

$$\begin{aligned} Q^-_{\rm rad} &= \int_{-\rm H}^{\rm H} \left(-\frac{4acT^3}{3\kappa\rho}\frac{dT}{dz}\right) dz \\ &= \frac{8acT_{\rm c}^2}{3\tau}, \end{aligned} \tag{1.20}$$

where a, $T_{\rm c}$, and τ are the radiation constant, the gas temperature at equatorial plane of the disk, and the optical depth.

Note that, because of the assumption that the disk is optically thick, energy is emitted as blackbody radiation corresponding to temperature at the disk surface. Therefore, defining the disk surface temperature by $T_{\rm eff}$, $Q^-_{\rm rad}$ can also be written using the Stefan-Boltzmann law,

$$Q^-_{\rm rad} = 2\sigma T^4_{\rm eff}. \tag{1.21}$$

Here, σ represents the Stefan-Boltzmann constant. The coefficient of 2 means radiation from both sides of the disk surface. Comparing Equations 1.20 and 1.21, the following relation exists between $T_{\rm c}$ and $T_{\rm eff}$:

$$T_{\rm eff} = \frac{16T_{\rm c}^4}{3\tau}. \tag{1.22}$$

Equation of state

The equation of state is

$$P = \frac{R_{\rm gas}}{\bar{\mu}}\rho T_{\rm c} + \frac{aT_{\rm c}^4}{3}, \tag{1.23}$$

where $R_{\rm gas}$ and $\bar{\mu}$ mean the gas constant and average molecular weight, respectively. The second term on the right-hand side represents the radiation pressure in the blackbody radiation field. The factor 1/3 is due to the assumption that radiation is isotropic and homogeneous. Integrating Equation 1.23 in the vertical direction, we obtain,

$$\Pi = \frac{R_{\rm gas}}{\bar{\mu}}\Sigma T_{\rm c} + \frac{1}{3}aT_{\rm c}^4 2H, \tag{1.24}$$

where $\Pi\,(= \int P dz)$ is the total pressure integrated into the vertical direction.

Opacity

In the standard disk model, the gas opacity is defined as

$$\kappa = \kappa_{\rm es} + \kappa_{\rm ff}, \tag{1.25}$$

Equation of continuity in z-direction	$\rho = \Sigma/2H$
Equation of continuity in r-direction	$\dot{M} = -2\pi r v_r \Sigma$
Equation of motion in z-direction	$H = c_s/\Omega$
Equation of motion in r-direction	$\Omega = \sqrt{GM/r^3}$
Equation of motion in φ-direction	$\nu\Sigma = \frac{\dot{M}}{3\pi}\left(1 - \sqrt{\frac{r_{\rm in}}{r}}\right)$
Equation of energy	$\frac{8acT_c^4}{3\tau} = \frac{9}{4}\nu\Sigma\Omega^2$
Equation of state	$P = P_{\rm gas} + P_{\rm rad} = \frac{R_{\rm gas}}{\bar{\mu}}\rho T + \frac{a}{3}T^4$
Polytropic relation	$c_s^2 = P/\rho$
Kramer's law	$\tau = (\kappa_{\rm es} + \kappa_{\rm ff})\rho H = (\kappa_{\rm es} + \kappa_0 \rho T^{-3.5})\rho H$
Alpha viscosity model	$\nu = \frac{2}{3}\alpha c_s H$

Figure 1.11: Basic equations of standard disk model.

where $\kappa_{\rm es}$ is the opacity of electron scattering, and $\kappa_{\rm ff}$ is the opacity of free-free absorption. $\kappa_{\rm es}$ is independent of frequency and temperature,

$$\kappa_{\rm es} = 0.4[{\rm cm^2 g^{-1}}]. \tag{1.26}$$

On the other hand, $\kappa_{\rm ff}$ has frequency and temperature dependence, but using the frequency-averaged Kramers' equation, only the temperature dependence remains.

$$\kappa_{\rm ff} \sim 6.24 \times 10^{22} \rho T^{-7/2} [{\rm cm^2 g^{-1}}] \tag{1.27}$$

Since $\kappa_{\rm ff} \propto T^{-7/2}$, free-free absorption is important up to roughly $\sim 10^6$K, and electron scattering becomes dominant at higher temperatures. The optical depth is

$$\tau = \int (\kappa_{\rm es} + \kappa_{\rm ff})\, \rho dz = (\kappa_{\rm es} + \kappa_{\rm ff})\, \rho H. \tag{1.28}$$

Viscous model

The $r\varphi$ component of the viscous stress tensor $t_{r\varphi}$ appeared in the equations of motion, which included the kinetic viscosity η. Although the disk viscosity is recently thought to be magnetic origin, in the standard disk model, following assumption is introduced:

$$t_{r\varphi} = \eta r \frac{d\Omega}{dr} = -\alpha P. \tag{1.29}$$

This equation follows the physical intuition that the friction between gases increases as the pressure P increases. The proportionality constant α is also called the viscosity parameter and is considered to

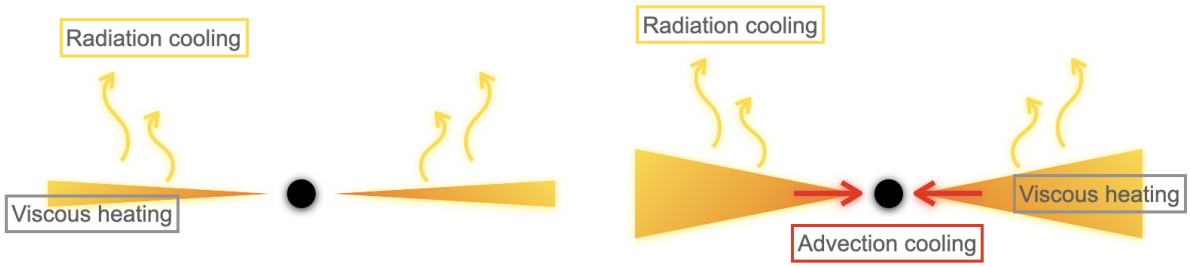

Figure 1.12: Images of the standard disk model (left) and the advection-dominated model (right).

have a value of $0 < \alpha \leq 1$ based on theoretical speculation and results of numerical simulations when viscosity is considered to be of magnetic turbulent origin.

Short summary of standard disk model

Finally, we summarize the standard disk model as follows. The number of unknown variable is 10; the gas density ρ, surface density Σ, scale height H, radial velocity v_r, sound speed c_s, angular velocity Ω, total pressure P, gas temparture T, optical depth τ, and kinematic viscosity ν. The number of the basic equations is also 10 as summarised in the Figure 1.11. Since the number of equations and the number of variables are the same, and since all of the basic equations are algebraic equations, the solutions can be obtained algebraically. To solve these equations, we need to decide the three parameters; the BH mass M, accretion rate $\dot{M}$, and viscosity parameter α. Since the equation of state and the opacity equation involve a summation formula, the solution is obtained by separating the cases (see reference book; Kato et al., 2008).

1.3.4 Advection-dominated disk model

The standard disk model was first proposed, but many astronomical objects have been found that this model cannot explain well. In the standard disk model, the assumptions that radiative cooling works efficiently is introduced, so the temperature of the disk around a stellar-mass BHs is theoretically predicted to be about tens of millions of Kelvin. However, X-ray observations have found gas with extremely high temperatures, reaching several billion Kelvin. These observations cannot be explained by the standard disk model, and new disk models are needed.

A model capable of addressing the brightness and temperature of accretion disks that cannot be explained by the standard thin disk model has been developed, termed "Advection Dominated Accretion Flow" (ADAF). In this model, the effect of advection is incorporated, although advection is not effective in the standard disk model since the radial velocity and vertical velocity are negligibly small compared to the rotational velocity. By incorporating the radial flow of energy, this model can explain observational phenomena such as extremely hot disks or exceptionally bright disks. Herein, we elucidate why the inclusion of advection enables theoretical explanations for these observational facts.

The ADAFs are divided into two categories: super-Eddington accretion disks, where the mass accretion rate exceeds the Eddington accretion rate, and Radiatively Inefficient Accretion Flows (RIAFs), where the mass accretion rate is much lower than the Eddington rate. If the mass accretion rate is extremely low, as in RIAF, efficient cooling does not occur and the disk becomes thickened, dominated by gas pressure. Conversely, in the case of high accretion rates, the disk expands mainly due to radiation pressure.

Super-Eddington accretion model (Slim disk model)

Abramowicz et al. (1988) proposed the concept of a super-Eddington accretion disk, also known as a slim disk. In this model, the inclusion of advection effects enabled the theoretical reproduction of a geometrically thick structure for the disk. Additionally, optical thickness is assumed to be much larger than unity is assumed. The fundamental equations for this model are as follows. It should be noted that in our simulations, we employ only the standard thin disk as a subgrid model related to the geometric structure of the accretion disk (for the angular distribution of radiation). Therefore, detailed explanations of the equations are omitted.

1. Continuity equation
   Same as standard disk model (Equation 1.3).

2. Equation of motion

$$v_r \frac{dv_r}{dr} = \frac{v_\varphi^2}{r} - \frac{GM}{r^2} - \frac{1}{\rho}\frac{dP}{dr} \tag{1.30}$$

   The advection term on the left-hand side and the pressure gradient force term in the third term on the right-hand side are neglected in the standard disk model.

3. Angular momentum equation
   Same as standard disk model (Equation 1.16).

4. Equation of hydrostatic equilibrium
   Same as standard disk model (Equation 1.8).

5. Energy equation
   By introducing advection cooling, which represents the transfer of the energy in the radial direction, as $Q^-_{\rm adv}$, energy equation is obtained as

$$Q^+_{\rm vis} = Q^-_{\rm rad} + Q^-_{\rm adv}, \tag{1.31}$$

   Here, we introduce the advection parameter f (advection parameter) and rewritten Equation 1.31 as follows:

$$Q^-_{\rm rad} = (1-f)Q^+_{\rm vis} \tag{1.32}$$

   When the advection parameter f is zero, there is only radiative cooling, which leads back to the standard disk model. Conversely, when $f = 1$, radiative cooling is zero and the cooling mechanism is entirely advection. Advection cooling corresponds to the difference between the energy flowing in from the outside and the energy flowing out to the inside.

As can be seen from the basic equations shown above, the energy transfer to the central object occurs when the advection effect is introduced. In this model, such phenomenon is called as photon trapping by which a large number of photons repeatedly collide with gas particles, and are swallowed into the central black hole instead of escaping from the disk. In other words, the radiation energy is swallowed into the BH together with the gas. Although the radiative efficiency is low because of the photon trapping, the slim disk shines brighter than the standard disk model due to its large mass accretion rate.

RIAF model

The RIAF model is proposed by Ichimaru et al. (1977) and Narayan et al. (1994), and the mass accretion rate is the smallest among the three models. The density of the flow is very small. Therefore, unlike the super-Eddington disk model and standard disk model, photons are less likely to be produced inside the disk, resulting in a lower luminosity of the disk (the mechanism of photon generation, such as bremsstrahlung, is less likely to occur). Since the radiative cooling is very inefficient, the gas of the flow becomes very hot. From the above, a faint and extremely high temperature disk emerge when the mass accretion rate is much smaller than the Eddington rate.

Chapter 2

Accretion onto the Wandering Black Holes

As already explained in Chapter 1, recent observations and simulations suggest that the compact objects are universally wandering in the interstellar medium. This process is important for understanding the formation process of the supermassive BHs. Here, we briefly review the accretion physics around such wandering compact objects from the theoretical aspects.

2.1 Hoyle-Lyttleton accretion

Accretion onto the wandering gravitational objects was first investigated by Hoyle & Lyttleton (1939). Therefore, the phenomenon in which gravitational objects wandering in the interstellar medium gain mass due to swallowing the surrounding gas by its gravity is called "Hoyle-Lyttleton accretion". The gravity of the objects gathers the gas into the wake, which is accreted. They derive the accretion rate with some assumptions as follows:

- The spatial distribution of matter around the gravitational object is uniform at infinity.
- Consider only the gravity of the objects (self gravity of the surrounding matter is ignored)
- The gas pressure is ignored (assuming supersonic motion)
- When the matter collides at the wake, the momentum perpendicular to the collision axis (accretion axis) is assumed to be zero. This corresponds to not considering the dissipation process of thermal energy near the accretion axis.
- To judge whether accretion occurs or not by comparing the velocity of the material after the component that is perpendicular to the accretion axis is set to zero (i.e., the axial velocity) with the escape velocity.

Considering the above assumptions, the ballistic trajectories of the particle (matter) are solved in the Lagrangian manner. In the following, we refer to Edgar's excellent review of the Hoyle-Lyttleton accretion (Edgar, 2004). First of all, we consider a streamline with a collision parameter ζ (see Figure 2.1). Here, the polar coordinate (R, φ, θ) is applied, and a particle is assumed to flow in from infinity at velocity v_∞ along the negative direction of the z-axis. In other words, the rest frame of the gravitational

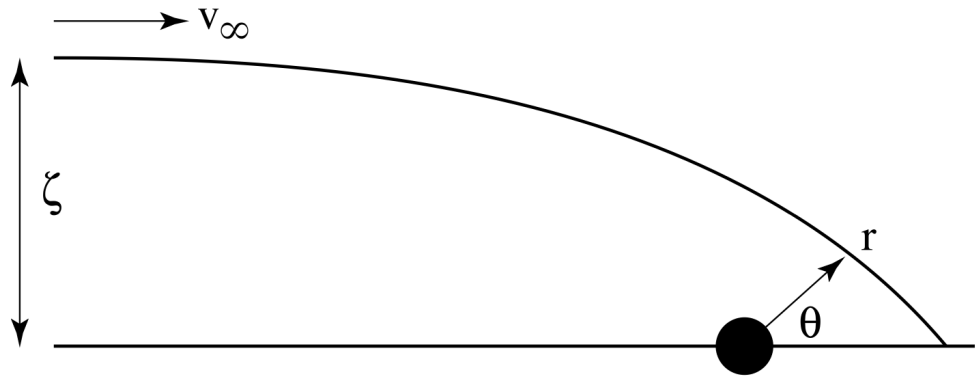

Figure 2.1: Sketch of the Bondi–Hoyle–Lyttleton accretion geometry. Cited from Edgar (2004).

objects is employed. The time development equations in the radial (R) and polar (θ) directions are,

$$\frac{d^2R}{dt^2} - R\left(\frac{d\theta}{dt}\right)^2 = -\frac{GM}{R^2} \tag{2.1}$$

$$R^2\frac{d\theta}{dt} = \zeta v_\infty. \tag{2.2}$$

Since only a central force acts on the matter, Equation 2.2 implies that angular momentum around the axis of $\varphi = 0$ (the axis perpendicular to the paper surface) is conserved. Thus, we define the right-hand side of Equation 2.2 as the constant h. Furthermore, introducing $u = R^{-1}$, Equation 2.1 can be rewritten as follows:

$$\frac{d^2u}{d\theta^2} + u = \frac{GM}{h^2}. \tag{2.3}$$

Assuming A, B, and C are arbitrary constants, the general solution of Equation 2.3 is $u = A\cos\theta + B\sin\theta + C$. When we substitute this solution into Equation 2.3, $C = GM/h^2$ can be obtained. The constants A and B can be obtained by giving the boundary conditions. The boundary conditions at infinity ($\theta \to \pi$) are set as follows:

$$u \to 0 \tag{2.4}$$

$$\frac{dR}{dt}\left(= -h\frac{du}{d\theta}\right) \to -v_\infty. \tag{2.5}$$

Equation 2.4 represents that $\theta \to \pi$ corresponds to the position at infinity, and Equation 2.5 represents that the velocity at infinity is $-v_\infty$. The minus sign means that the motion direction of a matter is inward in the radial direction, i.e., a matter at infinity flows in the direction toward the gravity object. Applying these boundary conditions to Equation 2.3 leads to arbitrary constants $A = GM/h^2$ and $B = -v_\infty/h$. Therefore, the general solution of Equation 2.3 is

$$u = \frac{GM}{h^2}(1 + \cos\theta) - \frac{v_\infty}{h}\sin\theta. \tag{2.6}$$

This is the solution for the ballistic trajectories of the matter in the Hoyle-Lyttleton accretion phenomenon. Next, let's consider situations when the matter reaches the accretion axis ($\theta = 0$). Substituting $\theta = 0$ into Equation 2.6, we can obtain the position of the matter on the accretion axis:

$$u = \frac{2GM}{h^2} \tag{2.7}$$

$$\to \frac{1}{R} = \frac{2GM}{h^2}. \tag{2.8}$$

Matter is recognized to be bound by the central object at the accretion axis when the following condition is satisfied:

$$\frac{1}{2}v_\infty^2 - \frac{GM}{R} < 0. \tag{2.9}$$

Substituting the general solution (Equation 2.8) on the accretion axis into this accretion condition (Equation 2.9), we obtain

$$\zeta < \frac{2GM}{v_\infty^2} \equiv R_{\rm HL}, \tag{2.10}$$

which is defined as the critical impact parameter, Hoyle–Lyttleton radius $R_{\rm HL}$. Equation 2.10 means that when ζ has a value less than $2GM/v_\infty^2$, the matter can accrete onto gravitational object. The mass accretion rate is therefore

$$\begin{aligned} \dot{M}_{\rm HL} &= \pi R_{\rm HL}^2 \rho_\infty v_\infty \\ &= \frac{4\pi\rho_\infty G^2 M^2}{v_\infty^3}, \end{aligned} \tag{2.11}$$

which is known as the Hoyle–Lyttleton accretion rate $\dot{M}_{\rm HL}$. The velocity and density distribution of matter was obtained by Bisnovatyi-Kogan et al. (1979). The solutions obtained by solving the orbital equation (Equation 2.2, 2.1) are as follows:

$$v_R = -\sqrt{v_\infty^2 + \frac{2GM}{R} - \frac{\zeta^2 v_\infty^2}{R^2}} \tag{2.12}$$

$$v_\theta = \frac{r_\infty v_\infty}{R} \tag{2.13}$$

$$R = \frac{\zeta^2 v_\infty^2}{GM\left(1+\cos\theta\right) + \zeta v_\infty^2 \sin\theta}. \tag{2.14}$$

The density ρ can be obtained by solving the continuous equation under the condition of axisymmetric steady state:

$$\rho = \frac{\rho_\infty r_\infty^2}{R\sin\theta\left(2\zeta - R\sin\theta\right)}. \tag{2.15}$$

2.2 Bondi-Hoyle accretion

Bondi & Hoyle (1944) extended the argument of Hoyle & Lyttleton (1939) to take into account the accretion columns formed downstream due to collisions of matter. Here, the accretion column represents the wake region near the accretion axis at $\theta = 0$. In this section, we present the contents of Bondi & Hoyle (1944).

First, the mass flux injected into the region $[R, R+dR]$ of the accretion column is as follows (Figure 2.2):

$$\begin{aligned} \rho_\infty v_\infty \cdot \left[\pi\left(\zeta + d\zeta\right)^2 - \pi\zeta^2\right] &= \left[2\pi\zeta d\zeta + \pi\left(d\zeta\right)^2\right] \cdot \rho_\infty v_\infty \\ &\sim 2\pi\zeta d\zeta \rho_\infty v_\infty. \end{aligned} \tag{2.16}$$

Here, we made an approximation that ignores the second-order terms of $d\zeta$ when shifting from the first line to the second one. From the orbital equation of Hoyle-Lyttleton flows (Equation 2.14), the position

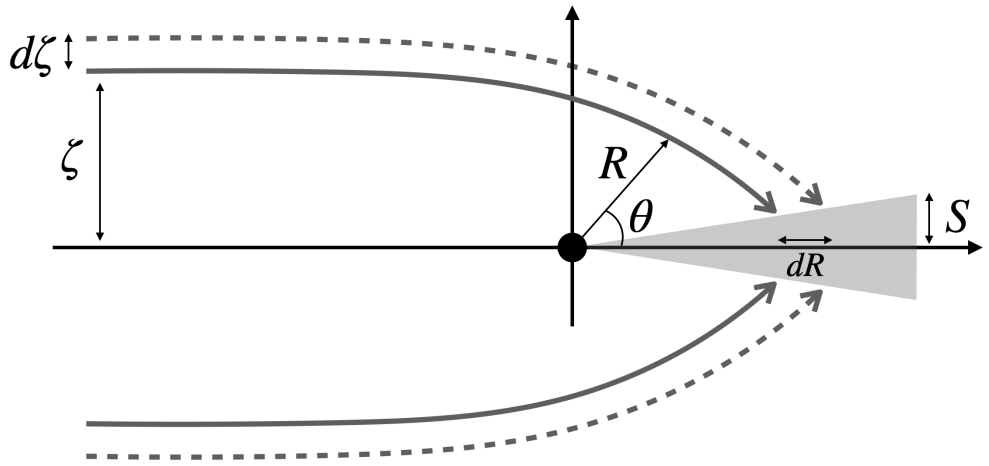

Figure 2.2: Sketch of the Bondi–Hoyle accretion geometry.

of the matter material when it arrives at the accretion axis $(\theta = 0)$ is as follows:

$$R_{\theta=0} = \frac{\zeta^2 v_\infty^2}{2GM} \tag{2.17}$$

Differentiating both sides of this by ζ yields

$$\begin{aligned} \frac{dR}{d\zeta} &= \frac{\zeta v_\infty^2}{GM} \\ \rightarrow d\zeta &= \frac{GM}{\zeta v_\infty^2} dR. \end{aligned} \tag{2.18}$$

Substituting this into Equation 2.16, we obtain the mass flux injected into the region $[R, R+dR]$ of the accretion column as follows

$$\begin{aligned} 2\pi\zeta d\zeta \cdot \rho_\infty v_\infty &= \frac{2\pi GM\rho_\infty}{v_\infty} dR \\ &= \Lambda dR, \end{aligned} \tag{2.19}$$

where the mass per unit time and length Λ is defined as below,

$$\Lambda \equiv \frac{2\pi GM\rho_\infty}{v_\infty}, \tag{2.20}$$

which is independent on R. The momentum flux in the θ direction through the region $[R, R+dR]$ is

$$\Lambda \cdot v_{\theta=0} \cdot \frac{1}{2\pi S} = \Lambda \frac{1}{2\pi S} \sqrt{\frac{2GM}{R}}, \tag{2.21}$$

where $v_{\theta=0}$ represents the theta-component of the velocity at the accretion axis. Also, s is the radius of the circular cross-section when the accretion column is cut perpendicularly to the accretion axis at $z = R$. In the right hand side of this equation, we substitute the general solution described by Equation 2.13 into $v_{\theta=0}$.

Here, we consider a scenario where the balance between the thermal pressure exerted from the inside of the accretion column and the ram pressure exerted by matters flowing into the accretion column at the velocity $v_{\theta=0}$ is assumed. This is a first-order approximation under the condition that the size of

the accretion column is constant in time. Based on this assumption, we obtain the following expression for the pressure inside the accretion column using Equation 2.21:

$$P_{\rm s} \approx \frac{\Lambda}{2\pi s}\sqrt{\frac{2GM}{R}}. \tag{2.22}$$

To compare the gas pressure gradient force with the gravity, we consider a part of the accretion column enclosed by the cross-sections at distances R and $R + dR$. The pressure gradient force acting on the matter in this region can be expressed as follows,

$$d(\pi s^2 P_{\rm s}) = \Lambda\sqrt{\frac{GM}{2}}d\left(\frac{s}{\sqrt{R}}\right). \tag{2.23}$$

Next, we estimate the gravity acting on the matter. The timescale for the matter to accrete from the collision point on the accretion axis, $R_{\theta=0}$ (Equation 2.17), to the central gravitational object is $R_{\theta=0}/v_\infty$. If this timescale is multiplied by the mass accretion rate $\dot{M}_{\rm HL}$ (Equation 2.11) and divided by the length of the accretion column, the mass per unit length of the accretion column, m, is obtained:

$$m \approx \frac{R_{\theta=0}}{v_\infty}\frac{1}{R_{\theta=0}}\dot{M}_{\rm HL} = \Lambda\frac{GM}{v_\infty^3} \tag{2.24}$$

From this, we can estimate the gravity acting on the matter in the tiny width dR on the accretion column as follows:

$$F_{\rm gr} = \frac{GMmdR}{R^2}. \tag{2.25}$$

We assume that the accretion column is approximately conical in shape ($ds/s \approx dR/R$). Using this approximation and Equations 2.23 and 2.25, the pressure gradient force and gravity can be approximately expressed as follows:

$$d(\pi s^2 P_{\rm s}) \sim \Lambda\sqrt{\frac{GM}{2}}\frac{s}{R^{2/3}}dR, \tag{2.26}$$

$$F_{\rm gr} \sim \Lambda\frac{G^2M^2}{v_\infty^3}\cdot\frac{dR}{R^2}. \tag{2.27}$$

The Hoyle-Lyttleton radius is given by $R \sim GM/v_\infty^2$, and it is considered that the matter in the accretion column within this distance accretes onto the wandering BHs. Here, we assume that the geometric thickness of the accretion column is much smaller than this Hoyle-Lyttleton radius, i.e., the accretion column is geometrically thin ($s \ll R$). Under this assumption, it is clear that the pressure gradient force is significantly smaller than the gravity (see Equation 2.26 and 2.27).

Assuming the average velocity of the matter in the accretion column is v, we can establish the mass conservation law and momentum one in the accretion column using the previously introduced variables m (Equation 2.24) and Λ (Equation 2.20),

$$\frac{d}{dR}(mv) = \Lambda, \tag{2.28}$$

$$\begin{aligned}\frac{d}{dR}(mv^2) &= \Lambda v_R - \frac{GMm}{R^2}\\ &= \Lambda\sqrt{v_\infty^2 + \frac{2GM}{r} - \left(\frac{2GM}{rv_\infty}\right)^2} - \frac{GMm}{R^2}\\ &= \Lambda\sqrt{v_\infty^2 + v_\theta v_\infty - v_\theta^2} - \frac{GMm}{R^2}\\ &= \Lambda v_\infty - \frac{GMm}{R^2}.\end{aligned} \tag{2.29}$$

In the second equality of Equation 2.29, we substitute the analytical solution for v_R (Equation 2.12), and in the final equality, an approximation is made by setting the velocity in the direction perpendicular to the accretion axis to zero ($v_\theta = 0$) on the accretion column. Hereafter, we introduce the dimensionless variables defined as follows for velocity v, distance R, and mass m:

$$\nu \equiv \frac{v}{v_\infty}, \tag{2.30}$$

$$\chi \equiv \frac{R}{GM/v_\infty^2}, \tag{2.31}$$

$$\mu \equiv \frac{m}{\Lambda GM/v_\infty^3}. \tag{2.32}$$

The dimensionless parameter $\chi = 2$ corresponds to the Hoyle-Lyttleton radius $R_{\rm HL}$. Substituting these dimensionless variables into Equations 2.28 and 2.29, we obtain the dimensionless mass conservation law and momentum conservation law in the accretion column;

$$\frac{d}{d\chi}(\mu\nu) = 1, \tag{2.33}$$

$$\frac{d}{d\chi}(\mu\nu^2) = 1 - \frac{\mu}{\chi^2}. \tag{2.34}$$

Integrating Equation 2.33 with respect to χ, we obtain:

$$\mu\nu = \chi - \alpha, \tag{2.35}$$

where α means integral constant. Since μ represents scaled mass and is always positive, ν changes sign at $\chi = \alpha$ based on Equation 2.35. Therefore, α denotes the stagnation point, where the matter that satisfies the condition $\chi < \alpha$ accretes.

Based on the above discussion, we estimate the accretion rate including the structure of the accretion column using α. Substituting Equation 2.35 into the momentum conservation equation (Equation 2.34), we obtain:

$$\nu\frac{d\nu}{d\chi} = \frac{\nu(1-\nu)}{\chi - \alpha} - \frac{1}{\chi^2}. \tag{2.36}$$

To understand the general behavior of this equation, we set the three boundary conditions:

- $\nu \to 1$ at $\chi \to \infty$ (velocity is v_∞ at infinity)
- $\nu = 0$ at $\chi = \alpha$ (velocity is zero at the stagnation point)
- $d\nu/d\chi > 0$ in any region (velocity is a monotonic function)

The first and second conditions can be satisfied for any value of α, but the last condition limits on α. To understand this, we introduce a new dimensionless variable, $\xi \equiv \chi/\alpha$. Substituting this into Equation 2.36, we obtain,

$$\nu\frac{d\nu}{d\xi} = \frac{\nu(\nu-1)}{\xi - 1} - \frac{1}{\alpha\xi^2}. \tag{2.37}$$

When $d\nu/d\xi = 0$ is satisfied, Equation 2.37 can be discribed as

$$\nu^2 - \nu + \frac{1}{\alpha\xi^2}(\xi - 1) = 0. \tag{2.38}$$

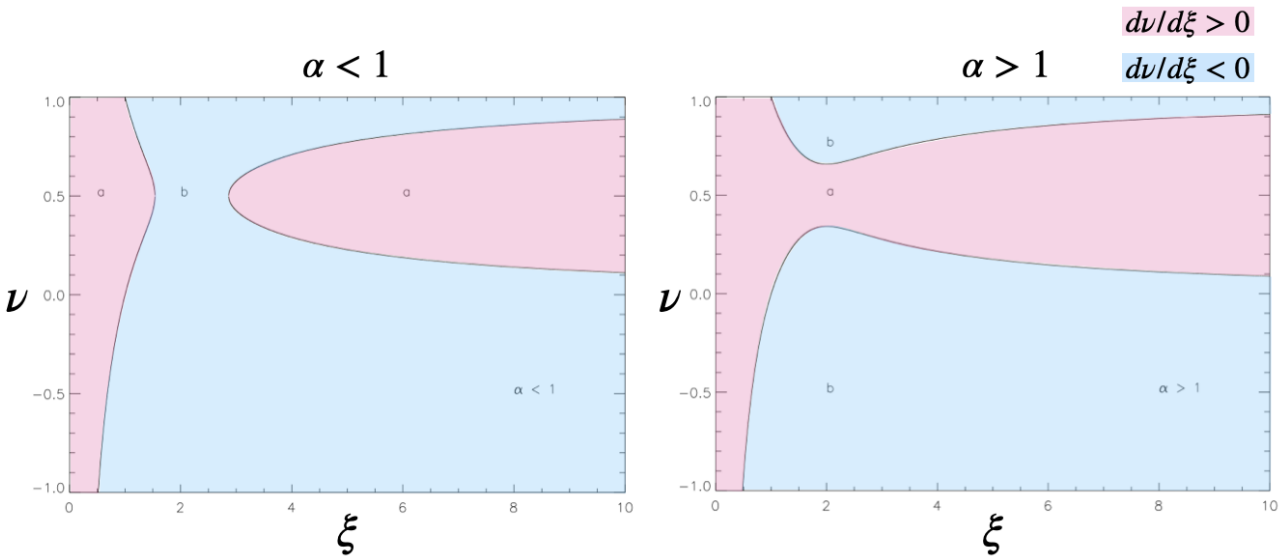

Figure 2.3: The regions where $d\nu$ changes sign, as dictated $d\xi$ by Equation 2.39. Left panel shows curves where $d\nu = 0$ for $\alpha > 1$. Right panel shows curves where $d\nu = 0$ for $\alpha < 1$. In the regions marked 'a', the derivative is $d\xi$ greater than zero. It is less than zero in the ' b ' regions. Cited from Edgar (2004) with some modification.

Solving this using the solution formulas for the quadratic equation, we obtain

$$\nu = \frac{1}{2} \pm \sqrt{\frac{1}{4} - \frac{1}{\alpha\xi^2}(\xi - 1)}. \tag{2.39}$$

Since ν represents the dimensionless quantity related to velocity, it should take real values. Then, we consider in what cases the discriminant expression becomes zero. From Equation 2.39, solving the discriminant of the quadratic equation with respect to ξ, we obtain the following:

$$\xi = \frac{2}{\alpha}(1 \pm \sqrt{1 - \alpha}). \tag{2.40}$$

This shows that ξ changes its behavior with $\alpha = 1$. Therefore, we plot the equation 2.39 by dividing the case $\alpha > 1$, $\alpha < 1$. Figure 2.3 cited from Edgar (2004) shows the region where the sign of $d\nu/d\xi$ changes (see Equation2.39). Considering the stable flows, the solution of ν should be monotonically increasing and should stay within the region marked 'a' (red region in Figure 2.3) as ξ changes. This is only possible when $\alpha > 1$. When $\alpha = 1$, undoing the dimensionless variables, we get $\chi = 1$, indicating that the stagnation point is halfway between the gravitational object and the Hoyle-Lyttleton radius. This means that the minimum accretion rate is $0.5\dot{M}_{\rm HL}$. Furthermore, Bondi & Hoyle (1944) showed that there is no unique stationary solution when $\alpha > 2$. Based on the above discussion, Bondi & Hoyle (1944) suggested that the mass accretion rate is about half of the Hoyle-Lyttleton accretion rate $\dot{M}_{\rm HL}$ (Equation 2.11), by including the downstream accretion column.

2.3 Bondi accretion

In the discussions by Hoyle & Lyttleton (1939) and Bondi & Hoyle (1944), it was assumed that the gas pressure could be neglected compared to the pressure due to the motion of the gas flow (ram pressure). Bondi (1952) investigated spherically symmetric accretion onto point-like gravitational objects considering the gas pressure, under the assumption that dynamical effect (ram pressure) could be neglected. In this section, we briefly outline the content of Bondi (1952).

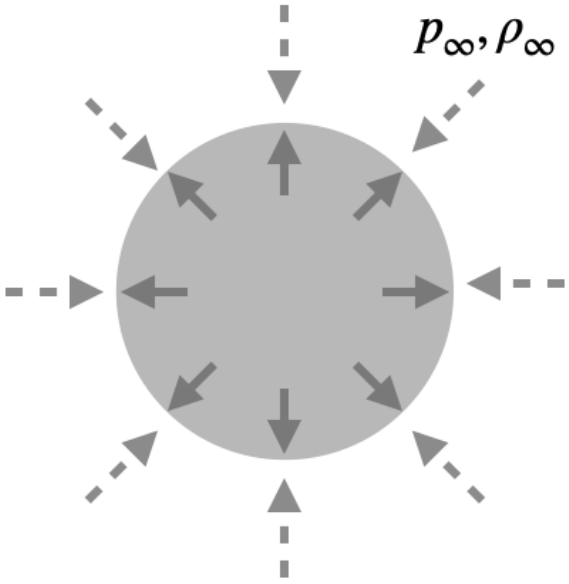

Figure 2.4: Sketch of the Bondi accretion geometry.

In Bondi (1952), They set the rest frame of a gravitational object with mass M. The gravitational object is immersed in the medium with uniform density ρ_∞, uniform pressure p_∞ and zero velocity at infinity. Additionally, the motion of the matter is steady and spherically symmetric. Neglecting the increase in mass of the gravitational object due to the accretion, the gravitational field remains constant for time. They assume that the relation between pressure p and density ρ follows the polytropic relation everywhere and at all times,

$$\frac{p}{p_\infty} = \left(\frac{\rho}{\rho_\infty}\right)^\gamma, \tag{2.41}$$

where γ represents the polytropic index, which is a constant given by $1 < \gamma < \frac{5}{3}$. Under these assumptions, the continuity equation becomes as follows:

$$4\pi r^2 \rho_\infty v = \dot{M} = \text{constant}, \tag{2.42}$$

where $\dot{M}$ is accretion rate. The Bernoulli equation (equation of motion in integral form) is,

$$\frac{v^2}{2} + \int_{p_\infty}^{p} \frac{dp}{\rho} - \frac{GM}{r} = \text{constant} = 0. \tag{2.43}$$

Here, the first term of the left hand side represents the kinetic energy of the fluid, the second term represents the enthalpy, and the third term represents the gravitational potential energy, respectively. The last equation arises from the boundary condition that the matter is stationary at infinity. Applying the polytropic relation (Equation 2.41) to the equation of motion (Equation 2.43), we obtain the following:

$$\frac{v^2}{2} + \frac{\gamma}{\gamma - 1}\frac{p_\infty}{\rho_\infty}\left[\left(\frac{\rho}{\rho_\infty^{\gamma-1}} - 1\right)\right] = \frac{GM}{r}. \tag{2.44}$$

Here, we define the sound speed as $c_s = \gamma p_\infty / \rho_\infty$, and introduce the following dimensionless quantities

for r, v, and ρ:

$$x \equiv \frac{r}{xGM/c_{\rm s}} \tag{2.45}$$

$$y \equiv \frac{v}{c_{\rm s}} \tag{2.46}$$

$$z \equiv \frac{\rho}{\rho_\infty} \tag{2.47}$$

Using these dimensionless variables, the continuity equation (Equation 2.41) and the equation of motion (Equation 2.43) can be rewritten as follows:

$$x^2 yz = \lambda, \tag{2.48}$$

$$\frac{1}{2}y^2 + \frac{z^{\gamma-1}-1}{\gamma-1} = \frac{1}{x}, \tag{2.49}$$

where λ is introduced as

$$\dot{M} = \frac{4\pi\lambda G^2 M^2 \rho\infty}{c_{\rm s}^3}. \tag{2.50}$$

From the definition of λ, we can see that it is a dimensionless parameter that determines the accretion rate. To solve Equations 2.48 and 2.49, we introduce the following variables:

$$u = yz^{-(\gamma-1)/2}. \tag{2.51}$$

Substituting this into the continuity equation (Equation 2.48) and solving for y and z, we obtain the following:

$$y = u^{2/(\gamma-1)} \left(\frac{\lambda}{x^2}\right)^{(\gamma-1)/(\gamma+1)} \tag{2.52}$$

$$z = \left(\frac{\lambda}{x^2 u}\right)^{2/(\gamma-1)}. \tag{2.53}$$

$$\tag{2.54}$$

Then, the equation of motion (Equation 2.49) becomes:

$$\frac{1}{2}u^{4/(\gamma+1)} \left(\frac{\lambda}{x^2}\right)^{2(\gamma-1)/(\gamma+1)} + \frac{1}{\gamma-1}\left(\frac{\lambda}{x^2 u}\right)^{2(\gamma-1)/(\gamma+1)} = \frac{1}{x} + \frac{1}{\gamma-1}. \tag{2.55}$$

Multiplying each term of this equation by $(x^2/\lambda)^{2(\gamma-1)/(\gamma+1)}$ and sorting of terms, we obtain:

$$f(u) = \lambda^{-2(\gamma-1)/(\gamma+1)} g(x), \tag{2.56}$$

where $f(x)$ and $g(x)$ are defined as:

$$f(u) = u^{4/(\gamma+1)} \left(\frac{1}{2} + \frac{1}{\gamma-1}\frac{1}{u^2}\right) \tag{2.57}$$

$$g(x) = \frac{x^{4(\gamma-1)/(\gamma+1)}}{\gamma-1} + x^{-(5-3\gamma)/(\gamma+1)}. \tag{2.58}$$

By examining the functions f and g, we can determine u as a function of λ and x. First, we assume $1 < \gamma < \frac{3}{5}$. Under this assumption, since f and g are sums of positive and negative powers of variables, each of them has a minimum value. When $u = u_{\rm min} = 1$, $f(u)$ takes the following minimum value:

$$f_{\rm min} = \frac{\gamma+1}{2(\gamma-1)}. \tag{2.59}$$

TABLE I

γ	1	1·2	1·4 = $\frac{7}{5}$	1·5	$\frac{5}{3}$
λ_c	$\frac{1}{4}e^{3/2} \doteqdot 1{\cdot}12\ldots$	$\frac{1}{4}(0{\cdot}7)^{-3{\cdot}5} \doteqdot 0{\cdot}872\ldots$	0·625	0·500	0·250

Figure 2.5: This table gives the value λ_c for a few values γ. Cited from Bondi (1952).

Also, when $x = x_{\rm min} = (5-3\gamma)/4$, $g(x)$ takes the following minimum value:

$$g_{\rm min} = \frac{\gamma+1}{4(\gamma-1)}\left(\frac{5-3\gamma}{4}\right)^{(5-3\gamma)/(\gamma+1)}. \tag{2.60}$$

The quantity x represents a dimensionless variable denoting distance, ranging from the surface of the central object to infinity. For instance, for the Sun, the value of x at its surface is approximately 5×10^{-6}. Therefore, since x reaches the value $x_{\rm min}$ over a physically significant interval, at some point within that interval, the right-hand side of Equation 2.56 become of the same order as $\lambda^{-2(\gamma-1)/(\gamma+1)}g_{\rm min}$. However, as f cannot reach a minimum value lower than $f_{\rm min}$, λ cannot exceed a critical value λ_c defined by as follows (see Table 2.5):

$$\begin{aligned}\lambda_c &= \left(\frac{g_{\rm min}}{f_{\rm min}}\right)^{(\gamma+1)/2(\gamma-1)} \\ &= \left(\frac{1}{2}\right)^{(\gamma+1)/2(\gamma-1)}\left(\frac{5-3\gamma}{4}\right)^{-(5-3\gamma)/2(\gamma-1)}.\end{aligned} \tag{2.61}$$

Based on the above considerations, Bondi (1952) concluded that in the case of spherically symmetric accretion taking into account gravity and pressure, the accretion rate $\dot{M}$ cannot exceed the following value:

$$\dot{M}_{\rm B} = \frac{4\pi\lambda_c G^2M^2\rho_\infty}{c_{\rm s}^3}. \tag{2.62}$$

In general, this is called Bondi accretion rate.

2.4 Bondi-Hoyle-Lyttleton accretion

Based on Hoyle & Lyttleton (1939) and Bondi & Hoyle (1944), Bondi (1952) proposed the following interpolation equation as the accretion rate of the wandering gravitational objects:

$$\dot{M}_{\rm BHL} = \frac{2\pi G^2M^2\rho_\infty}{(c_\infty^2+v_\infty^2)^{3/2}}, \tag{2.63}$$

where c_∞ is the sound speed at infinity. [1] When $c_\infty \ll v_\infty$ (the condition where gas pressure can be neglected), it matches the Hoyle-Lyttleton accretion rate (Equation 2.9). We note that numerical simulations performed by Shima et al. (1985) indicate that a factor of 2 is needed in the formula proposed by Bondi (1952) (Equation 2.63): [2]

$$\dot{M}_{\rm BHL} = \frac{4\pi G^2M^2\rho_\infty}{(c_\infty^2+v_\infty^2)^{3/2}}. \tag{2.64}$$

[1] The subscripts are based on the definitions in each literature: $c_{\rm s} = c_\infty$

[2] Hoyle-Lyttleton accretion and Bondi-Hoyle-Lyttleton accretion are often defined ambiguously. In general, the case in which the gas pressure can be ignored is called Hoyle-Lyttleton accretion, and the case in which the gas pressure is can be ignored is called Bondi-Hoyle-Lyttleton accretion.

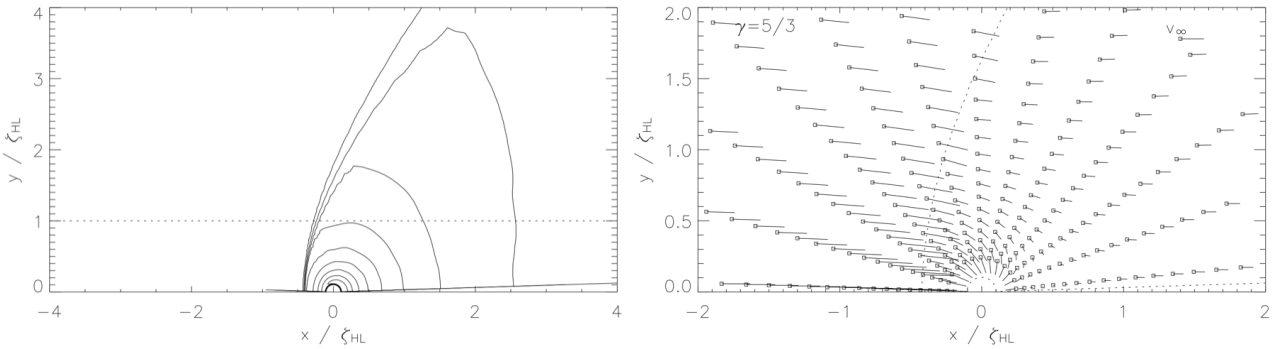

Figure 2.6: Left panel: density contours of Bondi–Hoyle–Lyttleton flows obtained by hydrodynamics simulations. The flow with mach number of $\mathcal{M} = 1.4$ is incident from the left. The specific heat ratio is $\gamma = 5/3$. The contours represent the gas density spaced over logarithmically. The dotted line indicates Hoyle-Lyttleton radius $\zeta_{\rm HL}$. Right panel: velocity field. The position of the bow shock is shown by a dotted line. Cited from Edgar (2004).

So far, we outlined a basic overview of the accretion mechanism of wandering gravitational objects. However, many simplifications have been made in the discussion, e.g., the effects of the fluid (gas pressure gradient forces) outside of the accretion column have not been considered. Hydrodynamics simulations that take into account the gravity of the central object successfully reproduced the accretion rate. On the other hand, the density and velocity structures derived analytically (e.g. Bisnovatyi-Kogan et al., 1979) are different from the results of hydrodynamics simulations.

Figure 2.6 shows the density structure (top) and velocity structure (bottom) from hydrodynamics simulations performed by Edgar (2004). These results are for a Mach number $\mu = 1.4$, a radius of gravitational object $0.1R_{\rm HL}$, and a specific heat ratio $\gamma = 3/5$. The density contours show that the shock waves form upstream of the flows ($x < 0$). The velocity structure indicates that after passing through the shock front (represented by the dashed line), the velocities decrease (the length of the streamlines correspond to the magnitude of the velocities). Furthermore, unlike the analytical solution by Bisnovatyi-Kogan et al. (1979) (Equation 2.15), the flows almost radially toward the gravitational object at downstream of the shock.

To summarize, the inclusion of hydrodynamic effects, such as shock waves, results in density and velocity structures that differ significantly from the analytical solution. However, hydrodynamics simulations have shown that the mass accretion rate nearly consistent with the analytical predictions by Hoyle & Lyttleton (1939) and Bondi (1952) (Equation 2.64) (see Figure 7 in Edgar, 2004). Thus, despite the simplifications in the discussions by Hoyle & Lyttleton (1939), Bondi (1952), and Bisnovatyi-Kogan et al. (1979), their predictions for the mass accretion rate are reproduced even when hydrodynamics effects are taken into account.

2.5 Bondi-Hoyle-Lyttleton accretion considering radiation feedback

In the classical Bondi-Hoyle-Lyttleton accretion proposed by Bondi (1952), the radiation from the central objects is not taken into account. However, considering the realistic situation where the seed BHs are wearing the accretion disks, the complex accretion structures are thought to appear due to the anisotropic radiation generated there. The increase in the sound speed of the gas near the BHs due to X-ray and UV heating (Ostriker et al., 1976, 2010; Cowie et al., 1978; Bisnovatyi-Kogan et al., 1979; Krolik et al., 1983; Vitello et al., 1984; Wandel et al., 1984), and the acceleration of gas and dust away

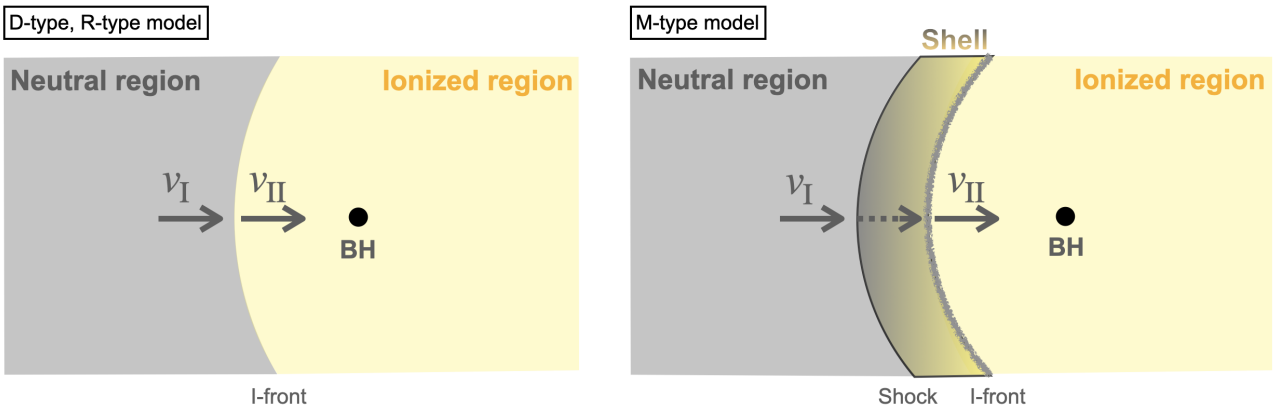

Figure 2.7: Left panel: Schematic image of the ionized and neutral regions for D-type and R-type case. Right panel: Schematic image of the ionized and neutral regions for M-type case. In this case, the dense shell appears in front of the I-front.

from the BHs by radiation pressure (Shapiro et al., 1973; Ostriker et al., 1976; Begelman et al., 1985; Ricotti et al., 2008), are responsible for this phenomenon. Indeed, the maximum accretion rate that can be achieved in most cases is the Eddington rate because of these radiation feedbacks.

In this section, we summarize the fundamentals and recent studies of the accretion process of wandering BHs considering the radiative feedback from the accretion disk.

2.5.1 Park & Ricotti 2013

Two-dimensional axisymmetric hydrodynamics simulations by Park & Ricotti (2013) showed that a comet-like ionized region is formed around the wandering BHs in the interstellar medium when radiative feedback is taken into account. Furthermore, they successfully reproduce their results on accretion rates by combining the classical Bondi-Hoyle-Lyttleton accretion model with an ionization front model (D-type, R-type). In this section, we review their work. Hereafter, we refer to Park & Ricotti (2013) as PR13.

In their model, Bondi-Hoyle-Lyttleton accretion occurs within the ionized region, i.e., the Bondi-Hoyle-Lyttleton radius is assumed to exist within the ionized region (see left panel of Figure 2.10) [3]. Therefore, assuming that the ionized gases come along parallel to the accretion axis (that is, ignoring complex motions), the mass accretion rate in PR13 can be expressed as follows:

$$\dot{M}_{\rm PR13} = 4\pi \frac{G^2 M^2 \rho_{\rm II}}{(v_{\rm II}^2 + c_{\rm II}^2)^{3/2}}, \tag{2.65}$$

where $\rho_{\rm II}$, $c_{\rm II}$ and $v_{\rm II}$ denote the gas density in the ionized region, sound speed in the ionized region, and gas velocity in ionized region. From Equation 2.65, it can be seen that physical quantities in the ionized region are needed to model the accretion rate of wandering BHs under radiation feedback. First, we introduce the density and velocity jump conditions across the ionization front (I-front).

Jump conditions across the I-front

The propagation of the ionization front (I-front) is considered here as a one-dimensional problem. Applying the rest frame of the I-front, the physical quantities in the neutral region are denoted as gas velocity $v_{\rm I}$, gas pressure $p_{\rm I}$, gas density $\rho_{\rm I}$, and gas temperature $T_{\rm I}$. The physical quantities in the ionized

[3] This assumption fails when the density is very high or the black hole mass is large (more details later).

region are denoted as $v_{\rm II}$, $p_{\rm II}$, $\rho_{\rm II}$, and $T_{\rm II}$, respectively. The jump conditions for mass and momentum conservation on the I-front are as follows:

$$\rho_{\rm I} v_{\rm I} = \rho_{\rm II} v_{\rm II} \tag{2.66}$$

$$\rho_{\rm I} v_{\rm I}^2 + p_{\rm I} = \rho_{\rm II} v_{\rm II}^2 + p_{\rm II}. \tag{2.67}$$

Assuming isothermal system both in the ionized region and in the neutral region, the sound speed can be expressed as $c_{\rm I} = \sqrt{p_{\rm I}/\rho_{\rm I}}$ and $c_{\rm II} = \sqrt{p_{\rm II}/\rho_{\rm II}}$. Substituting this into Equation 2.67, we obtain following equation:

$$\rho_{\rm I}(v_{\rm I}^2 + c_{\rm I}^2) = \rho_{\rm II}(v_{\rm II}^2 + c_{\rm II}^2). \tag{2.68}$$

Solving Equations 2.66 and 2.67 simultaneously yields the following solution:

$$\frac{\rho_{\rm II}}{\rho_{\rm I}} = \frac{v_{\rm I}}{v_{\rm II}} = \frac{v_{\rm I}^2 + c_{\rm I}^2 \pm \sqrt{(v_{\rm I}^2 + c_{\rm I}^2)^2 - 4 v_{\rm I}^2 c_{\rm II}^2}}{2 c_{\rm II}^2} \tag{2.69}$$

$$\equiv \Delta^{(\pm)}\left(v_{\rm I}, c_{\rm I}, c_{\rm II}\right). \tag{2.70}$$

In order for Equation 2.69 to have a real solution, the below conditions are needed:

$$v_{\rm I} \geqq v_{\rm R} \equiv c_{\rm II} + \sqrt{c_{\rm II}^2 - c_{\rm I}^2} \tag{2.71}$$

$$v_{\rm I} \leqq v_{\rm D} \equiv c_{\rm II} - \sqrt{c_{\rm II}^2 - c_{\rm I}^2} \tag{2.72}$$

In generally, the I-fronts with $v_{\rm I} < v_{\rm D}$ and $v_{\rm I} > v_{\rm R}$ are called D-type and R-type, respectively. Since there is a relation, $c_{\rm II} \gg c_{\rm I}$ (typically $c_{\rm II} \sim O(10)$km/s, $c_{\rm I} \sim O(1)$km/s), $v_{\rm R}$ and $v_{\rm D}$ can be approximated as

$$v_{\rm R} \approx 2 c_{\rm II} \tag{2.73}$$

$$v_{\rm D} \approx \frac{c_{\rm I}^2}{2 c_{\rm II}} \ll 1\text{km/s}. \tag{2.74}$$

R-type I-front

In the case with $v_{\rm I} > v_{\rm R} \sim 2c_{\rm II}$, the gas can directly reach the I-front with $v_{\rm I} = v_\infty$ and $\rho_{\rm I} = \rho_\infty$ because the shock wave does not appear in front of the I-front (more details later). The I-front becomes R-type (i.e., the minus sign is taken in Equation 2.69), and the density and velocity within the ionized region are given as shown below:

$$\rho_{\rm II,R} = \Delta^{(-)}\left(v_{\rm I}, c_{\rm I}, c_{\rm II}\right) \rho_{\rm I}, \tag{2.75}$$

$$v_{\rm II,R} = \frac{v_{\rm I}}{\Delta^{(-)}\left(v_{\rm I}, c_{\rm I}, c_{\rm II}\right)}, \tag{2.76}$$

$$\Delta^{(-)} = \frac{v_{\rm I}^2 + c_{\rm I}^2 - \sqrt{(v_{\rm I}^2 + c_{\rm I}^2)^2 - 4 v_{\rm I}^2 c_{\rm II}^2}}{2 c_{\rm II}^2} \tag{2.77}$$

$$\approx \frac{v_{\rm I}^2}{2 c_{\rm II}^2}\left(1 - \sqrt{1 - \frac{4 c_{\rm II}^2}{v_{\rm I}^2}}\right) \quad (c_{\rm II} \gg c_{\rm I}). \tag{2.78}$$

In this R-type model, the density jump and velocity jump is weak, since $\Delta^{(-)}$ takes a maximum value of 2 ($c_{\rm I} \ll c_{\rm II}$) at $v_{\rm I} = v_{\rm R}$ and approaches unity as $v_{\rm I}$ increases.

The accretion rate of R-type case can be estimated applying the density and velocity inside the ionized region obtained above to the classical Bondi–Hoyle– Lyttleton formula (Equation 2.65):

$$\dot{M}_{\rm R} = \frac{4\pi G^2 M^2 \rho_{\rm II,R}}{\left(v_{\rm II,R}^2 + c_{\rm II}^2\right)^{3/2}} \tag{2.79}$$

$$= \frac{4\pi G^2 M^2 \Delta^{(-)}\left(v_{\rm I}, c_{\rm I}, c_{\rm II}\right) \rho_{\rm I}}{\left(\left(\frac{v_{\rm I}}{\Delta^{(-)}(v_{\rm I}, c_{\rm I}, c_{\rm II})}\right)^2 + c_{\rm II}^2\right)^{3/2}} \tag{2.80}$$

$$\approx \frac{4\pi G^2 M^2 \rho_{\rm I}}{\left(v_{\rm I}^2 + c_{\rm II}^2\right)^{3/2}} \quad (c_{\rm II} \gg c_{\rm I}, \quad v_{\rm I} \gg v_{\rm R} \sim 2c_{\rm II}) \tag{2.81}$$

D-type I-front

In the case with $v_{\rm I} < v_{\rm D} \sim c_{\rm I}^2/(2c_{\rm II}) \ll c_{\rm I}$, the I-front becomes D-type (i.e., the plus sign is taken in Equation 2.69), and the density and velocity within the ionized region are given as described below:

$$\rho_{\rm II,D} = \Delta^{(+)}\left(v_{\rm I}, c_{\rm I}, c_{\rm II}\right) \rho_{\rm I}, \tag{2.82}$$

$$v_{\rm II,D} = \frac{v_{\rm I}}{\Delta^{(+)}\left(v_{\rm I}, c_{\rm I}, c_{\rm II}\right)}, \tag{2.83}$$

$$\Delta^{(+)} = \frac{v_{\rm I}^2 + c_{\rm I}^2 + \sqrt{(v_{\rm I}^2 + c_{\rm I}^2)^2 - 4v_{\rm I}^2 c_{\rm II}^2}}{2c_{\rm II}^2} \tag{2.84}$$

$$\approx \frac{c_{\rm I}^2}{2c_{\rm II}^2}\left(1 + \sqrt{1 - \frac{4v_{\rm I}^2 c_{\rm II}^2}{c_{\rm I}^4}}\right) \quad (c_{\rm II} \gg c_{\rm I}). \tag{2.85}$$

In this D-type model, the density jump and velocity jump is large, since $\Delta^{(+)}$ takes a value of $v_{\rm I}/c_{\rm II}$ ($c_{\rm I} \ll c_{\rm II}$) at $v_{\rm I} = v_{\rm D}$ and becomes larger as $v_{\rm I}$ decreases.

The accretion rate of D-type case can be estimated applying the density and velocity inside the ionized region obtained above to the classical Bondi–Hoyle– Lyttleton formula (Equation 2.65): Lyttleton formula (Equation 2.65) as

$$\dot{M}_{\rm D} = \frac{4\pi G^2 M^2 \rho_{\rm II,D}}{\left(v_{\rm II,D}^2 + c_{\rm II}^2\right)^{3/2}} \tag{2.86}$$

$$= \frac{4\pi G^2 M^2 \Delta^{(+)}\left(v_{\rm I}, c_{\rm I}, c_{\rm II}\right) \rho_{\rm I}}{\left(\left(\frac{v_{\rm I}}{\Delta^{(+)}(v_{\rm I}, c_{\rm I}, c_{\rm II})}\right)^2 + c_{\rm II}^2\right)^{3/2}}. \tag{2.87}$$

M-type I-front

In the case where ($v_{\rm D} < c_{\rm I} <$) $v_{\rm I} < v_{\rm R}$, the jump conditions in Equation 2.69 cannot be satisfied. Thus, the extra structures should be taken into account. In this range, it is known that a shock forms ahead of the I-front. The dense shell is composed between the shock and the I-front (see left panel of Figure 2.7). The I-front becomes the D-type because the gas transitions to below $v_{\rm D}$ in front of the I-front due to two effects. Firstly, the velocities are reduced by $(v_{\rm I}/c_{\rm I})^2$ while the densities increase by the same factor due to the isothermal shock. Secondly, the tangentially diverging motion is expexted to slow down the gas in the shell [4]. In PR13, the I-front is assumed critical D-type (i.e., $v_{\rm sh} = v_{\rm D}$). Therefore,

[4]This process is discussed in Sugimura & Ricotti (2020)

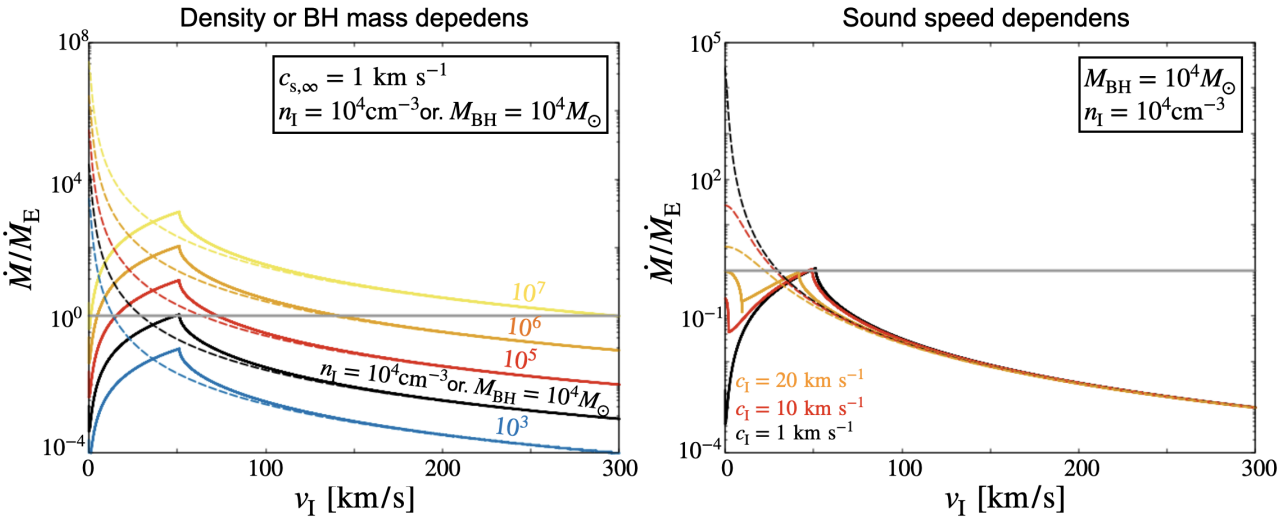

Figure 2.8: The accretion rate for PR13 model normalized by Eddington accretion rate defined as $\dot{M}_{\rm E} = L_{\rm E}/(\eta c^2)$, where we assume radiative effiency $\eta = 0.1$. The left panel shows the dependence of the accretion rate on BH mass or gas density, while the right panel shows the dependence on sound speed.

the velocity inside the ionized region is given by

$$v_{\rm II,M} = \frac{v_{\rm sh}}{\Delta^{(+)}\left(v_{\rm sh}, c_{\rm sh}, c_{\rm II}\right)} \tag{2.88}$$

$$= \frac{v_{\rm D}}{\Delta^{(+)}\left(v_{\rm D}, c_{\rm sh}, c_{\rm II}\right)} \quad (v_{\rm sh} = v_{\rm D}) \tag{2.89}$$

$$\approx c_{\rm II} \quad (c_{\rm sh} \ll c_{\rm II})\,. \tag{2.90}$$

Here, we assume that the total gas pressure $p_{\rm tot} = \rho(v^2 + c_{\rm s}^2)$, which is the sum of the ram pressure $p_{\rm ram} = \rho v^2$ and the thermal pressure $p_{\rm th} = \rho c_{\rm s}^2$, remains constant across both the shock and the I-front. It also remains constant within the shocked shell, where the flow is subsonic, because $p_{\rm tot}$ is approximately equal to $p_{\rm th}$ and $p_{\rm th}$ is conserved due to the nearly constant pressure. Using Equation 2.90 and $p_{\rm tot} = \rho_{\rm I}(v_{\rm I}^2 + c_{\rm I}^2)$, we can determine the density inside the ionized region:

$$\rho_{\rm II,M} = \frac{\rho_{\rm I}\left(v_{\rm I}^2 + c_{\rm I}^2\right)}{2c_{\rm II}^2}. \tag{2.91}$$

The accretion rate of M-type case can be estimated applying the density and velocity inside the ionized region obtained above to the classical Bondi–Hoyle– Lyttleton formula (Equation 2.65):

$$\dot{M}_{\rm M} = \frac{4\pi G^2 M^2 \rho_{\rm II,M}}{\left(v_{\rm II,M}^2 + c_{\rm II}^2\right)^{3/2}} \tag{2.92}$$

$$= \frac{4\pi G^2 M^2 \rho_{\rm I}\left(v_{\rm I}^2 + c_{\rm I}^2\right)}{2c_{\rm II}^2\left(\left(\frac{v_{\rm sh}}{\Delta^{(-)}(v_{\rm sh}, c_{\rm sh}, c_{\rm II})}\right)^2 + c_{\rm II}^2\right)^{3/2}} \tag{2.93}$$

$$\approx \frac{\pi G^2 M^2 \rho_{\rm I}\left(v_{\rm I}^2 + c_{\rm I}^2\right)}{\sqrt{2}c_{\rm II}^5} \quad (c_{\rm sh} \ll c_{\rm II})\,. \tag{2.94}$$

Here, to estimate the accretion rate of wandering BHs under the radiation feedback, we used the density $\rho_{\rm II}$ and velcity $v_{\rm II}$ in the ionized region. In summary, the accretion rate under the condition that the

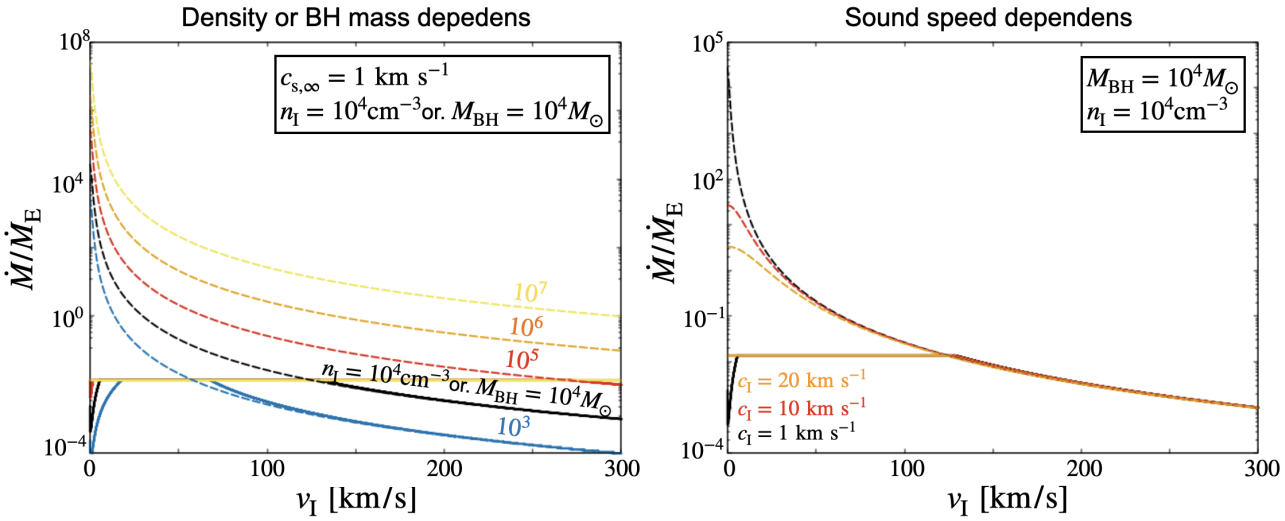

Figure 2.9: The accretion rate for PR13 model limited by Eddington accretion rate. The accretion rate is normalized by Eddington accretion rate defined as $\dot{M}_{\rm E} = L_{\rm E}/(\eta c^2)$, where we assume radiative efficiency $\eta = 0.1$. The left panel shows the dependence of the accretion rate on BH mass or gas density, while the right panel shows the dependence on sound speed.

size of the ionized region is smaller than the Bondi-Hoyle-Lyttleton radius can be expressed as follows:

$$\dot{M}_{\rm RFB} = \frac{4\pi G^2 M^2 \rho_{\rm II}}{(v_{\rm II}^2 + c_{\rm II}^2)^{3/2}} \begin{cases} \dot{M}_{\rm D} & v_{\rm I} < v_{\rm D} \\ \dot{M}_{\rm M} & v_{\rm D} < v_{\rm I} < v_{\rm R} \\ \dot{M}_{\rm R} & v_{\rm I} > v_{\rm R} \end{cases} . \tag{2.95}$$

The classical Bondi-Hoyle-Lyttleton accretion predicts that the accretion rate decreases monotonically as the velocity of the BHs relative to the ambient gas increases. However, under the radiative feedback, the accretion rate shows a very different dependence on the relative velocity. Figure 2.8 shows the accretion rate normalized by Eddington rate of PR13 model as described by Equation 2.95. The left panel shows the dependence of the accretion rate on the BH mass or the gas density, while the right panel shows the dependence on the sound speed. In the D-type regime, the accretion rate decreases steeply as the velocity of the BHs relative to the ambient gas increases. The accretion rate is approximately three orders of magnitude smaller than that of no radiation feedback case (ex. $v_{\rm I} = 1$ km/s and $c_{\rm I} \sim 10$ km/s case in right panel). Interestingly, as the BH motion becomes faster and the bow-shock (and dense shell) is formed (M-type regime), the accretion rate increases as the velocity increases. This result is definitely different from that predicted from the classical Bondi-Hoyle-Littleton model. In the R-type regime, the accretion rate decreases monotonically as a function of relative velocity. This sense is nearly consistent with the classical Bondi–Hoyle–Lyttleton solution shown as a dashed line in Figure 2.8. In this high-velocity regime, the shocks are not formed, and the flows are weakly affected by radiative feedback.

2.5.2 Park and Ricotti model + radiation force

In PR13, the accretion rate is dramatically smaller due to the radiation feedback than that of the classical model. The PR13 model is valid for cases where the accretion rate is less than the Eddington rate, because the Eddington rate is considered the upper limit due to the prevention of accretion by radiation pressure.

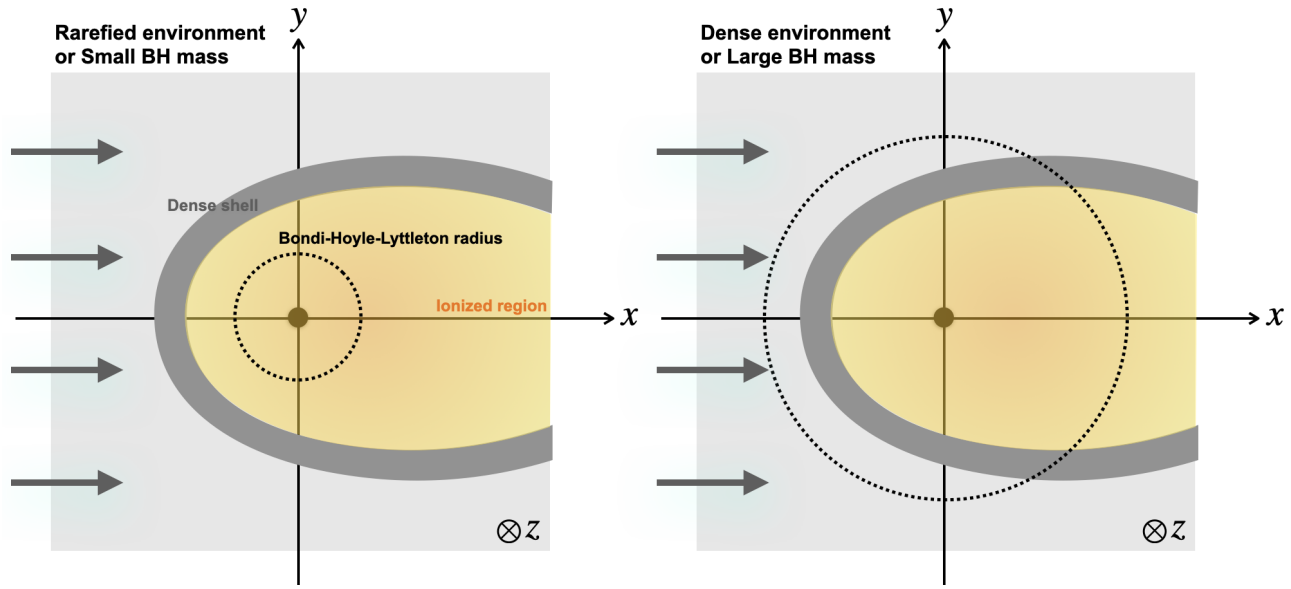

Figure 2.10: The relation between the size of the ionized region and the Bondi-Hoyle-Lyttleton radius. The left and right figures are for the cases where the surrounding medium is rarefied and dense, or where the BH mass is small and large.

Figure 2.9 is the same as Figure 2.8, but the Eddington accretion rate for dusty gas is set as the upper limit of the accretion rate. Here, the upper limit of the accretion rate is set to be $L_{\rm E,dg} = 4\pi cGM/(\kappa_{\rm es}+\kappa_{\rm d})$, where $L_{\rm E,dg}$ is the Eddington luminosity for dusty gas, $\kappa_{\rm es}$ is the electron scattering opacity, and $\kappa_{\rm d}$ is the absorption opacity by the dusty gas for the UV range. A metallicity of $0.1Z_{\odot}$ and a radiative efficiency of $\eta = 0.1$ are assumed. This figure shows that over a wide velocity range, the accretion rate is limited by the Eddington limit.

2.5.3 Ionized region vs. Gravitaional region

Recently, Inayoshi et al. (2016) proposed quantitatively the condition for the supercritical accretion in spherically symmetric systems considering the strong radiation from the BHs with luminosity $L \sim L_{\rm E}$. If the size of the ionized region surrounding the BHs is smaller than the gravitaional radius (Bondi radius, Bondi-Hoyle-Lyttleton radius), the ionized region collapses by intense inflows that consist of neutral gas, and thus the accretion system transitions to an isothermal Bondi accretion. Thus, the relation between the gravitational radius and the size of the ionized region is important for understanding the evolution of BHs. Here, we introduce the transition criterion.

Ionized region for Bondi-Hoyle-Lyttleton accretion

Here, we explain the Strömgren radius, which is one of the key physical quantities when studying the effect of radiation feedback on accretion phenomena of wandering BHs. When the interstellar medium is exposed to UV light produced by luminous objects, the matter is photoionized. Since the cooling and heating rates of the ionized gas are different from those of neutral gas, it is important to estimate how far the ionized region extends, measured from the BHs, in order to determine the accretion rate to the BHs. The location of the boundary between the ionized and neutral regions is called the Strömgren radius, after Bengt Strömgren, who first studied it.

The Strömgren radius can be roughly estimated from the balance between the number of ionizing photons injected into the interstellar medium from the luminous object per unit time and the number of recombined atoms of ionizing photons per unit time. First, the number of ionizing photons $\dot{N}_{\rm ion}$ injected into the interstellar medium from the luminous source per unit time is

$$\dot{N}_{\rm ion} = \int \frac{L_\nu}{h\nu} d\nu \sim \frac{L}{\langle h\nu \rangle}, \tag{2.96}$$

where L_ν is the luminosity at frequency ν, $h\nu$ is the energy per photon, L is the bolometric luminosity, and $\langle h\nu \rangle$ is the average energy per ionizing photon. Since the photoionization of the gas is caused by the UV light, the integration range is in the UV range. The last approximation holds when the SED is mainly composed of UV light. Next, the number of atoms that recombine per unit time $\dot{N}_{\rm rec}$ is

$$\dot{N}_{\rm rec} = \frac{4\pi}{3} R^3_{\rm II,st} n_{\rm e} n_{\rm II} \alpha, \tag{2.97}$$

where $R_{\rm II,st}$, $n_{\rm e}$, $n_{\rm II}$, and α indicate the Strömgren radius, number density of electron in the ionized region, number density of ionized gas, and recombination rate per unit time. If the interstellar medium is fully ionized, $n_{\rm e} = n_{\rm II}$. Thus, the number of atoms that recombine per unit time is $\dot{N}_{\rm rec} = 4\pi R^3_{\rm II,st} n^2_{\rm II} \alpha / 3$.

Assuming that Equation 2.96 and 2.97 are equal, we can obtain the Strömgren radius as follows:

$$R_{\rm II,st} = \left(\frac{3\dot{N}_{\rm ion}}{4\pi n^2_{\rm II} \alpha} \right)^{1/3}. \tag{2.98}$$

Previously, we introduce the size of the ionized region (Strömgren radius) by implicitly assuming that the surrounding interstellar medium is static. In the case of the Bondi-Hoyle-Lyttleton accretion mechanism, the effect of the inflow of neutral gas into the ionized region should be considered. However, it is difficult to discuss the size of the ionized region by including at once the effects of both recombination and incoming neutral gas. Thus, for simplicity, the size of the ionized region is estimated in two ways: the balance between the ionization rate and the recombination rate within the ionized region (Strömgren radius), and the balance between the ionization rate and the inflow rate of neutral gas across the I-front (see more details, Sugimura & Ricotti, 2020). We define the former (Strömgren radius) as $R_{\rm II,st}$ and later as $R_{\rm II,flow}$. We adopt the size of the ionized region determined by the smaller between $R_{\rm II,st}$ and $R_{\rm II,flow}$.

In the following, we estimate the size of the ionized region using the flow rate of the neutral gas. The balance between the number of ionizing photons injected from the luminous object per unit of time and the number of neutral gas flowing in from outside the ionized region per unit of time is expressed as follows,

$$\dot{N}_{\rm ion} = 4\pi R^2_{\rm II,flow} n_{\rm I} v_{\rm I}. \tag{2.99}$$

Sorting this out for $R_{\rm II,flow}$, and further using the conservation law of the number of particles at $R_{\rm II,flow}$ is $n_{\rm II} v_{\rm II} = n_{\rm I} v_{\rm I}$, we obtain:

$$R_{\rm II,flow} = \left(\frac{\dot{N}_{\rm ion}}{4\pi n_{\rm II} v_{\rm II}} \right)^{1/2}. \tag{2.100}$$

From Equation 2.100, we see that the larger velocity of the gas coming in from outside the ionized region, $v_{\rm I}$, the smaller the size of inoized region, $R_{\rm II,flow}$.

Here, we estimate the condition $R_{\rm II,st} > R_{\rm II,flow}$, which determines the size of the ionized region by the inflow of neutral gas from the outside, to see the critical velocity. First, let the temperature of the ionized

region be $T_{\rm II} = 4 \times 10^4$K and the frequency-averaged energy of the ionizing photons be $\langle h\nu \rangle = 41$eV. Assuming that the photons emitted during recombination to the ground state ionize the immediately surrounding neutral gas (case-B recombination), the recombination rate of ionized hydrogen atoms, $\alpha \equiv \alpha_{\rm B}$, excluding recombination to the ground state, is roughly inversely proportional to temperature and described as below (Ferland et al., 1992):

$$\alpha_{\rm B} = 2.6 \times 10^{-13} \left(\frac{T_{\rm II}}{10^4 {\rm K}} \right)^{-0.85} {\rm cm}^3 {\rm s}^{-1}. \tag{2.101}$$

The injection rate of ionizing photons per unit time is given by $\dot{N}_{\rm ion} \sim L / < h\nu >$, where the luminosity L is related to the energy conversion efficiency η by $L = \eta \dot{M} c^2$. The Eddington luminosity for dusty gas is used as L. To estimate the inflow rate of the neutral gas, we assume the R-type solution, which is solution for high-velocity cases. Solving for the condition $R_{\rm II,st} > R_{\rm II,flow}$ with respect to the velocity $v_{\rm I}$, we obtain the following result:

$$\begin{aligned}
R_{\rm II,st} &> R_{\rm II,flow} \\
\left(\frac{3\dot{N}_{\rm ion}}{4\pi n_{\rm II}^2 \alpha} \right)^{1/3} &> \left(\frac{\dot{N}_{\rm ion}}{4\pi n_{\rm I} v_{\rm I}} \right)^{1/2} \\
\frac{v_{\rm II}^4}{v_{\rm I}} &> \frac{\alpha^2 n_{\rm I} \dot{N}_{\rm ion}}{36\pi} \\
\frac{v_{\rm I}^3}{\Delta^{(-)4}} &> \frac{\alpha^2 n_{\rm I} L_{\rm E,dg}}{36\pi \langle h\nu \rangle} \\
v_{\rm I} &> \left(\frac{\alpha^2 c G M n_{\rm I} \Delta^{(-)4}}{9(\kappa_{\rm es} + \kappa_{\rm dust}) \langle h\nu \rangle} \right)^{1/3} \\
&\sim 371 \left(\frac{n_{\rm I} M}{10^8 M_\odot {\rm cm}^{-3}} \right)^{1/3} {\rm km/s}.
\end{aligned} \tag{2.102}$$

For example, when the BH mass $M = 10^4 M_\odot$ and the number density of neutral gas $n_{\rm I} = 10^4 {\rm cm}^{-3}$, if the neutral gas has a velocity greater than 370km/s, the size of the ionized region must be estimated using $R_{\rm II,flow}$. Conversely, if the velocity of the neutral gas is 370km/s or lower, the inflow of neutral gas does not affect the size of the ionized region. [5]

The size of ionized region vs. classical Bondi-Hoyle-Lyttleton radius

To estimate the transition criterion, $R_{\rm BHL} > R_{\rm II,st}$, we use the classical Bondi-Hoyle-Lyttleton radius $R_{\rm BHL}$ and the size of ionized region described by Equation 2.98:

$$\begin{aligned}
R_{\rm BHL} &> R_{\rm II,st} \\
\rightarrow \frac{2GM}{(v_{\rm I}^2 + c_{\rm I}^2)} &> \left(\frac{3\dot{N}_{\rm ion}}{4\pi n_{\rm II}^2 \alpha_{\rm B}} \right)^{1/3} \\
\rightarrow \frac{8G^3 M^3}{(v_{\rm I}^2 + c_{\rm I}^2)^3} &> \frac{12 c_{\rm II}^4 L_{\rm E,dg}}{4\pi n_{\rm I}^2 (c_{\rm I}^2 + v_{\rm I}^2)^2 \alpha_{\rm B} \langle h\nu \rangle} \\
M n_{\rm I} &> \left(\frac{3 c c_{\rm II}^4 \left(v_{\rm I}^2 + c_{\rm I}^2 \right)}{2G^2 \alpha_{\rm B} \langle h\nu \rangle \left(\kappa_{\rm es} + \kappa_{\rm dust} \right)} \right)^{1/2}.
\end{aligned} \tag{2.103}$$

[5] Here, we adopt the Eddington luminosity for dusty gas to evaluate the $\dot{N}_{\rm ion}$. We note that, if the luminosity is more smaller than this value, the velocity range in which the effect of Inflow becomes effective is smaller than the value in Equation 2.102.

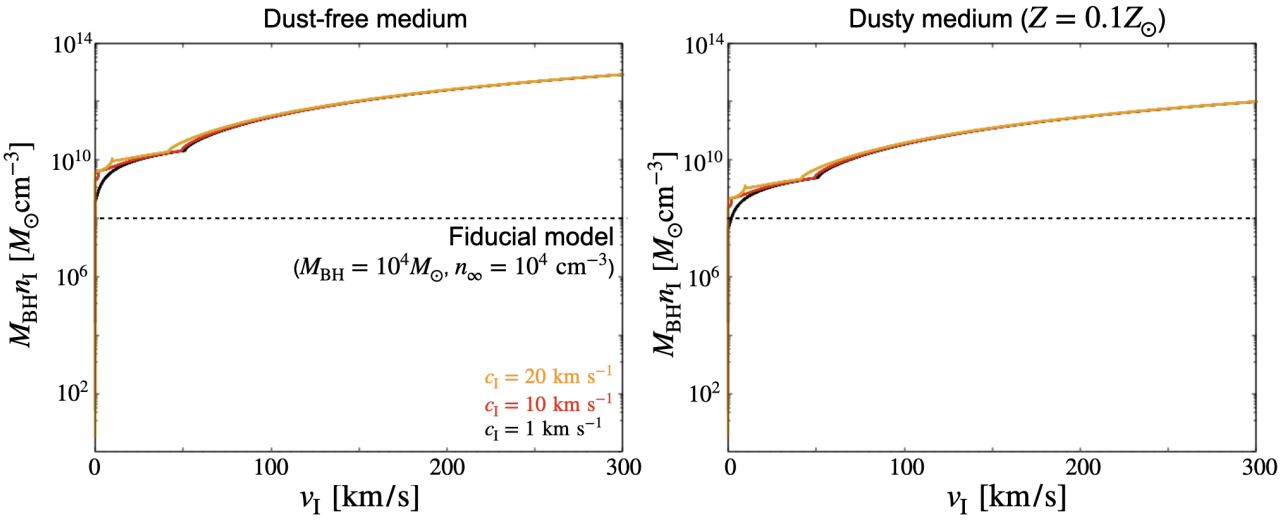

Figure 2.11: The figure shows the line where the Bondi-Hoyle-Lyttleton radius is equal to the size of the ionization region, with the product of the BH mass and gas density on the vertical axis and the relative velocity between the BHs and surrounding gas on the horizontal axis. The difference between the left and right figures is whether the Eddington luminosity is applied to electron scattering (left panel) or the Eddington luminosity is applied to dusty gas (rigth panel) when estimating the size of the ionized region.

We suppose that the system is in a quasi-steady state where the momentum flux is conserved across the ionization front, namely $2n_{\rm II}c_{\rm II}^2 = n_{\rm I}(c_{\rm I}^2 + v_{\rm I}^2)$.

Figure 2.11 shows Equation 2.103. From this figure, we see that massive BHs and extremely dense environments may lead to the collapse of ionized regions as predicted by Inayoshi et al. (2016) and classical Bondi-Hoyle-Lyttleton accretion could be realized.

2.5.4 Effects of dust grains on Bondi-Hoyle-Lyttleton accretion flow

Dust grains in the Universe

Interstellar dust grains consist of solid particles with size on the order of a few micrometers, existing within the interstellar medium. In our galaxy, the composition of dust grains is primarily carbon C and silicon Si, and the ratio of dust mass to the total mass of the interstellar gas, accounting for abundance, is suggested to be approximately 0.01. The composition and abundance of the dust grains depend on various physical processes such as condensation formation of the gas and destruction by the shock waves. We first introduce the formation process of the dust grains.

How is dust grain formed?

The formation of the solid phase (dust grains) from the gaseous phase occurs through the formation of stable nuclei by collision and deposition of atoms and molecules and their growth. The composition of the dust grains in the interstellar medium consists of heavy elements. Therefore, it is believed that dust grains are formed in the regions abundant with heavy elements. The promising dust formation sites in space are “in the stellar winds of Asymptotic Giant Branch (AGB) stars” which evolved from stars with initial masses less than 10 times that of the Sun, and “in the ejecta" which ejected during the gravitational collapse of the massive stars. In the early universe with redshifts greater than 6, the contribution of AGB stars to the dust supply is expected to be small. This is because most low-mass stars are unable to outgrow the main sequence and become AGB stars within the cosmic age of less

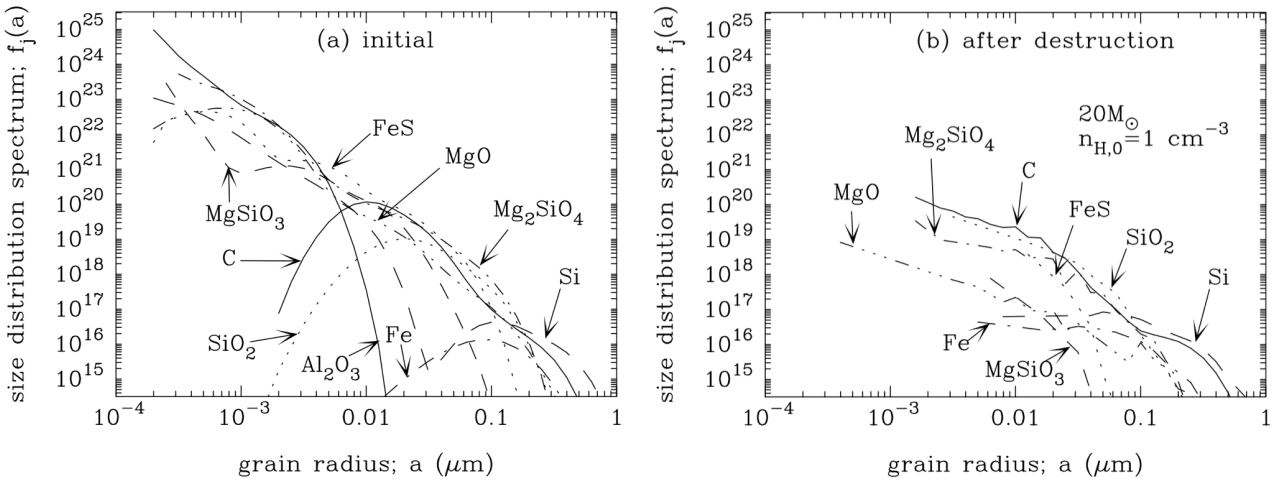

Figure 2.12: The grain size distribution of each dust species: (a) is the initial distribution before destruction, and (b) is the distribution of the surviving dust after destruction. Cited from Nozawa et al. (2007).

than 1 billion years ($z \sim 6$). Therefore, the main formation site of dust grains in the early universe is in the ejecta by supernova explosions which is the final stage of massive stars with short lifetimes. The mechanism of dust formation in the ejecta model is as follows. As the gases expand outward during a supernova explosion, the gas temperature decreases. When the temperature of the gas drops to around 10^3K, the heavy element gas becomes supersaturated, leading to the condensation and formation of dust grains.

The left panel of Figure 2.12 shows the simulation results of size distribution of the dust grains in ejecta generated by supernova explosions (Nozawa et al., 2007). The horizontal axis represents the radius of the dust grains, and the vertical axis represents the mass spectrum. From the left panel, we can see that the size of the dust grains formed via supernova explosions range from a few angstroms to a few micrometers, varying depending on the dust compositions. The size variation for each composition of the dusts strongly depends on the relative abundance of heavy elements. For example, since the abundance of Al is relatively small compared to other heavy elements, it is expected that the average radius of Al_2O^3 dust, which utilizes Al as a material, is also small. The size of dust grains composed of relatively abundant atoms such as Si and Fe is larger (around 0.1μm) compared to that of the dust grains composed of other materials. Such geometric sizes of the dust grains are crucial when considering the extinction process of the dust grains, as will be discussed in next subsection.

Destruction of dust grains

For several hundred days after a supernova explosion, dust grains are formed through the condensation process described in Section 2.5.4. However, not all of such the dust grains is released directly into interstellar space. Dust destruction occurs due to the shock waves.

Initially, the shock waves propagate outward from the supernova explosion. As these shock waves propagate outward, they decelerate due to interactions with the surrounding gas. When the decelerated ejecta and additional ejecta coming from the interior collide, the reverse shock waves are generated. These reverse shock waves lead to the destruction of the dust grains.

From a microscopic perspective, dust destruction by shock waves involves a phenomenon called sputtering, where atoms are ejected from the surface of the dust grains. As a result of the sputtering,

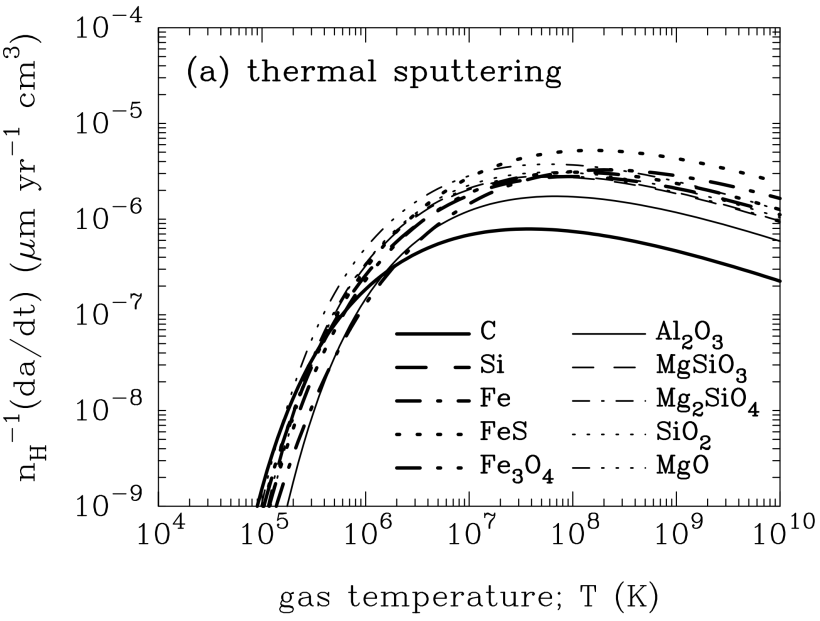

Figure 2.13: Erosion rate of each dust species caused by sputtering calculated for the metallicity of $Z = 10^{-4} Z_\odot$. Cited from Nozawa et al. (2006).

the radius of the dust grains gradually decrease. Figure 2.13, cited from Nozawa et al. (2006), shows this process. We can see that the reduction in dust radius due to the sputtering is effective at gas temperatures $T \gtrsim 10^5$K. Moreover, at temperatures $T \gtrsim 10^7$K, the rate of radius reduction does not significantly depend on the dust composition or gas temperature, with a erosion rate of 10^{-6}yr^{-1}cm^3. Considering the initial dust radius to be approximately $\sim 0.1\mu$m (refer to the left panel of Figure 2.12), this implies that the dust radius becomes zero on a timescale of around $\sim 10^7$yr.

Furthermore, the mass spectrum distribution of dust radii after the progress of dust destruction by shock waves is represented in the right panel of Figure 2.12 (Nozawa et al., 2007). Comparing the mass spectrum distribution after dust destruction by shock waves (right panel of Figure 2.12) with the mass spectrum distribution at the time of dust formation (left panel of Figure 2.12), it is clear that dust grains with small radius of $10^{-4} \sim 10^{-2}\mu$m has significantly decreased due to destruction. Therefore, based on the results from Nozawa et al. (2007), it can be inferred that the typical radius of dust grains released into interstellar space is $\gtrsim 0.1\mu$m.

As seen thus far, the distribution of dust in interstellar space undergoes significant changes due to dust destruction by shock waves. A more quantitative representation of the decrease in total dust mass compared to its formation is depicted in Figure 2.14 (Nozawa et al., 2007). Examining this figure, when the number density of surrounding interstellar gas is 0.1cm^{-3}, it becomes apparent that approximately 80% of the dust formed in the ejecta survives. Conversely, in cases where the interstellar gas density is higher, between $10\% - 30\%$ of the dust survives. The decrease in the total mass of surviving dust grains with increasing gas density can be attributed to the faster penetration of reverse shock waves as the gas density increases, leading to higher efficiency of sputtering.

Photon absorption by dust grains

In the dusty gas, where dust grains and gases coexist, photons with energies in the UV range are absorbed by the dust grains and scattered by electrons in the gas. In this section, we introduce the

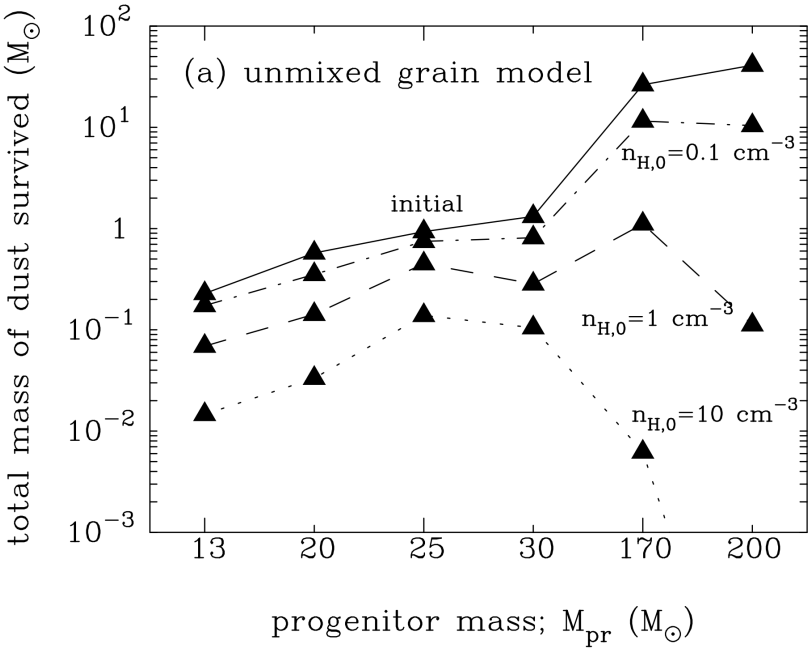

Figure 2.14: Total mass of survived dust for the various progenitor masses, $M_{\rm pr}$. Each solid line represents the gas number density. Cited from Nozawa et al. (2006).

opacity $\kappa_{\rm dg}$ of dusty gas.

First, we set some parameters for dust grains with reference to Nozawa et al. (2007) and Yajima et al. (2017):

- Geometric radius of dust grain: $a_{\rm dust} = 0.1\mu{\rm m} = 10^{-5}{\rm cm}$
- Cross section of dust absorption: $\sigma_{\rm dust} = Q_{\rm abs}\pi a_{\rm dust}^2 {\rm cm}^2$
- Absorption coefficient to geometrical cross section: $Q_{\rm abs} = 1$
- Opacity for UV photons: $\kappa_{\rm dust} = \frac{\sigma_{\rm dust}}{m_{\rm dust}} = \frac{\sigma_{\rm dust}}{\rho_{\rm s} 4\pi a_{\rm dust}^3/3} = \frac{3Q_{\rm abs}}{4a_{\rm dust}\rho_{\rm s}} = 2.8\times10^4 Q_{\rm abs}{\rm g}^{-1}{\rm cm}^2$
- Dust-to-gas mass ratio: $f_{\rm dg} = 0.01$

Here, $m_{\rm dust}$ is the mass of the dust and $\rho_{\rm s}$ is the solid density of the dust. The dust radius $a_{\rm dust}$ is reasonable because the average radius of the dust after experiencing a reverse shock shock wave is $a_{\rm dust} \sim 0.1\mu$m in the simulation of dust formation from a supernova explosion by Nozawa et al. (2007). The dust absorption cross section $\sigma_{\rm dust}$ is defined by multiplying the geometric cross section estimated using the dust radius $a_{\rm dust}$ (assuming the dust is spherical) by a factor less than 1 called the absorption coefficient $Q_{\rm abs}$. From Draine et al. (1984), when the wavelength of the incident electromagnetic wave is smaller than $\sim 2\pi a_{\rm dust}$, the absorption coefficient is $Q_{\rm abs} \sim 1$. The dust-to-gas mass ratio $f_{\rm dg}$ is proportional to the metallicity. Observations of nearby galaxies show that for $Z_\odot$, $f_{\rm dg} \sim 0.01$ (Draine et al., 2007).

Applying the above parameters, the opacity $\kappa_{\rm dg}$ of dusty-gas is obtained as follows. We sum each

absorption cross-section of gas and dust with the weight of their abundance,

$$\begin{aligned}\kappa_{\rm dg} &= \frac{n_{\rm gas}\sigma_{\rm T} + n_{\rm dust}\sigma_{\rm dust}}{\rho_{\rm gas} + \rho_{\rm dust}} \\ &= \frac{\frac{\sigma_{\rm T}}{m_{\rm gas}} + \frac{n_{\rm dust}\sigma_{\rm dust}}{\rho_{\rm gas}}}{1 + f_{\rm dg}} = \frac{\sigma_{\rm T}}{m_{\rm gas}}(1 + f_{\rm dg}) + \frac{\sigma_{\rm dust}}{m_{\rm dust}} f_{\rm dg}(1 + \rho_{\rm dust}) \\ &\simeq \frac{\sigma_{\rm T}}{m_{\rm gas}} + f_{\rm dg}\frac{\sigma_{\rm dust}}{m_{\rm dust}} \\ &= \kappa_{\rm es} + f_{\rm dg}\kappa_{\rm dust} = 0.4 + 280 Q_{\rm abs} \ \ {\rm g}^{-1}{\rm cm}^3, \end{aligned} \tag{2.104}$$

where $\sigma_{\rm T}$ is the cross section of electron scattering and $\kappa_{\rm es} = 0.4{\rm g}^{-1}{\rm cm}^3$ is the opacity of electron scattering. Also, in the fourth equality, we made an approximation that ignores $f_{\rm dg}$ and $\rho_{\rm dust}$ as small compared to 1. From Equation 2.104, the ratio of dusty gas opacity to electron scattering opacity is $\kappa_{\rm dg}/\kappa_{\rm es} \sim 1000$ if $Q_{\rm abs} \sim 1$. Therefore, the radiation force on dust becomes about 1000 times stronger than that on gas, and the structure of the Bondi-Hoyle-Lyttleton accretion flow is expected to differ significantly depending on the presence or absence of dust.

Sublimation of dust grains

When wandering BHs are wearing by accretion disks, the dust (solid particle) is heated by the radiation emitted from the accretion disks and evaporates into a gas. This process is called the dust sublimation. If the dust sublimation radius (the boundary between the region where dust is sublimated and the region where dust is not sublimated) is inside the Bondi-Hoyle-Lyttleton radius, it is necessary to perform Bondi-Hoyle-Lyttleton scale simulations considering dust sublimation process. This is because the radiation force acting on the dust is enormously greater than the radiation force acting on the gas, and thus the presence/absence of dust is expected to have a significant effect on the accretion rate. Conversely, if the dust sublimation radius exists outside of the Bondi-Hoyle-Lyttleton region, it is not necessary to consider the presence of dust for the Bondi-Hoyle-Lyttleton scale simulations. Therefore, here we estimate the size of the region where dust is heated and sublimated by the luminous accretion disk and compare it to the Bondi-Hoyle-Lyttleton radius.

We suppose that the dust emits blackbody radiation. The equation for the balance between the radiation flux absorbed by the dust and the radiation flux re-emitted by the dust is as follows:

$$Q_{\rm abs}\frac{L}{4\pi R_{\rm subl}^2} = Q_{\rm emit}\sigma_{\rm SB}T_{\rm subl}^4, \tag{2.105}$$

where $R_{\rm subl}$ is sublimation radius, $T_{\rm subl}$ is sublimation temperature, $\sigma_{\rm SB}$ is Stefan-Boltzmann constant, L is luminosity of radiation source, $Q_{\rm abs}$ is dimensionless absorption coefficient, $Q_{\rm emit}$ is dimensionless emission coefficient, respectively. The $Q_{\rm abs}$ and $Q_{\rm emit}$ are generally normalized by its geometric cross section $\pi a_{\rm d}^2$:

$$Q_{\rm abs} = \frac{\sigma_{\rm abs}}{\pi a_{\rm d}^2}, \quad Q_{\rm emit} = \frac{\sigma_{\rm emit}}{\pi a_{\rm d}^2}. \tag{2.106}$$

Here, $\sigma_{\rm abs}$ and $\sigma_{\rm emit}$ are the effective cross sections which the dust absorbs and re-emits photons. Since $\sigma_{\rm abs}$ and $\sigma_{\rm emit}$, as well as $Q_{\rm abs}$ and $Q_{\rm emit}$, depend on the wavelength of the radiation incident on the dust. Solving Equation 2.105 for the sublimation radius,

$$R_{\rm subl} = \left(\frac{Q_{\rm abs}}{Q_{\rm emit}}\frac{L}{4\pi\sigma_{\rm SB}T_{\rm subl}^4}\right)^{1/2}. \tag{2.107}$$

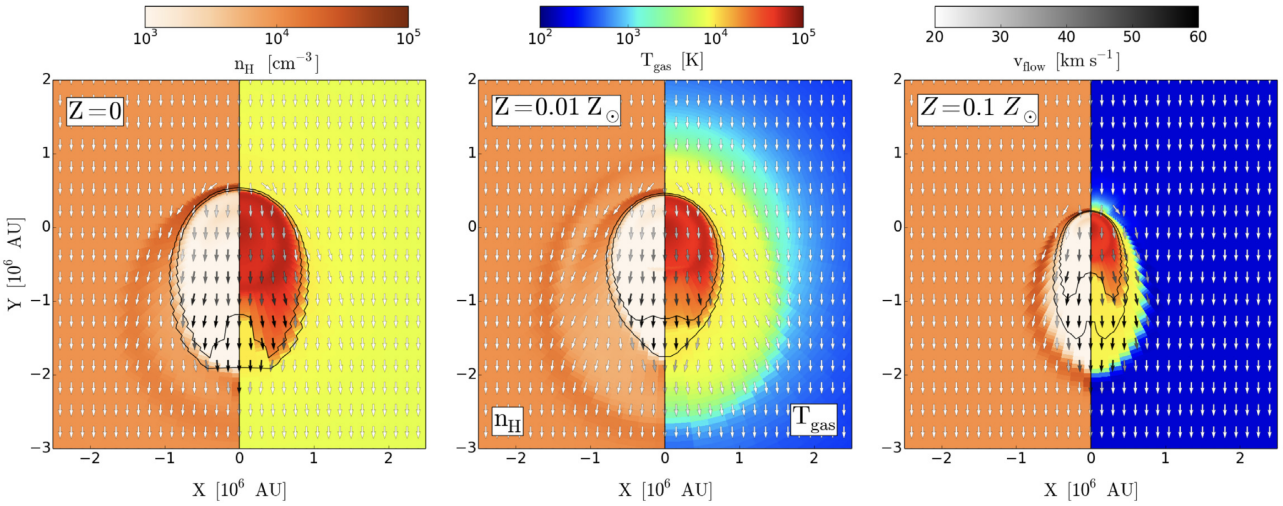

Figure 2.15: Metallicity dependence of the gas number density and gas temperature around a moving intermediate-mass BH. The panels show snapshots for the medalists $Z = 0$,$Z = 0.01Z_\odot$, and $Z = 0.1Z_\odot$ models from the left- to right-hand panels. The arrows represent the velocity vectors of the gas. Cited from Toyouchi et al. (2020).

We would like to know where the dust sublimation radius $R_{\rm subl}$ is located relative to the Hoyle-Lyttleton radius $R_{\rm BHL}$, so we calculate the ratio,

$$\begin{aligned}\frac{R_{\rm subl}}{R_{\rm BHL}} &= \left(\frac{Q_{\rm abs}}{Q_{\rm emit}}\frac{L}{4\pi\sigma_{\rm SB}T_{\rm subl}^4}\right)^{1/2}\times\frac{(v_{\rm I}^2+c_{\rm I}^2)}{2GM}\\ &= \left(\frac{Q_{\rm abs}}{Q_{\rm emit}}\frac{c(v_{\rm I}^2+c_{\rm I}^2)^2}{4GM\sigma_{\rm SB}T_{\rm subl}^4}\right)^{1/2}\\ &\sim 10^{-4}\frac{Q_{\rm abs}^{1/2}}{Q_{\rm emit}^{1/2}}\left(\frac{M}{10^4M_\odot}\right)^{-1/2}\left(\frac{T_{\rm subl}}{10^3\ {\rm K}}\right)^{-2}\left(\frac{\sqrt{v_{\rm I}^2+c_{\rm I}^2}}{20\ {\rm km/s}}\right)^2\end{aligned} \tag{2.108}$$

Here, the Eddington luminosity $L_{\rm E,dg}$ for dusty-gas is applied as the luminosity L. The sublimation temperature of the dust is assumed to be $T_{\rm subl} = 1000$K. This value is not significantly inconsistent with the estimated sublimation temperatures given by Barvainis et al. (1987), which are about $1500-1900$K for graphite and abou$1000-1400$K for silicate.

We can see that $R_{\rm subl} \ll R_{\rm BHL}$ is satisfied. Therefore, it is important to consider the dust sublimation process when studying the Bondi-Hoyle-Lyttleton accretion with radiation.

Simulations of wandering BHs in the dusty-gas

Toyouchi et al. (2020) investigate the Bondi-Hoyle-Lyttleton accretion flow considering dust grains and isotropic radiation field. Figure 2.15 shows the distributions of the number density of the hydrogen and the gas temperature. Each panel shows the different models for the metallicities of $Z = 0, 0.01, 0.1Z_\odot$. It clear that, in the all models, an ionized region elongated downstream. Additionally, the dense shell appears in the upstream side of the I-front. These features are generally consistent with PR13 (see Section 2.5.1). In the model of $Z = 0$, there are two thermal structures: warm region (10^4K, yellow region) and the hot region ($T \sim 5\times10^4$K, red region). On the other hand, in the model of $Z = 0.01, 0.1Z_\odot$, the cold region ($T \sim 10^2$K, blue region) appears around the warm region. In the cold

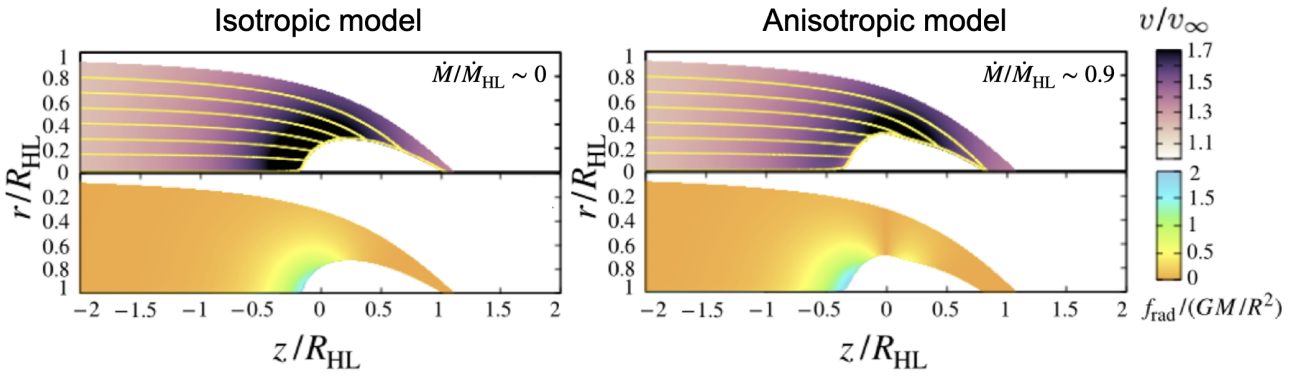

Figure 2.16: Velocity field (upper color contour) and the ratio of radiation force to gravity (lower color contour) of the isotropic model (left panel) and anisotropic model (right panel). The yellow lines overlaid in velocity distribution show the streamlines. Cited from Ogata et al. (2021).

region, the gas is in a thermal equilibrium state where heating by the background radiation and metal-line cooling are balanced. In addition, only in the model of $Z = 0.01Z_\odot$, the thermal structure along the boundary between the cold and warm regions appears ($T \sim 10^3$K, light-blue and green regions). The temperature in this region is determined by the balance between photoionization heating and Ly α cooling, because the gas is partly ionized by X-ray photons leaking from the ionized region. Such a double-layered temperature structure outside of the ionized region disappears for the higher metallicity $Z = 0.1Z_\odot$. In the high-metallicity case, metal cooling is much more efficient, and as a result, a sharp transition between the cold and hot region occurs. The kinetic structure is common in all models. Figure 2.15 also shows the velocity distribution. We can see that the velocities increase after crossing the I-front ($v \sim 50$ km s^{-1} in the ionized region, black arrows). The gas is accelerated because of the thermal pressure in the ionized region. They also show the time evolution of mass accretion rates onto the wandering BHs. For $Z = 0$, the mass accretion rates converge to ~ 10 per cent of the Eddington value evaluated from the electron scsattering. This result also showed in Park & Ricotti (2013). For $Z = 0.01, 0.1Z_\odot$, the accretion rates are smaller for higher metallicities. This is because the higher the metallicities, the more efficiently radiation force acts on the dust.

Ogata et al. (2021) investigates Bondi-Hoyle-Lyttleton accretion flows in dusty gas, taking into account the anisotropy of the radiation field due to the accretion disk. As a first step to investigate the effect of anisotropic radiation field on the dynamics around a wandering black hole, they focused on the situation where the relative velocity between the BH and srrouding gas is sufficiently larger than the sound speed. They developed a particle-like radiation dynamics code that simplifies the hydrodynamic effects. This is pioneering work that deals simultaneously with the gravity of the wandering black hole, the anisotropic radiation produced by the accretion disk, and the attenuation process of radiation by the solid particles in the interstellar medium. Our previous simulations simulations show that around the axis of rotation of the disk, the solid particles, which are greatly affected by the radiation (1000 times larger than the gas), move away from the BH, while in the direction along the disk surface, the matter is hardly affected by the radiation and is eventually swallowed into the BH. They also found that when the attenuation by solid particles is effective (e.g., when the density of the interstellar medium is large), the region where the radiation force is effective is drastically shrunk, and the matter is swallowed into the BH from almost all directions.

Ogata et al. (2021) revealed the effect of anisotropic radiation produced by a accretion disk on the distribution of matter around a fast-moving BH. However, since they employed a particle method that

	Hydrodynamics	Radiation filed (related to black hole accretion disks)	Dust sublimation
Toyouchi et al. 2020	○	Isotropic	×
Ogata et al. 2021	×	Anisotropic	×
Ogata et al. 2024a	○	Anisotropic	○

Figure 2.17: Comparison of previous research and this study.

simplified fluid effects (gas pressure gradient force, ram pressure) and chemical reaction processes (ionization of atoms, dissociation of molecules, sublimation of solid particles), it is necessary to investigate the material distribution and compositional more realistically.

2.6 Position and purpose of this research

So far, we reviewed the theoretical and observational properties of the wandering BHs, including the recent numerical simulations of the accretion flows onto wandering BHs. Wandering BHs exist all over the universe and their origin is diverse. In this study, we focus on intermediate-mass BHs in order to contribute to the understanding of the formation process of supermassive BHs. The strengths of this study compared to recent previous studies on Bondi-Hoyle-Lyttleton accretion are summarized in Table 2.17. The strengths of this study are that the Bondi-Hoyle-Lyttleton accretion onto a black hole accretion disk, one of the universal phenomena in the universe, is investigated in terms of (i)an anisotropic radiation field produced by the black hole accretion disk, (ii)sublimation of interstellar dust by strong radiation from the accretion disk, and (iii) hydrodynamics effects associated with i and ii.

As mentioned above, the previous study by Toyouchi et al. (2020) assume isotropic radiation field, in which case the gas accretion rate decreases significantly compared to the classical Bondi-Hoyle-Lyttleton rate due to radiation feedback in all directions. However, the radiation field is expected to be anisotropic due to the geometry of the accretion disk that forms around the BH. Furthermore, the disk wind is expected to shield ionizing photons from the vicinity of the BH, which would also cause the radiation field to be anisotropic. In such a case, the region where feedback is effective and the region where accretion proceeds could be separated and accretion could proceed efficiently. Hence, one of the goals of this study is to establish a theoretical model of gas accretion onto wandering BHs under anisotropic radiation feedback.

Second, the dust in the interstellar medium is speculated to be heated and sublimated by the strong radiation from black hole accretion disks or other luminous sources. Interstellar dust is affected by radiation force that is 1000 times greater than that of gas, and thus the flow structure could be significantly different in regions where the dust sublimates compared to regions where the dust does not sublimate. However, there is no radiation hydrodynamics simulation of wandering BHs that takes into account the dust sublimation process. We implement dust sublimation into the simulation code and investigate the effect of dust sublimation on the evolution of wandering BHs.

Finally, we investigate the effect of the hydrodynamics in the system assuming anisotropic radiation from the accretion disk and the sublimation process of the dust (i and ii). In the previous study Ogata et al. (2021), although anisotropic radiation from the accretion disk was taken into account, the calculations were performed assuming a system with a large Mach number (the speed of wandering

BHs relative to the sound speed of the surrounding matter), and thus hydrodynamics effects were not considered. However, if the ultraviolet photons emitted from the accretion disk generate an ionized region around the black hole, the gas pressure gradient force is expected to become dominant over the gravity and radiation forces near the boundary between the ionized and neutral regions, where the temperature and density are very different from each other. Therefore, it is important to perform the simulations of wandering BHs with accretion disks that include gas pressure gradient forces.

From the above, (i) anisotropic radiation field, (ii) dust sublimation process, and (iii) hydrodynamics effect are important effects in accretion phenomena onto wandering BHs. This is because understanding the accretion phenomenon on wandering BHs leads to the clarification of the formation process of supermassive BHs, which is one of the most important issues in astronomy. We have succeeded for the first time in the world in a three-dimensional radiation hydrodynamics simulations that incorporates all three of these elements. We describe our simulation method and results in detail below.

Chapter 3

Radiation Hydrodynamics Simulations

As previously mentioned, the intermediate-mass BHs with accretion disks have strong gravity and radiation fields. In addition, the composition of the interstellar medium around BHs significantly changes due to the interactions between matter and photons and matter and matter (chemical reaction). Therefore, Radiation HydroDynamics (RHD) simulations considering the chemical reaction are required to model the flow structure around the intermediate-mass BHs wandering in the dusty gas. This chapter introduces the basic equations and simulation method of RHD.

3.1 Fundamental of RHD simulations

First, we outline the basic structure and properties of typical RHD simulations.

3.1.1 Structure of RHD code

RHD can be understood as a multilayered problem: radiation which propagates over long distances, fluid which propagates over medium distances, and atomic processes on a microscopic scale. Figure 3.1 shows the structure of the typical RHD code. Numerical methods have been developed independently for each of the three components: Hydrodynamics part, Radiative Transfer part, and Atomic Process part. Most RHD codes adopt a coupled calculation scheme in which the governing equations corresponding to each part are solved by different methods and physical quantities are exchanged between each part.

Hydrodynamics part

In the hydrodynamics part, the hydrodynamic equations in which the interaction term with radiation is added are solved. For example, if the fluid is a non-viscous and compressible one, the radiation hydrodynamics equations are expressed as follows:

$$\frac{\partial \rho}{\partial t} + \nabla \cdot (\rho \boldsymbol{v}) = 0, \tag{3.1}$$

$$\frac{\partial (\rho \boldsymbol{v})}{\partial t} + \nabla \cdot (\rho \boldsymbol{v} \otimes \boldsymbol{v} + P \boldsymbol{I}) = \rho \boldsymbol{f}, \tag{3.2}$$

$$\frac{\partial (\rho E)}{\partial t} + \nabla \cdot [(\rho E + P)\, \boldsymbol{v}] = \rho \boldsymbol{f} \cdot \boldsymbol{v} + \Gamma - \Lambda, \tag{3.3}$$

where ρ, $\boldsymbol{v}$, P, $E = |\boldsymbol{v}|^2/2 + (\gamma - 1)^{-1} P/\rho$, $\boldsymbol{f}$, Γ, and Λ represent density, velocity, pressure, total energy (kinetic energy + thermal energy), radiation force, heating rate, and cooling rate. The additional terms to the hydrodynamics equations are radiation force in the right hand side of equation of motion

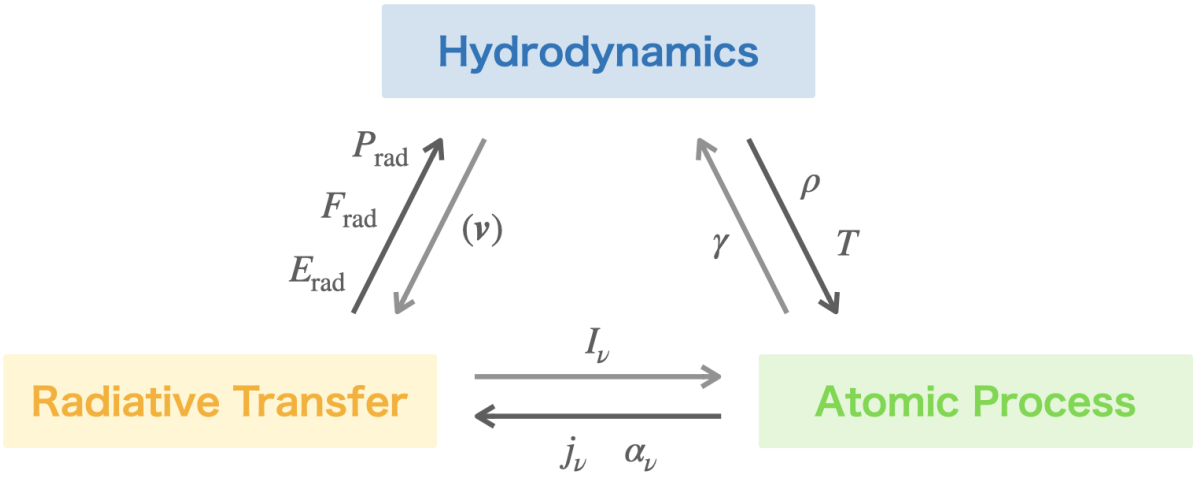

Figure 3.1: Structure of RHD code.The radiation hydrodynamics code is categorized into three major parts, and physical quantities are exchanged between each of the three parts.The physical quantities in brackets in the figure are used if a transformation of the inertial system is required (e.g. relativistic system).

(Equation 3.2), the power due to radiation pressure, and heating and cooling rate caused by interaction between radiation and matter in the right hand side of energy equation (Equation 3.3). These terms can be obtained by solving the equation of the radiation transfer and chemical reaction.

Radiation transfer part

In the radiation transfer part, the radiation transfer equation governing the specific radiation intensity $I_\nu(\boldsymbol{r}, t, \nu, \boldsymbol{l})$ is solved to obtain the physical quantities related to radiation. The specific radiation intensity depends on the position $\boldsymbol{r}$, time t, frequency ν, and direction of propagation. The radiation transfer equation can be derived from the Boltzmann equation for the distribution function of photons and described as follows:

$$\frac{1}{c}\frac{\partial I_\nu}{\partial t} + (\boldsymbol{l}\cdot\nabla)I_\nu = j_\nu - \alpha_\nu I_\nu + \sigma_\nu \int_{4\pi} \left[I_\nu(\boldsymbol{r}, t, \nu, \boldsymbol{l}')\phi(\boldsymbol{l}', \boldsymbol{l}) - I_\nu(\boldsymbol{r}, t, \nu, \boldsymbol{l})\phi(\boldsymbol{l}, \boldsymbol{l}')\right] d\Omega', \tag{3.4}$$

where, c and $\boldsymbol{l} = (\sin\theta\cos\varphi, \sin\theta\sin\varphi, \cos\theta)^{\mathsf{T}}$ is speed of light and direction cosine vector. Here, j_ν [erg cm^{-3} s^{-1} Hz^{-1} sr^{-1}], α_ν [cm^{-1}], σ_ν [cm^{-1}] represent the emissivity, absorption coefficient, and scattering coefficient. $\phi(\boldsymbol{l}', \boldsymbol{l})$ is the scattering probability density from direction $\boldsymbol{l}'$ to direction $\boldsymbol{l}$, which is $1/4\pi$ for isotropic scattering. Thus, when the scattering occurs isotropically, the radiation transfer equation become

$$\frac{1}{c}\frac{\partial I_\nu}{\partial t} + (\boldsymbol{l}\cdot\nabla)I_\nu = j_\nu - (\alpha_\nu + \sigma_\nu)I_\nu + \sigma_\nu J_\nu, \tag{3.5}$$

where J_ν is the mean radiation intensity defined as

$$J_\nu \equiv \frac{1}{4\pi}\oint I_\nu d\Omega. \tag{3.6}$$

In the case of the general radiation transfer equation (Equation 3.4), there is a scattering term with an integral of the radiation specific intensity, thus the equation is a differential-integral system. Furthermore, the radiation specific intensity has seven variables (time1, position3, direction2, frequency1), making the radiation transfer equation very difficult to solve. The above considerations require a technique to solve the radiation transfer equation with some simplification. Therefore, the researchers need

Table 3.1: Comparison of calculation methods for radiative transfer

	Moment scheme	Ray tracing	Monte Carlo
computational cost	low	high	medium
anisotropic field	poor	fine	fine
time dependence	available	N/A	available
opaque field	fine	medium	poor

*The evaluation here is based on the basic idea of each method. Note that we do not consider new improvements in each method.

to know the various approximation and their application range for each astronomical problem (see Section 3.1.2).

The quantities associated with the radiation, radiation energy density $E_{\rm rad}$, radiation flux $\boldsymbol{F}_{\rm rad}$, and radiation pressure tensor $\boldsymbol{P}_{\rm rad}$ are introduced as moments in the direction of propagation of the radiation specific intensity as shown below:

$$E_{\rm rad} = \int_0^\infty \int_{4\pi} \frac{1}{c} I_\nu(\boldsymbol{r}, t, \nu, \boldsymbol{l}) d\Omega d\nu \tag{3.7}$$

$$\boldsymbol{F}_{\rm rad} = \int_0^\infty \int_{4\pi} I_\nu(\boldsymbol{r}, t, \nu, \boldsymbol{l}) l^i d\Omega d\nu \tag{3.8}$$

$$\boldsymbol{P}_{\rm rad} = \int_0^\infty \int_{4\pi} \frac{1}{c} I_\nu(\boldsymbol{r}, t, \nu, \boldsymbol{l}) l^i l^j d\Omega d\nu. \tag{3.9}$$

Atomic Process part

In the atomic process part, we solve for the interaction between photon and matter. Photon absorption and emission have the effect of heating and cooling the matter. Thus, in order to self-consistently implement these interactions, we evolve along with them the thermal energy density ε of the matter and the abundances of the species that interact with the photons. The set of non-equilibrium thermochemistry equations solved in the typical RHD code consists of:

$$\frac{\partial (y_s n_{\rm H})}{\partial t} = y_s n_{\rm H} R_s(\rho, T, I_\nu), \tag{3.10}$$

$$\frac{\partial \varepsilon}{\partial t} = \Gamma(\rho, T, y_s) - \Lambda(\rho, T, y_s), \tag{3.11}$$

where $n_{\rm H}$ is the number density of hydrogen, $y_s = n_s/n_{\rm H}$ is the fractional abundance of the s-th specie, and R_s is the chemical reaction rate of the s-th specie. The chemical reaction rates depend on the radiation specific intensity, gas density, and temperature. The cooling and heating rates are functions of the gas density, temperature, and fractional abundance of each chemical specie.

3.1.2 Various methods for solving the radiative transfer equation

Here we present some typical methods for solving the radiation transfer equation.

Monte Carlo method

The Monte Carlo method is one of the oldest methods for solving radiation transfer equations. In this method, the evolution of the radiation field is tracked by randomly generating photons, which are repeatedly given stochastic events. In general, the Monte Carlo schemes reduce the computational cost by sampling the radiation field, both in the angular and frequency dimensions, into photon packets that

are emitted and traced away from the source. In general, Monte Carlo methods control computational cost by sampling the radiation field in both the angular and frequency dimensions into photon packets, which are then emitted and tracked from the source. An advantage of the Monte Carlo approach to tracking individual photon packets is that it allows for keeping track of the scattering of photons. Note that, if the mean free path is used as the collision interval in the optically thick case, the photons can hardly travel through space under the limited computational resources. Therefore, the Monte Carlo method is suitable for optically thin cases.

Ray tracing method

The solving method in which the radiation transfer equation is integrated along the photon path from the radiation source toward the point where the solution is needed is called the ray tracing method. In this method, various calculation methods have been proposed. The simplest solution is to cast rays from each radiation source to each cell (or volume element) and sum up the optical depth at each endpoint. With the optical depths in hand, I_ν is known everywhere and the rates of various chemical reaction processes, heating and cooling can be calculated. While this method has the advantage of being simple and easy to parallelize (each radiation source calculation is independent of the other), there is a lot of redundancy, since any cell that is close to a radiation source is traversed by many rays cast to further-lying cells, and is thus queried many times for its contribution to the optical depth. Thus, this method requires more computational cost than other methods. Note that this method is useful for systems where scattering can be neglected because of the difficulty in dealing with scattering.

Moment-based method

The radiation transfer equation is a differential-integral equation with seven independent variables. As previously mentioned, this equation is solved using methods such as the Monte Carlo method or ray-tracing method. Since those methods are computationally expensive, various approximate methods have been developed. One prominent approach is to reduce the angular dimensions by taking the angular moments of the radiation transfer equation. The equations taking the directional moments of the radiation transfer equation are described as:

$$\frac{\partial E_{\mathrm{rad},\nu}}{\partial t} + \nabla \cdot \boldsymbol{F}_{\mathrm{rad},\nu} = j_\nu - c\alpha_\nu E_{\mathrm{rad},\nu} \tag{3.12}$$

$$\frac{1}{c}\frac{\partial \boldsymbol{F}_{\mathrm{rad},\nu}}{\partial t} + c\nabla \cdot \boldsymbol{P}_{\mathrm{rad},\nu} = -(\alpha_\nu + \sigma_\nu)\boldsymbol{F}_{\mathrm{rad},\nu}. \tag{3.13}$$

Intuitively this can be thought of as switching from a beam description to that of a field or a fluid, where the individual beams are replaced with a bulk that represents an average of all the photons crossing a given volume element in space. This infers useful simplifications: two angular dimensions are eliminated from the problem (which means significantly reducing the computational cost compared to the non-moment-based schemes) and the equations take the form of conservation laws, such as the Euler equations of hydrodynamics. The former is, in other words, this method is not good at capturing anisotropy. The directionality is largely lost in the moment approximation and the radiation becomes somewhat diffusive, which is generally a good description in the optically thick limit, where the radiation scatters a lot, but not in the optically thin regime where the radiation is free-streaming. The latter indicates that we can solve radiation with numerical methods designed for hydrodynamics. Note that the computational cost is independent of the number of radiation sources since radiation is not tracked individually from each source, but only added to the external field.

These methods are summarized in Table 3.1. For a given astronomical problem, we need to select an appropriate calculation method that takes into account the degree of optical depth, the importance of scattering, the importance of calculation accuracy, and the limitation of calculation resources.

3.1.3 Solving method of moment-based equations

Here, we introduce the solution method of the moment equations (Equations 3.12, 3.13). The moment equations have fewer dimensions than the original radiation transfer equation as they lack the directional vector. However, in exchange, the number of unknown variables increases from I_ν to $E_{\mathrm{rad},\nu}$, $\boldsymbol{F}_{\mathrm{rad},\nu}$, and $\boldsymbol{P}_{\mathrm{rad},\nu}$. For three unknown variables, the solutions cannot be obtained with only two moment-based equations (Equations 3.12, 3.13). If higher order moments are considered to increase the number of equations, new unknown variables are introduced and the system of equations cannot be closed. To address this problem, we introduce a closure relation as following section.

Eddington Approximation

The moment-based equations are implicitly assumed isotropy of the radiation field, since they are integrated over all solid angles. We then introduce the mean specific radiation intensity J_ν again (see Equation 3.6), assuming that the radiation field is completely isotropic. The K-integral, K_ν [erg s^{-1} cm^{-2} Hz^{-1} sr^{-1}], which is averaged over all solid angles of the second-order moments (radiation pressure) is given by

$$\begin{aligned} K_\nu &\equiv \frac{1}{4\pi}\int I_\nu \cos\theta^2 d\Omega \\ &= \frac{J_\nu}{4\pi}\int_0^{2\pi} d\phi \int_0^{\pi} \sin\theta\cos\theta^2 d\theta \\ &= \frac{1}{3}J_\nu. \end{aligned} \tag{3.14}$$

From the definition, there are relations between J_ν and $E_{\mathrm{rad},\nu}$, $J_\nu = cE_{\mathrm{rad},\nu}/4\pi$, and between K_ν and $P_{\mathrm{rad},\nu}$, $K_\nu = cP_{\mathrm{rad},\nu}/4\pi$, so Equation 3.14 can be rewritten as

$$P_{\mathrm{rad},\nu} = \frac{1}{3}E_{\mathrm{rad},\nu}. \tag{3.15}$$

The method that closes the moment-based equations using Equation 3.14 (or Equation 3.15) by assuming that the radiation field is "nearly" isotropic, is called the Edington approximation.

I explain why I emphasize the word "nearly" here. Let's relax the assumption of complete isotropy of the radiation field and assume that the radiation field has a component proportional to $\cos\theta(\equiv \mu)$. We consider a system of infinite parallel-plate atmospheres for simplification. In that system, specific radiation intensity having the angular dependence can be described as $I(z,\mu) = a_\nu(z) + b_\nu(z)\mu$. The

mean specific intensity J_ν and the K-integral are given by:

$$\begin{aligned} J_\nu &\equiv \frac{1}{4\pi}\int (a_\nu(z) + b_\nu(z)\mu) d\Omega \\ &= \frac{a_\nu}{4\pi}\int_0^{2\pi} d\phi \int_0^{\pi} \sin\theta d\theta \\ &= a_\nu \end{aligned} \tag{3.16}$$

$$\begin{aligned} K_\nu &\equiv \frac{1}{4\pi}\int (a_\nu(z) + b_\nu(z)\mu) \cos\theta^2 d\Omega \\ &= \frac{a_\nu}{4\pi}\int_0^{2\pi} d\phi \int_0^{\pi} \sin\theta \cos\theta^2 d\theta \\ &= \frac{1}{3}a_\nu = \frac{1}{3}J_\nu \end{aligned} \tag{3.17}$$

This equation shows that the relation $K_\nu = \frac{1}{3}J_\nu$ (or $P_\nu = \frac{1}{3}E_\nu$) also holds even when the radiation intensity has a linear component proportional to μ. Therefore, the Eddington approximation is applicable if the radiation field is "nearly" isotropic.

Generalizing the above discussion to three dimensions, the Eddington approximation can be expressed as

$$\boldsymbol{P}_{\mathrm{rad},\nu} = \frac{1}{3}E_{\mathrm{rad},\nu}\boldsymbol{I}. \tag{3.18}$$

To summarize so far, the Eddington approximation (Equation 3.18) is a good approximation if the radiation field is nearly isotropic. In a system that is optically thick, the radiation field is isotropic. [1] This is because in such a system, the mean free path of a photon is sufficiently short, and the photon is expected to diffuse randomly as it is repeatedly absorbed and scattered by the material. Therefore, for optically thick systems, the Eddington approximation based on isotropy of the radiation field is a good closure relation.

In many astronomical phenomena, optically thin and optically thick regions coexist. In optically thin systems, the radiation field is not isotropic. This is because photons are hardly absorbed or scattered, and go straight as a free stream. In such a system, $F_{\mathrm{rad},\nu} = cE_{\mathrm{rad},\nu} = cP_{\mathrm{rad},\nu}$ is expected to hold. Based on this idea, the Eddington approximation is extended as follows so that it can be used in optically thin systems:

$$\boldsymbol{P}_{\mathrm{rad},\nu} = E_{\mathrm{rad},\nu}\boldsymbol{D}_{\mathrm{rad},\nu}. \tag{3.19}$$

Eddington tensor $\boldsymbol{D}_{\mathrm{rad},\nu}$ becomes 1/3 for optically thick systems and 1 for optically thin systems. As to satisfy these conditions for the optically thick/thin limit, the Eddington tensor is defined by the flux-limited diffusion approximation and the M1 method, described in the following sections.

Flux-limited diffusion approximation

The flux-limited diffusion (FLD) approximation is based on an extended version of the diffusion approximation for the radiation flux and the Eddington approximation for the radiation pressure. Therefore, as for moment-based equations, we solve only the zeroth-order equation related to the radiation energy density.

[1] Note that optically thick (thin) is not the same sense as isotropic (anisotropic) radiation field.

The FLD method assumes a diffusion process in the optically thick limit. The radiation flux can be obtained by adopting the Fick's law,

$$\boldsymbol{F}_{\mathrm{rad},\nu} = -\frac{c}{3(\kappa_\nu + \sigma_\nu)\rho}\nabla E_{\mathrm{rad},\nu}. \tag{3.20}$$

To handle the radiation flux in optically thin systems, in which $\boldsymbol{F}_{\mathrm{rad},\nu} = cE_{\mathrm{rad},\nu}$ is realized,the radiation flux by Fick's law (Equation 3.20) is extended as follows:

$$\boldsymbol{F}_{\mathrm{rad},\nu} = -\frac{c\lambda_\nu}{(\kappa_\nu + \sigma_\nu)\rho}\nabla E_{\mathrm{rad},\nu}. \tag{3.21}$$

The λ_ν introduced here is called the flux limiter, and this is a function that varies in the range $0 \leqq \lambda_\nu \leqq 1/3$.

The radiation pressure $\boldsymbol{P}_{\mathrm{rad},\nu}$ can be obtained by applying Eddington approximation (Equation 3.19). The Eddington tensor $\boldsymbol{D}_{\mathrm{rad},\nu} = \boldsymbol{D}_{\mathrm{FLD},\nu}$ is expressed as follows:

$$\boldsymbol{D}_{\mathrm{FLD},\nu} = \frac{1-\chi_{\mathrm{FLD},\nu}}{2}\boldsymbol{I} + \frac{3\chi_{\mathrm{FLD},\nu}-1}{2}\boldsymbol{n}_{\mathrm{FLD}} \otimes \boldsymbol{n}_{\mathrm{FLD}} \tag{3.22}$$

$$\boldsymbol{n}_{\mathrm{FLD}} \equiv \frac{\nabla E_\nu}{|E_\nu|}, \tag{3.23}$$

where $\boldsymbol{n}_{\mathrm{FLD}}$ is unit vector in the gradient direction of the radiative energy density. The Eddington factor $\chi_{\mathrm{FLD},\nu}$ is,

$$\chi_{\mathrm{FLD},\nu} = \lambda_\nu + \lambda_\nu^2 R_\nu^2 \tag{3.24}$$

$$R_\nu = \frac{|\nabla E_{\mathrm{rad},\nu}|}{\kappa_\nu \rho E_{\mathrm{rad},\nu}}. \tag{3.25}$$

The various methods for determining the flux limiter λ_ν have been proposed. For example, Levermore et al. (1981) introduced λ_ν as described below:

$$\lambda_\nu = \frac{2+R_\nu}{6+3R_\nu+R_\nu^2}. \tag{3.26}$$

In the optically thick limit ($R_\nu \to 0$), we obtain $\lambda_\nu \to 1/3$ and $\boldsymbol{n}_{\mathrm{FLD}} \to 1/3$. In the optically thin limit ($R_\nu \to \infty$), we obtain $\lambda_\nu \to 1/R_\nu$ and $\boldsymbol{n}_{\mathrm{FLD}} \to 1 - 1/R_\nu$.

M1 closure

In the M1 closure method, we obtain $E_{\mathrm{rad},\nu}$ and $F_{\mathrm{rad},\nu}$ by solving both the zeroth- and first-order moment-based equations. The radiation pressure tensor $P_{\mathrm{rad},\nu}$ is obtained by applying the Eddington approximation (Equation 3.19). The Eddington tensor $\boldsymbol{D}_{\mathrm{rad},\nu} = \boldsymbol{D}_{\mathrm{M1},\nu}$ is expressed in the same form as in the FLD method as shown below:

$$\boldsymbol{D}_{\mathrm{M1},\nu} = \frac{1-\chi_{\mathrm{M1},\nu}}{2}\boldsymbol{I} + \frac{3\chi_{\mathrm{M1},\nu}-1}{2}\boldsymbol{n}_{\mathrm{M1}} \otimes \boldsymbol{n}_{\mathrm{M1}}. \tag{3.27}$$

Unlike the FLD method, the direction of the unit vector $\boldsymbol{n}_{\mathrm{M1}}$ is defined using the direction of the radiation flux,

$$\boldsymbol{n}_{\mathrm{M1}} = \frac{\boldsymbol{F}_{\mathrm{rad},\nu}}{|\boldsymbol{F}_{\mathrm{rad},\nu}|}. \tag{3.28}$$

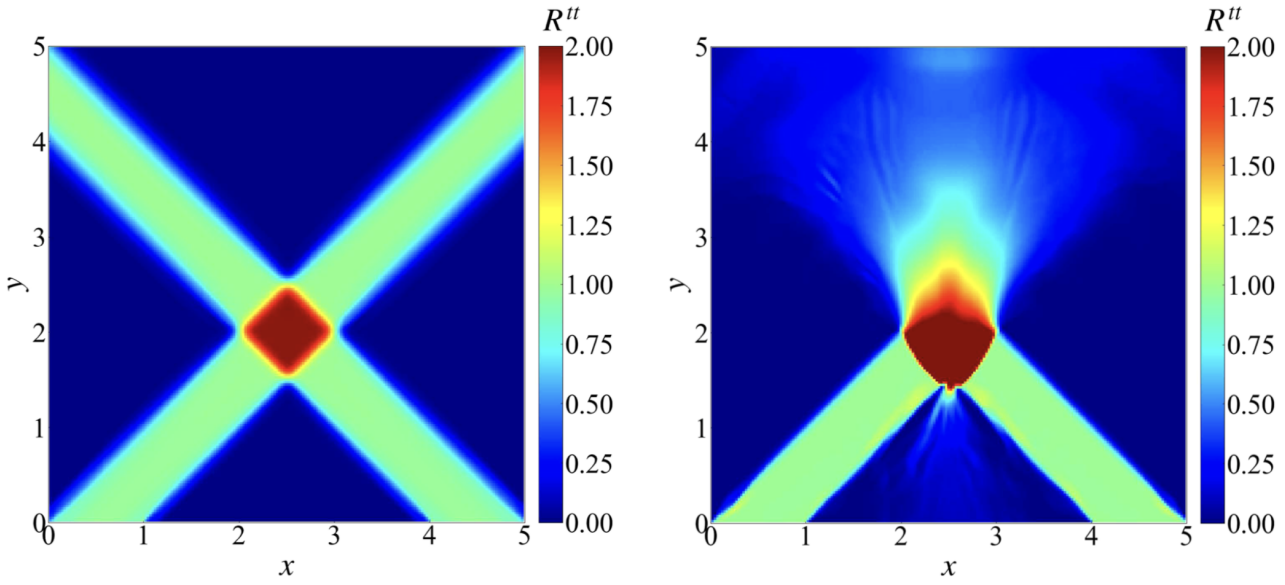

Figure 3.2: Left panel: distribution of the radiation energy density obtained by solving the Boltzmann's equation. Right panel: same as the left panel but using the M1 closure method. In this case, unphysical radiation collision occurs. Cited from Asahina et al. (2020)

The Eddington factor $\chi_{\mathrm{M1},\nu}$ is obtained by

$$\chi_{\mathrm{M1},\nu} = \frac{3+4\xi_\nu^2}{5+2\sqrt{4-3\xi_\nu^2}}, \quad \xi_\nu = \frac{|\boldsymbol{F}_{\mathrm{rad},\nu}|}{cE_{\mathrm{rad},\nu}}. \tag{3.29}$$

This approximation is accurate in the optically thick and optically thin limit as well as the FLD method: $\xi_\nu \to 0,\ \boldsymbol{D}_{\mathrm{M1},\nu} \to \frac{1}{3}$ (optically thick limit), $\xi_\nu \to 1,\ \boldsymbol{D}_{\mathrm{M1},\nu} \to 1$ (optically thin limit).

The M1 closure method is more accurate than the FLD method because the radiation flux can be obtained by solving the first-order moment-based equation. However, the M1 closure method cannot track the radiation accurately when fluxes from different directions collide. The right panel of Figure 3.2 cited from Asahina et al. (2020) shows the distribution of the radiation energy density obtained by M1 closure method, and left panel shows the one obtained by solving a grid-based Boltzmann Equation. We can see that unphysical radiation collision occurs in M1 closure method. If several radiation sources are distributed, the above effects need to be taken into account. In this study, there is only one radiation source, so this is not an important issue.

3.2 RHD simulations in SFUMATO-M1

In this study, we perform three-dimensional radiation hydrodynamics simulations with SFUMATO-M1 (Fukushima & Yajima, 2021). This code is based on SFUMATO-RT (Sugimura & Ricotti, 2020), which is the modified version of SFUMATO (Matsumoto, 2007; Matsumoto et al., 2015). In SFUMATO-M1, the module with the M1-closure technique is adapted instead of the adoptive ray- tracing solver developed in Sugimura & Ricotti (2020). We further include the anisotropic radiation field and dust sublimation for the current purpose (see Figure 3.3). In this section, we introduce the basic equations and solving method of RHD simulations in SFUMATO-M1.

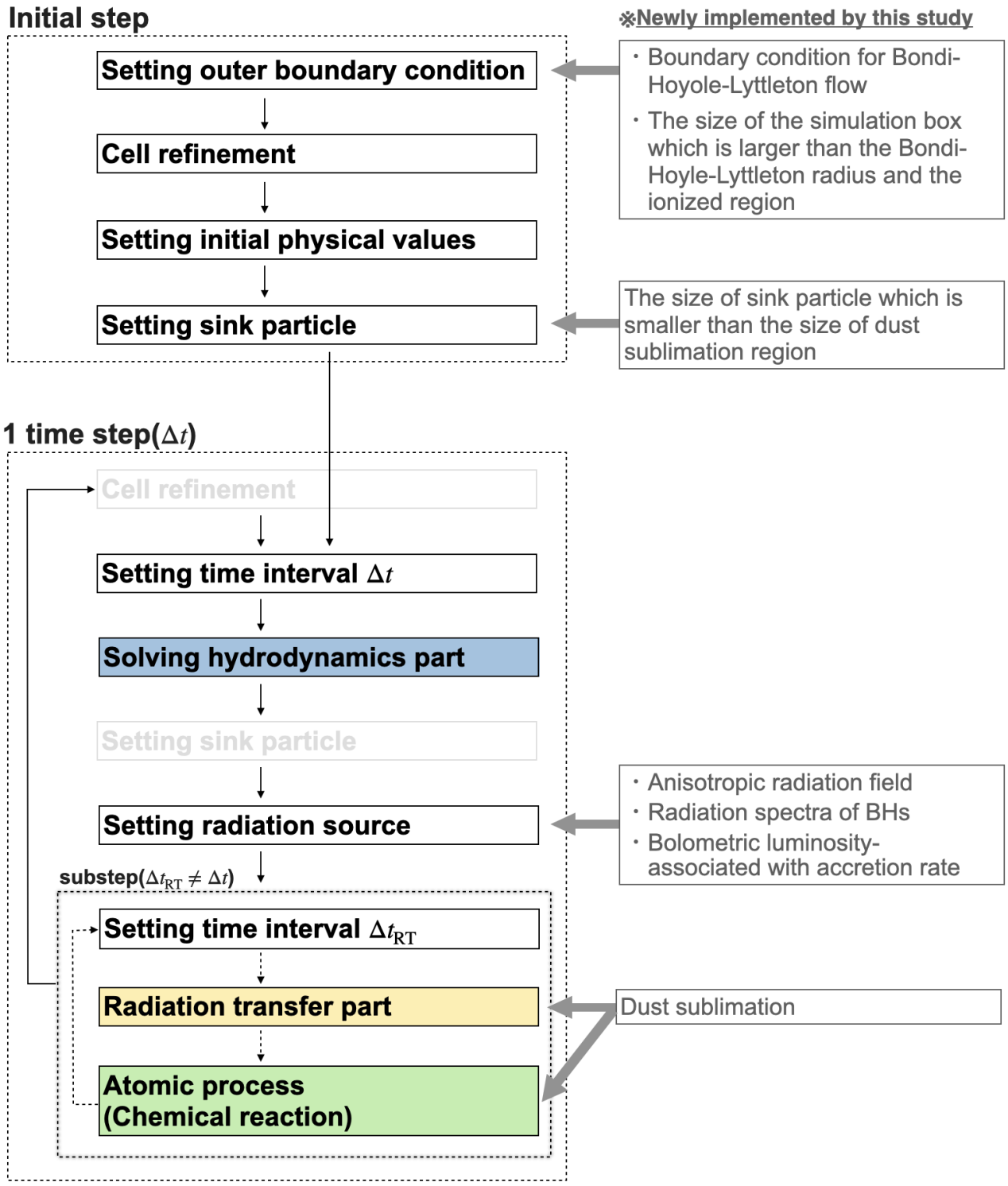

Figure 3.3: Flowchart of RHD simulation code SFUMATO-M1.

3.2.1 Overview of simulation process in SFUMATO-M1

First of all, we outline the simulation process performed in SFUMATO-M1. Each simulation process is described in detail in the following sections.

Figure 3.3 shows the flowchart of simulation process in SFUMATO-M1. First, we set the outer boundary

condition. In our simulations, the size of the simulation box is set to be sufficiently larger than the Bondi-Hoyle-Lyttleton radius and the size of the ionized region. The boundary conditions are given as inflow-boundary and free-boundary (see Section 4.2.1 for more details). The next step is to refine cells. In our simulations, since the nested grid continues to be employed for all of the simulation time, the refinement is done only once in the initial step (see Section 3.2.2). Note that in a typical AMR code, the cell is refined applying the refinement condition at every time step. Next, we set the initial distribution of the physical quantities of the fluid (density, velocity, temperature, and pressure). Then, sink particle is incorporated so that it is present at the maximum refinement level. The size of the sink particle is set to be smaller than the size of the dust sublimation region. In our simulations, we generate a sink particle only at the beginning of the simulation and do not add new sink particles thereafter. The procedure up to this point is carried out in the initial step. After finishing the initial setup, the time interval for solving the radiation hydrodynamics equations, Δt, is set (see Section 3.2.4). Then, we solve the radiation hydrodynamics equations without the source term (hydrodynamics part). The next step is setting the radiation source (BH accretion disk) which is the source term in the radiation transfer equations. We prepare the radiation source based on the BH accretion disk theory (see Section 4.2.3 and 4.2.4). Finally, we set the time interval $\Delta t_{\rm RT}$, which is defined based on the speed of light (see Section 3.2.7), and solve the equations of radiation transfer and the chemical reaction (radiation transfer part and atomic process part). Then, we can estimate the radiation force and cooling and heating rate, and we can calculate the radiation hydrodynamics equations (equation of motion and energy equation) including source term. Since the time step of radiation transfer part is smaller than that of the hydrodynamics part, the calculation of the radiation transfer part and the atomic process part is repeated until it catches up with the 1-step of the hydrodynamics part (sub-step routine).

3.2.2 Adaptive mesh refinement method

The AMR method applied in this code is a powerful technique for simulations of the mesh schemes to require a high dynamic range. The grids of differing resolutions can realize local high-resolution. In a typical AMR code, a finer grid is inserted and its location is changed according to the given refinement conditions (see Section 3.2.2).

Refinement conditions

In `SFUMATO-M1`, which is a simulation code that has developed in the field of star formation, the Jeans condition is employed as a refinement condition; the blocks are refined when the Jeans length $(\pi c_{\rm s}^2/G\rho)^{1/2}$ is shorter than 4-16 (user can set the numbers) times of cell width. In our simulations, we do not adopt the Jeans condition since we do not consider the self-gravity.

We apply the nested grid approach. In the nested grid approach, the grids are refined adaptively, while the sizes and positions of the sub-grids are fixed. Therefore, the problems in which this method can be applied are limited to ones in which the object requiring fine grid resolution is located in the center of the computational domain. The reason for applying this approach in our simulations is that the rest frame of the BH is is adopted, and the BH is always centered for the all simulation time. This approach also has the advantage of being less computationally expensive than a typical AMR code because it does not need to check whether the refinement condition is satisfied at each time step.

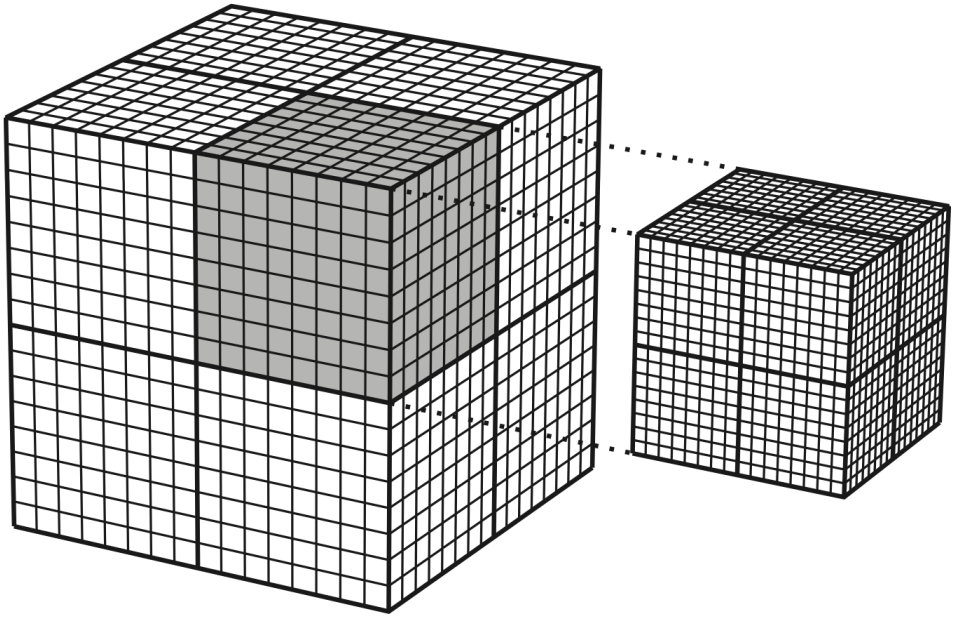

Figure 3.4: Schematic figure of the grid refinement process. The thick and thin lines represent the boundaries of the blocks and the cells, respectively. In this figure, Each block consists of $8^3 = 512$ cells. The block which satisfies the refinement condition is refined into 8 child blocks (right panel). Cited from Matsumoto (2007).

Grid Refinement

We adopt a self-similar block-structured grid. In each block, there are $N_x \times N_y \times N_z$ cells. Here, N_x, N_y, and N_z represent the number of cells in the x-, y-, and z-directions, and each block has the same number of cells. In our simulations, we set the number of cells to $N_x = N_y = N_z = 8$. The number of cells in a block is fixed, but the cell width depends on the grid level. Thus, the blocks are self-similar. Figure 3.4 shows a schematic diagram of a block-structured grid. A block with the same number of cells ($N = 8$) as in our simulation is shown.

When a refinement condition is satisfied for some cells, the block including these cells is divided into 8 child (fine) blocks. Furthermore, each cell in the parent (coarse) block is also divided into 8 child cells (see Figure 3.4). Thus, the cell width of the child grid is half of the parent one, and this means that the refinement ratio is two. In a typical AMR code, the coarser the grid, the smaller the numbers labeled. In this code, the most coarse-grid level is labeled $l = 0$, and the most fine-grid level is labeled $l = l_{\rm max}$. As explained above, the l-th grid-level has a 2^l times higher spatial resolution than that of the most coarse grid level. Such a layer-structure is managed by the octree structure, with the parent block links with 8 child blocks. Also, a block links with its neighboring blocks. Every time the grid is refined, these lists are reconstructed (Note that in our simulations, the number of levels is fixed from the beginning to the end of the calculation).

Conservative variables of the parent cells

After child cells are generated, we need to estimate the conservative variables of its. Using the the conservative variables of the parent cells $\boldsymbol{\mathcal{U}}^H_{I,J,K}$, we obtain those of the child cells $\boldsymbol{\mathcal{U}}^h_{i,j,k}$. In this code, linear interpolation with a slope limiter is employed,

$$\boldsymbol{\mathcal{U}}^h_{i,j,k} = \boldsymbol{\mathcal{U}}^H_{I,J,K} + \overline{\nabla \boldsymbol{\mathcal{U}}^H} \cdot \left(\boldsymbol{r}^h_{i,j,k} - \boldsymbol{r}^H_{I,J,K} \right), \tag{3.30}$$

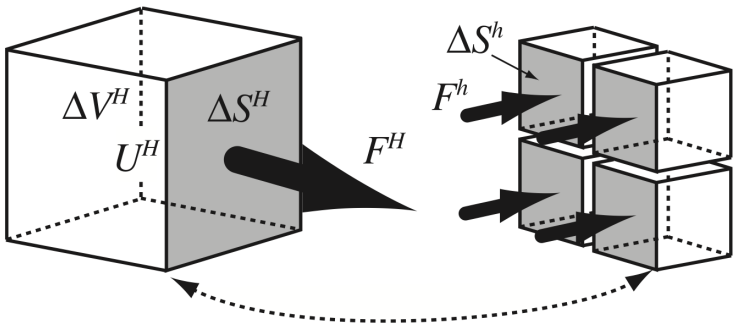

Figure 3.5: Re-fluxing procedure at the interface between coarse (l-th level) and fine ($l+1$-th level) cells. Cited from Matsumoto (2007).

where $\boldsymbol{r}^h_{i,j,k}$ and $\boldsymbol{r}^H_{I,J,K}$ are the position vectors in the direction of the centers of the child and parent cells, respectively. The gradient in the parent cells is limited as follows:

$$\overline{\nabla \boldsymbol{\mathcal{U}}^H} = \begin{pmatrix} \mathrm{minmod}\left(\partial_{\mathrm{x}}\boldsymbol{\mathcal{U}}^{\mathrm{H}}_{\mathrm{I}+1/2,\mathrm{J},\mathrm{K}}, \partial_{\mathrm{x}}\boldsymbol{\mathcal{U}}^{\mathrm{H}}_{\mathrm{I}-1/2,\mathrm{J},\mathrm{K}}\right) \\ \mathrm{minmod}\left(\partial_{\mathrm{y}}\boldsymbol{\mathcal{U}}^{\mathrm{H}}_{\mathrm{I},\mathrm{J}+1/2,\mathrm{K}}, \partial_{\mathrm{y}}\boldsymbol{\mathcal{U}}^{\mathrm{H}}_{\mathrm{I},\mathrm{J}-1/2,\mathrm{K}}\right) \\ \mathrm{minmod}\left(\partial_{\mathrm{z}}\boldsymbol{\mathcal{U}}^{\mathrm{H}}_{\mathrm{I},\mathrm{J},\mathrm{K}+1/2}, \partial_{\mathrm{z}}\boldsymbol{\mathcal{U}}^{\mathrm{H}}_{\mathrm{I},\mathrm{J},\mathrm{K}-1/2}\right) \end{pmatrix}. \tag{3.31}$$

In the refinement process, this interpolation method conserves the conservative variables,

$$\int_{\Omega^H_{I,J,K}} \boldsymbol{\mathcal{U}}^H(\boldsymbol{r})d\boldsymbol{r} = \int_{\Omega^H_{I,J,K}} \boldsymbol{\mathcal{U}}^h(\boldsymbol{r})d\boldsymbol{r}, \tag{3.32}$$

where $\Omega^H_{I,J,K}$ is the zone of a parent cell.

Re-fluxing at the interfaces between fine and coarse cells

To ensure that conservation laws satisfied, and to maintain consistency between the fine and coarse grid-levels during time development, the re-fluxing procedure is adopted. In Figure 3.5, re-fluxing procedure at the interface between fine and coarse cells is shown. Gray surfaces of coarse and fine cells are tangent to each other. The conservative quantity $\boldsymbol{\mathcal{U}}^H$, is integrated in time using the numerical flux of the coarse cells, $\boldsymbol{\mathcal{F}}^H$, and the $\boldsymbol{\mathcal{U}}^h$ is also integrated in time using the numerical flux of the fine cells, $\boldsymbol{\mathcal{F}}^h$. The following relation must be satisfied to conserve between coarse and fine cells,

$$\boldsymbol{\mathcal{F}}^{\mathrm{H}}\Delta S^{\mathrm{H}} = \sum_{\mathrm{surface}} \boldsymbol{\mathcal{F}}^{\mathrm{h}}\Delta S^{\mathrm{h}}. \tag{3.33}$$

Here the sum of the right-hand side is the sum of the four fine cells neighboring the coarse cell. The areas of the gray surfaces of coarse and fine cells, ΔS^{H} and ΔS^{h} , are introduced as follows;

$$\Delta S^{\mathrm{H}} = \sum_{\mathrm{surface}} \Delta S^{\mathrm{h}}. \tag{3.34}$$

In general, without any considering, Equation 3.33 is not satisfied completely when integrating over time. Therefore, $\boldsymbol{\mathcal{U}}^H$ is corrected as follows,

$$\boldsymbol{\mathcal{U}}^{\mathrm{H,new}} = \boldsymbol{\mathcal{U}}^{\mathrm{H}} - \frac{1}{\Delta V^{\mathrm{H}}}\left(\sum_n \sum_{\mathrm{surface}} \boldsymbol{\mathcal{F}}^{\mathrm{h,n}}\Delta S^{\mathrm{h}}\Delta t^{\mathrm{h},n} - \boldsymbol{\mathcal{F}}^{\mathrm{H}}\Delta S^{\mathrm{H}}\Delta t^{\mathrm{H}}\right). \tag{3.35}$$

Here ΔV^{H} denotes the volume of the coarse cells. The subscript n is the subcycle (time interval) of the fine level during which the coarse level advances one step:

$$\Delta t^{\mathrm{H}} = \sum_{n} \Delta t^{\mathrm{h},n}. \tag{3.36}$$

We explain the details of time interval in the Section 3.2.4.

3.2.3 Setting of sink particle

Due to the limitation of computational resources, the AMR method cannot refine the grids infinitely, so it is necessary to stop the refinement at some point. The sink particle is introduced to make this compromise. Inside the sink particle, the accurate calculation is given up.

Assume that the sink particle is not a point mass and has an extent of radius r_{sink}. This radius is called the sink radius, and the inside of the sphere whose radius is the sink radius is called the sink region. In `SFUMATO-M1`, which has been used in the context of star formation, a check for the generation of a sink particle is carried out at every time step of the hydrodynamics calculation. A sink particle is generated at the center of cell $i(s), j(s), k(s)$ when all of the following conditions are satisfied:

- Gas density of the cell exceeds the threshold ($\rho_{i(s),j(s),k(s)} > \rho_{\mathrm{sink}}$)
- Gas is falling into the cells
  This condition requires that all three eigenvalues of the symmetric component $(1/2)\left(\partial v_l/\partial r_m + \partial v_m/\partial r_l\right)_{i(s),j(s),k(s)}$ of the tensor of velocity gradient in cell $i(s), j(s), k(s)$, must be negative. Here, the subscripts $l, m = 1, 2, 3$ denote the x, y, z components. [2]
- Cells have minimum gravitational potential
- Gases within the sink region are gravitationally bound
  This means that the total energy in the sink region is negative:

$$\int_{|\boldsymbol{r}-\boldsymbol{r}_{i(s),j(s),k(s)}|<r_{\mathrm{sink}}} \left[\frac{1}{2}\rho\left(\boldsymbol{v}-\boldsymbol{v}_{i(s),j(s),k(s)}\right)^2 + \frac{P}{\gamma-1}\right] dV - \frac{3GM_{\mathrm{sink}}}{5r_{\mathrm{sink}}} < 0 \tag{3.37}$$

$$M_{\mathrm{sink}} = \int_{|\boldsymbol{r}-\boldsymbol{r}_{i(s),j(s),k(s)}|<r_{\mathrm{sink}}} \rho dV. \tag{3.38}$$

  The integrals in Equation 3.37 and 3.38 represent volume integrals within the sink region, but in the simulation, the integrand values in each cell are summed.

- Sink regions do not overlap with other sink particles

So far, we introduced the general method of generating the sink particles incorporated in `SFUMATO-M1`. In our simulations, only one sink particle (black hole + accretion disk system) is generated at the center of the simulation box at the start of the simulation. Note that no additional sink particles are generated as the time evolution.

The accretion process in the sink region

Sink particles accrete gas in the sink region. There are several ways of gas accretion, such as the method that gas is accreted equally from every cell in the sink region, or the method that gas is

[2] The condition that the divergence of velocity is negative, $(\nabla \cdot \boldsymbol{v})_{i(s),j(s),k(s)} < 0$, is not enough.

weighted according to distance from the center of the sink region and more gas is accreted from cells that are closer to the center of the sink region. In our simulations, we adopt the former method. In this method, the density exceeding the threshold $\rho_{\rm sink}$ in the sink region is accreted to the sink particles.

$$\rho_{\rm acc}(\boldsymbol{r}) = \max\left(\rho(\boldsymbol{r}) - \rho_{\rm sink}, 0\right), \tag{3.39}$$

$$\rho^{\rm new}(\boldsymbol{r}) = \rho(\boldsymbol{r}) - \rho_{\rm acc} = \min\left(\rho(\boldsymbol{r}), \rho_{\rm sink}\right), \tag{3.40}$$

$$\Delta M_{\rm sink} = \int_{|\boldsymbol{r}-\boldsymbol{r}_{\rm sink}|<r_{\rm sink}} \rho_{\rm acc}(\boldsymbol{r}) dV. \tag{3.41}$$

Here $\rho_{\rm acc}$ is the gas density undergoing mass accretion, $\rho_{\rm new}$ is the gas density after accretion, $\Delta M_{\rm sink}$ is the mass increase of sink particles, and $\boldsymbol{r}_{\rm sink}$ is the position of sink particles.

Sink particles accrete not only mass but also momentum. The momentum increase of the sink particle $\Delta\boldsymbol{p}_{\rm sink}$ and the velocity after mass accretion $\boldsymbol{v}_{\rm sink}^{\rm new}$ can be calculated as follows,

$$\Delta\boldsymbol{p}_{\rm sink} = \int_{|\boldsymbol{r}-\boldsymbol{r}_{\rm sink}|<r_{\rm sink}} \rho_{\rm acc}(\boldsymbol{r})\boldsymbol{v}(\boldsymbol{r}) dV, \tag{3.42}$$

$$\boldsymbol{v}_{\rm sink}^{\rm new} = \frac{M_{\rm sink}\boldsymbol{v}_{\rm sink} + \Delta\boldsymbol{p}_{\rm sink}}{M_{\rm sink} + \Delta M_{\rm sink}}, \tag{3.43}$$

where $M_{\rm sink}$ and $\boldsymbol{v}_{\rm sink}$ are the mass and velocity of the sink particle before accretion, respectively. The gas velocity is not changed by mass accretion. This is because the momentum of the mass accreting gas is proportional to $\rho_{\rm acc}$. Sink particles also accrete energy, but for the same reason, accretion does not change the internal energy per unit mass of gas.

So far, we introduced the accretion process implemented in `SFUMATO-M1`. In our simulations, the increase in the mass of sink particle due to mass accretion is taken into account. Note that the mass increase over the computation time is negligibly small relative to the initial mass. Also, our simulations do not consider changes in the momentum of the sink particle. For all times in the simulation, the sink particles remain stationary at the origin (and do not change the momentum of the surrounding gas).

Gravity acting on gas by sink particles

The gravity induced by the sink particle on the gas is a point source, but the gravity is softened to avoid extremely large acceleration of the gas in the vicinity of the sink particle.

In `SFUMATO`, the gravity produced by point sources (sink particles) is expressed as (Matsumoto et al., 2015):

$$\boldsymbol{g} = \begin{cases} -GM_{\rm sink}\frac{\boldsymbol{r}-\boldsymbol{r}_{\rm sink}}{|\boldsymbol{r}-\boldsymbol{r}_{\rm sink}|^3} & (|\boldsymbol{r}-\boldsymbol{r}_{\rm sink}| \geq r_{\rm sink}) \\ -GM_{\rm sink}\frac{\boldsymbol{r}-\boldsymbol{r}_{\rm sink}}{r_{\rm sink}^3} & (|\boldsymbol{r}-\boldsymbol{r}_{\rm sink}| < r_{\rm sink}) \end{cases}$$

In the outside of the sink region, this gravity equals that of the point source; in the inside of the sink region, it is proportional to the distance from the sink particle.

3.2.4 Setting time interval

The time-marching proceeds in units at the grid-level. In this code, two modes of time-marching are incorporated: an adaptive (left panel of Figure 3.6) and a synchronous time-step mode (right panel of Figure 3.6). Which mode is used depends on whether the gas is non-self-gravitational or self-gravitational (w/o radiation transfer or w/ radiation transfer). The adaptive time-step mode is appropriate for non-self-gravitational gases or w/o radiation transfer, and is based on the method of Berger & Colella (1989).

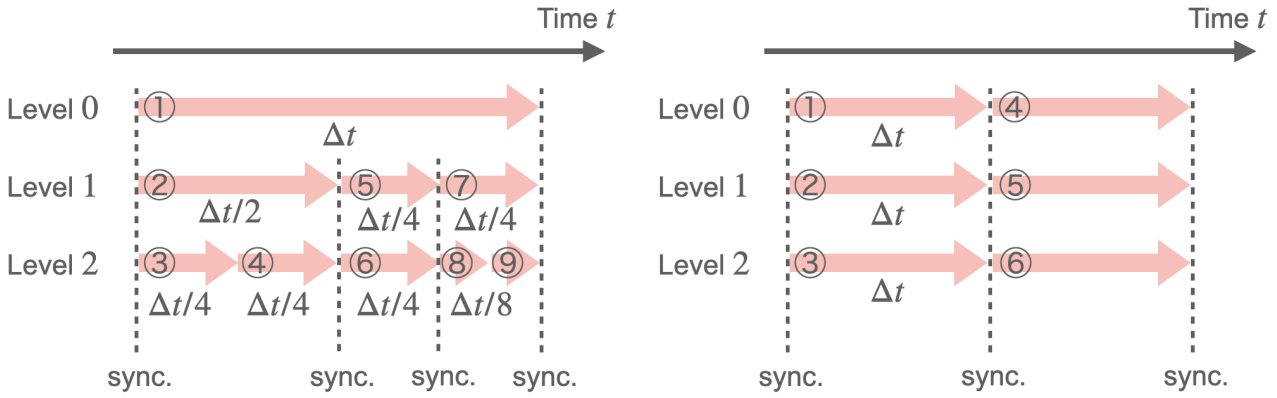

Figure 3.6: The methods of time interval in `SFUMATO-M1`.

In this mode, a coarser grid has a longer time step than a finer grid. In contrast, the synchronous mode is appropriate for self-gravitational gases or w/ radiation-transfer, and every grid-level has the same time step. This is because evolution on the fine grid affects the detached coarse grid immediately due to self-gravity or radiation, and so the same time step must to be chosen for every grid-level. In our simulations, we take into account the radiation, thus we adopt the synchronous time-step mode.

Figure 3.6 shows the order in which the grid-levels proceed for the adaptive time-step mode and synchronous time-step mode schematically. The numbers associated with the thick arrows denote the order of time-marching. Coarser grid-levels precede finer grid-levels.

In the adaptive time-step mode, the fine grid-level undergoes several sub-cycles until the time level of the fine grid-level is synchronized with that of the coarse grid-level. The time step of a finer grid-level, Δt^h, is given by

$$\Delta t^h = \frac{\Delta t^{\mathrm{H}}}{2^n}, \tag{3.44}$$

where n is defined as

$$n = \min\left(m \in \mathbb{N} | \Delta t^{\mathrm{H}}/2^m \leq \Delta t^{\mathrm{h}}_{\mathrm{CFL}}\right). \tag{3.45}$$

where $\Delta t^{\mathrm{h}}_{\mathrm{CFL}}$ denotes the time step calculated directly by the CFL condition at the fine grid-level, and Δt^{H} denotes the time step at the coarser grid-level.

In the synchronous time-step mode, a common time step Δt is used at all grid-levels, and is given by

$$\Delta t = \min_{0 \leq l \leq l_{\max}} \left(\Delta t^l_{\mathrm{CFL}}\right), \tag{3.46}$$

where $\Delta t^l_{\mathrm{CFL}}$ denotes the time stepcalculated by the CFL condition at grid-level l.

3.2.5 Governing equations in SFUMATO-M1

Basic equations of hydrodynamics (+radiation)

Using Cartesian coordinates, the basic equations of hydrodynamics based on the mass conservation law, momentum conservation law, and energy conservation law can be expressed as follows:

$$\frac{\partial \rho}{\partial t} + \nabla \cdot (\rho \boldsymbol{v}) = 0, \tag{3.47}$$

$$\frac{\partial (\rho \boldsymbol{v})}{\partial t} + \nabla \cdot (\rho \boldsymbol{v} \otimes \boldsymbol{v} + P \boldsymbol{I}) = \rho (\boldsymbol{g} + \boldsymbol{f}), \tag{3.48}$$

$$\frac{\partial (\rho E)}{\partial t} + \nabla \cdot [(\rho E + P) \boldsymbol{v}] = \rho (\boldsymbol{g} + \boldsymbol{f}) \cdot \boldsymbol{v} + \Gamma - \Lambda. \tag{3.49}$$

The total energy E is defined as

$$E = \frac{|\boldsymbol{v}|^2}{2} + (\gamma - 1)^{-1} \frac{P}{\rho}. \tag{3.50}$$

Barotropic and isothermal equations of state are also implemented in the this code. In these equations of state, P is expressed as a function of ρ:

$$P = \frac{\rho k_{\rm B} T_{\rm g}}{\mu m_{\rm p}}, \tag{3.51}$$

where $k_{\rm B}$, $T_{\rm g}$, μ, and $m_{\rm p}$ means Boltzmann constant, gas temperature, average molecular weight, and proton mass.

Basic equations of radiation transfer

In this code, we do not consider the contribution of scattering process of photons. Thus, radiation trasnfer equation is discribed as

$$\frac{1}{c}\frac{\partial I_\nu}{\partial t} + \boldsymbol{n} \cdot \nabla I_\nu = j_\nu - \alpha_\nu I_\nu. \tag{3.52}$$

In order to obtain the zero-th and first moment equations, we integrate radiation transfer equation (Equation 3.52) over all solid angles, [3]

$$\frac{\partial E_{\rm rad}}{\partial t} + \nabla \cdot \boldsymbol{F}_{\rm rad} = S_{\rm rad} - \alpha_{\rm E} \tilde{c} E_{\rm rad} \tag{3.53}$$

$$\frac{1}{\tilde{c}}\frac{\partial \boldsymbol{F}_{\rm rad}}{\partial t} + \tilde{c} \nabla \cdot \boldsymbol{P}_{\rm rad} = -\alpha_{\rm F} \boldsymbol{F}_{\rm rad}, \tag{3.54}$$

where $S_{\rm rad}$ is the source term, and $\alpha_{\rm E}$ and $\alpha_{\rm F}$ are the absorption coefficient weighted radiation energy density and radiation flux. Note that we have removed the frequency subscript, since these equations is solved independently for each frequency bins over the time-step. $\tilde{c}$ indicates the reduced light speed (e.g. Rosdahl et al., 2013). In the Section 3.2.7, we discuss the specific methods for solving the radiation transfer equations and limiting the speed of light in more detail.

In the momentum-based method, the radiation pressure tensor is defined with the Eddington tensor $\boldsymbol{D}_{\rm rad}$ and the radiation energy density $E_{\rm rad}$. If we solve the Equation 3.52, we can obtain the accurate values of Eddington tensor. However, solving it directly is computationally expensive. Therefore, we apply the M1 closure scheme.

[3] In Equation 3.53 and 3.54, we adopt the reduced speed of light approximation. Accurately, $E_{\rm rad}$ on the right-hand side of Equation 3.53 is defined by $cE_{\rm rad}/\tilde{c}$. However, considering that the source function on the right-hand side is not related to the light speed limit, we assume the original value $cE_{\rm rad}/\tilde{c}$ to be $E_{\rm rad}$.

Basic equation of chemical reaction

We take into account the chemical networks of 11 species as explained in Section 3.2.8. The number density of the s-th specie is calculated as

$$\frac{\partial(y_s n_{\rm H})}{\partial t} + \nabla \cdot (y_s n_{\rm H} \boldsymbol{v}) = y_s n_{\rm H} R_s. \tag{3.55}$$

Conservative form of basic equations

The basic equations 3.47-3.49 and 3.53-3.54 can be summarized as

$$\frac{\partial \boldsymbol{\mathcal{U}}}{\partial t} + \frac{\partial \boldsymbol{\mathcal{F}}_x}{\partial x} + \frac{\partial \boldsymbol{\mathcal{F}}_y}{\partial y} + \frac{\partial \boldsymbol{\mathcal{F}}_z}{\partial z} = \boldsymbol{\mathcal{S}}, \tag{3.56}$$

where $\boldsymbol{\mathcal{U}}$ is a vector of conservative variables, $\boldsymbol{\mathcal{F}}_x$, $\boldsymbol{\mathcal{F}}_y$, and $\boldsymbol{\mathcal{F}}_z$ are numerical fluxes, and $\boldsymbol{\mathcal{S}}$ is the source term vector. The form of equation (3.56) is called conservative form. In this form, we can solve the basic equations with guaranteeing the law of mass conservation, energy conservation, and momentum conservation if there is no external force.

For our simulations, the vectors in Equation 3.56 are expressed by

$$\boldsymbol{\mathcal{U}} = \begin{pmatrix} \rho \\ \rho v_x \\ \rho v_y \\ \rho v_z \\ \rho E \\ E_{\rm rad} \\ F_{{\rm rad},x}/c^2 \\ F_{{\rm rad},y}/c^2 \\ F_{{\rm rad},z}/c^2 \\ y_s n_{\rm H} \end{pmatrix}, \tag{3.57}$$

$$\boldsymbol{\mathcal{F}}_x = \begin{pmatrix} \rho v_x \\ \rho v_x v_x + P \\ \rho v_x v_y + P \\ \rho v_x v_z + P \\ \rho H v_x \\ F_{{\rm rad},x} \\ E_{\rm rad}\left(\frac{1-\chi_{\rm M1}}{2} + \frac{3\chi_{\rm M1}-1}{2} n_{{\rm M1},x} n_{{\rm M1},x}\right) \\ E_{\rm rad}\left(\frac{1-\chi_{\rm M1}}{2} + \frac{3\chi_{\rm M1}-1}{2} n_{{\rm M1},x} n_{{\rm M1},y}\right) \\ E_{\rm rad}\left(\frac{1-\chi_{\rm M1}}{2} + \frac{3\chi_{\rm M1}-1}{2} n_{{\rm M1},x} n_{{\rm M1},z}\right) \\ y_s n_{\rm H} v_x \end{pmatrix}, \tag{3.58}$$

$$\boldsymbol{\mathcal{F}}_y = \begin{pmatrix} \rho v_y \\ \rho v_y v_x + P \\ \rho v_y v_y + P \\ \rho v_y v_z + P \\ \rho H v_y \\ F_{\mathrm{rad},y} \\ E_{\mathrm{rad}} \left(\frac{1-\chi_{\mathrm{M1}}}{2} + \frac{3\chi_{\mathrm{M1}}-1}{2} n_{\mathrm{M1},y} n_{\mathrm{M1},x} \right) \\ E_{\mathrm{rad}} \left(\frac{1-\chi_{\mathrm{M1}}}{2} + \frac{3\chi_{\mathrm{M1}}-1}{2} n_{\mathrm{M1},y} n_{\mathrm{M1},y} \right) \\ E_{\mathrm{rad}} \left(\frac{1-\chi_{\mathrm{M1}}}{2} + \frac{3\chi_{\mathrm{M1}}-1}{2} n_{\mathrm{M1},y} n_{\mathrm{M1},z} \right) \\ y_s n_{\mathrm{H}} v_y \end{pmatrix}, \tag{3.59}$$

$$\boldsymbol{\mathcal{F}}_z = \begin{pmatrix} \rho v_z \\ \rho v_z v_x + P \\ \rho v_z v_y + P \\ \rho v_z v_z + P \\ \rho H v_z \\ F_{\mathrm{rad},z} \\ E_{\mathrm{rad}} \left(\frac{1-\chi_{\mathrm{M1}}}{2} + \frac{3\chi_{\mathrm{M1}}-1}{2} n_{\mathrm{M1},z} n_{\mathrm{M1},x} \right) \\ E_{\mathrm{rad}} \left(\frac{1-\chi_{\mathrm{M1}}}{2} + \frac{3\chi_{\mathrm{M1}}-1}{2} n_{\mathrm{M1},z} n_{\mathrm{M1},y} \right) \\ E_{\mathrm{rad}} \left(\frac{1-\chi_{\mathrm{M1}}}{2} + \frac{3\chi_{\mathrm{M1}}-1}{2} n_{\mathrm{M1},z} n_{\mathrm{M1},z} \right) \\ y_s n_{\mathrm{H}} v_z \end{pmatrix}, \tag{3.60}$$

$$\boldsymbol{\mathcal{S}} = \begin{pmatrix} 0 \\ \rho \left(g_x + f_x \right) \\ \rho \left(g_y + f_y \right) \\ \rho \left(g_z + f_z \right) \\ \rho \left(\boldsymbol{g} + \boldsymbol{f} \right) \cdot \boldsymbol{v} + \Gamma - \Lambda \\ S_{\mathrm{rad}} - \alpha_{\mathrm{E}} \tilde{c} E_{\mathrm{rad}} \\ -\frac{1}{\tilde{c}} \alpha_{\mathrm{F}} F_{\mathrm{rad},x} \\ -\frac{1}{\tilde{c}} \alpha_{\mathrm{F}} F_{\mathrm{rad},y} \\ -\frac{1}{\tilde{c}} \alpha_{\mathrm{F}} F_{\mathrm{rad},z} \\ y_s n_{\mathrm{H}} R_s \end{pmatrix}. \tag{3.61}$$

Here, H is enthalpy per unit of mass which is defined as

$$H = E + \frac{P}{\rho}. \tag{3.62}$$

3.2.6 Solving method for hydrodynamics part

We adopt the operator-splitting method to advance the time step Δt, i.e., the hyperbolic part and the source term in Equation 3.56 are solved separately:

$$\frac{\partial \boldsymbol{\mathcal{U}}}{\partial t} = -\frac{\partial \boldsymbol{\mathcal{F}}_x}{\partial x} - \frac{\partial \boldsymbol{\mathcal{F}}_y}{\partial y} - \frac{\partial \boldsymbol{\mathcal{F}}_z}{\partial z}, \tag{3.63}$$

$$\frac{\partial \boldsymbol{\mathcal{U}}}{\partial t} = \boldsymbol{\mathcal{S}}. \tag{3.64}$$

In the hydrodynamics part, we solve conservative form of governing equations without radiation transfer equations, i.e. the conservative variables, the numerical fluxes, and the source term in hydrodynamics part are described as below:

$$\boldsymbol{\mathcal{U}} = \begin{pmatrix} \rho \\ \rho v_x \\ \rho v_y \\ \rho v_z \\ \rho E \\ y_s n_{\mathrm{H}} \end{pmatrix}, \tag{3.65}$$

$$\boldsymbol{\mathcal{F}}_x = \begin{pmatrix} \rho v_x \\ \rho v_x v_x + P \\ \rho v_x v_y + P \\ \rho v_x v_z + P \\ \rho H v_x \\ y_s n_{\mathrm{H}} v_x \end{pmatrix}, \tag{3.66}$$

$$\boldsymbol{\mathcal{F}}_y = \begin{pmatrix} \rho v_y \\ \rho v_y v_x + P \\ \rho v_y v_y + P \\ \rho v_y v_z + P \\ \rho H v_y \\ y_s n_{\mathrm{H}} v_y \end{pmatrix}, \tag{3.67}$$

$$\boldsymbol{\mathcal{F}}_z = \begin{pmatrix} \rho v_z \\ \rho v_z v_x + P \\ \rho v_z v_y + P \\ \rho v_z v_z + P \\ \rho H v_z \\ y_s n_{\mathrm{H}} v_z \end{pmatrix}, \tag{3.68}$$

$$\boldsymbol{\mathcal{S}} = \begin{pmatrix} 0 \\ \rho\left(g_x + f_x\right) \\ \rho\left(g_y + f_y\right) \\ \rho\left(g_z + f_z\right) \\ \rho\left(\boldsymbol{g} + \boldsymbol{f}\right) \cdot \boldsymbol{v} + \Gamma - \Lambda \\ y_s n_{\mathrm{H}} R_s \end{pmatrix}. \tag{3.69}$$

In the hydrodynamics part, we solve Equation 3.63 with time interval Δt evaluated from CFL condition. Equation 3.64 is calculated in the radiation transfer part and the atomic process part with time interval Δt_{RT} (see section 3.2.7). In this section, we introduce the solving method for former equation.

First of all, we explain notation of discretization in this paper. The computational domain is divided into cells, each of size $\Delta x \times \Delta y \times \Delta z$. Each cell is labeled by (i, j, k) the indices of the cell in the x-, y-, and z-directions, respectively. The location of the cell center is indicated by the position vector $\boldsymbol{r}_{i,j,k}$. The

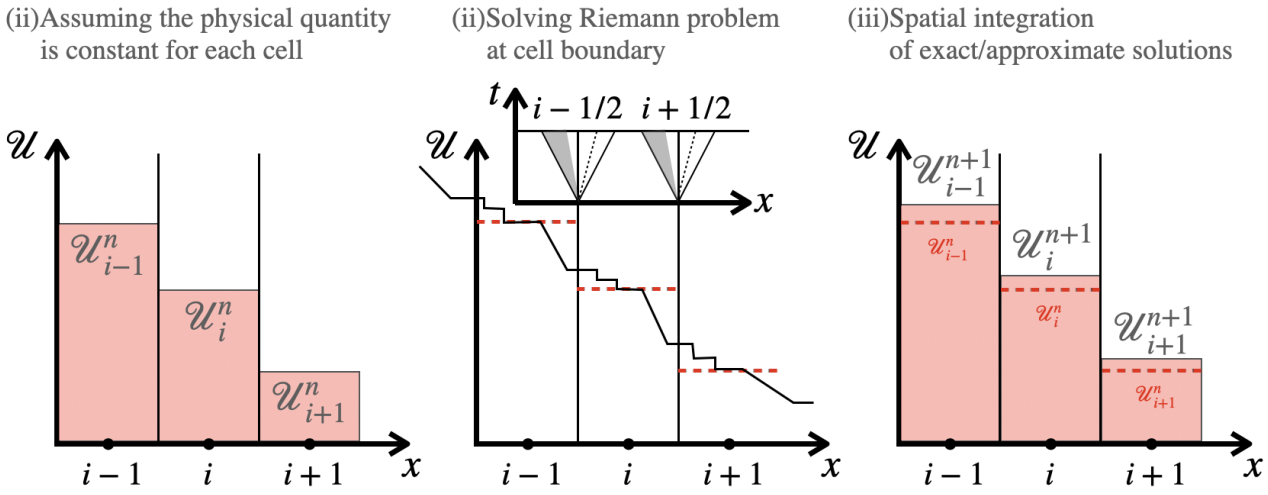

Figure 3.7: Schematic diagram of the calculation procedure for Godunov-type scheme.

conservative variables $\boldsymbol{\mathcal{U}}$, and the source term $\boldsymbol{\mathcal{S}}$ are defined at the cell center, i.e., $\boldsymbol{\mathcal{U}}_{i,j,k} := \boldsymbol{\mathcal{U}}_{i,j,k}(\boldsymbol{r}_{i,j,k})$, and $\boldsymbol{\mathcal{S}}_{i,j,k} := \boldsymbol{\mathcal{S}}_{i,j,k}(\boldsymbol{r}_{i,j,k})$. The numerical fluxes $\boldsymbol{\mathcal{F}}_x$, $\boldsymbol{\mathcal{F}}_y$, and $\boldsymbol{\mathcal{F}}_z$ are defined at the cell surfaces with normals in the x-, y-, and z-directions, respectively. For convenience, the notation of $\boldsymbol{\mathcal{F}}x, i \pm 1/2, j, k := \boldsymbol{\mathcal{F}}_x(\boldsymbol{r}_{i,j,k} \pm (\Delta x/2)\hat{\boldsymbol{x}})$ is introduced, where $\hat{\boldsymbol{x}}$ denotes the unit vector in the x-direction. We introduce the following notation to describe the spatial differences,

$$\frac{\partial Q_{i+1/2,j,k}}{\partial x} = \frac{Q_{i+1,j,k} - Q_{i,j,k}}{\Delta x} \tag{3.70}$$

$$\frac{\partial Q_{i,j,k}}{\partial x} = \frac{Q_{i+1/2,j,k} - Q_{i-1/2,j,k}}{\Delta x} \tag{3.71}$$

$$\frac{\partial^2 Q_{i,j,k}}{\partial x} = \frac{Q_{i+1,j,k} - 2Q_{i,j,k} - Q_{i-1,j,k}}{\Delta x^2}. \tag{3.72}$$

The differences in the y- and z-directions are expressed in a similar manner.

To integrate Equation 3.63, the numerical flux is obtained using the linearized Riemann solver in this code (Roe, 1981). Roe method is one of the Godunov methods. For the Godunov method, when solving the Riemann problem at the cell boundary, the exact solution is used as the solution to the Riemann problem. However, the computational cost of this scheme is not small, as an iterative method such as Newton's method is required to find a solution to the Riemann problem. Therefore, several methods have been proposed which use approximate solutions to the Riemann problem. One of these is the Roe method. The Roe method is based on the idea of an upwind differences scheme [4]. This is the methods that assume an analytical solution to make the Riemann problem easier to compute. Such an extension of the Godunov method using an approximate solution to the Riemann problem is called a Godunov-type scheme (see Figure 3.7).

Godunov-type schemes are first-order accuracy in both space and time. In this code, the MUSCL method and the midpoint method are incorporated to achieve second-order accuracy in both space and time. The Godunov-type scheme is first-order accuracy in space because the spatial derivative is approximated by the upwind difference and the physical quantity inside the cell is assumed to be constant. The upwind difference is based on the forward and backward differences and thus is a first-

[4]Note that in the radiation transfer part, fluxes are evaluated using the HLL and GLF methods.

order spatial accuracy [5]. Even for upwind differences, if the physical quantities inside the cell are approximated by a linear function, the spatial difference becomes second-order accuracy. This method is generally called the MUSCL (Monotone Upstream-centered Scheme for Conservation Laws) method. Our code incorporates the MUSCL method. However, it is known to be unstable if only the spatial difference is second-order accuracy and the time difference is left as first-order accuracy. Therefore, this code incorporates the midpoint method to ensure the time accuracy is also second-order [6]. The midpoint method is a method that first advances time by half (predictor step) and then advances time using the numerical flux of the half-advanced time (corrector step). This method is called the predictor-corrector method.

In the predictor step, time is advanced from n to $n+1/2$ steps with a forward difference of first-order accuracy in time, and the physical quantities at $n+1/2$ steps is obtained, i.e., $\boldsymbol{\mathcal{U}}^n_{i,j,k}$ is updated to $\boldsymbol{\mathcal{U}}^{n+1/2}_{i,j,k}$ (see Figure 3.8):

$$\boldsymbol{\mathcal{U}}^{n+1/2}_{i,j,k} = \boldsymbol{\mathcal{U}}^n_{i,j,k} - \frac{\Delta t}{2}\left(\partial_x \boldsymbol{\mathcal{F}}^n_{x,i,j,k} + \partial_y \boldsymbol{\mathcal{F}}^n_{y,i,j,k} + \partial_z \boldsymbol{\mathcal{F}}^n_{z,i,j,k}\right), \tag{3.73}$$

where the superscript n denotes the time level, and $\Delta t = t^{n+1} - t^n$. The numerical flux $\boldsymbol{\mathcal{F}}^n$, which is defined at the cell boundaries, is calculated using the primitive variables,

$$\boldsymbol{\mathcal{P}} = \begin{pmatrix} \rho \\ v_x \\ v_y \\ v_z \\ P \end{pmatrix}. \tag{3.74}$$

The advantage of evaluating numerical fluxes using the primitive values $\boldsymbol{\mathcal{P}}$ is that monotonicity is guaranteed by the supplementation of density and pressure. When the supplementation is done by the conservative variable $\boldsymbol{\mathcal{U}}$, the density and pressure could be negative.

In the corrector step, a spatially second-order numerical flux $\boldsymbol{\mathcal{F}}^{n+1/2}$ is obtained by applying MUSCL extrapolation to the amplitudes of the eigenmodes, which are converted from $\boldsymbol{\mathcal{U}}^{n+1/2}$. Using this flux, $\boldsymbol{\mathcal{U}}^n_{i,j,k}$ is upadated to $\boldsymbol{\mathcal{U}}^{n+1}_{i,j,k}$ by a full time step,

$$\boldsymbol{\mathcal{U}}^{n+1}_{i,j,k} = \boldsymbol{\mathcal{U}}^n_{i,j,k} - \Delta t\left(\partial_x \boldsymbol{\mathcal{F}}^{n+1/2}_{x,i,j,k} + \partial_y \boldsymbol{\mathcal{F}}^{n+1/2}_{y,i,j,k} + \partial_z \boldsymbol{\mathcal{F}}^{n+1/2}_{z,i,j,k}\right). \tag{3.75}$$

Since central differences are used in time, the accuracy becomes second-order in time as well as in space [7].

[5] The forward difference and backward difference are

$$\left(\frac{\partial \mathcal{U}}{\partial x}\right)_i = \frac{\mathcal{U}_{i+1} - \mathcal{U}_i}{\Delta x} + \mathcal{O}(\Delta x), \qquad \left(\frac{\partial \mathcal{U}}{\partial x}\right)_i = \frac{\mathcal{U}_i - \mathcal{U}_{i-1}}{\Delta x} + \mathcal{O}(\Delta x).$$

[6] Another method for achieving second-order time accuracy is Heun's method. In Heun's method, time is advanced using a trapezoidal formula. This method is often referred to as the Runge-Kutta method in the field of astrophysics. In this method, the numerical fluxes of first-order accuracy in time are obtained in n and $n+1$ steps, and these are averaged to obtain second-order accuracy in time, i.e., unlike the midpoint method, fractional steps such as $n+1/2$ do not appear. The time steps are all integer steps.

[7] The central difference is

$$\left(\frac{\partial \mathcal{U}}{\partial x}\right)_i = \frac{\mathcal{U}_{i+1} - \mathcal{U}_{i-1}}{2\Delta x} + \mathcal{O}(\Delta x^2).$$

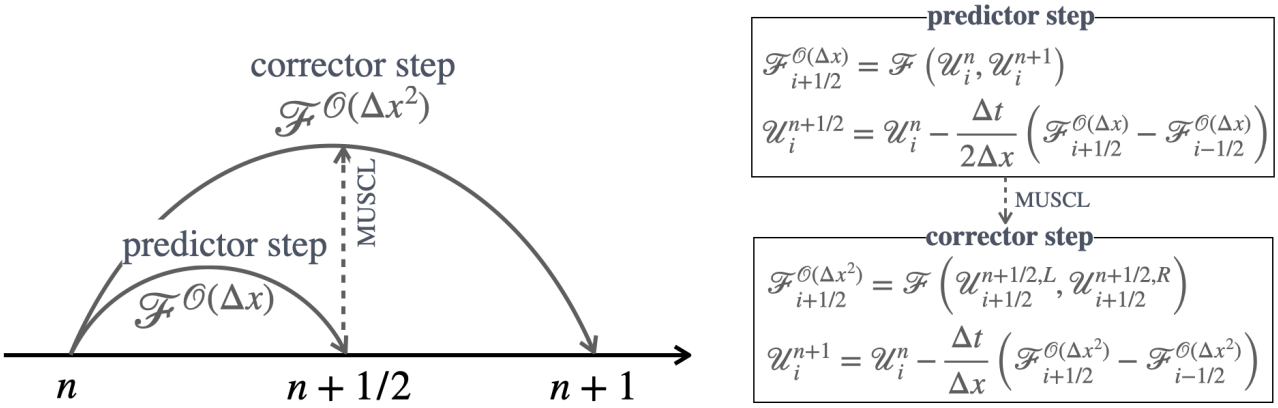

Figure 3.8: The predictor-corrector method.

3.2.7 Solving method for radiation transfer part

In the radiation transfer part, we solve the moment-based radiation transfer equations. As a result, we can calculate the physical quantities related to radiation such as radiation force $\boldsymbol{f}$, heating rate Γ, cooling rate Λ (To be precise, Γ and Λ are obtained after solving the atomic process part). Thus, we can calculate the source term of governing hydrodynamics equations. Moment-based radiation transfer with M1-closure is applied for extreme ultraviolet (EUV), far-ultraviolet (FUV), and in-frared (IR) photons (e.g. Rosdahl et al., 2013; Rosdahl & Teyssier, 2015; Kannan et al., 2019). In this section, we summrize the details of the radiation transfer part of `SFUMATO-M1`, which is developed by Fukushima & Yajima (2021).

Time-step of radiation transfer

The radiation transfer step is computationally expensive, so we use basic trick to speed up the calculation. In each iteration before the three radiation transfer steps (Injection step, Transfer step, and Thermochemistry step), we need to determine the length of the time-step $\Delta t_{\rm RT}$:

$$\Delta t_{\rm RT} = C_{\rm RT}\frac{\Delta x}{3\tilde{c}}. \tag{3.76}$$

where Δx is the cell width in each level of the AMR grid, and $C_{\rm RT}$ is Courant number which is adapted $C_{\rm RT} = 0.8$ in this simulations. We relax the Courant condition by changing the speed of light to a reduced light speed $\tilde{c} << c$. Gnedin & Abel (2001) introduce this idea, generally called the reduced speed of light approximation. In this approximation, reducing the speed of light, while keeping it faster than the typical speed of hydrodynamics in the system, yield the correct solution at a much reduced CPU cost. We split radiation transfer part from the hydrodynamics part. If the time-step in the hydrodynamic part is larger than the that in the radiation transfer part $\Delta t_{\rm RT}$, we calculate radiation transfer as the subcycle steps. The sub-sycle ends when the integration time of the radiation transport step is the same as the hydrodynamics part.

Although not applied in this calculation, there is another way to solve the radiation transport equation using an implicit rather than an explicit solution method. Solving implicitly ensures that the computation is always stable, no matter how large the time step, and removes the coolant condition. However, this does not imply that the calculation is accurate; in fact, some time step conditions are necessary to maintain accuracy. Furthermore, such conditions usually have to be checked by trial and

error. Such trial-and-error time-stepping is a global process that is very computationally expensive. Thus, in our code, we do not apply the implicit method.

Computational procedure for EUV and FUV photons

In our simulations, we split the frequency into three parts, infrared photons (IR), far-ultraviolet (FUV; 11.6eV $\leq$ hν < 13.6eV), and extreme ultraviolet (EUV; 13.6eV $\leq$ h$\nu \leq$ 1keV) photons. First of all, we describe the details of the computational methods for EUV and FUV bins.

In this code, we calculate transfer of the photon number density directly instead of equations 3.53 and 3.54 for EUV and FUV photons. [8] This is because it is convenience to calculate the photoionization and the photodissociation rates which are evaluated by the number density of EUV and FUV photons (Rosdahl et al., 2013). The equations of the photon number density and photon number flux are

$$\frac{\partial N_\gamma}{\partial t} + \nabla \cdot \boldsymbol{F}_\gamma = \dot{N}_{\gamma,*} - \bar{\alpha}\tilde{c}N_\gamma, \tag{3.77}$$

$$\frac{\partial \boldsymbol{F}_\gamma}{\partial t} + \tilde{c}^2\nabla \cdot \boldsymbol{P}_\gamma = -\bar{\alpha}\tilde{c}\boldsymbol{F}_\gamma. \tag{3.78}$$

Here, N_γ, $\boldsymbol{F}_\gamma$, and $\dot{N}_{\gamma,*}$ are the photon number density, the photon number flux, and the photon injection rate by radiation source. The radiation pressure tensor $\boldsymbol{P}_\gamma$ is calculated from the M1 closure method (see Equations **??** and 3.27). The frequency-averaged absorption coefficient $\bar{\alpha}$ is given as

$$\bar{\alpha} = n_i\bar{\sigma}_i, \tag{3.79}$$

where the frequency dependent cross-section $\bar{\sigma}_i$ is defined as

$$\bar{\sigma}_i = \frac{\int_{\nu 1}^{\nu 2} \frac{4\pi J_\nu}{h\nu}\sigma_i(\nu)d\nu}{\int_{\nu 1}^{\nu 2} \frac{4\pi J_\nu}{h\nu}d\nu}. \tag{3.80}$$

Here, J_ν is the mean intensity:

$$J_\nu = \frac{1}{4\pi}\int I_\nu d\Omega = \frac{\tilde{c}}{4\pi}E_{\mathrm{rad},\nu}. \tag{3.81}$$

Each grid has four variables associated with radiation transfer equatinos ($N_\gamma, \boldsymbol{F}_\gamma$) for EUV and FUV bins. Fukushima & Yajima (2021) adopt the operator-splitting method to advance the time-step Δt with reference to Rosdahl et al. (2013). Here, we introduce calculation step of moment-based radiation transfer equations following three steps.

STEP1: Injection step

In this step, the photons emitted from the radiation sources are injected:

$$N_\gamma^{n+1} = N_\gamma^n + \dot{N}_{\gamma,*}\Delta t_{\mathrm{RT}}, \tag{3.82}$$

where $\dot{N}_{\gamma,*}$ is the injection rate from the luminous sources and defined as:

$$\dot{N}_{\gamma,*} = \frac{S_i}{\Delta V}. \tag{3.83}$$

Here, S_i is photon emissivity and ΔV is the volume of each cell. In this study, we assume the injection rate with photon emissivity of EUV, FUV, and IR components is related to the mass accretion rate onto the sink region.

[8] In contrast to the EUV and FUV cases where the photon number density is solved, the moment equations for radiation transfer (Equation 3.53 and 3.54) are solved in the IR range (see Section 3.2.7).

STEP2: Transfer step

In this step, the photon propagation without the source and absorption terms in equations 3.77 and 3.78 are calculated,

$$\frac{\partial N_\gamma}{\partial t} + \nabla \cdot \boldsymbol{F}_\gamma = 0, \tag{3.84}$$

$$\frac{\partial \boldsymbol{F}_\gamma}{\partial t} + \tilde{c}^2 \nabla \cdot \boldsymbol{P}_\gamma = 0. \tag{3.85}$$

If we introduce the following variables,

$$\boldsymbol{\mathcal{U}} = \begin{pmatrix} N_\gamma \\ F_{\gamma,x}/\tilde{c}^2 \\ F_{\gamma,y}\tilde{c}^2 \\ F_{\gamma,z}\tilde{c}^2 \end{pmatrix}, \tag{3.86}$$

$$\boldsymbol{\mathcal{F}}_x = \begin{pmatrix} F_{\gamma,x} \\ E_\gamma\left(\frac{1-\chi_{\rm M1}}{2} + \frac{3\chi_{\rm M1}-1}{2} n_{{\rm M1},x} n_{{\rm M1},x}\right) \\ E_\gamma\left(\frac{1-\chi_{\rm M1}}{2} + \frac{3\chi_{\rm M1}-1}{2} n_{{\rm M1},x} n_{{\rm M1},y}\right) \\ E_\gamma\left(\frac{1-\chi_{\rm M1}}{2} + \frac{3\chi_{\rm M1}-1}{2} n_{{\rm M1},x} n_{{\rm M1},z}\right) \end{pmatrix}, \tag{3.87}$$

$$\boldsymbol{\mathcal{F}}_y = \begin{pmatrix} F_{\gamma,y} \\ E_\gamma\left(\frac{1-\chi_{\rm M1}}{2} + \frac{3\chi_{\rm M1}-1}{2} n_{{\rm M1},y} n_{{\rm M1},x}\right) \\ E_\gamma\left(\frac{1-\chi_{\rm M1}}{2} + \frac{3\chi_{\rm M1}-1}{2} n_{{\rm M1},y} n_{{\rm M1},y}\right) \\ E_\gamma\left(\frac{1-\chi_{\rm M1}}{2} + \frac{3\chi_{\rm M1}-1}{2} n_{{\rm M1},y} n_{{\rm M1},z}\right) \end{pmatrix}, \tag{3.88}$$

$$\boldsymbol{\mathcal{F}}_z = \begin{pmatrix} F_{\gamma,z} \\ E_\gamma\left(\frac{1-\chi_{\rm M1}}{2} + \frac{3\chi_{\rm M1}-1}{2} n_{{\rm M1},z} n_{{\rm M1},x}\right) \\ E_\gamma\left(\frac{1-\chi_{\rm M1}}{2} + \frac{3\chi_{\rm M1}-1}{2} n_{{\rm M1},z} n_{{\rm M1},y}\right) \\ E_\gamma\left(\frac{1-\chi_{\rm M1}}{2} + \frac{3\chi_{\rm M1}-1}{2} n_{{\rm M1},z} n_{{\rm M1},z}\right) \end{pmatrix}, \tag{3.89}$$

these equations (Equation 3.84 and 3.85) are summarized as following form:

$$\frac{\partial \boldsymbol{\mathcal{U}}}{\partial t} + \frac{\partial \boldsymbol{\mathcal{F}}_x}{\partial x} + \frac{\partial \boldsymbol{\mathcal{F}}_y}{\partial y} + \frac{\partial \boldsymbol{\mathcal{F}}_z}{\partial z} = 0. \tag{3.90}$$

In each time step, we solve the explicit formula of Equation 3.90:

$$\frac{\mathcal{U}^{n_{\rm RT}+1} - \mathcal{U}^n_{\rm RT}}{\Delta t_{\rm RT}} + \frac{\mathcal{F}^{n_{\rm RT}}_{i+1/2} - \mathcal{F}^{n_{\rm RT}}_{i-1/2}}{\Delta x} + \frac{\mathcal{F}^{n_{\rm RT}}_{j+1/2} - \mathcal{F}^{n_{\rm RT}}_{j-1/2}}{\Delta y} + \frac{\mathcal{F}^{n_{\rm RT}}_{k+1/2} - \mathcal{F}^{n_{\rm RT}}_{k-1/2}}{\Delta z} = 0, \tag{3.91}$$

where $n_{\rm RT}$ is the time step number in radiation transfer part, and i, j, and k are the indices of cells in x-, y-, and z-directions. The inter-cell fluxes, for example $\mathcal{F}^n_{i+1/2}$, are calculated using the flux between the i-th cell and the $(i+1)$-th cell. In this study, we adopt the global Global Lax-Friedrich (GLF) scheme, in which the inter-cell fluxes are evaluated as:

$$(\mathcal{F}_{\rm GLF})^{n_{\rm RT}}_{i+1/2} = \frac{\mathcal{F}^{n_{\rm RT}}_i + \mathcal{F}^{n_{\rm RT}}_{i+1}}{2} - \frac{\tilde{c}}{2}(\mathcal{U}^{n_{\rm RT}}_{i+1} - \mathcal{U}^{n_{\rm RT}}_i). \tag{3.92}$$

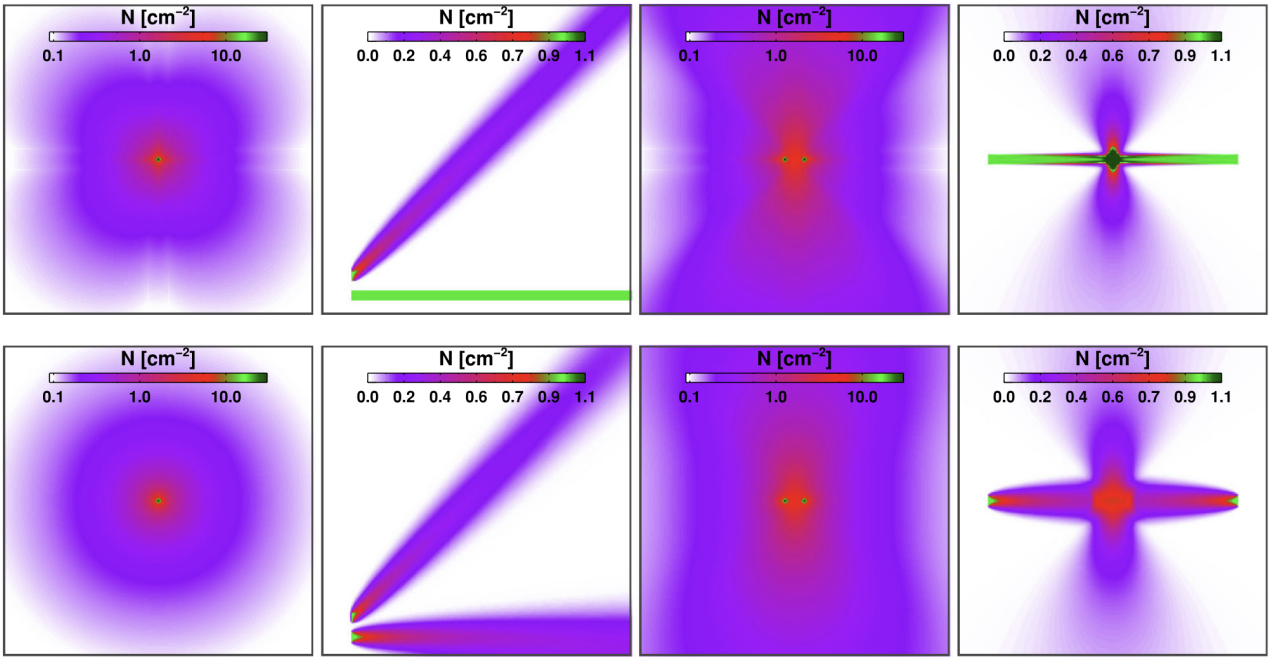

Figure 3.9: Comparison with the HLL (top) and GLF (bottom) flux functions. The distribution of the photon density obtained by 2D RAMSES-RT simulations (no photon–gas interaction) is plotted. Cited from Rosdahl et al. (2013).

Incidentally, `SFUMATO-M1` provides two options for solving the inter-cell flux, including Harten-Lax-van Leer method (HLL) as well as GLF (Harten et al., 1983). In the HLL method, the inter-cell fluxes are calculated as:

$$(\mathcal{F}_{\rm HLL})^{n_{\rm RT}}_{i+1/2} = \frac{\lambda^+ \mathcal{F}^{n_{\rm RT}}_i - \lambda^- \mathcal{F}^{n_{\rm RT}}_{i+1} + \lambda^+\lambda^- (\mathcal{U}^{n_{\rm RT}}_{i+1} - \mathcal{U}^{n_{\rm RT}}_i)}{\lambda^+ - \lambda^-}, \tag{3.93}$$

where λ^+ and λ^- are the maximum and minimum eigenvalues of the Jacobian $\partial\mathcal{F}/\partial\mathcal{U}$,

$$\lambda^+ = \max\left(0, \lambda^{\rm max}_i, \lambda^{\rm max}_{i+1}\right), \tag{3.94}$$

$$\lambda^- = \min\left(0, \lambda^{\rm min}_i, \lambda^{\rm min}_{i+1}\right). \tag{3.95}$$

The computation of these eigenvalues is rather time-consuming because we need them at each iteration in a time step and at each interface of the mesh. However, since they only depend on two parameters, the reduced flux $f_{\rm rad}$ (Equation 3.29) and the angle of incidence of the flux vector to the cell interface $\theta_{\rm rad}$, they can be tabulated easily. We therefore decided to compute them once for a set of $f_{\rm rad}$ and $\theta_{\rm rad}$ and to interpolate the value needed. This method performs well because the eigenvalues have a smooth behavior.

As can be seen from Equation 3.92 and 3.93, GLF corresponds to the replacement of the eigenvalue of HLL by the speed of light ($\lambda^+ = c, \lambda^- = -c$). Therefore, GLF has the effect of making the radiative transport more diffusive than that of HLL. Figure 3.9 cited from Rosdahl et al. (2013) shows that comparison of radiation transfer with the HLL (top) and GLF (bottom) flux functions, using isotropic radiation source and beams in 2D RAMSES-RT runs. From this figure, it is clear that beams are better modelled with the HLL flux function than with the GLF one. On the other hand, the inherent directionality in the HLL function results in radiation around isotropic sources which is noticeably

asymmetric, due to the preference of the axis directions. Since the GLF function is better to follow the isotropic radiation, we adopt the GLF function in this study.

STEP3: Thermochemistry step

Here, we solve for the interaction between photons and gas. This is done by solving Equation 3.77 and 3.78 with zero divergence and stellar injection terms.

3-1. First of all, we solve the energy equations and non-equilibrium chemistry. We estimate the photoionization and photoheating rates of neutral hydrogen ($R_{\rm HI}, \Gamma_2$), photodissociation rates of H_2 and CO molecules ($R_{\rm H_2}, R_{\rm CO}$), and dust absorption rate of EUV, FUV, and IR photons.

EUV: In our code, the EUV photons are absorbed by neutral hydrogen and dust grains. The total absorption coefficient is calculated by

$$\bar{\alpha} = \bar{\alpha}_{\rm HI} + \bar{\alpha}_{\rm d}. \tag{3.96}$$

Here, we difine $\bar{\alpha}_{\rm HI}$ and $\bar{\alpha}_{\rm d}$ are the absorption coefficients for neutral hydrogen and dust grains. Thease frequency-averaged absorption coefficient $\bar{\alpha}_{\rm HI}$ and $\bar{\alpha}_{\rm d}$ are given as Equation 3.79 and 3.80. When we solve Equation 3.79 and 3.80, it is necessary to have information of the frequency dependent cross-section of neutral hydrogen $\sigma_{\rm HI}(\nu)$ and that of dust grains $\sigma_{\rm d}(\nu)$. In this code, $\sigma_{\rm HI}(\nu)$ is given by Osterbrock & E. (1989) and $\sigma_{\rm d}(\nu)$ is given by Laor et al. (1993).

The photoionization and photoheating rates ($R_{\rm HI}, \Gamma_2$) are estimated as

$$R_{\rm HI} = \bar{\sigma}_{\rm HI} \tilde{c} N_{\gamma,\rm EUV}, \tag{3.97}$$

$$\Gamma_2 = n_{\rm HI} \bar{\sigma}_{\rm HI} \tilde{c} N_{\gamma,\rm EUV} \bar{\gamma}_{\rm HI} \tag{3.98}$$

where $N_{\gamma,\rm EUV}$ is the number density of EUV photons, and $\bar{\sigma}_{\rm HI}$ is frequency-mean cross section given by Equation 3.80. Here, the heating rate per a hydrogen atom $\bar{\gamma}_{\rm HI}$ is calculated as

$$\bar{\gamma}_{\rm HI} = \frac{\int_{\nu 1}^{\nu 2} \frac{4\pi J_\nu}{h\nu} \sigma_{\rm HI}(\nu)[h(\nu - \nu_{\rm L})] d\nu}{\int_{\nu 1}^{\nu 2} \frac{4\pi J_\nu}{h\nu} d\nu}. \tag{3.99}$$

FUV: We calculate the photodissociation rates ($R_{\rm H_2}, R_{\rm CO}$) using FUV photon number density $N_{\gamma,\rm FUV}$,

$$R_i = f_{{\rm shield},i} \sigma_i \tilde{c} N_{\gamma,\rm FUV} \quad (i = {\rm H_2}, {\rm CO}) \,. \tag{3.100}$$

Here, the cross-sections of H_2 and CO are estimated from the reaction rates referenced from Draine & Bertoldi (1996) and Lee et al. (1996). The FUV photons are absorbed by dust grains. We take the self-shielding factor $f_{{\rm shield},i}$ in Equation 3.100. In general, the self-shielding is evaluated by the column density along the photon trajectory (Draine & Bertoldi, 1996). However, in the moment method applied in this code, the photon trajectories can not be followed. Thus, to get the self-shielding factor, we evaluate the column density only from local variables as

$$N_i = n_i \min\left(\lambda_{\rm J}, l_{\rm Sob}\right) \quad (i = {\rm H_2}, {\rm CO}) \,, \tag{3.101}$$

where $l_{\rm Sob}$ is the Sobolev length defined as

$$l_{\rm Sob} = \frac{v_{\rm th}}{dv/ds}, \tag{3.102}$$

$\lambda_{\rm J}$ is the local Jeans length, $v_{\rm th}$ is the thermal velocity of molecules, and dv/ds is the velocity gradient. We obtain the self-shielding factor by applying above column density to formula for the H_2 given by Wolcott-Green & Haiman (2019) and for the CO given by Lee et al. (1996). Note that, we overestimate the column density of Equation 3.101 in the static media. Hence, we adopt the column density estimated with the local Jeans length as the upper limits of that estimated with the local Sobolev length.

3-2. Next, we estimate the photon emission via recombination process and the photon absorption of each frequency bins. The moment equations (Equations 3.77 and 3.78) without the transfer terms are

$$\frac{\partial N_\gamma}{\partial t} = \dot{N}_{\gamma,rec} - \bar{\alpha}\tilde{c}N_\gamma, \tag{3.103}$$

$$\frac{\partial \boldsymbol{F}_\gamma}{\partial t} = -\bar{\alpha}\tilde{c}\boldsymbol{F}_\gamma, \tag{3.104}$$

where $\dot{N}_{\gamma,rec}$ is the emissivity of the recombination process. We note that this term is included only for EUV photon transfer and estimate it by following equation:

$$\dot{N}_{{\rm rec},\gamma} = \left(k_{\rm H1,A} - k_{\rm H1,B}\right) n_{\rm II} n_e \Delta t_{\rm RT}. \tag{3.105}$$

Here, $k_{\rm H1,A}$ and $k_{\rm H1,B}$ mean the case-A and case-B recombination rates. These values are tabulated in Table 3.11 cited from Fukushima & Yajima (2021).

We solve these equations (Equation 3.103 and 3.104) implicitly to avoid the photon number density being negative as shown below:

$$N_\gamma^{n_{\rm RT}+1} = \frac{1}{1+\bar{\alpha}\tilde{c}\Delta t_{\rm RT}}\left[N_\gamma^{n_{\rm RT}} + \dot{N}_{\gamma,rec}\Delta t_{\rm RT}\right], \tag{3.106}$$

$$\boldsymbol{F}_\gamma^{n_{\rm RT}+1} = \frac{1}{1+\bar{\alpha}\tilde{c}\Delta t_{\rm RT}}\boldsymbol{F}_\gamma^{n_{\rm RT}}. \tag{3.107}$$

Equations 3.106 and 3.107 are solved numerically using a partly semi-implicit Euler formulation, in the sense that they are implicit in the photon density and flux but otherwise explicit (temperature and the ion abundances, see Section 3.2.8).

In summary, for each frequency bins, we solve the set of equations 3.77-3.78 with an operator splitting strategy, which involves decomposing the equations into three steps that are executed in sequence over the same time-step $\Delta t_{\rm RT}$, which has some pre-determined length. The steps are: [STEP1] Photon injection step, where radiation from stellar and other radiation sources (other than gas recombinations) is injected into the grid. This corresponds to the $\dot{N}_{\gamma,*}$ term in Equation 3.77. [STEP2] Photon transport step, where photons are propagated in space. This corresponds to solving Equation 3.77-3.78 with the right-hand side being equal to zero. [STEP3] Thermochemistry step, where the rest of the right-hand side of Equation 3.77-3.78 is solved. This is where the photons and the gas couple, so here we evolve not only the photon densities and fluxes, but also the ionization state and temperature of the gas (see Section 3.2.8).

Computational procedure for IR photons

Second, we describe the details of the computational methods for IR bin. In contrast to the EUV and FUV cases where the photon number density is solved, the moment equations for radiation transfer

(Equation 3.53 and 3.54) are solved in the IR bin. Thus, each grid has four variables associated with radiation transfer equatinos ($E_{\rm rad}, \boldsymbol{F}_{\rm rad}$). In STEP 1 and STEP 2, we only need to replace ($N_\gamma, \boldsymbol{F}_\gamma$) with ($E_{\rm rad}, \boldsymbol{F}_{\rm rad}$). We explain only STEP 3 in this section.

STEP3: Thermochemistry step

The computational methods for thermochemical evolution and photon absorption in IR bins are incorporated as described below.

3-1. First of all, we solve the energy equations and non-equilibrium chemistry.

Infrared photons are emitted from dust grains mainly as thermal radiation. In this code, the temperatures of gas $T_{\rm g}$ and dust grains $T_{\rm d}$ are calculated separately. We estimate the dust temperature based on the energy equilibrium state among (1) energy transfer between gas and dust, (2) dust thermal emission, (3) absorption of IR photons, and (4) absorption of EUV photons as

$$C_{\rm g}(T_{\rm d} - T_{\rm g}) + \kappa_{\rm d}(T_{\rm d}) a c T_{\rm d}^4 = \kappa_{\rm d}(T_{\rm IR}) \tilde{c} E_{\rm IR} + \mathcal{E}_{\rm EUV}, \tag{3.108}$$

where $C_{\rm g}$ is the coefficient of the energy transfer which is given as (Hollenbach & McKee, 1979; Omukai, 2000; Omukai et al., 2005)

$$C_{\rm g} = 5.83 \times 10^{-8} n_{\rm H} \left(\frac{T_{\rm g}}{10^3 {\rm K}} \left[1 - 0.8 \exp\left(75 {\rm K} / {\rm T_g} \right) \right] \right). \tag{3.109}$$

In Equation 3.108, $\mathcal{E}_{\rm EUV} = \kappa_{\rm d,EUV} \tilde{c} E_{\rm EUV}$ means the absorption rate of dust for EUV photons. Here, $E_{\rm IR}$ and $E_{\rm EUV}$ are the energy density of IR and EUV radiation. We prepare the pre-calculated table of the plank opacity related to the absorption of IR radiation $\kappa_{\rm d}(T_{\rm IR})$ and the dust thermal emission $\kappa_{\rm d}(T_{\rm d})$. This is the function of IR radiation temperature $T_{\rm IR}$ and dust temperature $T_{\rm d}$, and derived from the opacity table derived in Laor et al. (1993). In this code, we apply the these opacity $\kappa_{\rm d}$ and the coefficient of the energy transfer $C_{\rm g}$ at $Z = Z_\odot$ since the energy balance on a single dust grain (Equation 3.108) is not related to the amount of dust grains.

3-2. Next, we estimate the photon emission via thermal emission process and the photon absorption by dust grains. The zero-th moment equation (Equation 3.53) with out the transfer terms is

$$\frac{\partial E_{\rm IR}}{\partial t} = \rho \left[\kappa_{\rm d}(T_{\rm d}) a c T_{\rm d}^4 - \kappa_{\rm d}(T_{\rm IR}) \tilde{c} E_{\rm IR} \right]. \tag{3.110}$$

Here, the radiation temperature $T_{\rm IR}$ for IR range is only calculated from the IR radiation energy density. However, in order to calculate dust temperature $T_{\rm d}$ in the first term on the right-hand side of Equation 3.110, we need to include irradiation from radiation sources and the energy transport between the gas and dust grain. Thus, we adopt a semi-implicit scheme to solve Equation 3.110, assuming the energy balance on dust grains. Equation 3.109 and 3.110 are then discredited as follows

$$C_{\rm g}(T_{\rm d}^{n_{\rm RT}+1} - T_{\rm g}^{n_{\rm RT}}) + \kappa_{\rm d}(T_{\rm d}^{n_{\rm RT}}) a c (T_{\rm d}^{n_{\rm RT}+1})^4 = \kappa_{\rm d}(T_{\rm IR}^{n_{\rm RT}}) \tilde{c} E_{\rm IR}^{n_{\rm RT}+1} + \mathcal{E}_{\rm EUV} \tag{3.111}$$

$$\frac{E_{\rm IR}^{n_{\rm RT}+1} - E_{\rm IR}^{n_{\rm RT}}}{\Delta t_{\rm RT}} = \rho \left[\kappa_{\rm d}(T_{\rm d}^{n_{\rm RT}}) a c (T_{\rm d}^{n_{\rm RT}+1})^4 - \kappa_{\rm d}(T_{\rm IR}^{n_{\rm RT}}) \tilde{c} E_{\rm IR}^{n_{\rm RT}+1} \right]. \tag{3.112}$$

We assume that dust opacity is constant during the update phase of the infrared radiant energy density because the sensitivity of opacity to dust temperature is lower than the $T_{\rm d}^4$ term. Equation 3.112 has a nonlinear term that makes it difficult to be solved, so we linearize this term as follows

$$\begin{aligned} (T_{\rm d}^{n_{\rm RT}+1})^4 &= (T_{\rm d}^{n_{\rm RT}} + \Delta T_{\rm d})^4 \\ &\simeq (T_{\rm d}^{n_{\rm RT}})^4 + 4 (T_{\rm d}^{n_{\rm RT}})^3 \Delta T_{\rm d}, \end{aligned} \tag{3.113}$$

where we define $\Delta T_{\rm d} = T_{\rm d}^{n_{\rm RT}+1} - T_{\rm d}^{n_{\rm RT}}$. Substituting Equation 3.113 into 3.111, and using the relation of Equation 3.108 at timestep $n_{\rm RT}$, the relation between $\Delta T_{\rm d}$ and $\Delta E_{\rm IR} = E_{\rm IR}^{n_{\rm RT}+1} - E_{\rm IR}^{n_{\rm RT}}$ is obtained as

$$\Delta T_{\rm d} = \frac{\kappa_{\rm d}^0 \left(T_{\rm IR}^{n_{\rm RT}}\right) \tilde{c}}{C_{\rm g} + 4\kappa_{\rm d}^0 \left(T_{\rm d}^{n_{\rm RT}}\right) ac \left(T_{\rm d}^{n_{\rm RT}}\right)^3} \Delta E_{\rm IR}. \tag{3.114}$$

Substituting Equation 3.113 and 3.114 into Equation 3.112, we obtain the rate of change of IR energy density,

$$\Delta E_{\rm IR} = \frac{\rho \Delta t_{\rm RT} \left[\kappa_{\rm d} \left(T_{\rm d}^{n_{\rm RT}}\right) ac \left(T_{\rm d}^{n_{\rm RT}}\right)^4 - \kappa_{\rm d} \left(T_{\rm IR}^{n_{\rm RT}}\right) \tilde{c} E_{\rm IR}^{n_{\rm RT}}\right]}{\left[1 + \rho \Delta t_{\rm RT} \kappa_{\rm d} \left(T_{\rm IR}^{n_{\rm RT}}\right) \tilde{c} / \left(1 + \chi\right)\right]}. \tag{3.115}$$

Here, we define χ as

$$\chi = \frac{4\kappa_{\rm d}^0 \left(T_{\rm d}^{n_{\rm RT}}\right) ac \left(T_{\rm d}^{n_{\rm RT}}\right)^3}{C_{\rm g}}. \tag{3.116}$$

The first moment equation (Equation 3.54) with out the transfer terms is

$$\frac{\partial \boldsymbol{F}_{\rm IR}}{\partial t} = -\rho \kappa_{\rm d}(T_{\rm IR}) \tilde{c} \boldsymbol{F}_{\rm IR}. \tag{3.117}$$

We solve this equation explicitly as shown below:

$$\frac{\boldsymbol{F}_{\rm IR}^{n_{\rm RT}+1} - \boldsymbol{F}_{\rm IR}^{n_{\rm RT}}}{\Delta t_{\rm RT}} = -\rho \kappa_{\rm d}(T_{\rm IR}^{n_{\rm RT}}) \tilde{c} \boldsymbol{F}_{\rm IR}^{n_{\rm RT}}. \tag{3.118}$$

Radiation force

To solve the basic equations for radiation hydrodynamics simulations (Equation 3.48 3.49), we need to calculate the radiation force $\boldsymbol{f}$. We evaluate it using the photon number flux $\boldsymbol{F}_\gamma$ in EUV and FUV bins, and radiation flux $\boldsymbol{F}$ in IR bin,

$$\boldsymbol{f} = \frac{y_{\rm HI}\bar{\sigma}_{\rm HI} + \bar{\sigma}_{\rm d}}{c(1+4y_{\rm He})m_p}(h\bar{\nu}\boldsymbol{F}_\gamma)_{\rm EUV} + \frac{\bar{\sigma}_{\rm d}}{c(1+4y_{\rm He})m_p}(h\bar{\nu}\boldsymbol{F}_\gamma)_{\rm FUV} + \frac{\kappa_{\rm d}(T_{\rm IR})}{c}\boldsymbol{F}_{\rm IR}. \tag{3.119}$$

Here, $m_{\rm p}$ and $h\bar{\nu}$ are proton mass and mean energy of EUV and FUV photons.

3.2.8 Solving method for atomic process part

Thermal update

The gas temperature is updated by solving

$$\frac{\partial T_{\rm g}}{\partial t} = \frac{(\gamma-1)\mu m_{\rm p}}{\rho k_{\rm B}} \left(\Gamma - \Lambda\right). \tag{3.120}$$

Equation 3.120 is solved numerically using implicit formulation. The temperature is updated to [9]

$$T_{\rm g}^{n_{\rm RT}+1} = T_{\rm g}^{n_{\rm RT}} + \frac{(\gamma-1)\mu m_{\rm p}}{\rho k_{\rm B}} \left(\Gamma(T_{\rm g}^{n_{\rm RT}+1}) - \Lambda(T_{\rm g}^{n_{\rm RT}+1})\right) \Delta t_{\rm RT}. \tag{3.121}$$

[9] In the hydrodynamics part, we already have calculated gas density $\rho = \rho^{n+1}$.

Number	Process	Rate (erg cm^{-3} s^{-1})	Reference
		Heating	
1	H_2 formation	$\Gamma_1 = [\,3.73(1+n_{\rm cr}/n_{\rm H})^{-1}k_{\rm H2}n({\rm H})n({\rm H}^-) + 4.48(1+n_{\rm cr}/n_{\rm H})^{-1}k_{\rm H6}n^3({\rm H})$ $+ \left(0.2+4.2(1+n_{\rm cr}/n_{\rm H})^{-1}\right)k_{\rm H18}n^2({\rm H})]$ eV $n_{\rm cr} = 10^6 T^{-1/2}/\{1.6n({\rm H})/n_{\rm H}\exp[-(400/T)^2] + 1.4n({\rm H_2})/n_{\rm H}\exp[-1200/(T+1200)]\}$ cm^{-3}	1,2
2	H photoionization	Γ_2	equation (C27)
3	H_2 photodissocian	Γ_3, see the reference	1
		Cooling	
1	H_2 dissociation	$\Lambda_1 = 4.48\,[\,k_{\rm H4}n({\rm H_2})n({\rm e}) + k_{\rm H5}n({\rm H_2})n({\rm H}) + k_{\rm H8}n^2({\rm H_2})\,]$ eV	1,2
2	H ionization	$\Lambda_2 = 13.6k_{\rm H0}n({\rm H})n({\rm e})$eV	1,2
3	H recombination	$\Lambda_3 = \exp[\ln 10\times(-26.02+0.9187\log_{10}T-3.733(\log_{10}T))^2 + 0.1174(\log_{10}T))^3$ $-0.01707(\log_{10}T))^4 + 8.119\times10^{-4}(\log_{10}T))^5]n({\rm H^+})n({\rm e})$	3, 4
4	H^- free–bound	$\Lambda_4 = 0.755k_{\rm H9}n({\rm H})n({\rm e})$	5
5	H excitation	$\Lambda_5 = 7.50\times10^{-19}[1+(T/10^5)^{1/2}]^{-1}\exp[-118348/T]n({\rm e})n({\rm H^+})$	6
6	He^+ excitation	$\Lambda_6 = 5.54\times10^{-17}T^{-0.397}[1+(T/10^5)^{1/2}]^{-1}\exp[-473638/T]n({\rm e})n({\rm He^+})$	6
7	Free-free	$\Lambda_7 = 1.426\times10^{-27}T^{1/2}g_{\rm ff}(T)n({\rm H^+})n({\rm e})$ $g_{\rm ff}(T) = 0.79464 + 0.1243\log_{10}T$ $T < 3.2\times10^5$ K $= 2.13164 - 0.1240\log_{10}T$ $T > 3.2\times10^5$ K	7
8	Compton	$\Lambda_8 = 1.017\times10^{-37}T_{\rm CMB}^4(T-T_{\rm CMB})n({\rm e})$	6
9	Line cooling	$\Lambda_9 = \Lambda_{\rm H_2} + \Lambda_{\rm CII} + \Lambda_{\rm CO} + \Lambda_{\rm OI} + \Lambda_{\rm OII} + \Lambda_{\rm OIII}$	
10	Gas-grain heat transfer	$\Lambda_{10} = 5.83\times10^{-8}n_{\rm H}\rho(T/10^3)^{1/2}[1-0.8\exp(-75/T)](T-T_{\rm d})(Z/Z_\odot)$	1,2

References. (1) Hollenbach & McKee (1979), (2) Omukai (2000), (3) Ferland et al. (1992), (4) Sugimura et al. (2017), (5) Hosokawa et al. (2016), (6) Cen (1992), (7) Shapiro & Kang (1987).

Figure 3.10: Thermal processes incorporated into `SFUMATO-M1`. Cited from Fukushima & Yajima (2021).

Here, $T_{\rm g}^{n_{\rm RT}}$ is a provisional value of gas temperature in the middle of the calculation, which is calculated from equation of continuum and energy equation without advection and source term. We solve this equation for $T_{\rm g}^{n_{\rm RT}+1}$ using the Newton-Raphson method.

In Table 3.10, we summarize the cooling and heating processes applied in `SFUMATO-M1` (Fukushima & Yajima, 2021). Line cooling of rovibrational transitions of H_2 and metal line cooling of C^+, CO, O, O^+, and O^{2+} are incorporated. The fitting function derived in Glover (2015) is adopted for line cooling caused by rovibrational transitions in H_2, and the escape probabilities are given in Fukushima et al. (2018). The cooling rates for C^+, O, O^+, and O^{2+} are evaluated by solving the statistical equilibrium for each energy level as in Fukushima et al. (2020). Since the ionization energies of O and H are nearly the same, we assume that the ionization rate of O is the same as that of H. As in Fukushima et al. (2020), we solve the equilibrium state between O^+ and O^{2+}. The energy transport between gas and dust grains is a function of the dust temperature $T_{\rm d}$ (Omukai et al., 2005).

Chemical reactions in `SFUMATO-M1`

In Table 3.11 (Fukushima & Yajima, 2021), we summarize the chemical reaction associated with H, H_2, H^+, H^-, H_2^+, CO, C^+, O, O^+, O^{2+}, and e (metal species: CO, C^+, O, O^+, O^{2+}). In the `SFUMATO-M1`, the chemical network is applied of Nelson & Langer (1997) for CO formation.

We take into account the chemical networks of 11 species as explained above. In the atomic process part, we solve without advection term of Equation 3.55, [10]

$$\frac{\partial(y_s n_{\rm H})}{\partial t} = y_s n_{\rm H} R_s. \tag{3.122}$$

Equation 3.122 is solved semi-implicitly:

$$(y_s n_{\rm H})^{n_{\rm RT}+1} = (y_s n_{\rm H})^{n_{\rm RT}} + (y_s n_{\rm H})^{n_{\rm RT}} R_s^{n_{\rm RT}+1}\Delta t_{\rm RT}. \tag{3.123}$$

[10] In the hydrodynamics part, we solve Equation 3.55 including the advection term and not including the source term.

Number	Reaction	Rate coefficient	Reference
H0	$H + e \rightarrow H^+ + 2e$	$k_{H0} = \exp[-32.71396786 + 13.536556 \times (\ln T(\mathrm{ev})) - 5.73932875(\ln T(\mathrm{ev}))^2$ $+1.563154998(\ln T(\mathrm{ev}))^3 - 0.2877056(\ln T(\mathrm{ev}))^4 + 3.48255977 \times 10^{-2}(\ln T(\mathrm{ev}))^5$ $-2.63197617 \times 10^{-3}(\ln T(\mathrm{ev}))^6 + 1.11954395 \times 10^{-4}(\ln T(\mathrm{ev}))^7 -$ $2.03914985 \times 100^{-6}(\ln T(\mathrm{ev}))^8$	1
H1	$H^+ + e \rightarrow H + \gamma$	$k_{H1,A} = 1.269 \times 10^{-13}(315614/T)^{1.503}[1 + (604625/T)^{0.47}]^{-1.923}$ (case A) $k_{H1,B} = 2.753 \times 10^{-14}(315614/T)^{1.5}[1 + (115188/T)^{0.407}]^{-2.242}$ (case B)	2, 3
H2	$H^- + H \rightarrow H_2 + e$	$k_{H2} = 1.35 \times 10^{-9}[T^{0.098493} + 0.32852T^{0.5561} + 2.771 \times 10^{-7}T^{2.1826}]$ $/[1 + 6.191 \times 10^{-3}T^{1.0461} + 8.9712 \times 10^{-11}T^{3.0424} + 3.2576 \times 10^{-14}T^{3.7741}]$	4
H3	$H_2 + H^+ \rightarrow {H_2}^+ + H$	$k_{H3} = 3 \times 10^{-10}\exp(-21050/T)\ T < 10^4$ K $1.5 \times 10^{-10}\exp(-14000/T)\ T > 10^4$ K	5
H4	$H_2 + e \rightarrow 2H + e$	$k_{H4} = 4.4 \times 10^{-10}T^{0.35}\exp(-102000/T)$	5
H5	$H2 + H \rightarrow 3H$	see the reference	6
H6	$3H \rightarrow H_2 + H$	$k_{H6} = 6 \times 10^{-32}T^{-0.25} + 2 \times 10^{-31}T^{-0.5}$	7
H7	$2H + H_2 \rightarrow 2H_2$	$k_{H7} = k_{H6}/8$	8
H8	$2H_2 \rightarrow 2H + H_2$	$k_{H8} = k_{\mathrm{high}}^{1-a}k_{\mathrm{low}}^{a}$ $k_{\mathrm{low}} = 1.18 \times 10^{-10}\exp(-6.95 \times 10^4/T)$ $k_{\mathrm{high}} = 8.125 \times 10^{-8}T^{-1/2}\exp(-5.2 \times 10^4/T)[1 - \exp(-6000/T)]$ $a = (1 + n/n_{\mathrm{cr}})^{-1}$, $\log_{10}(n_{\mathrm{cr}}) = 4.845 - 1.3\log_{10}(T/10^4) + 1.62[\log_{10}(T/10^4)]^2$	8
H9	$H + e \rightarrow H^- + \gamma$	$k_{H9} = 1.4 \times 10^{-18}T^{0.928}\exp(-T/16200)$	5
H10	$2H \rightarrow H^+ + e + H$	$k_{H10} = 1.7 \times 10^{-4}k_{H0}$	5
H11	$H^- + e \rightarrow H + 2e$	$k_{H11} = \exp[-18.01849334 + 2.3608522 \times (\ln T(\mathrm{ev})) - 0.28274430(\ln T(\mathrm{ev}))^2 +$ $1.62331664 \times 10^{-2}(\ln T(\mathrm{ev}))^3$ $-3.36501203 \times 10^{-2}(\ln T(\mathrm{ev}))^4 + 1.17832978 \times 10^{-2}(\ln T(\mathrm{ev}))^5 - 1.65619470 \times 10^{-3}(\ln T(\mathrm{ev}))^6$ $+1.06827520 \times 10^{-4}(\ln T(\mathrm{ev}))^7 - 2.63128581 \times 10^{-6}(\ln T(\mathrm{ev}))^8$	1
H12	$H^- + H^+ \rightarrow {H_2}^+ + e$	$k_{H12} = 6.9 \times 10^{-9}/T^{0.35}\ T < 8000$ K $9.6 \times 10^{-7}/T^{0.9}\ T > 8000$ K	5
H13	$H^- + H^+ \rightarrow 2H$	$k_{H13} = 6.3 \times 10^{-8} + 5.7 \times 10^{-6}/\sqrt{T} - 9.2 \times 10^{-11}\sqrt{T} + 4.4 \times 10^{-13}T$	5
H14	$H + H^+ \rightarrow {H_2}^+ + \gamma$	$k_{H14} = 10^{-19.38 - 1.523\log T + 1.118(\log T)^2 - 0.1269(\log T)^3}$	5
H15	${H_2}^+ + H \rightarrow H_2 + H^+$	$k_{H15} = 6.4 \times 10^{-10}$	5
H16	${H_2}^+ + e \rightarrow 2H$	$k_{H16} = 2 \times 10^{-7}/\sqrt{T}$	5
H17	${H_2}^+ + H^- \rightarrow H_2 + H$	$k_{H17} = 2.3 \times 10^{-7}/\sqrt{T/300}$	9
H18	$2H + \mathrm{grain} \rightarrow H_2$	$k_{H18} =$ $6.0 \times 10^{-17}\sqrt{T/300}f_a\,(Z/Z_\odot)[1.0 + 4.0 \times 10^{-2}\sqrt{T + T_{\mathrm{gr}}} + 2.0 \times 10^{-3}T + 8.0 \times 10^{-6}T^2]^{-1}$ $f_a = [1.0 + \exp(7.5 \times 10^2(1/75 - T_{\mathrm{gr}}^{-1}))]^{-1}$	10
M1	$C^+ + O \rightarrow CO$	see the references	11,12
RH1	$H + \gamma \rightarrow H^+ + e$	R_{H1}	equation (C26)
RH2	$H_2 + \gamma \rightarrow 2H$	R_{H_2}	equation (C30)
RH3	$H^- + \gamma \rightarrow H + e$	R_{H^-}	13
RCO	$CO + \gamma \rightarrow C^+ + O$	R_{CO}	equation (C30)

References. (1) Abel et al. (1997), (2) Ferland et al. (1992), (3) Glover & Jappsen (2007), (4) Kreckel et al. (2010), (5) Galli & Palla (1998), (6) Martin, Keogh & Mandy (1998), (7) Forrey (2013), (8) Palla, Salpeter & Stahler (1983), (9) Millar (1991), (10) Tielens & Hollenbach (1985), (11) Nelson & Langer (1997), (12) Nakatani et al. (2018), (13) Hosokawa et al. (2016).

Figure 3.11: Chemical reactions incorporated into `SFUMATO-M1`. Cited from Fukushima & Yajima (2021).

Chapter 4

Accretion onto the Wandering Black Holes: Effects of Dust Sublimation

We perform three-dimensional RHD simulations to study the effect of dust sublimation on the growth rate of intermediate-mass BHs and flow structure. Although the radiation fields could be anisotopic because the BHs have the accretion disks that produce the photons, as the first step, we focus on the case that the radiation field is isotropic. Our results show that the accretion rate oscillates periodically, in contrast to models that do not consider sublimation (Toyouchi et al., 2020). On the other hand, the time-averaged accretion rate is about the Eddington accretion rate for the dusty gas, which is almost the same as the model that does not consider sublimation. We examine the flow structures and growth rates of the BHs in case the radiation field is anisotropic in Chapter 5.

4.1 Dust grains around the BHs

Dust grains are the solid matter in the interstellar medium less than a few micrometers in size. Such dust grains absorb and scatter UV and visible photons from the luminous objects, and re-emit the photons in the infrared wavelength range as thermal radiation, which significantly alters the spectral energy distribution (SED) specific to the luminous objects. The dust grains also receive momentum from the photons (radiation force). The radiation force acting on the dust grains are about 1000 times larger than that of the gas in the interstellar medium. Thus the dust grains are predicted to have contributed significantly to the diffusion of matter in space. In addition, since the beginning of this century (e.g. Bertoldi et al., 2003; Priddey et al., 2003), it has been discovered that large amounts of interstellar dust exist in distant galaxies with redshift larger than 5 (see Table 4.1). These observational results suggest that the simulations that included the dust grains in the interstellar medium are necessary to understand the evolution of intermediate-mass BHs in the early Universe.

The RHD simulations of wandering BHs, taking into account the radiation force acting on the dust grains and the effect of attenuation of the radiation by the dust grains in the interstellar medium, were performed by Toyouchi et al. (2020). They found that as metallicity changes, the growth rate of intermediate-mass BHs changes significantly. It was also found that the temperature distribution and the size of the ionized region also strongly depend on metallicity. This result indicates the need for simulations including the dust grains to predict the accurate SED of intermediate-mass BHs wandering in the early Universe.

However, previous simulations do not take into account the heating and sublimation processes of the dust grains. The dust grains consist mainly of solid particles composed of heavy elements such

Source	z	$t(\infty) - t(z)$ Gyr	M_d 10^8 $M_\odot$	$\dot{M}_*$ (min) $M_\odot$ yr^{-1}	$L_{\rm FIR}$ 10^{10} $L_\odot$	$M_{\rm bh}$ 10^9 $M_\odot$	$\dot{M}_{\rm acc}$ $M_\odot$ yr^{-1}
SDSS J1306+0356	5.99	0.99 (0.70)	2.6 (1.8)	26	520 (370)	4.4 (3.0)	95 (65)
SDSS J1044−0125	5.74	1.04 (0.74)	4.2 (3.0)	41	870 (610)	5.6 (4.0)	125 (85)
SDSS J0756+4104	5.09	1.21 (0.86)	9.6 (6.9)	80	1970 (1410)	2.1 (1.4)	45 (30)
SDSS J0338+0021	5.07	1.22 (0.87)	8.5 (6.1)	70	1750 (1250)	2.1 (1.4)	45 (30)
SDSS J1030+0524	6.28	0.93 (0.66)	<1.4 (1.0)	–	<280 (200)	4.4 (3.0)	95 (65)
SDSS J0836+0054	5.82	1.02 (0.73)	<2.1 (1.5)	–	<430 (300)	7.6 (5.2)	165 (115)
RD J0301+0020	5.50	1.10 (0.78)	1.4 (1.0)	13	290 (200)	0.06 (0.04)	1.4 (0.9)
SDSS J2216+0013	4.99	1.25 (0.89)	<2.0 (1.4)	–	<410 (300)	1.9 (1.4)	40 (30)

Figure 4.1: Quasars at $z > 5$ observed with SCUBA (Submillimetre Common-User Bolometer Array). Cited from Priddey et al. (2003).

as carbon, oxygen, silicon, magnesium, and iron. These elements are highly volatile and sublimate to the gas phase easily with even the slightest heating. The temperature required for dust sublimation is approximately $\sim 1000 - 1500$ K. In fact, even around protoplanetary disks, there is observational evidence of sublimation processes (e.g. Sakai et al., 2014). The accretion disks around the BHs produce more powerful radiation than the protoplanetary disks, so it is expected that the dust sublimation process can easily occur.

In the following, we estimate the size of the sublimation region around a wandering BH for our simulations. If an active galactic nucleus (AGN) isotropically emits in the UV/optical, the dust sublimation radius can be determined by the following equation:

$$\begin{aligned} \kappa_{\rm abs} \frac{L}{4\pi \times 4\pi R_{\rm subl}^2} &= \kappa_{\rm plank} \frac{\sigma_{\rm SB} T_{\rm d}^4}{\pi} \\ \rightarrow R_{\rm subl} &= \left(\frac{L \kappa_{\rm abs}}{16\pi \kappa_{\rm plank} \sigma_{\rm SB} T_{\rm d}^4} \right)^{1/2} \\ &\sim 5.52 \times 10^{-3} {\rm pc} \left(\frac{\rm L}{\rm L_{E,dg}} \right)^{\frac{1}{2}} \left(\frac{\rm T_d}{10^3 \ \rm K} \right)^{-2}, \end{aligned} \tag{4.1}$$

where $R_{\rm subl}$ and $\sigma_{\rm SB}$ denote the sublimation radius and Stefan-Boltzmann constant, respectively. We apply the UV opacity of $\kappa_{\rm abs} = 280(Z/Z_\odot)$ cm^{2}g^{-1} (e.g. Yajima et al., 2017). Also, we apply the thermal emission opacity of $\kappa_{\rm plank} = 5.880285$ cm^{2}g^{-1}, assuming the dust sublimation temperature is $T_{\rm d} = 1000$ K. In Equation 4.1, it is assumed that the radiation energy absorbed by the dust grains (left hand side) is balanced with the energy re-emitted by the dust grains (right hand side). Note that, in the re-radiation process, we assume that dust grains emit blackbody radiation. Substituting the Eddington luminosity of dusty-gas, $L_{\rm E,d}$, for luminosity of the central object, L, the dust sublimation radius is about 10^{-3} pc. The dust sublimation region is sufficiently larger than the typical size of the BH accretion disk ($\sim 10^{-5}$pc) so that the amount of matter supplied to the disk could be significantly affected by dust sublimation.

4.2 Models and Method

We perform three dimentional RHD simulations to investigate the effect of dust sublimation on the gas accretion process of wandering BHs. Specifically, we solve the dynamics of the flows around the

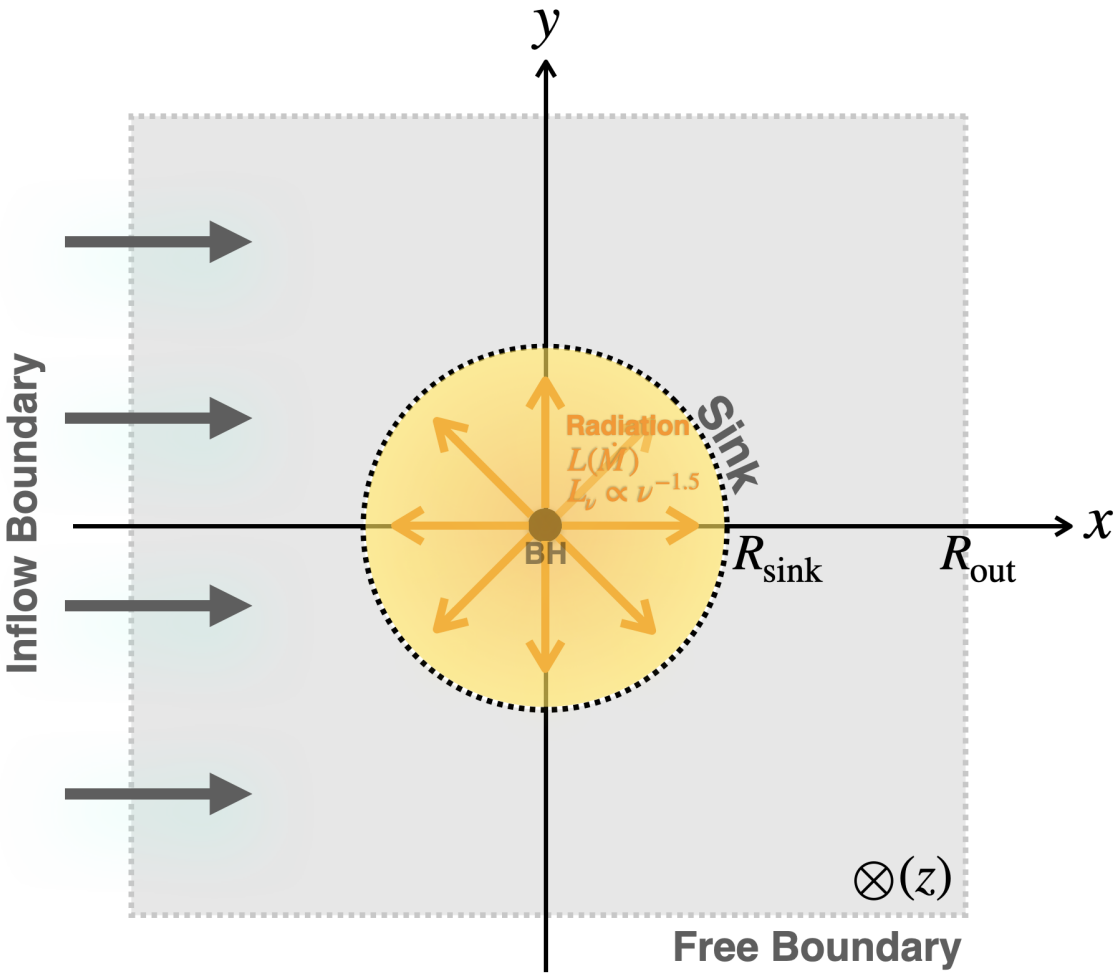

Figure 4.2: Schematic figure of our simulation settings for isotropic radiation case.

Bondi-Hoyle-Lyttleton radius. That is, the inner side of the BH accretion disk is covered by a central sink region, and ionizing photons are injected at in the sink region (see Figure 4.2).

4.2.1 Three-dimensional radiation hydrodynamics simulations

The simulation code used in this study is `SFUMATO-M1` (see Section 3.2). We adopt a cubic computational region, and perform the simulations with the Cartesian coordinate. The gas flows relative to a BH fixed at the origin are simulated. We set the size of a simulation box of $R_{\rm out} = 12.6$ pc, which is much larger than the Bondi-Hoyle-Lyttleton radius and the size of the ionized region for the parameter range of our simulations. The sink method is employed, and the sink radius is set to $R_{\rm sink} = 2.7 \times 10^{-3}$ pc, which is large enough to resolve the sublimation region of the dust. The BH grows due to mass accretion. However, the increase in the BH mass is negligibly small in the elapsed time of our simulations. Also, for simplicity, the acceleration of the BH, self-gravity of gas, and magnetic field are neglected.

We adopt the nested grid method to resolve the gas structures vicinity of the BH efficiently. In our simulations, the maximum refinement level is $l_{\rm max} = 10$, and the minimum cell size is $\Delta_{10} = 3.85 \times 10^{-4}$ pc.

The flow-in boundary is assumed at the upwind side ($x = -R_{\rm out}$), and the free boundary is assumed at the other surface. The gases at the upwind side have the uniform distribution of the number density,

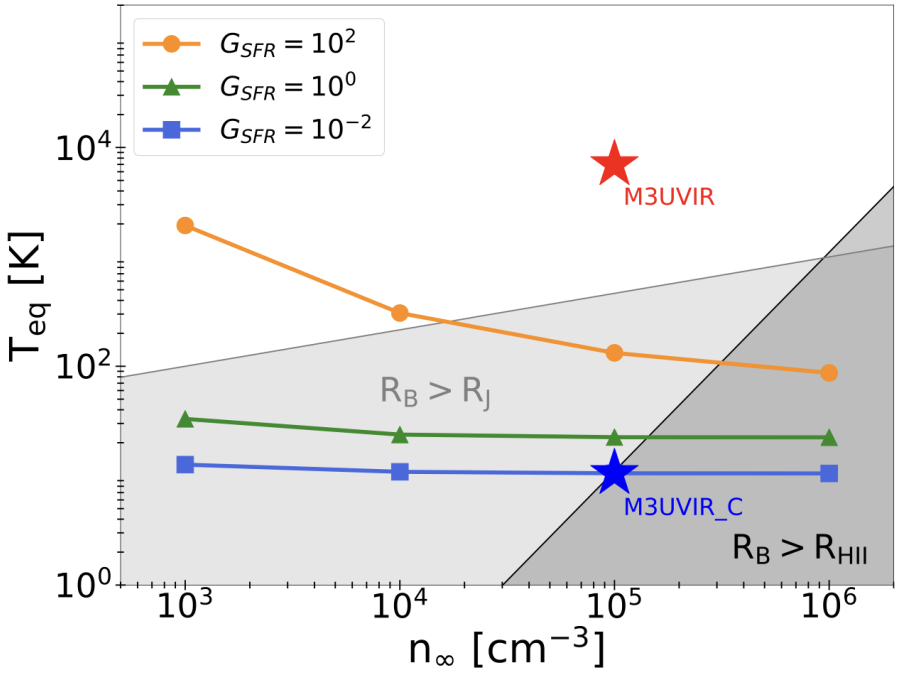

Figure 4.3: The metallicity-dependent of thermal equilibrium temperatures of the gas. The equilibrium temperatures at $Z = 10^2 Z_\odot$ are plotted as functions of number density of the gas, n_∞, and surface density of the star formation rate (solid lines). Cited from Toyouchi et al. (2019).

n_∞, gas temperature T_∞, positive x-direction velocity, v_∞, and metallicity $Z_\infty = 0.1 Z_\odot$ for the entire computation time. In the inner boundary (sink region, $< R_{\rm sink}$), the gas whose number density exceeds the threshold number density, 10^{-1} cm^{-3}, accretes to the sink region.

4.2.2 Cases examined

Table 4.1: Parameters and physical quantities for isotropic radiation model considering dust sublimation

Parameter	$M_{\rm BH}$	n_∞	v_∞	T_∞	Z_∞	L	L_ν
Unit	$[M_\odot]$	[cm^{-3}]	[km s^{-1}]	[K]	$[Z_\odot]$		
`isoN4V20`	10^4	10^4	20	180	0.1	Eq.4.2	$\propto \nu^{-1.5}$

First of all, we describe the parameters of our simulations which is also presented in Ogata et al. (2024). In our simulations, we set the following initial condition: the BH mass is $M_{\rm BH} = 10^4 M_\odot$, the gas number density is $n = 10^4$ cm^{-3}, the gas velocity is $v = 20$ km s^{-1}, the gas temperature is $T = 180$ K, the metallicity is $Z = 0.1 Z_\odot$. As boundary conditions at the upstream wind, we set the gas velocity in the $+x$ direction to $v_\infty = 20$km s^{-1}, the gas number density to $n_\infty = 10^4$ cm^{-3}, the gas temperature to $T_\infty = 180$ K, and the metallicity to $Z_\infty = 0.1 Z_\odot$ (see Table 4.1). These conditions are continuously injected at $x = -R_{\rm out}$. At the other surface, the free boundary conditions are assumed.

From the standpoint that this study is the first step toward understanding the formation process of supermassive BHs, we set the BH mass of $10^4 M_\odot$, which is the typical mass of the seed BHs. The gas velocity and gas number density are chosen in reference to numerical simulations that follow the Milky Way-size galaxy mergers (Mayer et al., 2007, 2010). This is because once galaxies harboring the seed BHs merge, the BHs are expected to drift in the remnant galaxy. The gas temperature

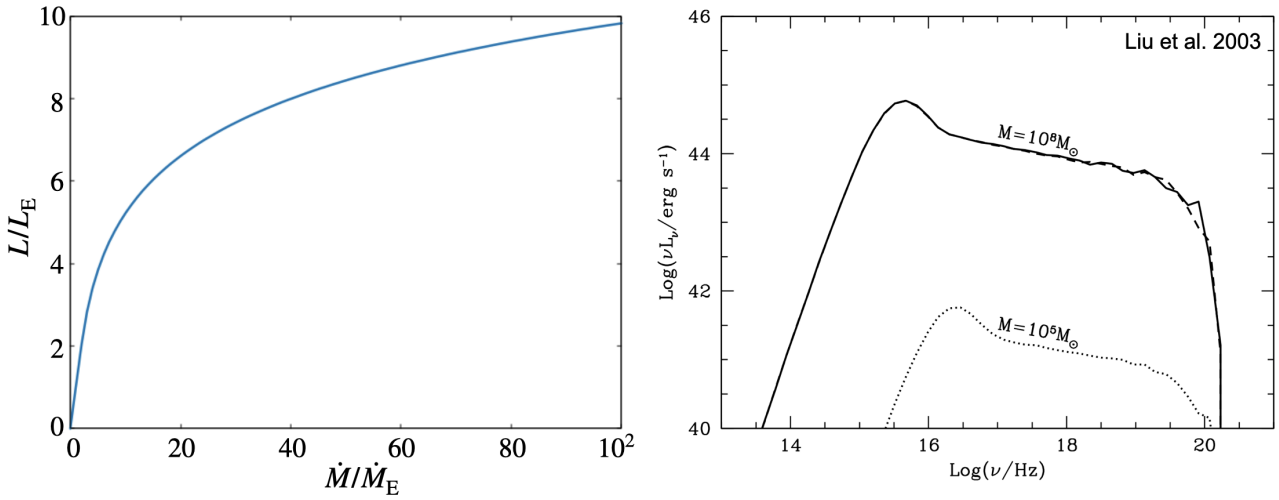

Figure 4.4: Left panel: Relation between accretion rate and luminosity in our simulations (see also Watarai et al., 2000). Right panel: Hard-state spectrum for $M = 10^5 M_\odot$ and $\dot{M} = \dot{M}_{\rm E}$ compared to that for $M = 10^8 M_\odot$ and $\dot{M} = \dot{M}_{\rm E}$. Cited from Liu et al. (2003).

is set to the equilibrium value. The equilibrium temperature depends on the metallicity owing to various cooling and heating processes by heavy elements in the gas and dust grains. [1] As heating sources, the FUV and X-ray background from nearby star-forming regions are considered. The FUV intensities and the X-ray background intensities are assumed to be proportional to $G_{\rm SFR}$, which denotes the averaged surface density of the star formation rate, and it is normalized with the galactic value $\Sigma_{\rm SFR} = 0.1 M_\odot {\rm yr}^{-1}$ kpc^{-2} (Wolfire et al., 1995) . Figure 4.3, cited from Toyouchi et al. (2019), shows the gas equilibrium temperatures with metallicity $Z = 10^{-2} Z_\odot$ as functions of the number density of gas, n_∞, and $G_{\rm SFR}$. The intensities of FUV and X-ray background are assumed to be proportional to $G_{\rm SFR}$. From this figure, we can see that the equilibrium temperature in the density range $n_\infty = 10^3 - 10^6 {\rm cm}^{-3}$ is about $\sim$ 100 K with active star formation, which is widely expected for young gas-rich galaxies. In our simulations, we assume an environment such that active star formation occurs as a result of galaxy-galaxy mergers and apply that the background radiation is 100 times stronger than that in the solar neighborhood. This correspond to the orange lines in Figure 4.3. Considering the gas density of $10^4 {\rm cm}^{-3}$ in our study, 180K is appropriate for the gas temperature.

4.2.3 Luminosity

In this simulation, the luminosity produced by the BH accretion disks, L, is determined as a function of the accretion rate $\dot{M}$ evaluated at the internal boundary at each time step. We adopt a fitting equation to model the luminosity (Watarai et al., 2000),

$$L = \begin{cases} 2L_{\rm E}\left[1 + \ln\left(\frac{\dot{M}}{2\dot{M}_{\rm E}}\right)\right] & (\dot{M}/\dot{M}_{\rm E} > 2) \\ L_{\rm E}\frac{\dot{M}}{\dot{M}_{\rm E}} & ({\rm otherwise}) \end{cases}, \tag{4.2}$$

where $L_{\rm E}$ ($\equiv 4\pi c G M_{\rm BH}/\kappa_{\rm es}$) and $\dot{M}_{\rm E}$ ($\equiv L_{\rm E}/\eta c^2$) are the Eddington luminosity and Eddington accretion rate. Here, η is the radiative efficiency, and the typical value is $\eta = 0.1$ for a thin disk around a non-spinning BHs (standard disk model, Shakura et al., 1973). [2] Equation 4.2 is obtained by Watarai et al.

[1] We note that the gas density is fixed in this discussions: In general, the equilibrium temperature depends on the gas density.

[2] Note that this definition of $\dot{M}_{\rm E}$ is 10 times larger than that often used where the radiative efficiency η is not included, $L_{\rm E}/c^2$). To compare our results with the previous study, which do not include the dust sublimation process, we adopt the same definition

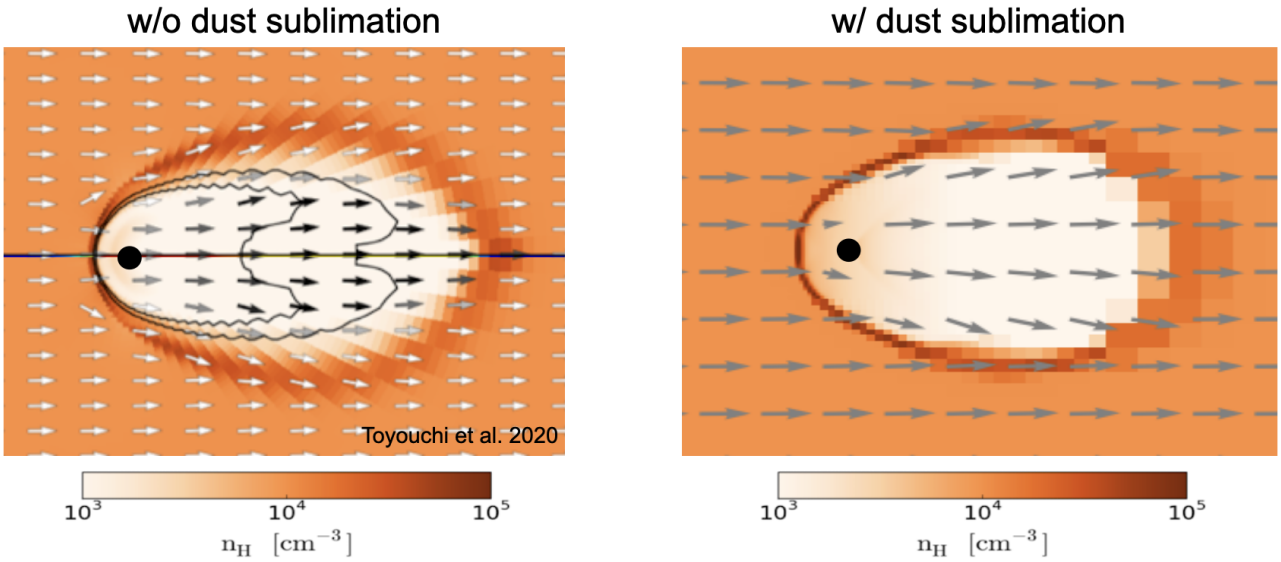

Figure 4.5: The distribution of gas number density in the case where dust sublimation is not taken into account (left panel, cited from Toyouchi et al., 2020) and in the case where dust sublimation is taken into account (right panel).

(2000) considering the appearance of the slim disk. In the case of low accretion rate ($\dot{M}/\dot{M}_{\rm E} < 2$), the radiative efficiency is fixed at 10%, which is consistent with that of the standard disk model. In the case of high accretion rate ($\dot{M}/\dot{M}_{\rm E} > 2$), the second term $2L_{\rm E} \ln\left(\dot{M}/2\dot{M}_{\rm E}\right)$ represents the luminosity from the innermost region of the accretion disk (slim disk), where the photon trapping reduces the radiative efficiency. The first term $2L_{\rm E}$ represents the luminosity from the outer region of accretion disk (standard thin disk). In the left panel of Figure 4.4, Equation 4.2 is plotted. The vertical axis is luminosity normalized by the Eddington one, and the horizontal axis is the accretion rate normalized by the Eddington one. We can see that the normalized luminosity does not exceed 10 in the range of $\dot{M}/\dot{M}_{\rm E} \lesssim 10^2$.

4.2.4 Spectrum of the BH radiation

The SED is simply assumed to be a power law with $L_\nu \propto \nu^{-\alpha}$ in the frequency range 11.2 eV $< h\nu <$ 1 keV, where h and ν are planck constant and photon frequency, respectively. Here, we adopt the power-law index of $\alpha = 1.5$, corresponding to the SED of active galactic nuclei in the high accretion state (Liu et al., 2003; Sazonov et al., 2004).

4.2.5 Chemical and thermal processes

We take into account the chemical network with 11 species: H, H^+, He, He^+, He^{2+}, CO, C^+, O, O^+, O^{2+}, and e. The main thermal processes in this simulations are; photo-ionization heating of H, photo-dissociation heating of H_2, H_2 formation heating, collisional ionization cooling of H, collisional dissociation cooling of H_2, recombination cooling of H^+, excitation cooling of H, He^+, free–free cooling of H, Compton cooling by cosmic microwave background (CMB) photons, line-cooling of He^{2+}, CO, C^+, O, O^+, andO^{2+}, and gas-grain heat transfer.

of $\dot{M}_{\rm E}$ including η as in the previous study.

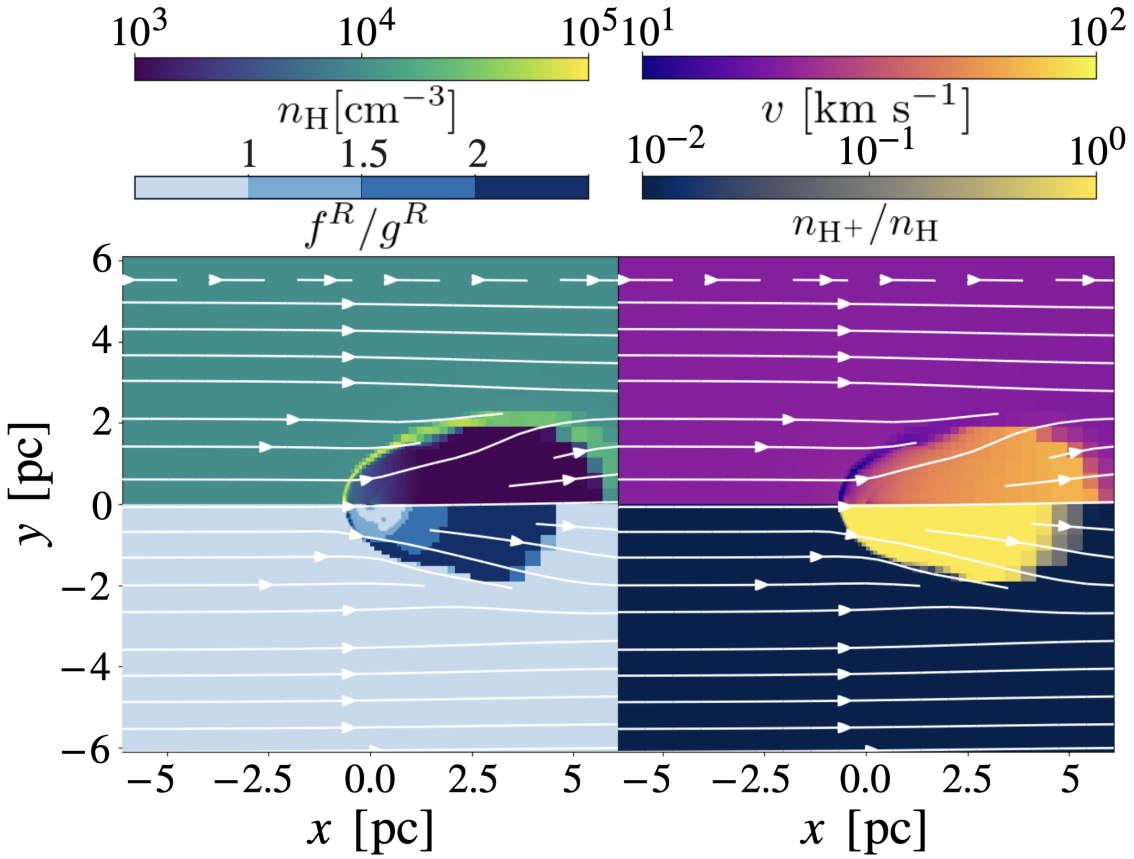

Figure 4.6: Gas flow structure on a 1 pc scale for the isotropic radiation model ('isoN4V20').Each panel shows distributions of the gas number density (upper left), velocity (upper right), and ionization degree (lower right). In the lower-left panel, we show the radiation force normalized by gravity in each cell. The white arrows represent streamlines to the $+x$ direction.

4.3 Result

Figure 4.5 shows the distribution of gas number density in the case where dust sublimation is not taken into account (left panel, cited from Toyouchi et al., 2020) and in the case where dust sublimation is taken into account (right panel). We see that the global flow structure is almost the same for models with and without dust sublimation. An elongated ionized region appears downstream, and a dense shell structure appears in front of the I-front. These features are generally consistent with previous results obtained in two dimensional RHD simulations for primordial case (Park & Ricotti, 2013) and three dimensional RHD simulations for dusty gas case (Toyouchi et al., 2020). We note that, such a shock structure is formed if the relative velocity of the ambient gas to the I-front is between the critical values of the D-type and R-type I-fronts ($v_{\rm D} < v_\infty < v_{\rm R}$), as also shown in Park & Ricotti (2013). Inside the shocked region, the gas slows to $v_{\rm D}$ at the ionization front. If the velocity v_∞ is higher than the critical value for the R-type ionization front $v_{\rm R}$, the shock does not appear.

In the model, where the metallicity is set to $0.1Z_\odot$, metal cooling is so efficient that the warm region ($\sim 10^4$K) does not extend outside the ionization region. As a result, a steep transition between cold ($\sim 10^2$K) and hot ($\sim 5 \times 10^4$K) medium occurs just before the upstream ionization front. The cold region corresponds to the ambient gas in thermal equilibrium, achieved by the balance between cooling of the metal line emission and heating by background radiation. The hot region is the ambient gas

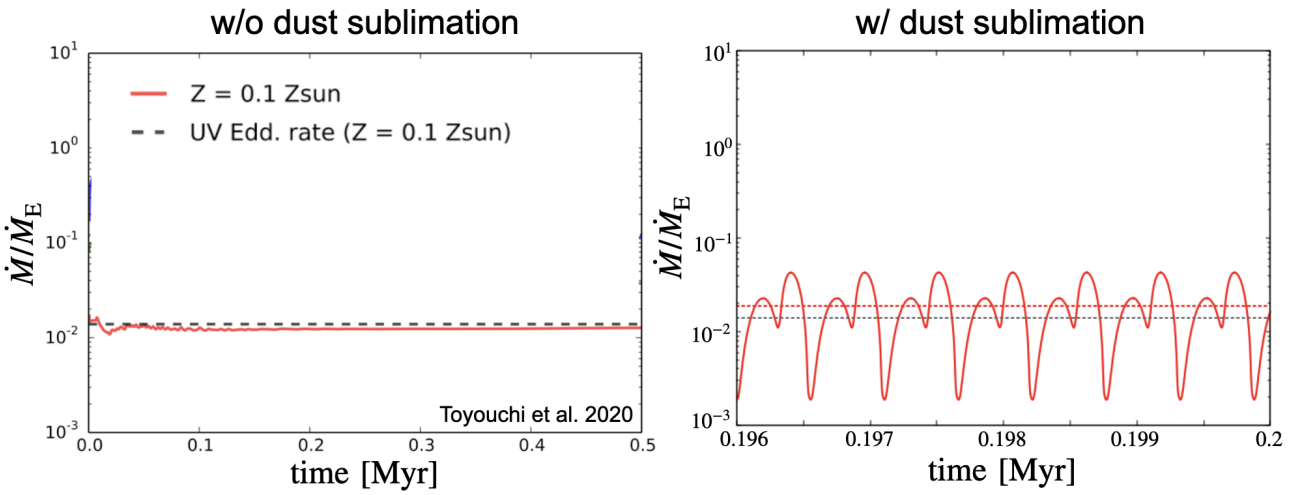

Figure 4.7: The time evolution of the mass accretion rate in the case where dust sublimation is not taken into account (left panel, cited from Toyouchi et al., 2020) and in the case where dust sublimation is taken into account (right panel). The black dashed line means the Eddington accretion rate for dusty gas $\dot{M}_{\rm E,dg}$ ($\equiv \kappa_{\rm es}\dot{M}_{\rm E}/(\kappa_{\rm es}+\kappa_{\rm d})$), where the dust opacity for UV light $\kappa_{\rm d}$ is given as $\kappa_{\rm d} = 2.8\times10^2(Z/Z_\odot)$ cm^2 g^{-1}.

of which temperature is determined by the balance between photoionization heating and Lyα cooling. The global structure of the velocity profiles is also almost the same for models with and without dust sublimation. The flow velocity gradually increases from 20km/s to around 50km/s after crossing the dense upstream shell. This acceleration occurs because of the increase in thermal pressure inside the ionization front caused by photoionization heating. We explain in detail in the following paragraphs.

Figure 4.6 shows distribution of gas number density (upper left), velocity (upper right), radiation force normalized by gravity in each cell (lower left), and ionization degree (lower right) in the case considering dust sublimation. The white arrows represent streamlines to the $+x$ direction. We find that an ionized region ($n_{\rm H+}/n_{\rm H}\sim1$) extends up to $x\sim5$ pc, and a dense shock shell is formed at the upstream ionization front ($x\sim-0.5$pc). The gas velocity gradually increases to ~50 km s^{-1} in the ionized region after passing through the dense shock shell. Such acceleration is caused by the thermal pressure increased by ionization heating. Increasing the gas velocity and increasing the gas temperature reduce the accretion rate since the Bondi-Hoyle-Lyttleton accretion rate decreases when the velocity and temperature are high. The outward radiation force also woks to reduce the accretion rate. Thus, the time-averaged accretion rate, $2\times10^{-2}\dot{M}_{\rm E}$, is three orders of magnitude smaller than the classical Bondi-Hoyle-Lyttleton accretion rate $\dot{M}_{\rm BHL}$.

Figure 4.7 shows the time evolution of the mass accretion rate. The black dashed line means the Eddington accretion rate for dusty gas $\dot{M}_{\rm E,dg}$ ($\equiv \kappa_{\rm es}\dot{M}_{\rm E}/(\kappa_{\rm es}+\kappa_{\rm d})$), where the dust opacity for UV light $\kappa_{\rm d}$ is given as $\kappa_{\rm d} = 2.8\times10^2(Z/Z_\odot)$ cm^2 g^{-1}. In the isotropic radiation model, the accretion rate oscillates periodically between $4.5\times10^{-2}\dot{M}_{\rm E}$ and $1.8\times10^{-3}\dot{M}_{\rm E}$ with a period of 5.5×10^{-4} Myr. The time-averaged accretion rate is about $2\times10^{-2}\dot{M}_{\rm E}$ ($4.3\times10^{-6}M_\odot$ yr^{-1}). The reason why the periodic oscillation of the accretion rate occurs can be understood from Figure 4.8. This figure shows the time evolution of flow structure and the radiation force normalized by gravity on the 10^{-2} pc scale in one period of oscillation. The time evolution of the accretion rate is also plotted. From this figure, we can see that the reason why the periodic oscillation of the accretion rate occurs due to the dust sublimation as desclibed below.

- When the gas accretion rate $\dot{M}$ is less than $\dot{M}_{\rm E,dg}$, the gravitational force overcomes the radiation

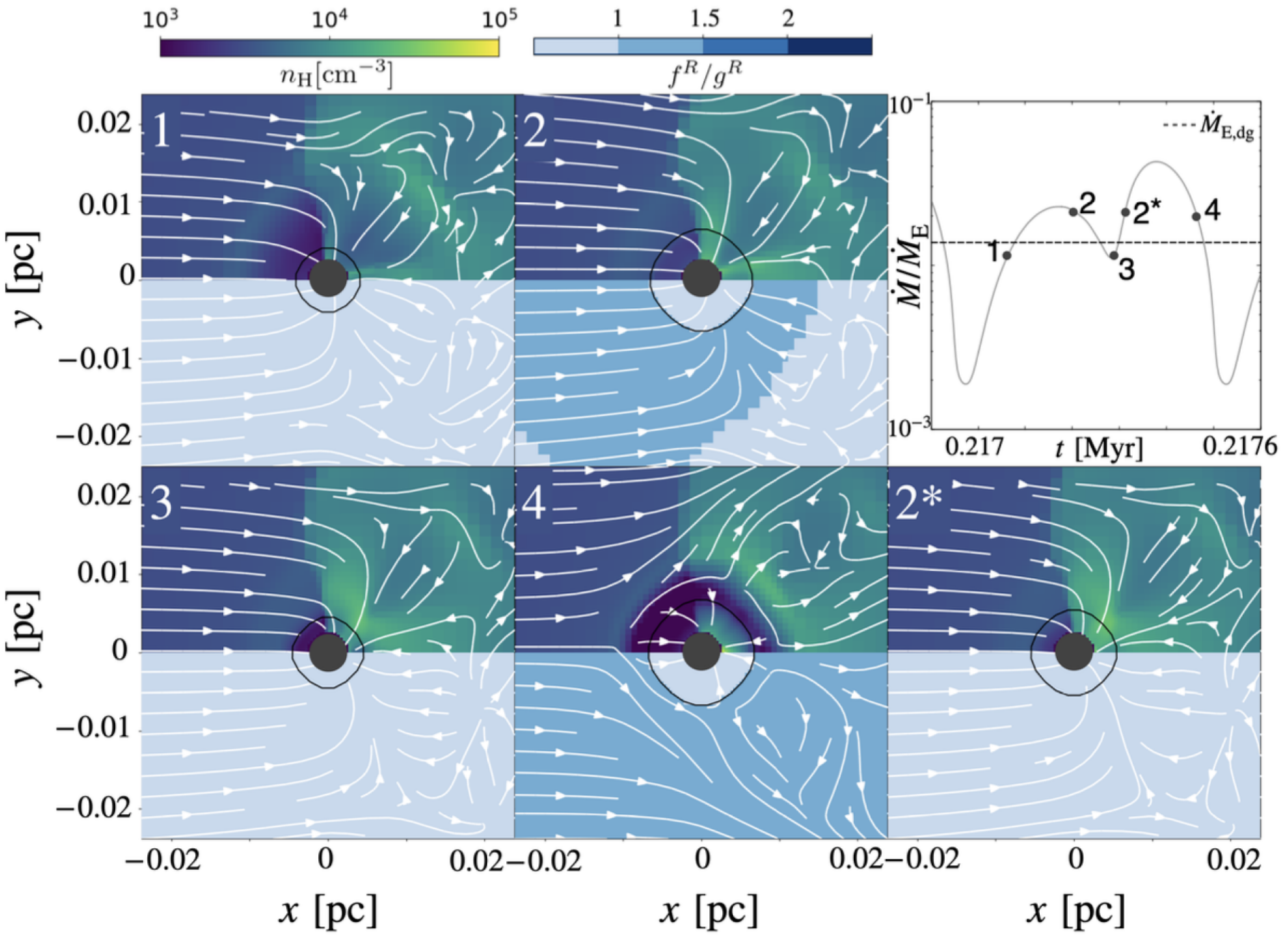

Figure 4.8: Time evolution of the gas flow in one oscillation period for the isotropic radiation model ('isoN4V20'). Each snapshot is the same as the bottom left panel in Figure 4.6. The black solid lines and filled gray circles represent the dust sublimation and sink regions. The upper right panel shows the time evolution of the accretion rate in one period of oscillation. The black filled circles mark the epochs for each snapshot 1-4.

force in the entire region. Gas accretes to the BH. The flow structures are similar to Bondi-Hoyle-Lyttleton accretion as shown in Figure 4.8-1.

- As the accretion rate exceeds $\dot{M}_{\rm E,dg}$, the radiation force deaccelerates gas (see Figure 4.8-2). Then, the gas is accumulated around the sublimation region. In fact, the averaged gas density near the sublimation radius in Figure 4.8-2 is approximately twice as large as in the case of Figure 4.8-1. After that, the accretion rate also begins to decrease. The radiation force caused by dust grains is inefficient inside the sublimation radius, and gas continues to accrete to the BH.

- As the accretion rate decreases to $\dot{M}_{\rm E,dg}$, the gravitational force overcomes the radiation pressure (see Figure 4.8-3). The accumulated gas accretes to the BH. Then the mass accretion rate increases and peaks at $\sim 3\dot{M}_{\rm E,dg}$. This peak value is higher than the previous one because high-density structures attenuate radiation. Indeed, the radiation flux near the sublimation radius at the first peak was $\sim 50\%$ of the analytical solution $L/(4\pi R^2)$ without attenuation, and $\sim 60\%$ for the second peak.

- The radiation force causes the outflow from the sublimation radius (see Figure 4.8-4). The gas inside the sublimation regions can accrete the BH, but the amount of gas is limited. Then the

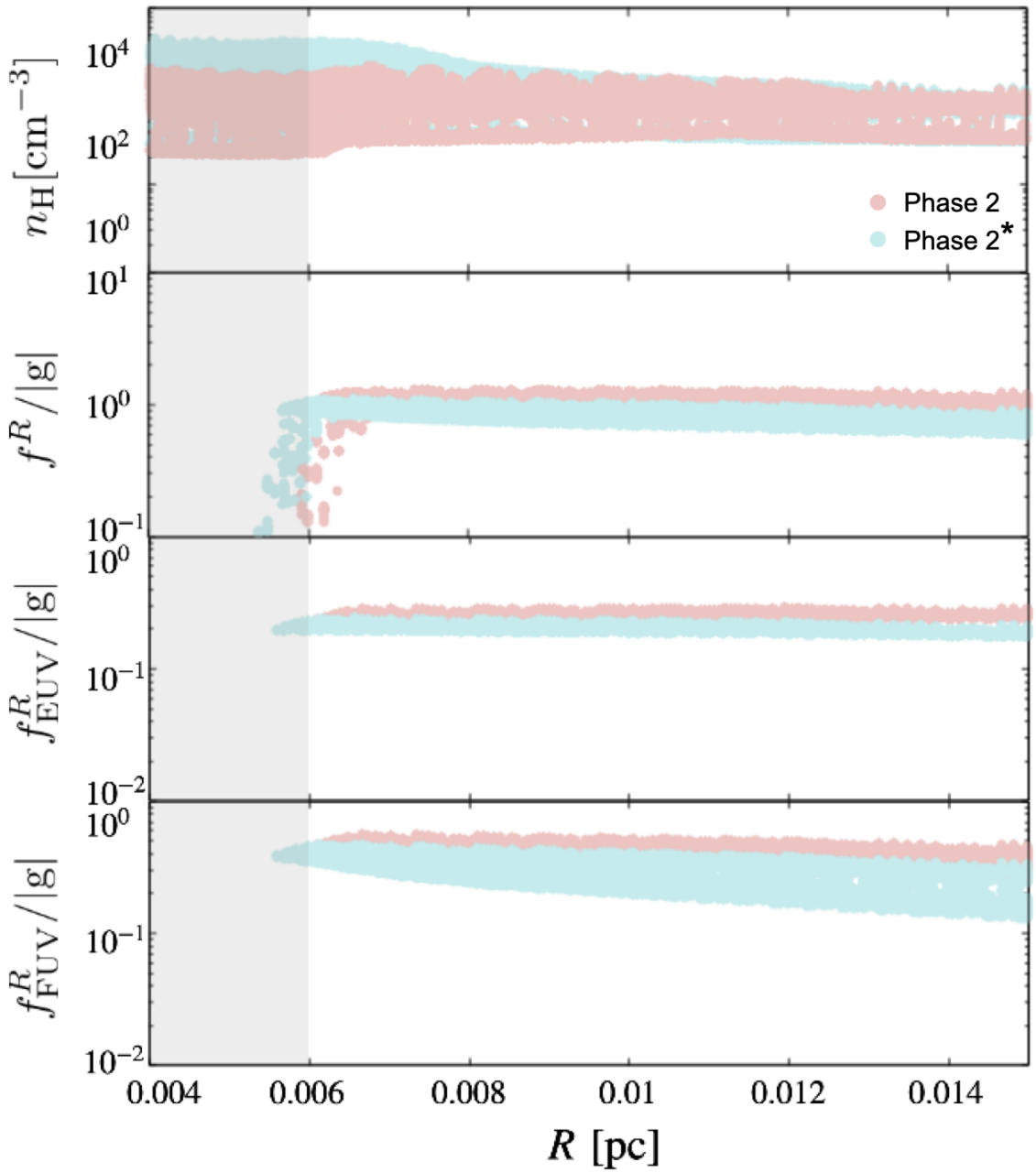

Figure 4.9: The number density $n_{\rm H}$ cm^{-3}, radiation force $f^R, f^R_{\rm EUV}, f^R_{\rm FUV}$ normalized by gravity g^R in Figure 4.8-2* (light-blue) and Figure 4.8-2 (pink). Here, f^R and gray region means $f^R = f^R_{\rm EUV} + f^R_{\rm FUV} + f^R_{\rm IR}$ and region of dust sublimation, respectively.

accretion rate dramatically decrease. After that, the gravitational force attracts the ambient gas again. The flow structure returns to that of Figure 4.8-1.

Here we explain why the second of the two peaks appearing in the burst has a larger accretion rate (luminosity). Figure 4.9 represents the number density ($n_{\rm H}$), ratio of radial component of total radiation force to gravity ($f^R/|g|$), ratio of radial component of radiation force doe to EUV to gravity ($f^R_{\rm EUV}/|g|$), and ratio of radial component of radiation force doe to FUV to gravity ($f^R_{\rm FUV}/|g|$) as a function of the distance from the intermediate-mass BH (R). The light-blue and pink mens the results at phase 4.8-2 ($t \sim 0.21715$ Myr) and phase 4.8-2* ($t \sim 0.2174$ Myr), respectively (see Figure 4.8). Phase 4.8-2 roughly

corresponds to the first peak, while phase 4.8-2* is a little before the second peak. The accretion rate in phase 4.8-2* is approximately equal to the accretion rate in phase 4.8-2.

It is found that the density is larger in the phase 4.8-2* than in phase 4.8-2 at slightly outside the dust sublimation region. This difference in density produces a difference in radiation flux (radiation force) through attenuation by absorption. Indeed, we find that the radiation force in the phase 4.8-2* is slightly weaker than that in the phase 4.8-2. In phase 4.8-2, the accretion rate starts to decrease due to radiation force, but in phase 4.8-2*, the accretion rate continues to increase further due to the weaker radiation force. Thus, the accretion rate (luminosity) is larger in second peak. Note that the main component of radiation force is due to FUV. The gas density is high in phase 4.8-2* because relatively large amount of gas that is not absorbed in the first peak remains around the BH. Conversely, the gas density in phase 4.8-2 is low because a large amount of gas is swallowed in the second peak.

4.4 Discussion

4.4.1 Comparison with previous works

Our present work shows that the global flow structures are generally in agreement with the previous results obtained by RHD simulations for the primordial cases. However, we find that the dust absorption effects (radiation force acting on dust grains, attenuation UV light) significantly change the flow structure vicinity of sublimation radius and accretion rate, compared to primordial cases. One reason for the such a small accretion rate may be due to the radiation force acting on the dust (see Toyouchi et al., 2020) [3]. Such an effect is incorporated in below equation:

$$L_{\rm E,dg} = \frac{\kappa_{\rm es}}{\kappa_{\rm es}+\kappa_{\rm d}} L_{\rm E} = \left(1 + 71\left(\frac{Z}{10^{-1}Z_{\odot}}\right)\right)^{-1} L_{\rm E}, \tag{4.3}$$

where $\kappa_{\rm es} = 0.4$ cm^2 g^{-1} is the opacity of electron scattering, and $\kappa_{\rm d} = 280$ cm^2 g^{-1}(Z/Z$_{\odot}$). Since the dust opacity is larger than the electron scattering value, the critical luminosity (Eddington luminosity) become more stringent limits. We note that the accretion rate predicted by $\dot{M}_{\rm E,dg} = L_{\rm E,dg}/(\eta c^2)$ well matches with the time-averaged accretion rate obtained by our simulations for $Z = 0.1Z_{\odot}$.

It is also important to take into account the dust sublimation. The time-averaged accretion rate is not much different between our simulation and the simulations by Toyouchi et al. (2020), but oscillation of the accretion rate occurs only in our simulation. Since the situational setting is almost the same, the cause of this difference is thought to be the treatment of dust sublimation.

4.4.2 The effect of dust sputtering

The destruction of dust in high-temperature gas occurs not only by sublimation but also by sputtering. Sputtering is a physical process in which energetic particles (in this case mainly hydrogen ions) collide with dust grains and flick off the atoms of the dust grain. If the collision is driven by the thermal motion of the ions, it is called thermal sputtering; if it is caused by the fast relative motion of the ions and the dust, it is called nonthermal sputtering. As atoms near the dust surface are lost one by one due to sputtering, the radius of the dust grain becomes smaller and smaller. The reduction rate of the dust radius due to sputtering depends on the quantities of the colliding ions, such as species, energy, number density, and composition of the dust. The right panel of Figure 4.10 shows the thermal

[3] In other word, the BH gravity is effectively weakened by the outward force of the radiation pressure boosted by the presence of dust grains within the ionized bubble(Ogata et al., 2021)

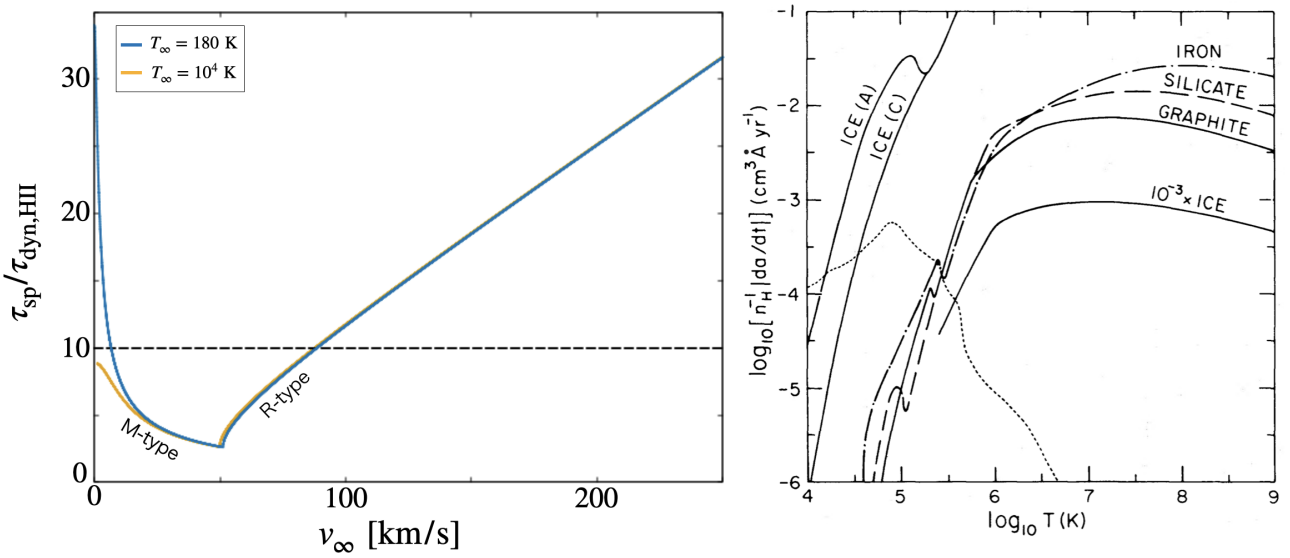

Figure 4.10: left panel: Time scale for dust sputtering $\tau_{\rm sp}$ normalized by dynamical time scale in the ionized region (see Equation 4.5 and 4.6). Right panel: Thermal sputtering rates as a function of temperature for iron, silicate, graphite, and H_2O grains cited from Draine & Salpeter (1979). The dotted curve is $\log_{10}\left[n_{\rm H}^{-1}|da/dt|\right]$ $\left({\rm cm^3 \AA yr^{-1}}\right)$ for radiative cooling of optically thin gas.

sputtering rates estimated for graphite, silicate grains, and iron grains for temperature $10^4 \lesssim T \lesssim 10^9$ K (Draine & Salpeter, 1979). Draine & Salpeter (1979) calculate the sputtering rates, and it can be approximated by

$$\frac{da}{dt} \approx -\frac{1\times10^{-6}}{1+T_6^{-3}}\left(\frac{n_{\rm H}}{\rm cm^{-3}}\right)\ \mu{\rm m\ yr^{-1}}, \tag{4.4}$$

where a is the radius of dust grains. Using this formula, we obtain a lifetime of dust grains,

$$\tau_{\rm sp} = \frac{a}{|da/dt|} \approx 1\times10^5\left[1+T_6^{-3}\right]\frac{(a/0.1\mu{\rm m})}{(n_{\rm H}/{\rm cm^{-3}})}\ {\rm yr}. \tag{4.5}$$

To see if sputtering is an important effect in the system of wandering BHs under the radiation feedback, we compare it to the dynamical timescale $\tau_{\rm dyn,II}$ in the ionized region, which is defined as

$$\tau_{\rm dyn,II} = \frac{R_{\rm II}}{v_{\rm II}}. \tag{4.6}$$

Here, $R_{\rm II}$ and $v_{\rm II}$ are the size of the ionized region and typical velocity of gas in the ionized region, respectively. We estimate the size of an ionized region by Strömgren radius, and gas velocity in ionized region by theoretical model of Park & Ricotti (2013). The gas velocity in the ionized region depends on gas velocity in the neutral region at infinity. The left panel of Figure 4.10 shows the time scale of dust sputtering normalized by dynamical time scale in the ionized region. We can see that the $\tau_{\rm sp} \gtrsim \tau_{\rm dyn,II}$ is satisfied for both M- and R-types. Therefore, we can ignore the effect of dust sputtering in our simulations. Note that, we cannot assert that sputtering does not work because there is no more than an order of magnitude difference between M-type and R-type ($\lesssim 100$ km/s).

Chapter 5

Accretion onto the Wandering Black Holes: Effects of Anisotropic Radiation Feedback

In this paper, we study the effect of anisotropy of radiation filed produced by accretion disk on Bondi-Hoyle-Lyttleton accretion flow. We have, for the first time, successfully performed three-dimensional radiation hydrodynamics simulations of the gas accretion onto intermediate-mass BHs wandering in the early Universe considering anisotropic radiation field. Additionally, the sublimation of the dust grains caused by the radiation from the accretion disks around BHs is taken into consideration. We found that the accretion rate and acceleration are $\sim 7 \times 10^{-6}\ M_{\odot}\ \mathrm{yr}^{-1}$ (0.6 per cent of the classical Bondi–Hoyle–Lyttleton rate) and $\sim 10^{-8}$ cm s^{-2} in environments with relatively high density ($\sim 10^{4}$ cm^{-3}) and low metallicity ($0.1Z_{\odot}$). These results suggest that intermediate-mass BHs keep floating in the galactic disk with insignificant mass growth. For extremely high density ($\gtrsim 10^{6}$ cm^{-3}), as suggested by recent observations from the James Webb Space Telescope (JWST), the accretion rate and acceleration rise significantly.

5.1 Anisotropic radiation field

Bondi-Hoyle-Lyttleton accretion flow was investigated through numerous hydrodynamics simulations from the 1970s to the late 1990s (Hunt, 1971; Shima et al., 1985; Fryxell et al., 1988; Ho et al., 1989; Matsuda et al., 1991; Ruffert et al., 1994, 1996), which showed that numerically obtained the accretion rates are consistent with the analytical estimates of Hoyle & Lyttleton (1939) and Bondi & Hoyle (1944). Subsequently, numerical simulations considering the radiation from the central object were performed (Blondin et al., 1990; Taam et al., 1991; Milosavljevic et al., 2008; Park & Ricotti, 2012; Park & Bogdanović, 2017; Sugimura & Ricotti, 2020; Toyouchi et al., 2020), showing that the accretion rates are significantly reduced by radiation feedback e.g., the radiation force and ionization heating.

However, all those calculations assume isotropic radiation, whereas in reality the radiation from the BH accretion disk should be anisotropic. The flow structure will be significantly altered in such anisotropic radiation field. We can expect that the accretion rates can not decrease significantly because the gas accretes through the region near the disk plane, where the radiation effect is relatively weak. Although Bondi-Hoyle-Lyttleton accretion onto the compact objects under the anisotropic radiation field produced by the accretion disk has been investigated in previous studies (Fukue, 1999; Hanamoto et al., 2001; Ogata et al., 2021), the effect of fluid dynamics such as gas pressure gradient force has not been

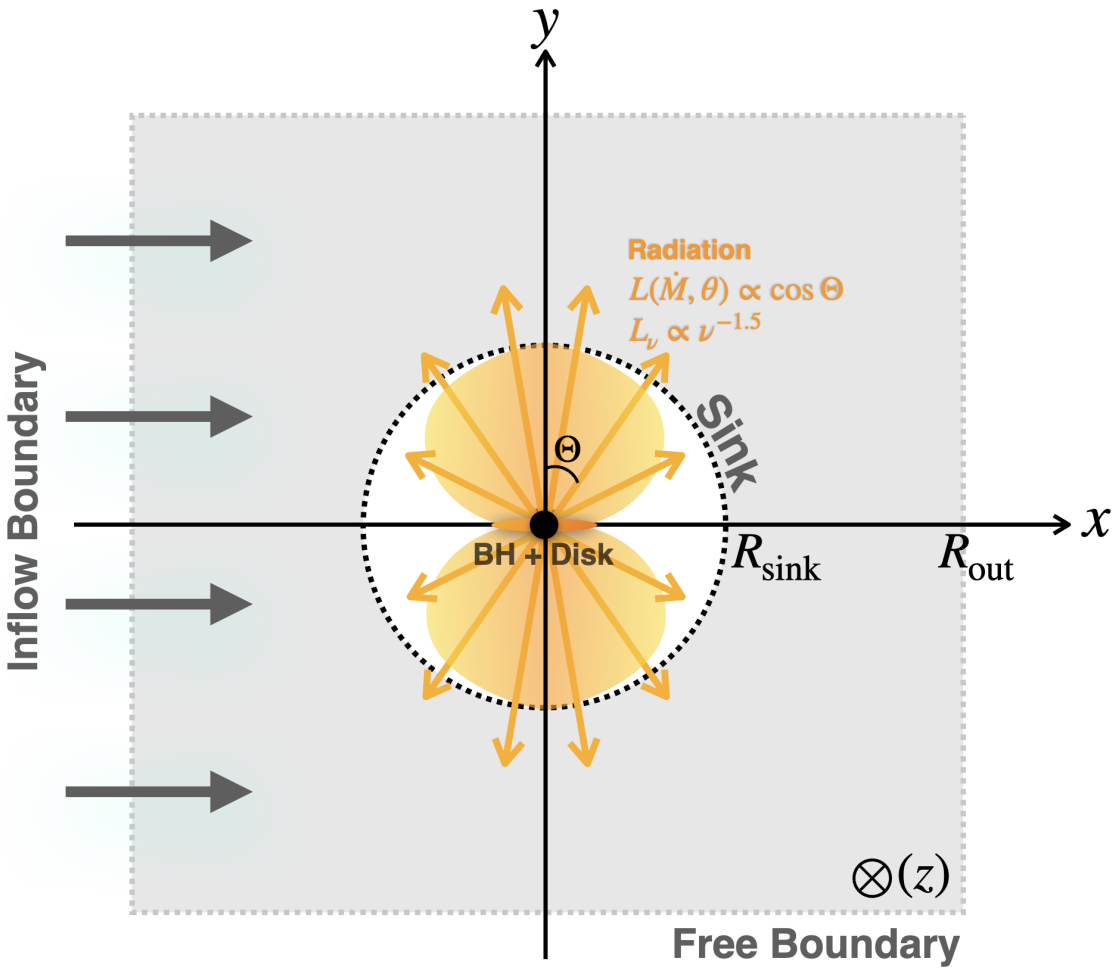

Figure 5.1: Schematic figure of our simulation settings for anisotropic radiation case.

taken into account. Therefore, radiation hydrodynamics simulation of Bondi-Hoyle-Lyttleton accretion including an anisotropic radiation field is required.

5.2 Models and Method

We perform three dimensional RHD simulations to investigate the effect of anisotropic radiation feedback on the gas accretion process of wandering BHs. Specifically, we solve the dynamics of the flow around the Bondi-Hoyle-Lyttleton radius to determine the accretion rate onto the BHs and disk system. The inner side of the BH accretion disk is covered by a central sink region, and ionizing photons are injected at in the sink region (see Figure 5.1). The calculation setup is similar to the isotropic radiation model introduced in Chapter 4. Therefore, in this section, we only introduce the angular distribution of the radiation field and parameters that differ from the isotropic radiation model.

5.2.1 Directional dependence of radiation field

We inject the extreme EUV and FUV photons at the sink region with the directional dependence as described below. The number of photons injected per unit time in a single cell is given as

$$\dot{N}_\nu^j = \dot{N}_\nu^{\rm sink} \times \frac{\mathcal{F}_j(\Theta, R)}{\sum_k \mathcal{F}_k(\Theta, R)}, \tag{5.1}$$

where $\dot{N}_\nu^{\rm sink}$ is the photon emissivity of the BH, and k and j are the cell numbers. The anisotopy factor $\mathcal{F}_j(\Theta, R)$ represents the direction dependence of the radiation as

$$\mathcal{F}_j(\Theta, R) = \begin{cases} 1/R^2 & \text{(isotropic radiation)} \\ 2\cos\Theta/R^2 & \text{(anisotropic radiation)} \end{cases}. \tag{5.2}$$

Here, the angle from the rotation axis of the disk to the center of each cell (Θ) is defined as

$$\cos\Theta = \boldsymbol{i}\cdot\boldsymbol{s} = \frac{1}{R}\left(x\cos\psi + y\sin\psi\cos\varphi + z\sin\psi\sin\varphi\right), \tag{5.3}$$

$$\boldsymbol{i} = (\cos\psi, \sin\psi\cos\varphi, \sin\psi\sin\varphi), \tag{5.4}$$

$$\boldsymbol{s} = \frac{1}{R}(x, y, z), \tag{5.5}$$

where $R(=\sqrt{x^2+y^2+z^2})$ is the distance of the origin, φ is the angle between y-axis and the disk rotation axis projected onto yz-plane, and ψ is the angle between x-axis and the disk rotation axis, respectively. We set $\varphi = 0$ in the present simulations.

We also solve the diffuse IR photons produced as the dust thermal emission. The energy absorbed by the dust is reprocessed as thermal emission at IR wavelengths. If a interstellar medium around wandering BHs is optically thick even for IR photons, the additional radiation pressure is exerted. This further suppresses the accretion onto BHs. In RHD simulations performed by Toyouchi et al. (2019), the radiative transfer is solved for both the direct ultraviolet lights emitted by an accretion disc and the diffuse infrared (IR) lights thermally emitted by dust grains. Their results show that the radiative force by the IR lights causes a strong feedback to regulate the mass accretion.

5.2.2 Cases considered

Table 5.1: Parameters and physical quantities for aisotropic radiation model

Parameter	$M_{\rm BH}$	n_∞	v_∞	T_∞	Z_∞	L	L_ν
Unit	$[M_\odot]$	$[{\rm cm}^{-3}]$	$[{\rm km\ s}^{-1}]$	[K]	$[Z_\odot]$		
`edgeN4V20`	10^4	10^4	20	180	0.1	Eq.4.2	$\propto \nu^{-1.5}$
`edgeN4V100`	10^4	10^4	100	180	0.1	Eq.4.2	$\propto \nu^{-1.5}$
`edgeN6V20`	10^4	10^6	20	180	0.1	Eq.4.2	$\propto \nu^{-1.5}$

First of all, we describe the parameters of our simulations which is also presented in Ogata et al. (2024). In our simulations, we set the BH mass to $M_{\rm BH} = 10^4 M_\odot$, gas number density to $n = 10^4$ cm^{-3}, gas velocity to $v = 20$ km s^{-1}, gas temperature to $T = 180$ K, metallicity to $Z = 0.1 Z_\odot$ as an initial condition. As boundary conditions, a gas with velocity $v_\infty = 20$km s^{-1} in the $+x$ direction, gas number density $n_\infty = 10^4$ cm^{-3}, gas temperature $T_\infty = 180$ K, and metallicity $Z_\infty = 0.1 Z_\odot$ is continuously injected at $x = -R_{\rm out}$, and a free boundary is assumed for the other surface (see Table 4.1). Here, $R_{\rm out}$ means the size of simulation box. Hereafter, we label each model according to the anisotropy factor

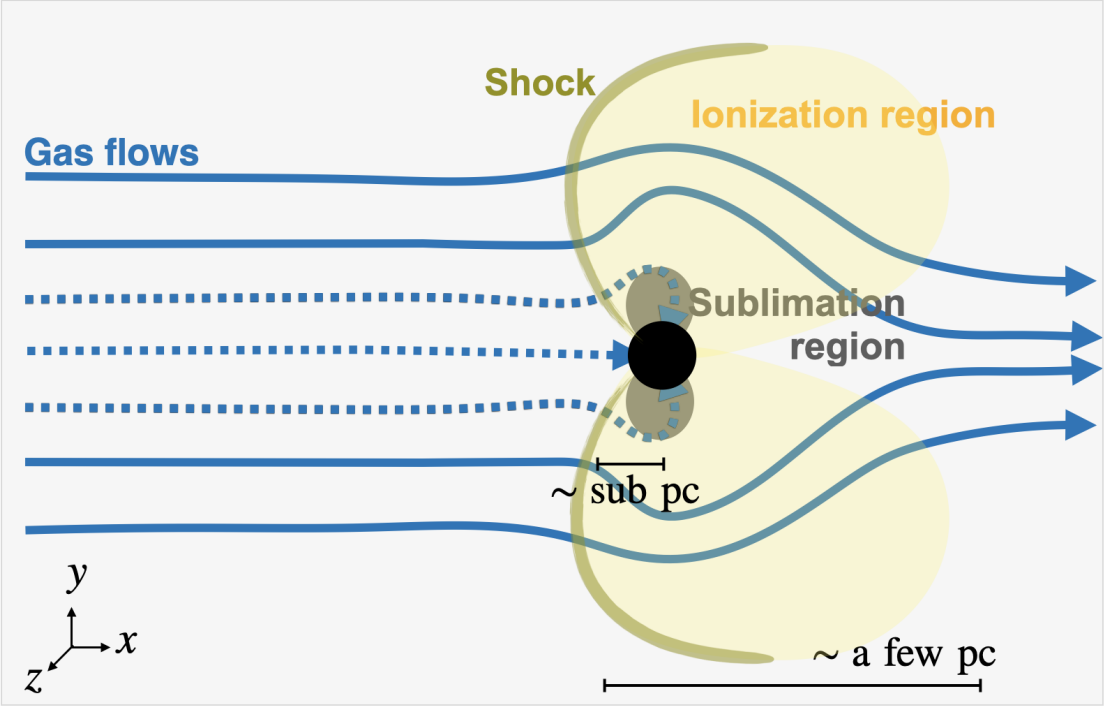

Figure 5.2: A schematic picture of a gas flow around a BH. We show a case with an edge-on radiation field. The BH floats in the interstellar medium (light gray). The black-filled circle represents the sink region. The solid and dotted blue lines show streamlines that pass through or accrete to BH. The yellow and gray regions present ionized and dust sublimation regions, respectively. The shocked region at the ionization front is painted dark yellow. The shapes of ionized and dust sublimation regions are different in the models with isotropic and pole-on radiation fields.

($\mathcal{F}_j$), the number density (n_∞), and gas velocity (v_∞) considered in each simulation. For example, 'edgeN4V20' represents the simulation model with the anisotropic radiation field, $n_\infty = 10^4$ cm^{-3}, and $v_\infty = 20$ km s^{-1}. We adopt $10^4 M_\odot$ as the mass of the BHs, which is a typical value for intermediate-mass BHs, from the standpoint that this study is the first step for understanding the formation process of supermassive black holes. The gas velocity and gas number density are chosen in reference to numerical simulations that follow the Milky Way-size galaxy mergers (Mayer et al., 2007, 2010). This is because once galaxies harboring intermediate-mass BHs merge, the BHs are expected to drift in the remnant galaxy. We additionally investigate the cases with high-velocity $v_\infty = 100$ km s^{-1} and high-density $n_\infty = 10^6$ cm^{-3} only in the models with edge-on anisotropic radiation. Such high-density environments would appear, for example, in merger remnant galaxies (e.g. Fiacconi et al., 2013; Lima et al., 2017). Also, Katz et al. (2023) has been reported the presence of relatively dense gas, $\gtrsim 10^4$cm^{-3}. The high-velocity situation, $v_\infty \sim 100$ km s^{-1}, might be realized when galaxy mergers occur (e.g. Mayer et al., 2007).

In the present study, $\psi = \pi/2$ (edge-on) is mainly adopted (see Figure 5.1). The gas inflow direction ($-x$ direction) at the upstream boundary is perpendicular to the rotation axis of the disk in this model. Such a situation appears naturally. The angular momentum vector of the gas injected from the upstream boundary relative to the origin (BH) is perpendicular to the x-axis. Therefore, although the gas density at the upstream boundary is assumed to be uniform in our simulations, if the density is non-uniform, the total angular momentum vector of the gas will be perpendicular to the x-axis. Thus, the gas falling

into the central region would form the accretion disk with the rotation axis perpendicular to the x-axis. Even if the rotation axis of the accretion disk is not perpendicular to the x-axis at the beginning, it should eventually become perpendicular to the x-axis since the gas in the initial disk is swallowed by the BHs, and the supplied gas becomes main component of the disk. The pole-on situation ($\psi = 0$) is realized only at the moment if the black hole happens to enter the gas cloud from the direction of the rotation axis of the disk, but it is adopted in order to compare with the edge-on models.

5.3 Results

Before examining the numerical results in more detail, we overview the flow structure and the accretion rates to BHs. Figure 5.2 schematically shows a flow structure around a BH. Ionizing photons emitted from the accreting BH create an ionized region over several pc. The shock structure is formed upstream ($-x$ direction) if the relative velocity of the ambient gas to the ionization front is between the critical values of the D-type and R-type ionization fronts ($v_{\rm D} < v_\infty < v_{\rm R}$), as also shown in Park & Ricotti (2013). Inside the shocked region, the gas slows to $v_{\rm D}$ at the ionization front. If the velocity v_∞ is higher than the critical value for the R-type ionization front $v_{\rm R}$, the shock does not appear. Dust grains are heated and sublimate close to the BH. In this region, radiation force cannot push out the gas, and the gas tends to accrete to the BH. In the outer region, where the dust grains are not sublimated, the gas is accelerated by radiation force and thermal pressure. Then it tends to pass through the ionized region without falling into the BH.

Figure 5.3 shows the time evolution of the mass accretion rate. The black dashed line means the Eddington accretion rate for dusty gas $\dot{M}_{\rm E,dg}$ ($\equiv \kappa_{\rm es}\dot{M}_{\rm E}/(\kappa_{\rm es} + \kappa_{\rm d})$), where the dust opacity for UV light $\kappa_{\rm d}$ is given as $\kappa_{\rm d} = 2.8 \times 10^2 (Z/Z_\odot)$ cm^2 g^{-1} (e.g. Yajima et al., 2017). As described before, in the isotropic radiation model 'isoN4V20', the accretion rate oscillates periodically between $4.5 \times 10^{-2}\dot{M}_{\rm E}$ and $1.8 \times 10^{-3}\dot{M}_{\rm E}$ with a period of 5.5×10^{-4} Myr. The time-averaged accretion rate is about $2 \times 10^{-2}\dot{M}_{\rm E}$ (4.3×10^{-6} $M_\odot$yr^{-1}). The accretion bursts (rapid increase in accretion rate) occur in the model 'edgeN6V20' with a period of ~ 0.01 Myr. The time-averaged accretion rate is about $2\dot{M}_{\rm E}$ ($4.2 \times 10^{-4} M_\odot$yr^{-1}). Although it does not appear in the figure, model 'edgeN4V20' also exhibits accretion bursts at the interval with ~ 0.15 Myr (we will discuss later). The time-averaged value in this model, $2 \times 10^{-2}\dot{M}_{\rm E}$ (4×10^{-6} $M_\odot$yr^{-1}), is slightly larger than the accretion rate shown in Fig. 5.3 because the bursts increase the time-averaged rate. The quasi-steady state is achieved in the models 'edgeN4V100' and 'poleN4V20', and the time-averaged rate is almost the same as in model 'edgeN4V20'.

5.3.1 Fiducial model

In the case of 'edgeN4V20' (fiducial model), the accretion rate is almost constant for most of the time (quiescent phase), but accretion bursts occur periodically (burst phase). Figure 5.4 presents the flow structure in the meridian ($z = 0$) and equatorial ($y = 0$) planes in the quiescent phase. Although the radiation field is anisotropic, the profiles of density and velocity on the ~ 1 pc scale are almost similar to that of the isotropic radiation model (see Figure 5.4-a). Also in this model, an ionized region extends up to several pc. Around the surface of the dense shock shell, the gas pressure gradient force by the high density and high temperature gas in the shell moves the gas away from the BH. Indeed, we find that some gas moves away from the x-axis along the shell (see streamlines). The effect of anisotropic radiation can be seen in Figure 5.4-b. It is found that the shape of the ionization region is like two spheres glued together at the equatorial plane. The dense shock shell appears near the ionization front.

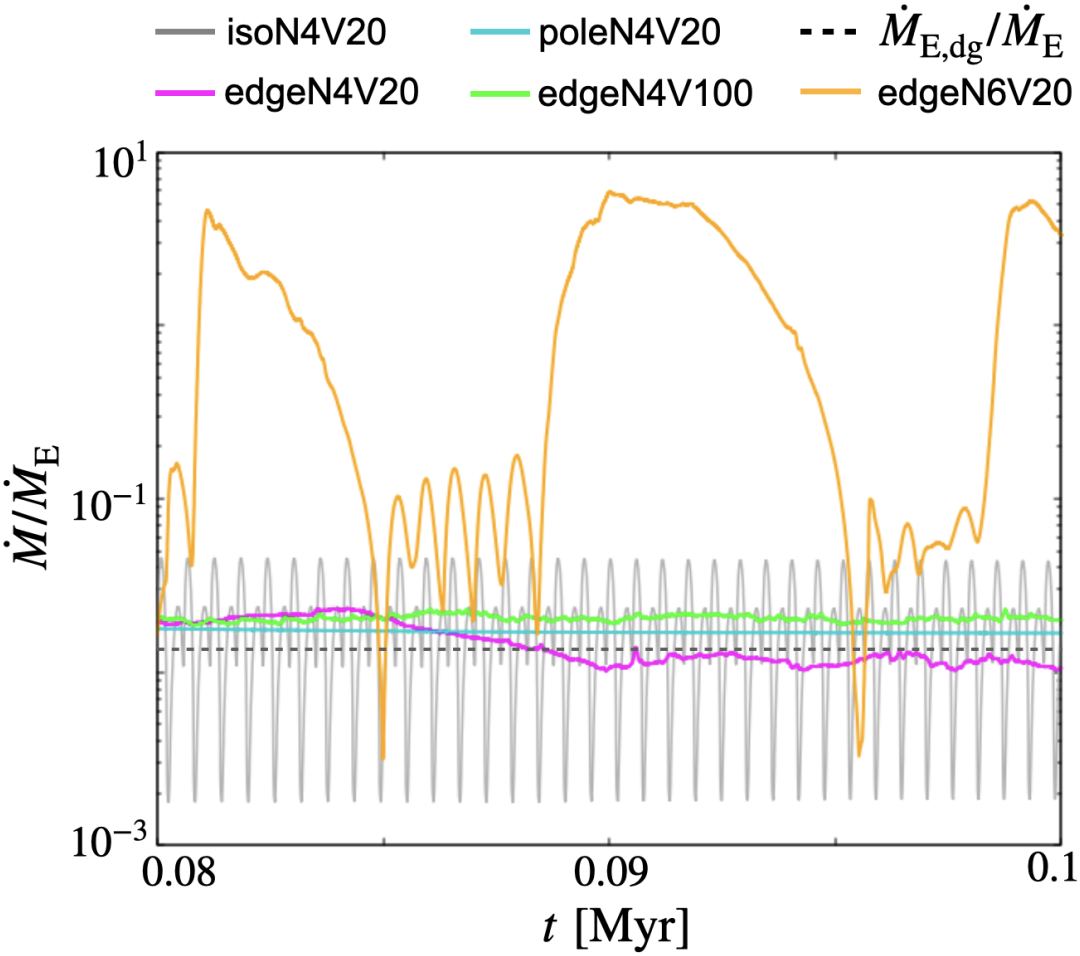

Figure 5.3: Time evolution of mass accretion rates. The vertical axis is normalized by the Eddington accretion rate $\dot{M}_{\rm E}$ estimated with the opacity of electron scattering. The gray and cyan lines show the models with isotropic radiation ('isoN4V20') and the pole-on radiation ('poleN4V20'). The magenta, green, and orange lines represent the edge-on fiducial ('edgeN4V20'), high-velocity ('edgeN4V100'), and high-density models ('edgeN6V20'). The black dotted lines represent the Eddington accretion rate for dusty gas $\dot{M}_{\rm E,dg}$.

The velocity and temperature of the gas that passes through the shell and enters the ionized region rapidly increases by gas pressure gradient force and the ionization heating. These increases in velocity and temperature work to reduce the rate of accretion by the Bondi-Hoyle-Lyttleton mechanism. We find in Figure 5.4-c that the gas accretes mainly from the equatorial plane since the radiation force is ineffective because BH irradiation is considerably weakened by absorption. In contrast, the strong radiation force works to prevent gas accretion around the rotation axis of the disk. As a result, the time-averaged accretion rate in the quiescent phase is much smaller than Bondi-Hoyle-Lyttleton rate ($\sim 0.3\%$ of $\dot{M}_{\rm BHL}$), and nearly comparable to $\dot{M}_{\rm dg}$.

The accretion bursts only increase the time-averaged accretion rate by about a factor of 2, and also hardly affect acceleration at all. The bursts occur when part of the dense shock shell (near the x-axis) flows into the sink. The dense shock shell is almost never moved due to the balance between the ram pressure gradient force and the gas pressure gradient force in the quiescent phase. However, part of the dense shock shell around the x-axis gradually moves inward due to the gravity of the BH and then flows into the sink leading to the burst phase. The accretion rate of the burst phase is $\sim \dot{M}_{\rm E}$ and about

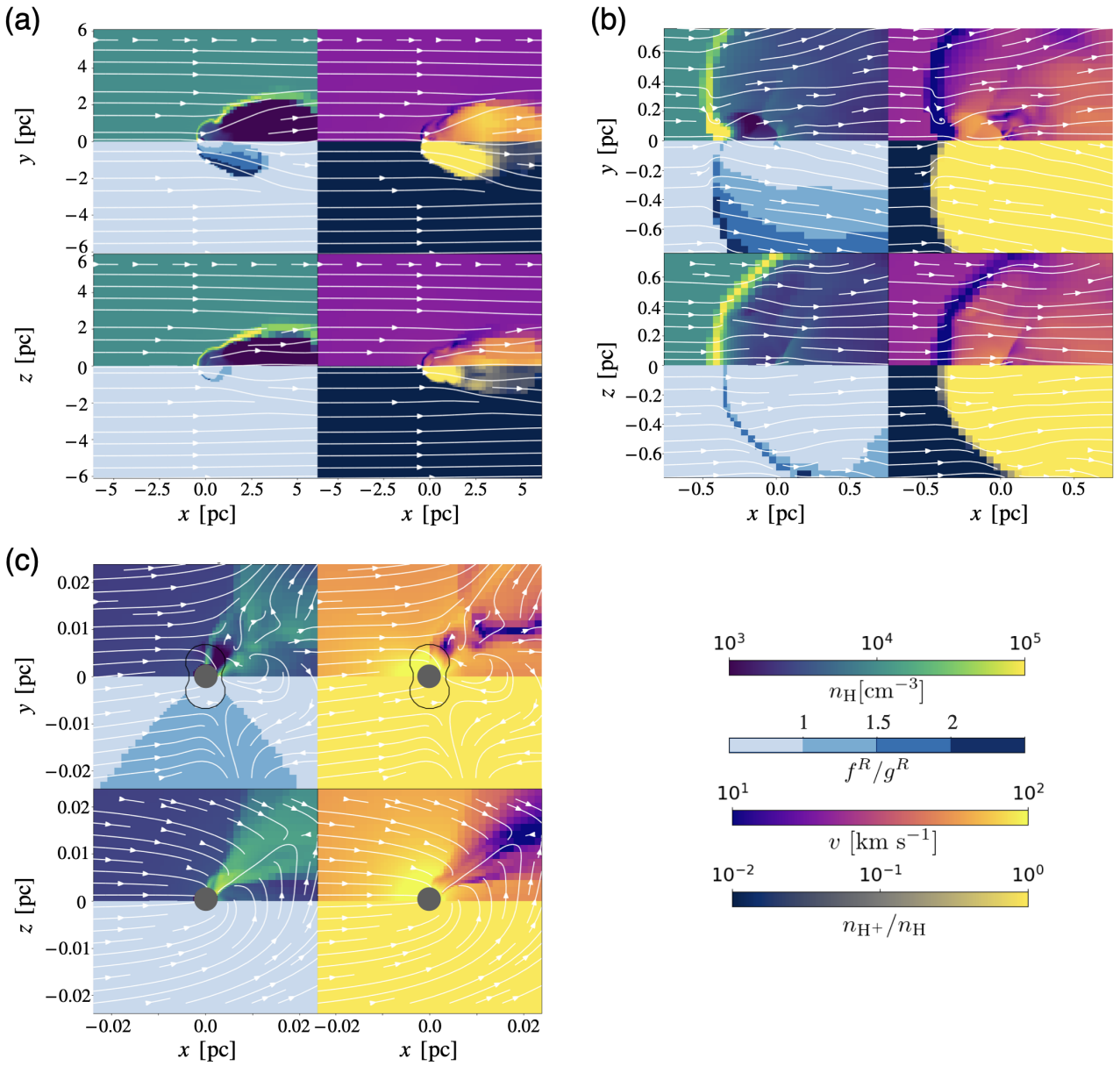

Figure 5.4: Same as Figure 4.6 but for the edge-on fiducial model ('edgeN4V20'). Each panel shows the flow structure on (a)1 pc, (b)10^{-1} and (c)10^{-2} pc scales at $t = 0.2$ Myr (0.04 Myr before the next accretion burst). Each column represents the flow structure in the meridian (xy-) and equatorial (xz-) planes from top to bottom.

half of the total accreting gas accretes during the burst phase. Due to the bursts, the time-averaged accretion rate is approximately twice the accretion rate during the quiescent phase (see Figure 5.3).

The burst interval, ~ 0.15Myr, can be understood approximately as follows. In the situation where gas pressure and ram pressure are approximately balanced at the dense shock shell, the gravity begins to pull the shell when the column number density of the shell ($N_{\rm shell}$) exceeds $n_\infty r_{\rm shell}^2 v_\infty^2/GM_{\rm BH}$ because

the gravity, $GM_{\rm BH}N_{\rm shell}/r_{\rm shell}^2$, becomes larger than the ram pressure (gas pressure), $n_\infty v_\infty^2$:

$$\frac{GM_{\rm BH}N_{\rm shell}}{r_{\rm shell}^2} > n_\infty v_\infty^2 \tag{5.6}$$

$$\rightarrow N_{\rm shell} > \frac{n_\infty v_\infty^2 r_{\rm shell}^2}{GM_{\rm BH}} \tag{5.7}$$

Since the distance of the dense shock shell from the BH, $r_{\rm shell}$, is about 0.5pc, the critical column number density obtained from the above relation is $\sim 10^{23}{\rm cm}^{-2}$, which is roughly consistent with that the burst in the present simulation. The timescale on which the column number density of the dense shock shell reaches $10^{23}{\rm cm}^{-2}$ is approximately:

$$\tau_{\rm burst} = \frac{N_{\rm shell}}{n_\infty v_\infty} \tag{5.8}$$

$$= \frac{n_\infty v_\infty^2 r_{\rm shell}^2}{GM_{\rm BH}} \times \frac{1}{n_\infty v_\infty} = \frac{v_\infty r_{\rm shell}^2}{GM_{\rm BH}} \tag{5.9}$$

$$\approx 1.1\ {\rm Myr} \left(\frac{\rm v_\infty}{20\ {\rm km/s}}\right) \left(\frac{\rm r_{shell}}{0.5\ {\rm pc}}\right)^2 \left(\frac{\rm M_{BH}}{10^4 {\rm M}_\odot}\right)^{-1}. \tag{5.10}$$

The timescale on which the burst occurs is determined by two factors: the timescale on which the gravity becomes stronger (the timescale on which the column density of the dense shell increases), as determined above (Equation 5.10), and the timescale on which the shell falls to the BH due to gravity (dynamical timescale). The dynamical timescale is $r_{\rm shell}/v_{\rm ff} \sim \sqrt{r_{\rm shell}^3/(2GM_{\rm BH})} \sim 0.04$ Myr. Therefore, the timescale on which the column number density of the dense shock shell reaches $10^{23}{\rm cm}^{-2}$ (Equation 5.10) is longer than the dynamical timescale so the burst interval is determined by the former timescale.

5.3.2 High-velocity model

Figure 5.5 shows the flow structure in the model 'edgeN4V100'. The most noticeable difference from the fiducial model is the absence of shock waves. This is because the relative velocity is largar than $v_{\rm R}$. We also confirm that the density does not change so much at the ionization front. The density change at the ionization front can be estimated analytically with the mass and momentum conservation laws as $\rho_{\rm II}/\rho_\infty \sim v_\infty^2 \left(1-\sqrt{1-4c_{\rm s,II}^2/v_\infty^2}\right)/2c_{\rm s,II}^2$ under the condition $c_{\rm s,II} \gg c_\infty$, where $\rho_{\rm II}$, $c_{\rm s,II}$, and c_∞ are the gas density of ionized gas and sound speeds of ionized and neutral gas (Spitzer et al., 1978). If $v_\infty \gg c_{\rm s,II}$, then we obtain $\rho_{\rm II} \sim \rho_\infty$. We confirm in our simulations that the condition of $v_\infty \gg c_{\rm s,HII}$ is satisfied. The somewhat low-density region appears over several pc downstream ($x > 0$, $y \lesssim 1$ pc, dark-purple in Fig. 5.5-a). This is because the gas is accelerated by radiation force and gas pressure gradient force in the ionized region.

The radiation force does not affect the the motion of gas at distances within the Bondi-Hoyle-Lyttleton radius from the x-axis so that the flow structure is similar to the classical Bondi Hoyle-Littleton accretion. Figure 5.5-(b) shows the flow structure in the 10^{-2} pc scale. Around the disk rotation axis, the radiation force is basically stronger than gravity, but only near the BH is it weaker than the gravity due to sublimation of the dust grains. Since the Bondi-Hoyle-Lyttleton radius is around 9×10^{-3} pc, and since the dust sublimation radius around the rotation axis is $\sim 7 \times 10^{-3}$pc, the radiation force does not affect the motion of gas at distances within the Bondi-Hoyle-Lyttleton radius from the x-axis. Thus, a quasi-steady flow similar to Bondi Hoyle-Littleton accretion appears. The accretion rate is roughly comparable to $\dot{M}_{\rm BHL}$.

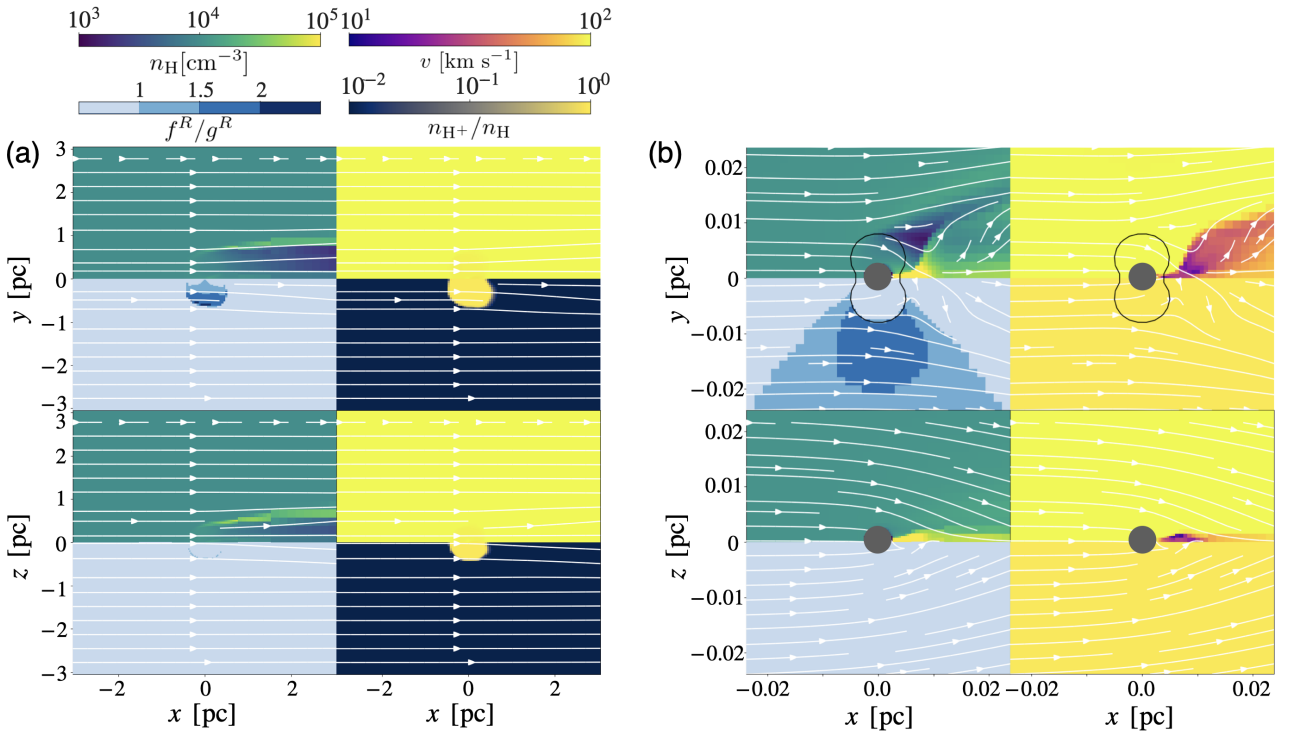

Figure 5.5: Same as Figure 5.4 but for the edge-on high-velocity model ('edgeN4V100'). Each panel shows the flow structure on (a) 1 pc and (b) 10^{-2} pc scales. The black solid lines in panel (b) represent the dust sublimation regions.

5.3.3 Dense model

Model 'edgeN6V20' differs from the fiducial model in that it produces more intense, shorter-interval accretion bursts. Figure 5.6 shows the time evolution of the gas density distribution in the meridian plane ($z = 0$) for the model 'edgeN6V20'. As shown in Figure 5.3, the accretion bursts occur periodically in this model. The burst mechanism is similar to that of fiducial model ($n_\infty = 10^4$ cm^{-3} model). In the quiescent phase, the dense shock shell exists near the ionization front, and it gradually becomes denser. After a while, the gravity causes part of the shell to reach the sink, and the burst phase begins (see Fig.5.6-a). In the burst phase, the accretion rate exceeds the Eddington limit. However, the radiation force is ineffective around the equatorial plane due to the attenuation of radiation and the thermal pressure of inoized bubbles cannot push outward these dense gas. After the significant part of the dense shock shell falls into the BH through the vicinity of the equatorial plane, it transitions to the quiescent phase (see Fig.5.6-b). After that, the part of the burst shell falls into the BH, and the burst accretion occurs again. The above process is repeated, resulting in periodic bursts. The interval of the accretion burst, ~ 0.01Myr, is much shorter than that of the fiducial model, ~ 0.15Myr. This is because the $r_{\rm shell}$ in this model, ~ 0.1 pc, is smaller than that of the fiducial model (it was shown in Section 5.3.1 that the burst interval depends on the $r_{\rm shell}$).

At the burst phase, the radius of the ionized region, $R_{\rm II}$, is comparable to or slightly smaller than the Bondi-Hoyle-Lyttleton radius, $R_{\rm BHL}$, at around the equatorial plane where gas mainly accretes. On the other hand, we find $R_{\rm II} > R_{\rm BHL}$ in regions other than the equatorial plane. This means that the condition for super-Eddington accretion "$R_{\rm II} < R_{\rm BHL}$" (Inayoshi et al., 2016) is satisfied locally. The effect of dust, which increases the radiation force and narrows the ionized region, on the condition for

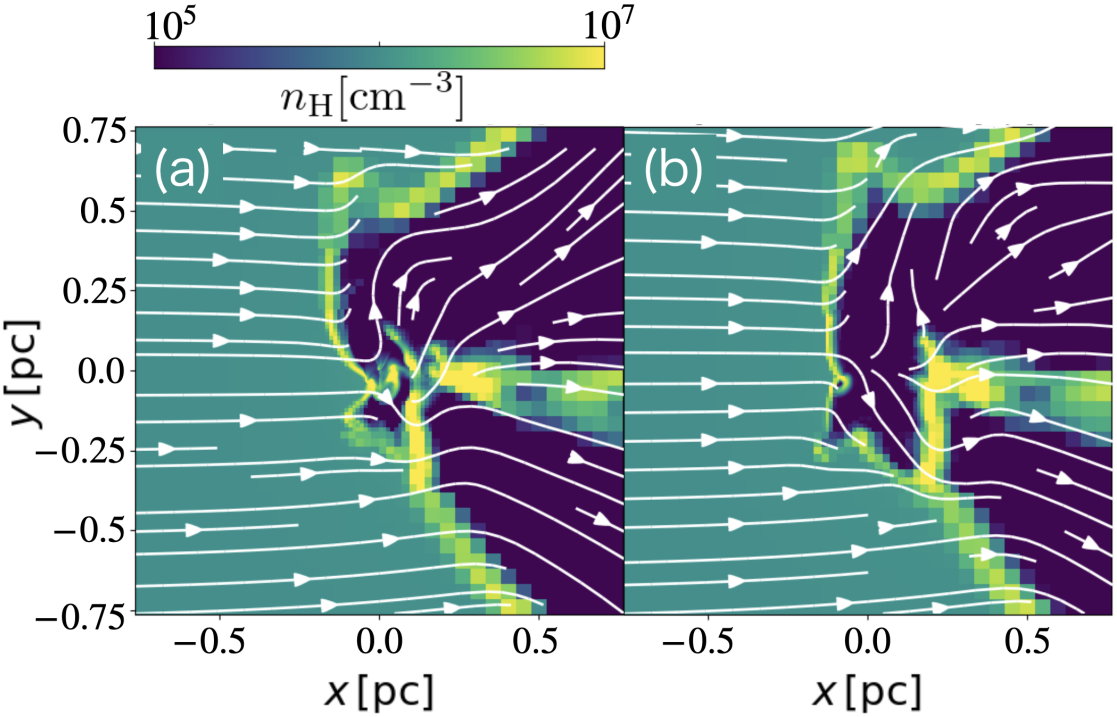

Figure 5.6: The flow structure on 10^{-1} pc scale for the edge-on high-density model ('edgeN6V20'). Each panel shows the number density distribution in the equatorial (xy-) plane at (a) the burst and (b) quiescent phases. We also show the mass accretion rates and the elapsed times in each panel.

super-Eddington accretion should be investigated in detail in the future.

Pole-on model

Figures 5.7-(a) and -(b) show the flow structure on a 1 pc and 10^{-2} pc scales of the pole-on radiation model ('poleN4V20'). The flow structure is quasi-steady and axisymmetric with respect to the x-axis. The structure on pc scale is almost the same as the fiducial model. The ionized region extends to several pcs, and the dense shock shell is formed at the ionization front (see Fig.5.7-(a)). As shown in Fig. 5.7-(b), this model also shows that gas accretion occurs mainly from near the equatorial plane ($x = 0$ plane), where the gravity is stronger than the radiation force. In addition, the gas that is attracted by the gravity but does not fall into the BH reaches near the x-axis at the downstream region and then flows out in the $+x$ direction. Unlike the fiducial model, the vortex flows appear in the upstream region. This is due to the radiation force pushing the gas in the $-x$ direction.

5.4 Discussion

5.4.1 Comparison with previous works: Hydrodynamics effect

Here, we compare the present study with our previous work that investigated the Bondi-Hoyle-Lyttleton accretion of dusty gas in an anisotropic radiation field without solving the hydrodynamics equations. The accretion rate is 0.6% of $\dot{M}_{\rm BHL}$ in the model 'edgeN4V20', while it is $20-30$% for the model of the previous work that have the same luminosity as that of the quiescent phase of model 'edgeN4V20'. We explain why the accretion rate is smaller in the presence of hydrodynamic effects below.

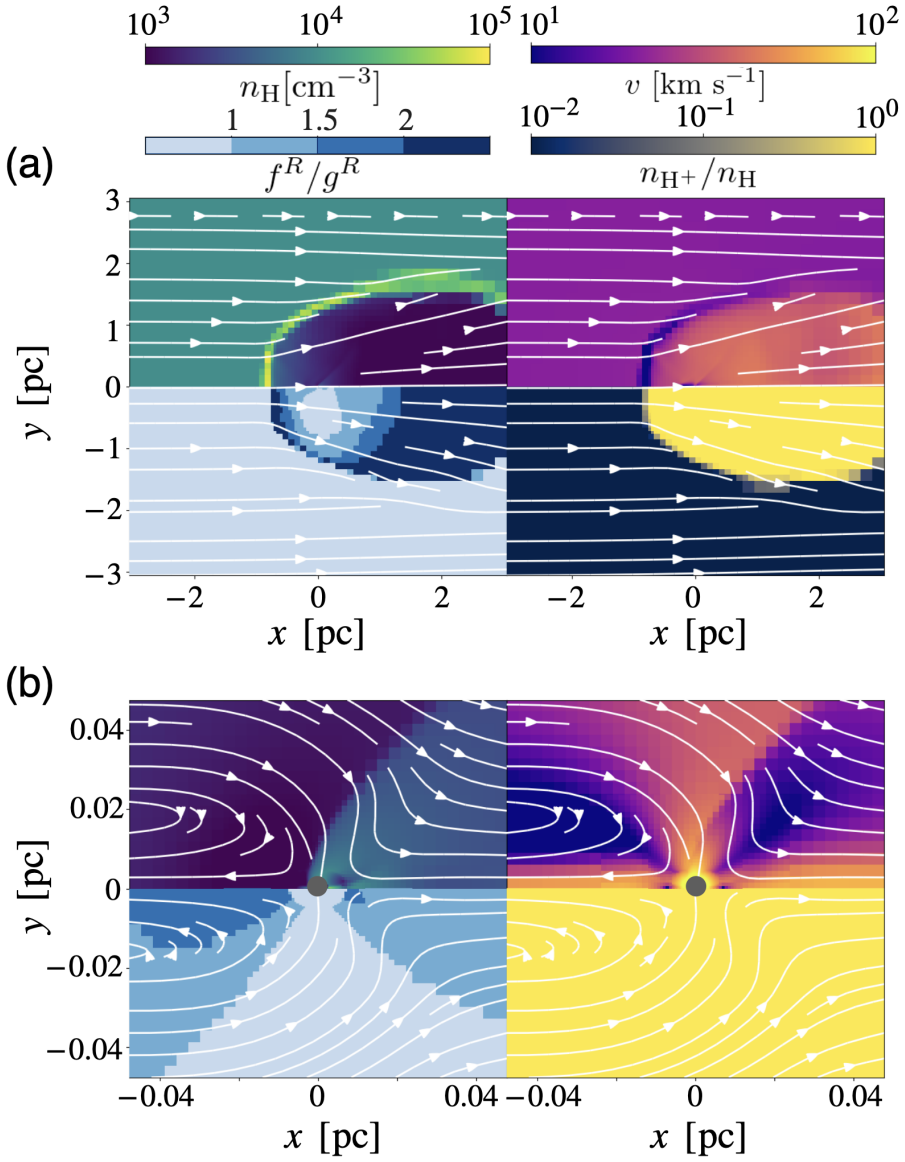

Figure 5.7: Same as Figure 5.4 but for the pole-on model ('poleN4V20'). Each panel shows the flow structure on (a) 1 pc and (b) 10^{-2} pc scales. We only show the snapshot in the xy-plane due to the axisymmetry of flow.

Figure 5.8 shows the flow structure without (left panel, cited from Ogata et al., 2021) and with (right panel) the hydrodynamics effect. In this figure, the BH is at the origin and the gas flows from the left side. Upper panel shows the gas velocity distribution, and bottom panel shows the radiation force normalized by gravity in each model.

Comparing the velocity distributions, it can be seen that both models have a region in common where the velocity suddenly drops on the upstream side (white region in the left panel, dark purple region in the right panel). In the model without hydrodynamics, the gas rapidly decelerates near the BH (inside the Bondi-Hoyle-Lyttleton radius $R_{\rm HL}$) due to the immense radiation force acting on the dust (see the light blue region in the lower panel of the left figure). In contrast, in the model considering hydrodynamics, deceleration begins in the region where gravity dominates over radiation force (the blue region in the lower panel of the right figure). This is because the incoming gas is subjected to gas

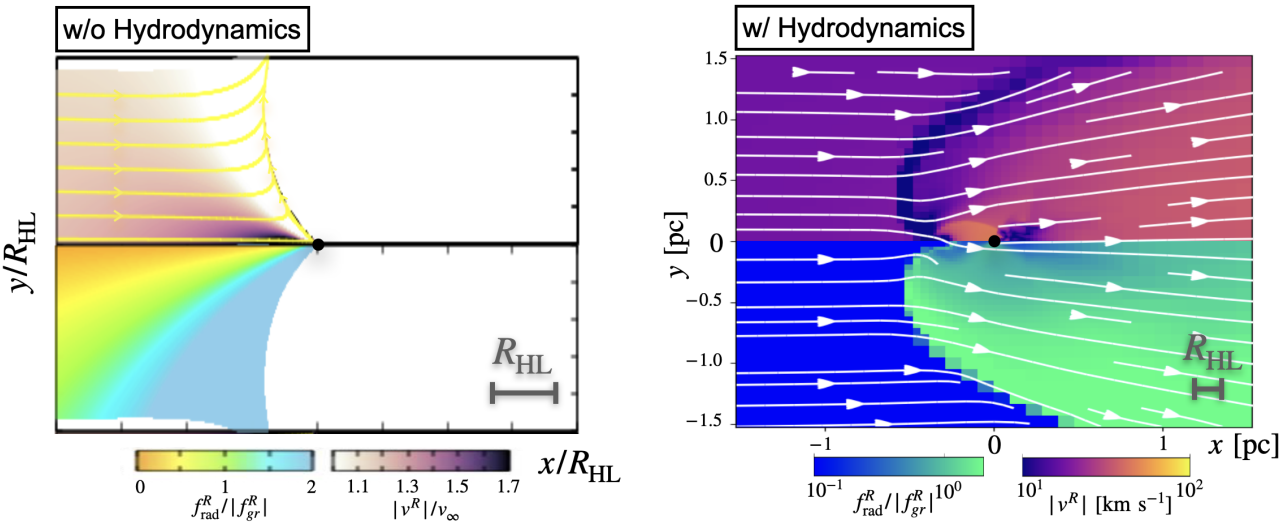

Figure 5.8: The flow structure without (left panel, cited from Ogata et al., 2021) and with (right panel) the hydrodynamics effect. In this figure, the BH is at the origin and the gas flows from the left side. Upper panel shows the gas velocity distribution, and bottom panel shows the radiation force normalized by gravity in each model.

pressure gradient force from the dense shell structure formed between the upstream ionized region and the neutral region (see Section 5.3.1). Threfore, it is clear that forces other than radiation pressure also significantly influence the structure of the accretion flow.

Figure 5.9 shows the three-dimensional structure of the density and streamlines for the 'edgeN4V20' model. From this figure, we see that under the conditions of $v_{\rm D} < v_\infty < v_{\rm R}$, there are primarily three types of streamlines (A-C) around the wandering BH when hydrodynamics are considered: (A)Streamlines surrounding the ionized region driven by gas pressure gradient force, (B)Streamlines driven by gas pressure gradient force in the ionized region, (C)Streamlines driven by radiation force around disk rotation axis in the ionized region. In the case where hydrodynamics effects are not considered, only streamline (C) appears. However, when hydrodynamics effect are taken into account, the gas pressure gradient force causes the appearance of streamlines (A) and (B) in addition to (C). Therefore, the reason why the accretion rate is smaller in the model that takes hydrodynamics into account than in the model that does not take hydrodynamics into account is due to the outflow driven by the gas pressure gradient force as shown in (A) and (B). This means that hydrodynamics calculations are necessary, at least when shock is formed. Otherwise, the accretion rate would be overestimated.

5.4.2 Dynamical friction

Gravity by non-uniform gas distribution around the BHs and momentum transport to the BHs by gas accretion induce acceleration of BHs. Figure 5.10 shows the acceleration in the x-direction $a_x(R)$ at the elapsed time $t = 8.5 \times 10^{-2}$ Myr, which is calculated as

$$a_x(R) = \int_0^{4\pi} \int_{R_{\rm sink}}^{R} \frac{G\rho x}{R'^3} dR' d\Omega + \int_{S_{\rm sink}} \rho v_x \boldsymbol{v} \cdot d\boldsymbol{S}_{\rm sink}, \tag{5.11}$$

where $d\Omega$ and $d\boldsymbol{S}_{\rm sink}$ are the solid angle and area vector. Here, a negative (positive) value of $a_x(R)$ means that the BH accelerates in the upstream (downstream) direction and the velocity of BH relative to the interstellar gas increases (decreases).

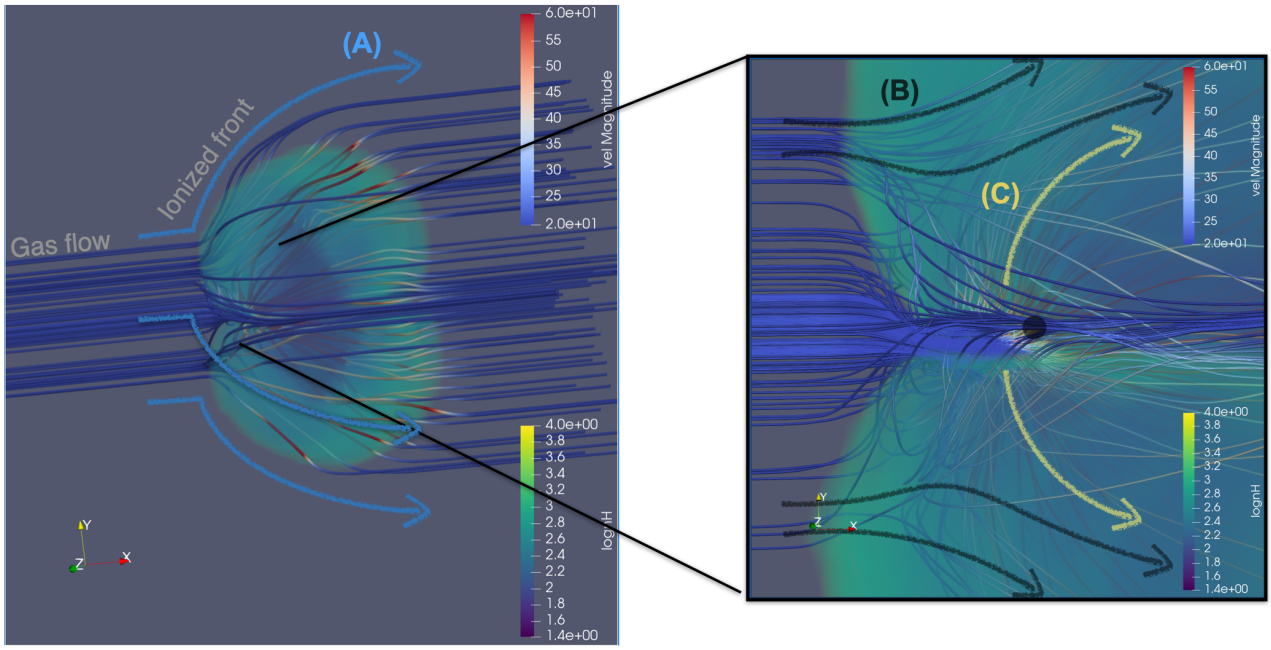

Figure 5.9: The three-dimensional structure of the density and streamlines for the 'edgeN4V20' model.

It is found that the acceleration $a_x(R_{\rm out})$ is about -10^{-8}cm s^{-2} in the models with $v_\infty = 20$ km s^{-1} and $n_\infty = 10^4$ cm^{-3} ('isoN4V20', 'poleN4V20', and 'edgeN4V20'). This is mainly due to gravity from the dense shock shell on the ionization front. This can be understood from the fact that the acceleration suddenly increases at around the star marks (the positions of the ionization front) and becomes nearly constant outside of them. In the model with the high-velocity $v_\infty = 100$ km/s ('edgeN4V100'), we find $a_x(R_{\rm out}) \sim 10^{-10}$cm s^{-2}, which is consistent with the result of Ostriker (1999), in which the acceleration of the central object of Bondi-Hoyle-Lyttleton flow has been evaluated. Positive acceleration is due to the accretion of gas with positive momentum ($\rho v_x > 0$) onto the BH. Although the gas density outside the sink in the upstream region is higher than that in the downstream, the negative acceleration due to this density difference is smaller than the positive acceleration via the gas accretion. In the high-density case ('edgeN6V20'), the acceleration in the burst phase is about $a_x(R_{\rm out}) \sim 10^{-7}$cm s^{-2}, and we find the gravity of the dense downstream gas induces the positive acceleration. Although the acceleration becomes negative due to the gravity of the dense shock shell in the quiescent phase, time-averaged acceleration is positive, $\sim 10^{-7}$cm s^{-2}.

5.4.3 Evolution of Intermediate-mass BHs

In the following, we discuss the evolution of the mass and velocity of the intermediate-mass BHs ($M_{\rm BH} \sim 10^4 M_\odot$) wandering in early galaxies ($z \gtrsim 6$) using our results of model 'edgeN4V20', 'edgeN4V100', and 'edgeN6V20'. Here, we use $a(R_{\rm out})$ at $t \sim 0.1$Myr presented in Figure 5.10 instead of the time-averaged value since the acceleration at larger distance ($R \gtrsim$several pc) does not change with time as much.

In the case that the gas density is $\sim 10^4$ cm^{-3}, the IMBHs continue to float without significant mass growth. For the model 'edgeN4V100', the acceleration is $\sim 10^{-10}$ cm s^{-2} so that the timescale of the slowdown is ~ 3 Gyr. This is much longer than the age of the universe at $z = 6$ (~ 900 Myr). This implies that the speed of intermediate-mass BHs does not change so much. On the other hand, the acceleration timescale of model 'edgeN4V20', ~ 6 Myr, is much shorter than the age of the universe

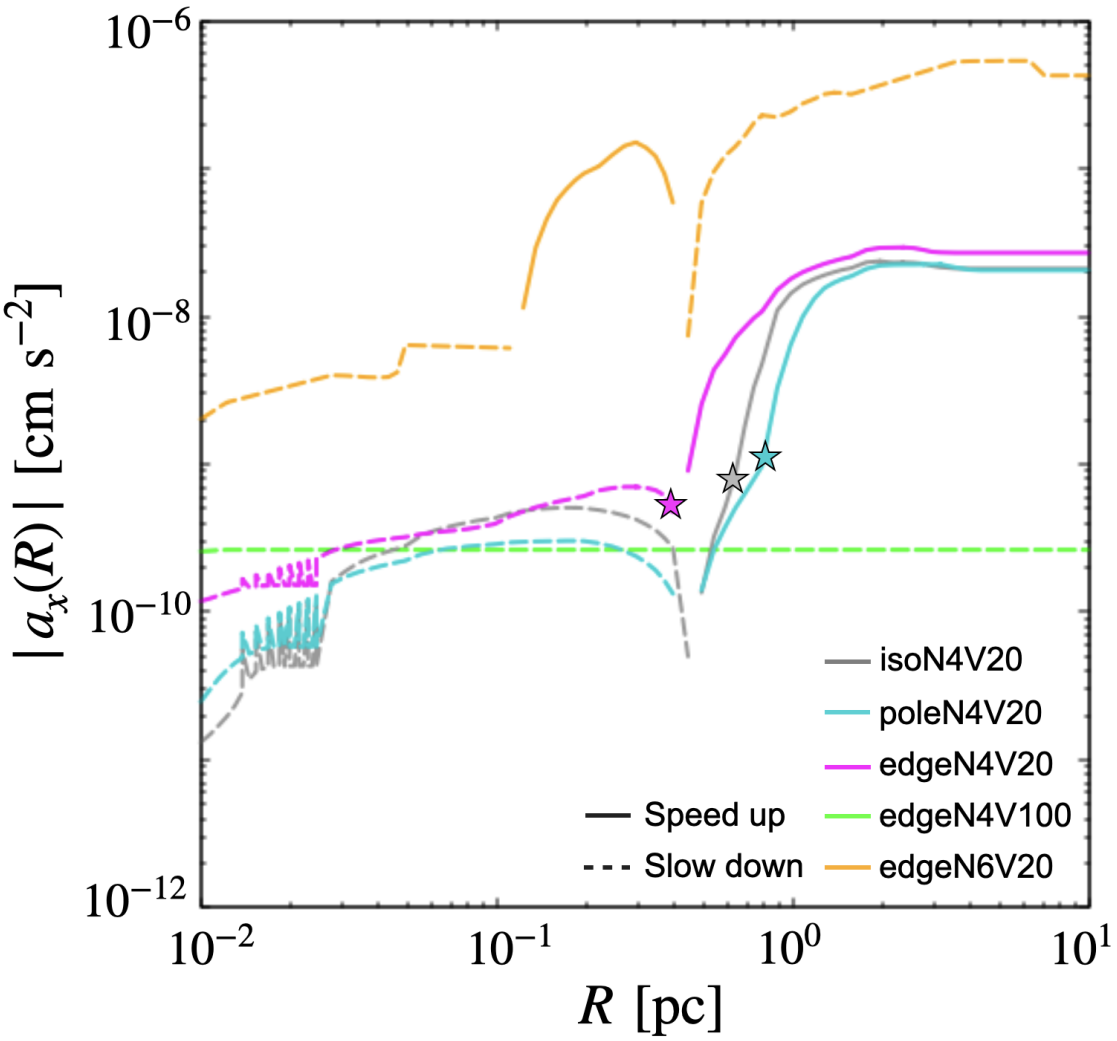

Figure 5.10: Acceleration in the x-direction of BHs at $t \sim 8.5 \times 10^{-2}$ Myr as a function of R. The solid (dotted) lines mean that the acceleration is negative (positive) and the speed of the BHs increases (decreases). The line colors are the same as in Figure 5.3. The star markers correspond to the positions of the ionization fronts.

at $z = 6$. Thus, if the initial velocity is relatively small, ~ 10 km s^{-1}, the intermediate-mass BHs will continue to speed up until the velocity reaches several $\times$ 10 km s^{-1} where the acceleration timescale becomes comparable to the age of the universe. The above discussion does not take into account the change in the mass of the intermediate-mass BHs, but this is appropriate. In both model 'edgeN4V100' and 'edgeN4V20', the timescale of mass growth derived from the accretion rate ($\sim 4 \times 10^{-6}$ $M_\odot$ yr^{-1}) is ~ 2 Gyr, which is much longer than the age of the universe at $z = 6$. Thus, we conclude that the intermediate-mass BHs continue to float at the velocity of $\gtrsim$ several $\times$ 10 km s^{-1} without significant mass growth.

For higher gas number densities ($\sim 10^6$ cm^{-3}), intermediate-mass BHs would slow down and increase in mass. Although we have not performed the simulations of high-density, high-velocity model ($n_\infty = 10^6$ cm^{-3} and $v_\infty = 100$km s^{-1}), the classical Bondi-Hoyle-Lyttleton type flow is expected to emerge because the flow structure in model 'edgeN4V100' is similar to the Bondi-Hoyle-Lyttleton accretion flow due to the small impact of radiation, and because the radiation impact is thought to be more ineffective as the density is increased. Hence the accretion rate can be inferred from the classical

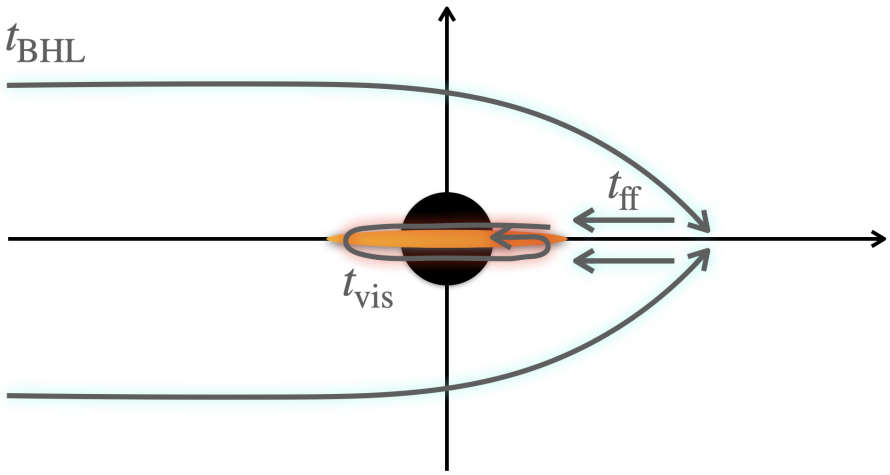

Figure 5.11: Schematic figure of timescale on Bondi-Hoyle-Lyttleton accretion system. $t_{\rm BHL}$ denotes Bondi-Hoyle-Lyttleton timescale for the gas to reach the accretion axis, $t_{\rm ff}$ denotes the free-fall time for the gas to travel from the accretion axis to the disk's outer edge, and $t_{\rm vis}$ is viscous timescale for the gas to be transported from the accretion disk to the BH.

Bondi-Hoyle-Lyttleton accretion theory as $\sim 6 \times 10^{-4} M_{\odot}{\rm yr}^{-1}$, and the acceleration is evaluated to be -4×10^{-8} cm s^{-2} based on the prediction of Ostriker (1999). The timescales of mass growth and slowdown of intermediate-mass BHs are expected to be $\sim$ 20 Myr and $\sim$ 7 Myr, respectively. This means that the relative velocity decrease faster than mass growth if the initial velocity is $\sim$ 100 km s^{-1}. This behavior is thought to continue even after the relative velocity drops to a few $\times$ 10 km s^{-1}. This is because that the slowdown is expected to be more pronounced due to the decrese of the velocity, while the mass accretion rate remains the same. Indeed, in the model 'edgeN6V20', the deceleration rate is $\sim 10^{-7}$ cm s^{-2} and the timescale of the slowdown, $\sim$ 0.4 Myr, is much shorter than the high-velocity case. The accretion rate (timescale of the mass growth), for v_{∞} = 20km s^{-1} and 100km s^{-1} is almost the same. Subsequently, a shift from Bondi-Hoyle-Lyttleton accretion to Bondi accretion might occur. Bondi accretion in an anisotropic radiation from accretion disks around BHs has been investigated by Sugimura et al. (2017), and the accretion rate has been reported to be 1% of the Bondi rate. Adopting n_{∞} and T_{∞} as number density and temperature of the gas, the timescale of the mass growth is 16 Myr, which is much shorter than the age of the universe. To sum up, the intermediate-mass BHs floating at speeds of $\sim 10-100$km s^{-1} rapidly slow down and grow. Eventually supermassive BHs may be formed.

In the present discussion, we only consider the interaction between a single BH and the surrounding gas. To more accurately investigate the evolution of intermediate-mass BHs, it should be necessary to consider their interactions with stars and other BHs.

5.4.4 Evolution of the direction of the disk rotational axis

In this research, we have adopted edge-on as the fiducial model. Here we demonstrate its versatility.

First, we consider the timescales for the entire Bondi-Hoyle-Lyttleton accretion mechanism, divided by regions (see Figure 5.11). The overall time from the gravitational attraction process that starts near the gravitational region to the accretion to the BH via the accretion disk is the sum of the Bondi-Hoyle-Lyttleton time $t_{\rm BHL}$ for the gas to reach the accretion axis, the time for the gas to travel from the accretion axis to the disk edge $t_{\rm ff}$, and the time for the gas to be transported from the accretion disk to the BH, $t_{\rm vis}$ (Figure5.11).

First, the Bondi-Hoyle-Lyttleton time $t_{\rm HL}$ for the gas to reach the accretion axis can be estimated using the Bondi-Hoyle-Lyttleton radius $R_{\rm BHL}$ as follows:

$$\begin{aligned} t_{\rm HL} &= \frac{R_{\rm BHL}}{v_\infty} \\ &= \frac{2GM}{v_\infty^3} \\ &\sim 8.4\times10^1 \left(\frac{M}{10^4 M_\odot}\right)\left(\frac{v_\infty}{100{\rm km/s}}\right)^{-3}\ {\rm yr} \end{aligned} \tag{5.12}$$

Next, the time for the gas to travel from the accretion axis to the edge of the disk can be estimated by $t_{\rm ff}$, the time for the gas particles to fall freely due to gravity, considering that the density of the gas is high at the accretion axis and that it is almost unaffected by radiation due to the shadow of the disk. Suppose that the gas particle arrives at the position $R_{\rm BHL}$ on the accretion axis, where it loses $X = 0.1$ times its initial momentum $R_{\rm HL}v_\infty$. In this case, $t_{\rm ff}$ is the following:

$$\begin{aligned} t_{\rm ff} &= \frac{R_{\rm BHL}}{X v_\infty} \\ &= \frac{2GM}{X v_\infty^3} \\ &\sim 8.4\times10^2 \left(\frac{M}{10^4 M_\odot}\right)\left(\frac{v_\infty}{100{\rm km/s}}\right)^{-3}\left(\frac{X}{0.1}\right)^{-1}\ {\rm yr} \end{aligned} \tag{5.13}$$

Finally, the time for gas transport from the accretion disk to the BH can be evaluated in terms of the viscosity time $t_{\rm vis}$ (typical timescale in the disk radial direction), assuming a standard disk.

Radial velocity solution in the outer edge region of the standard disk model is discribed as below (Kato et al., 2008):

$$\begin{aligned} |v_r| &= 5.4\times10^5 \alpha_{\rm vis}^{4/5} m^{-1/5} \dot{m}^{3/10} \hat{r}^{-1/4} f_{\rm in}^{-7/10}\ {\rm cm\ s^{-1}} \\ m &= \frac{M}{M_\odot},\ \dot{m} = \frac{\dot{M}}{L_{\rm Edd}/c^2},\ \hat{r} = \frac{r}{2GM/c^2} \\ f_{\rm in} &= 1 - \frac{r_i n}{r}. \end{aligned} \tag{5.14}$$

we can estimate $t_{\rm vis}$ using above solution,

$$\begin{aligned} t_{\rm vis} &= \frac{R_{\rm BHAD}}{|v_r|} \\ &\sim 9.1\times10^1 \left(\frac{\alpha_{\rm vis}}{0.1}\right)^{-\frac{4}{5}} \left(\frac{M}{10^4 M_\odot}\right)^{\frac{9}{10}} \left(\frac{v_\infty}{100\,{\rm km\ s^{-1}}}\right)^{-\frac{8}{5}} \left(\frac{n_\infty}{10^4\,{\rm cm^{-3}}}\right)^{-\frac{3}{10}} \left(\frac{\chi}{0.1}\right)^{\frac{5}{2}}\ {\rm yr}, \end{aligned} \tag{5.15}$$

where $R_{\rm BHAD}$ is the outer radius of the BH accretion disk, v_r is the radial gas velocity of the standard disk, and $\alpha_{\rm vis}$ is the viscosity parameter. The $f_{\rm in}$ is a factor related to the boundary conditions, and $f_{\rm in} = 1$ for simplicity. The outer edge radius of the accretion disk $R_{\rm BHAD}$ is estimated from the angular

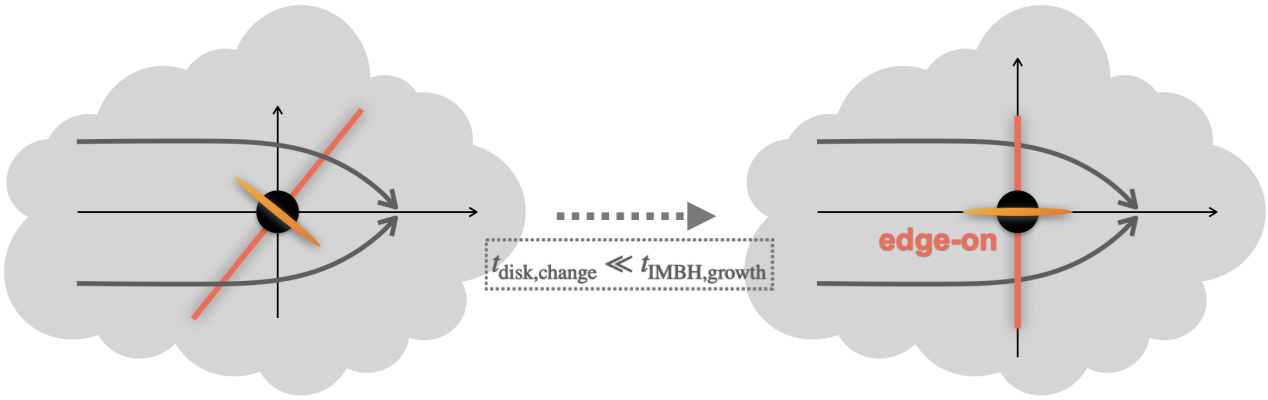

Figure 5.12: Image showing the changing inclination of the disk rotation axis.

momentum conservation law as follows:

$$\begin{aligned} X R_{\rm BHL} v_\infty &= R_{\rm BHAD} v_{\rm K} \\ &= R_{\rm BHAD} \sqrt{\frac{GM}{R_{\rm BHAD}}} \\ \rightarrow R_{\rm BHAD} &= \frac{X^2 R_{\rm BHL}^2 v_\infty^2}{GM} \\ &= X^2 \frac{4GM}{v_\infty^2}, \end{aligned} \tag{5.16}$$

where $v_{\rm K}$ denotes the Keplerian rotation velocity. Here, the angular momentum of the gas arriving at the accretion axis (x-axis) and accreting at the center is assumed to be $X = 0.1$ times $v_\infty R_{\rm BHL}$. The X is a constant less than 1 and is a quantity that depends on the anisotropy of density or velocity distribution. Also, in this study, the size of the accretion disk $R_{\rm BHAD}$ must be sufficiently smaller than the Bondi-Hoyle-Lyttleton scale $R_{\rm BHL}$ since the accretion disk is treated as a point source. From Equation 5.16, we can confirm that the condition $R_{\rm BHL} \gg R_{\rm BHAD}$ is satisfied if $X \lesssim 10^{-1}$.

From the above discussion, the typical timescale $t_{\rm disk}$ on which the rotational axis of the accretion disk around the intermediate mass BH changes is $t_{\rm disk} = t_{\rm BHL} + t_{\rm ff} + t_{\rm vis} \sim 10^3$ yr. As discussed in section 5.4.4, the timescale for the mass and velocity evolution of intermediate-mass BHs is a few Myr-Gyr from the simulation results of our fiducial model. The timescale of the disk change is much shorter than the timescale of the evolution of intermediate-mass BHs. Therefore, in the evolution process of intermediate-mass black holes, if the accretion phenomenon starts with the disk rotation axis orientation not being edge-on, it is expected that edge-on will be realized soon (see Figure 5.12).

Chapter 6

Future Issues

So far, we have investigated the dynamics of the accretion flows onto the wandering seed BHs considering the anisotropic radiation that is expected to be generated by the accretion disks, and sublimation of dust grains. In this section, we summarize the key issues that need to be addressed in the future to construct a theory of accretion onto a wandering BHs and clarify the supermassive BHs formation process.

In this study, the density distribution of the ambient dusty gas is assumed to be uniform. In reality, however, the interstellar medium is nonuniform, which could cause varying acceleration and accretion rates of the BHs. Ruffert et al. (1997, 1999) have reported that nonuniformity causes flows orbiting around the sink, which reduces the accretion rate. Recently, Lescaudron et al. (2022) suggested that turbulent medium could slow down BHs using the three-dimensional magneto-hydrodynamics simulations. In their simulations, the deceleration rate is tens of times higher than the analytical solution for uniform density (Ostriker, 1999). However, if radiation is taken into account, the moving BHs could be accelerated. Although Sugimura et al. (2018) calculated the accretion flows with angular momentum onto a static BH, the such simulations for moving BHs, considering the radiation feedback, have not yet been performed. These are important future work.

The handling of accretion disks around the BHs would also need to be modified. The direction of the rotation axis of the disk is likely to be perpendicular to the direction of motion of the ambient gases (edge-on). However, if the ambient gas is non-uniform, the gas accreting to the central region could have random angular momentum. In that case, edge-on disk is not maintained. Furthermore, immediately after the BHs encounter gas clouds, the situation is likely to be different from the edge-on case. In these cases, the properties of the ionization front and dense shock shell could be different from the results of the present work. To be realistic, the improvements mentioned above are needed.

In our simulations, we assume that the gas flowing into the sink region immediately accretes to the BH and alters the luminosity. To be more precise, however, the luminosity should increase with a delay of about the viscosity time. This time lag could not be ignored if the angular momentum of the accreting gas is large. Clarifying these points is an important future work.

The spectral energy distribution (SED) of the accretion disks depend on mass accretion rates. In this study, we assume the power-law SED. If the mass accretion rate is near or above the Eddington rate, the SED of the accretion disk would be multi-temperature blackbody radiation (Kato et al., 2008). In these case, X-ray is generated because of the Compton scattering by the high-temperature plasma around the disk (Kawashima et al., 2012). On the other hand, if the mass accretion rate is much lower than the Eddington rate, the SED widely distributes in the range between radio and gamma rays (Narayan & Yi, 1995; Manmoto et al., 1996; Yuan et al., 2003). Ionization and heating rates depend on the SED, thus different SEDs could lead to different flow structures and accretion rates. Two-dimensional RHD

simulations on Bondi scale considering the multi-temperature blackbody radiation model showed that the critical gas densityin which the transition to super-Eddington accretion occurs is slightly reduced compared to the power spectrum case (Takeo et al., 2018). This is because photoionization rate of the accretion disk spectrum model is less efficient than that of the single power spectrum. We need to study the Bondi-Hoyle-Lyttelton accretion considering more realistic SED.

In our simulations, the cosine function for the angular distribution of the radiation field produced by the accretion disks is assumed. If the mass accretion rate is above the Eddington rate, the disk could produce much stronger angular dependence (Watarai et al., 2005; Ohsuga et al., 2005). Conversely, if the accretion rate is much lower than the Eddington rate, the angular dependence of the radiation field is weak. The angular distribution also changes with time because of the precessional motion of the accretion disk. The multidimensional simulations of the accretion disk are needed to obtain more realistic models of the radiation field (Machida et al., 2000; Hawley & Krolik, 2001; Ohsuga et al., 2009; Ohsuga & Mineshige, 2011). Two-dimensional RHD simulations around a static BH have been performed with parameters such as the size of the shadow region (no-radiation feedback region) and angular distribution of the anisotropic radiation field (e.g. Sugimura et al., 2017; Takeo et al., 2018). Their study implies that the larger shadow size and the stronger anisotropy lead to a much higher mass accretion rate. The study of the dependence of shadow size and anisotropy of radiation feedback in the case of a moving BH remains a future task.

Outflow affects the gas flow around the BHs. Strong bipolar outflows have been observed around compact objectswhose mass accretion rates are above the Eddington rate (e.g. Fabrika et al., 2004). Jets have also been detected near many objects (e.g. Walker et al., 2018). The previous theoretical studies of moving BHs showed that outflows push out the ambient gas, and accretion rate is reduced to approximately $20-30\%$ of the Bondi-Hoyle-Lyttleton accretion rate (e.g. Li et al., 2020; Bosch-Ramon, 2022). They suggested that acceleration rate is $40-80\%$ smaller than that in the case of no outflow. For further study on the impacts of outflow, we will include these effects in future works.

Chapter 7

Summary and Conclusion

In the present work, we study the Bondi-Hoyle-Lyttleton accretion mechanism onto intermediate-mass BHs ($10^4 M_\odot$) by three-dimensional radiation hydrodynamics simulations, taking into account the anisotropic radiation field originating from the accretion disk. We consider the situation in which the gas with relatively low metallicity ($Z = 0.1 Z_\odot$) flows in perpendicular to the rotation axis of the accretion disk (parallel to the disk plane). We take into account the radiation force acting on the dusty gas and decrease in the absorption coefficient due to the dust sublimation. The luminosity of the accretion disk is supposed to increase with the mass accretion rate. Our major findings are summarized as follows.

If the density of dusty gas is relatively high ($\sim 10^4$ cm^{-3}) and the relative velocity between intermediate-mass BHs and the gas is low (~ 20 km s^{-1}), time-averaged accretion rate is 0.6 % of the Bondi-Hoyle-Lyttleton accretion rate ($4 \times 10^{-6} M_\odot \mathrm{yr}^{-1}$). It is found that an ionized region like two spheres glued together at the equatorial plane appears around the intermediate-mass BHs and the dense shock shell is formed nearby the ionization front. The radiation force around the rotation axis of the disk works to prevent gas accretion so that the gas mainly accretes through the disk equatorial plane. The gravity of the dense shock shell accelerate the intermediate-mass BHs at $\sim 10^{-8}$cm s^{-2}. Note that the accretion rate periodically increases, but does not significantly affect the time-averaged accretion rate and acceleration.

In the case of high relative velocity (~ 100 km s^{-1}), the accretion rate, $4 \times 10^{-6} M_\odot \mathrm{yr}^{-1}$, is approximately equal to the Bondi-Hoyle-Lyttleton accretion rate. This is because the radiation force hardly prevents the gas accretion. Even around the rotation axis of the disk, the radiation force is significantly small due to the dust sublimation. The dense shock shell is not formed, and the intermediate-mass BHs are decelerated due to the gas accretion.

When the gas density is extremely high ($\sim 10^6$ cm^{-3}), the time-averaged accretion rate is 0.6 % of the Bondi-Hoyle-Lyttleton accretion rate, $\sim 4 \times 10^{-4} M_\odot \mathrm{yr}^{-1}$. Due to the gravity by dense downstream gas, the intermediate-mass BHs are decelerated although the dense shock shell is formed at the vicinity of the ionization front. The accretion rate oscillates periodically as in the case of the density of $\sim 10^4$ cm^{-3}. This is because when the surface density of the shell increases to a certain degree, part of the shell falls due to the gravity of the intermediate-mass BHs. Periodic variations in accretion rate occur even when the radiation is isotropic. This result differs from previous work, possibly because we have taken into account dust sublimation.

Based on the present results, the intermediate-mass BHs are expected to continue floating in the early galaxies ($z \gtrsim 6$) at the velocity of $\gtrsim$ several $\times 10$ km s^{-1} without significantly mass growth, if the gas density of the galaxies is $\sim 10^4$ cm^{-3}. On the other hand, if the density of interstellar medium

is extremely high, $\sim 10^6$ cm^{-3}, even the intermediate-mass BHs with the initial velocity of about $\sim 100\,\mathrm{km\ s^{-1}}$ will slow down due to momentum transport caused by the mass accretion. If the Bondi accretion begins with decreasing the velocity, the intermediate-mass BHs could grow rapidly. This may lead to the evolution from intermediate-mass BHs to supermassive BHs.

Acknowledgement

First of all, I would like to extend my appreciation to Prof. Ken Ohsuga, whose advice and comments have always guided me. None of my achievements would have been possible without his support. I was able to learn not only astrophysics but also what a researcher is from him. I would like to make the most of those in my future life. I am indebted to him for his profound impact on my academic and personal development, and I am committed to making them proud by giving my best efforts in the future. I would like to express my deepest gratitude to my collaborator, Prof. Hajime Fukushima, for his invaluable support throughout this research. He generously provided the numerical simulation code and taught me how to use it from scratch. Whenever I faced difficulties in my research, he kindly provided constructive discussions. His guidance and kindness helped me complete this work. I would like to express my heartfelt gratitude to my collaborator, Prof. Hidenobu Yajima, for his invaluable support and guidance throughout this research. He taught me the fundamental physics of interstellar dust from the ground up, greatly enhancing my understanding of the subject. Additionally, he encouraged me to participate in various research meetings, which allowed me to connect with numerous researchers in this field. His support and encouragement have been crucial to the development and success of this work.

I am deeply grateful to all the professors and staff of the Theoretical Astrophysical Group at the University of Tsukuba, Masayuki Umemura, Masao Mori, Kohji Yoshikawa, Alexander Y. Wagner, Yuta Asahina, and Mayumi Obata for useful discussions and great support. I also would like to thank members of Ohsuga group, Takumi Ogawa, Yuh Tsunetoe, Akihiro Inoue, Mikiya Takahashi, Aoto Utsumi, Takuya Mushano, Shogo Yoshioka, Yuma Shimada, Koudai Takebayashi, Rintaro Takeda, Yutaro Kuroda, Kosuke Ueno, Ryui Kuriki, Albertken Perez, Ryusei Komine, Yuki Matsufuji, and Sogo Nakao. I appreciate the opportunity to discuss various studies with them: Naoki Yoshida, Kana Moriwaki, Tomoaki Matsumoto, Kazuyuki Sugimura, Kentaro Nagamine, Toru Tsuribe, Mariko Kimura, Keiya Hirashima, Rin Matsumoto, Hiroko Okada, Tomoya Suzuguchi, John Wise, Kunyang Li, Haojie Ho, Wenxiu Li, Francesco Bollati, Hyerin Cho, and Shashank Dattathri. I was also thank to all the members of Black Hole Lunch seminar for discussions: Shin, Mineshige, Keiichi Maeda, Mami Machida, Norita Kawanaka, Misaki Mizumoto, Takumi Ohmura, Haruka Sakemi, Nacho Botella Lasaga, Hiroki Okino, and Masayuki Furuno.

I would like to appreciate the Japan Society for the Promotion of Science (JSPS) fellowship for a grant that made it possible to complete my research. Numerical computations were performed with computational resources provided by the Multidisciplinary Cooperative Research Program in the Center for Computational Sciences, University of Tsukuba, Oakforest-PACS operated by the Joint Center for Advanced High-Performance Computing (JCAHPC), Cray XC 50 at the Center for Computational Astrophysics (CfCA) of the National Astronomical Observatory of Japan (NAOJ), the FUJITSU Supercomputer PRIMEHPC FX1000 and FUJITSU Server PRIMERGY GX2570 (Wisteria/BDEC-01) at the Information Technology Center, The University of Tokyo.

Finally, I am grateful to my family and friends for their unwavering support, understanding, and en-

couragement throughout this endeavor. Their love and encouragement have been my source of strength and motivation.

References

Abramowicz M. A., Czerny B., Lasota J. P., Szuszkiewicz E., Abramowicz M. A., Czerny B., Lasota J. P., Szuszkiewicz E., 1988, ApJ, 332, 646

Abramowicz M. A., Chen X., Kato S., Lasota J.-P., Regev O., 1994, ApJL, 438, L37

Asahina Y., Takahashi H. R., Ohsuga K., Asahina Y., Takahashi H. R., Ohsuga K., 2020, ApJ, 901, 96

Barvainis R., Barvainis Richard 1987, ApJ, 320, 537

Begelman M. C., 1978, MNRAS, 184, 53

Begelman M. C., Begelman C. M., 1985, ApJ, 297, 492

Berger M. J., Colella P., 1989, Journal of Computational Physics, 82, 64

Bertoldi F., Carilli C. L., Cox P., Fan X., Strauss M. A., Beelen A., Omont A., Zylka R., 2003, A&A, 406, 55

Bisnovatyi-Kogan G. S., et al., 1979, SvA, 23, 201

Blondin J. M., Kallman T. R., Fryxell B. A., Taam R. E., Blondin J. M., Kallman T. R., Fryxell B. A., Taam R. E., 1990, ApJ, 356, 591

Bondi H., 1952, Monthly Notices of the Royal Astronomical Society, 112, 195

Bondi H., Hoyle F., 1944, Monthly Notices of the Royal Astronomical Society, 104, 273

Bosch-Ramon V., 2022, A&A, 660, 5

Cowie L. L., Ostriker J. P., Stark A. A., Cowie L. L., Ostriker J. P., Stark A. A., 1978, ApJ, 226, 1041

Draine B. T., Bertoldi F., 1996, The Astrophysical Journal, 468, 269

Draine B. T., Salpeter E. E., 1979, The Astrophysical Journal, 231, 77

Draine B. T., Lee H. M., Draine B. T., Lee H. M., 1984, ApJ, 285, 89

Draine B. T., et al., 2007, The Astrophysical Journal, 663, 866

Edgar R., 2004, New Astronomy Reviews, 48, 843

Fabrika S., Fabrika S. 2004, ASPRv, 12, 1

Ferland G. J., et al., 1992, ApJ, 387, 95

Fiacconi D., Mayer L., Roškar R., Colpi M., 2013, The Astrophysical Journal Letters, 777, L14

Fryxell B. A., Taam R. E., Fryxell B. A., Taam R. E., 1988, ApJ, 335, 862

Fukue J., 1999, Publications of the Astronomical Society of Japan, 51, 703

Fukushima H., Yajima H., 2021, Monthly Notices of the Royal Astronomical Society, 506, 5512

Fukushima H., Omukai K., Hosokawa T., 2018, Monthly Notices of the Royal Astronomical Society, 473, 4754

Fukushima H., Hosokawa T., Chiaki G., Omukai K., Yoshida N., Kuiper R., 2020, Monthly Notices of the Royal Astronomical Society, 497, 829

Glover S. C., 2015, Monthly Notices of the Royal Astronomical Society, 453, 2901

Gnedin N. Y., Abel T., 2001, New Astronomy, 6, 437

Hanamoto K., Ioroi M., Fukue J., 2001, Publications of the Astronomical Society of Japan, 53, 105

Harten A., Lax P. D., van Leer B., 1983, SIAM Review, 25, 35

Hawley J. F., Krolik J. H., 2001, The Astrophysical Journal, 548, 348

Ho C., Taam R. E., Fryxell B. A., Matsuda T., Koide H., Shima E., 1989, Monthly Notices of the Royal Astronomical Society, 238, 1447

Hollenbach D., McKee C. F., 1979, ApJS, 41, 555

Hoyle F., Lyttleton R. A., 1939, Mathematical Proceedings of the Cambridge Philosophical Society, 35, 405

Hunt R., 1971, Monthly Notices of the Royal Astronomical Society, 154, 141

Ichimaru S., Ichimaru S. 1977, ApJ, 214, 840

Inayoshi K., Haiman Z., Ostriker J. P., 2016, Monthly Notices of the Royal Astronomical Society, 459, 3738

Inayoshi K., Visbal E., Haiman Z., 2020, https://doi.org/10.1146/annurev-astro-120419-014455, 58, 27

Izquierdo-Villalba D., Bonoli S., Dotti M., Sesana A., Rosas-Guevara Y., Spinoso D., 2020, Monthly Notices of the Royal Astronomical Society, 495, 4681

Kannan R., Vogelsberger M., Marinacci F., McKinnon R., Pakmor R., Springel V., 2019, Monthly Notices of the Royal Astronomical Society, 485, 117

Kato S., Fukue J., Mineshige S., 2008, Black-Hole Accretion Disks — Towards a New Paradigm —

Katsuda S., et al., 2018, The Astrophysical Journal, 856, 18

Katz J. I., 1977, ApJ, 215, 265

Katz H., et al., 2023, MNRAS, 518, 592

Kawashima T., et al., 2012, ApJ, 752, 18

Krolik J. H., London R. A., Krolik J. H., London R. A., 1983, ApJ, 267, 18

Laor A., Draine B. T., Laor A., Draine B. T., 1993, ApJ, 402, 441

Lee H. H., et al., 1996, AA, 311, 690

Lescaudron S., Dubois Y., Beckmann R. S., Volonteri M., Lescaudron S., Dubois Y., Beckmann R. S., Volonteri M., 2022, arXiv, p. arXiv:2209.13548

Levermore C. D., Pomraning G. C., Levermore C. D., Pomraning G. C., 1981, ApJ, 248, 321

Li X., Chang P., Levin Y., Matzner C. D., Armitage P. J., 2020, Monthly Notices of the Royal Astronomical Society, 494, 2327

Lima R. S., Mayer L., Capelo P. R., Bellovary J. M., 2017, The Astrophysical Journal, 838, 13

Liu B. F., Mineshige S., Ohsuga K., 2003

Machida M., Hayashi M. R., Matsumoto R., 2000, The Astrophysical Journal, 532, 67

Manmoto T., Takeuchi M., Mineshige S., Matsumoto R., Negoro H., 1996, The Astrophysical Journal, 464, L135

Marconi A., Hunt L. K., 2003, The Astrophysical Journal, 589, L21

Matsuda T., et al., 1991, AA, 248, 301

Matsumoto T., 2007, Publications of the Astronomical Society of Japan, 59, 905

Matsumoto T., Dobashi K., Shimoikura T., 2015, The Astrophysical Journal, 801, 77

Mayer L., Kazantzidis S., Madau P., Colpi M., Quinn T., Wadsley J., 2007, Science, 316, 1874

Mayer L., Kazantzidis S., Escala A., Callegari S., 2010, Nature 2010 466:7310, 466, 1082

Milosavljevic M., Couch S. M., Bromm V., 2008, ApJL, 696, L146

Narayan R., Yi I., 1995, The Astrophysical Journal, 452, 710

Narayan R., Yi I., Narayan R., Yi I., 1994, ApJL, 428, L13

Nelson R. P., Langer W. D., 1997, The Astrophysical Journal, 482, 796

Novikov I. D., Thorne K. S., 1973, in Black Holes (Les Astres Occlus). pp 343–450

Nozawa T., Kozasa T., Habe A., 2006, The Astrophysical Journal, 648, 435

Nozawa T., et al., 2007, ApJ, 666, 955

Ogata E., Ohsuga K., Yajima H., 2021, Publications of the Astronomical Society of Japan, 73, 929

Ogata E., Ohsuga K., Fukushima H., Yajima H., 2024, Monthly Notices of the Royal Astronomical Society, 528, 2588

Ohsuga K., Mineshige S., 2011, ApJ, 736, 2

Ohsuga K., Mineshige S., Mori M., Umemura M., 2002, ApJ, 574, 315

Ohsuga K., Mori M., Nakamoto T., Mineshige S., 2005, The Astrophysical Journal, 628, 368

Ohsuga K., Mlneshige S., Mori M., Kato Y., 2009, Publications of the Astronomical Society of Japan, 61, L7

Omukai K., 2000, THE ASTROPHYSICAL JOURNAL, 534, 809

Omukai K., Tsuribe T., Schneider R., Ferrara A., 2005, The Astrophysical Journal, 626, 627

Osterbrock E. D., 1989, agna, p. 408

Ostriker E. C., 1999, The Astrophysical Journal, 513, 252

Ostriker J. P., McCray R., Weaver R., Yahil A., Ostriker J. P., McCray R., Weaver R., Yahil A., 1976, ApJL, 208, L61

Ostriker J. P., Choi E., Ciotti L., Novak G. S., Proga D., 2010, The Astrophysical Journal, 722, 642

Park K., Bogdanović T., 2017, The Astrophysical Journal, 838, 103

Park K., Ricotti M., 2012, ApJ, 767, 163

Park K., Ricotti M., 2013, ApJ, 767, 163

Priddey R. S., Isaak K. G., Mcmahon R. G., Robson E. I., Pearson C. P., 2003, Mon. Not. R. Astron. Soc, 344, 74

Ricotti M., Ostriker J. P., Mack K. J., 2008, The Astrophysical Journal, 680, 829

Roe P. L., 1981, Journal of Computational Physics, 43, 357

Rosdahl J., Teyssier R., 2015, Monthly Notices of the Royal Astronomical Society, 449, 4380

Rosdahl J., Blaizot J., Aubert D., Stranex T., Teyssier R., 2013, Monthly Notices of the Royal Astronomical Society, 436, 2188

Ruffert M., Ruffert Maximilian 1994, ApJ, 427, 342

Ruffert M., Ruffert M. 1996, A&A, 311, 817

Ruffert M., Ruffert M. 1997, A&A, 317, 793

Ruffert M., Ruffert M. 1999, A&A, 346, 861

Sakai N., et al., 2014, Nature 2014 507:7490, 507, 78

Samsing J., et al., 2022, Nature 2022 603:7900, 603, 237

Sazonov S. Y., Ostriker J. P., Sunyaev R. A., 2004, Monthly Notices of the Royal Astronomical Society, 347, 144

Scheck L., Kifonidis K., Janka H. T., Müller E., 2006, Astronomy and Astrophysics, 457, 963

Shakura N. I., Sunyaev R. A., Shakura N. I., Sunyaev R. A., 1973, AA, 500, 33

Shapiro S. L., Shapiro L. S., 1973, ApJ, 180, 531

Shima E., Matsuda T., Takeda H., Sawada K., Shima E., Matsuda T., Takeda H., Sawada K., 1985, MNRAS, 217, 367

Spitzer L., Spitzer Lyman 1978, ppim

Sugimura K., Ricotti M., 2020, Monthly Notices of the Royal Astronomical Society, 495, 2966

Sugimura K., Hosokawa T., Yajima H., Omukai K., 2017, Monthly Notices of the Royal Astronomical Society, 469, 62

Sugimura K., Hosokawa T., Yajima H., Inayoshi K., Omukai K., 2018, Monthly Notices of the Royal Astronomical Society, 478, 3961

Susa H., Umemura M., 2004, ApJ, 600, 1

Sutherland R. S., Dopita M. A., 1993, ApJS, 88, 253

Taam R. E., Fu A., Fryxell B. A., Taam R. E., Fu A., Fryxell B. A., 1991, ApJ, 371, 696

Takeo E., Inayoshi K., Ohsuga K., Takahashi H. R., Mineshige S., 2018, Monthly Notices of the Royal Astronomical Society, 476, 673

Thoul A. A., Weinberg D. H., 1995, ApJ, 442, 480

Toyouchi D., Hosokawa T., Sugimura K., Nakatani R., Kuiper R., 2019, Monthly Notices of the Royal Astronomical Society, 483, 2031

Toyouchi D., Hosokawa T., Sugimura K., Kuiper R., 2020, Monthly Notices of the Royal Astronomical Society, 496, 1909

Untzaga J., Bonoli S., Izquierdo-Villalba D., Mezcua M., Spinoso D., 2024, MNRAS, 000, 1

Vitello P., Vitello P. 1984, ApJ, 284, 394

Walker R. C., Hardee P. E., Davies F. B., Ly C., Junor W., 2018, The Astrophysical Journal, 855, 128

Wandel A., Yahil A., Milgrom M., Wandel A., Yahil A., Milgrom M., 1984, ApJ, 282, 53

Watarai K. Y., Fukue J., Takeuchi M., Mineshige S., 2000, Publications of the Astronomical Society of Japan, 52, 133

Watarai K.-Y., Ohsuga K., Takahashi R., Fukue J., 2005, PASJ: Publ. Astron. Soc. Japan, 57, 513

Wolcott-Green J., Haiman Z., 2019, Monthly Notices of the Royal Astronomical Society, 484, 2467

Wolfire M. G., Hollenbach D., McKee C. F., Tielens A. G. G. M., Bakes E. L. O., 1995, ApJ, 443, 152

Yajima H., Ricotti M., Park K., Sugimura K., 2017, The Astrophysical Journal, 846, 3

Yuan F., Quataert E., Narayan R., 2003, The Astrophysical Journal, 598, 301

van Dokkum P., et al., 2023, The Astrophysical Journal Letters, 946, L50

Appendix A

Cooling Process

Cooling function and cooling process

The cooling function Λ [erg $s^{-1}cm^{-3}$] is the energy radiated per unit volume and unit time, and appears as a source term on the right-hand side of the energy equation for the radiation hydrodynamics. The cooling process depends on the composition ratio and temperature of the gas. In the following, we show the typical cooling process and cooling function considered in our simulation.

Atomic cooling process

Cooling processes by atoms such as hydrogen and helium include line emission (bound-bound transition), radiative recombination (free-bound transition), and collisional ionization (bound-free transition). In addition, thermal bremsstrahlung by free electrons (free-free transition) and cooling by Compton scattering are also important.

(i) Line emission

Cooling via line emission is the process of photon emission due to downward transitions between energy levels (binding-binding transitions). Considering levels i and j ($i > j$), the cooling function due to the line emission of atoms is as follows,

$$\Lambda^{\rm line} = \sum_i n_i \sum_{j<i} A_{ij} h\nu_{ij}, \tag{A.1}$$

where n_i[cm^{-3}], A_{ij}[s^{-1}], and $h\nu_{ij}$[erg] are number density of atoms, Einstein A coefficient (probability of transition from level i to j due to spontaneous emission), and energy difference between levels ij. Equation A.1 for the cooling function due to line emission of atoms is consistent with our intuition, which indicates that the larger the number density n_i of atoms, the larger the cooling rate.

(ii) Radiative recombination

Radiative recombination is a radiative phenomenon that occurs when a free electron with energy kT recombines with an ion (free-bound transition). The reason why the recombination is labeled "radiative" before the recombination is to distinguish it from the process of electron recombination without radiative emission. The cooling function due to radiative recombination of atoms is as follows,

$$\Lambda^{\rm rr} = \sum_k n_e n_k \alpha^{rr} kT, \tag{A.2}$$

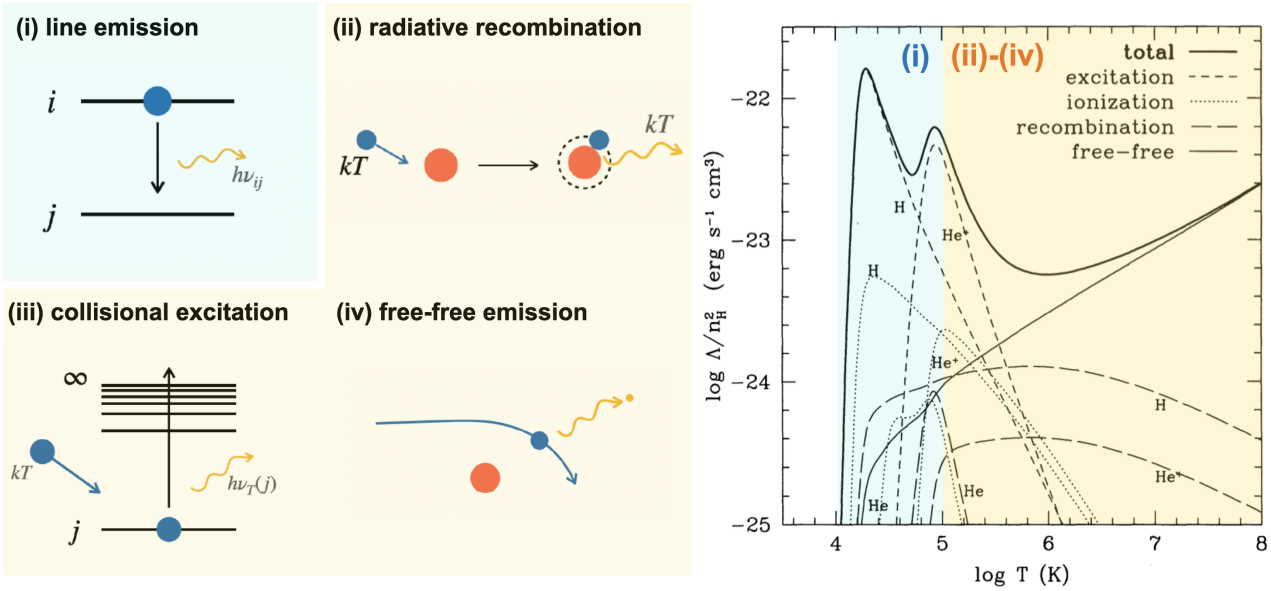

Figure A.1: Schematic figure of basic cooling process in `SFUMATO-M1`.

where n_e, n_k, and α^{rr} represent number density of electron, number density of ion, and recombination coefficient, respectively. Equation A.2 for the cooling function due to radiative recombination of atoms is proportional to the number densities of electrons and ions, n_e and n_k, which are the materials of recombination, and is also consistent with intuition.

(iii) Collisional ionization

Collisional ionization is the emission process when a free electron collides with an atom and excites the atom (the bound-free transition). When the colliding free electron has higher energy than the energy required to ionize the atom at level j, a photon with the energy that is the difference between the energy of the free electron and the ionization energy of the j is emitted. The cooling function due to collisional ionization of atoms is as follows,

$$\Lambda^{\rm ci} = \sum_j n_e n_j \alpha^{ci} h\nu_{\rm T}(j), \tag{A.3}$$

where n_j, $\alpha^{\rm ci}$, and $h\nu_{\rm T}$ mean number density of atoms with energy level j, collisional ionization coefficient, and energy of emitted photon (difference between energy of electron and ionization energy), respectively.

(iv) Thermal bremsstrahlung

Thermal bremsstrahlung is a cooling process in which a free electron is decelerated by the Coulomb interaction and emits a photon when it passes through the vicinity of an ion in a system in thermal equilibrium (free-free transition). The cooling function due to thermal bremsstrahlung is as follows,

$$\Lambda^{\rm ff} = \frac{32\pi e^6}{3^{3/2} h m_e c^3} \left(\frac{2\pi kT}{m_e}\right)^{1/2} g_{\rm ff} \sum_i Z_i^2 n_i, \tag{A.4}$$

where $g_{\rm ff}$, Z_i, and n_i are gaunt factor (correction factor for quantum mechanics), ionic charge, and number density of ion. Equation A.4 for the cooling function due to thermal bremsstrahlung is proportional to Z_i^2, which is consistent with the intuition that the stronger the charge, the greater the deceleration and the greater the energy release.

(v) Inverse Compton scattering

Inverse Compton scattering is a cooling process in which a fast-moving free electron collides with a photon with a frequency in the visible or infrared region, and gives energy to the photon. The cooling function resulting from inverse Compton scattering is as follows、

$$\Lambda^{\rm comp} = \sigma_{\rm T} c E_{\rm rad} n_e \frac{4kT - 4kT_{\rm rad}}{m_e c^2}, \tag{A.5}$$

where $\sigma_{\rm T}$, $E_{\rm rad}$, T, and $T_{\rm rad}$ are cross section of Thomson scattering, radiative energy density, gas temperture, and radiation temperture. Equation A.5 for the cooling function due to inverse Compton scattering is proportional to the electron density, which is the scattering material, and the radiative energy density, thus this equation is also consistent with intuition. As can be seen from the definition, the relationship $kT > kT_{\rm rad}$ holds for the inverse Compton scattering process. In the case of Compton scattering, this inverse relationship holds, so the sign of Equation A.5 of the cooling function by inverse Compton scattering is inverted, i.e., it becomes a heating process.

To summarize, the cooling function of a gas composed of H and He as a function of gas temperature T is shown in the right panel in Figure A.1 (Thoul & Weinberg, 1995). Here, the short dashed line represents line emission of atoms, the long dashed line represents radiative recombination, the dotted line represents collisional ionization, the thin solid line represents thermal bremsstrahlung, and the thick solid line represents a cooling function that takes all these cooling processes into account. From the overall cooling function in Figure A.1, we can see that line-cooling of H and He is responsible for cooling for $10^4 - 10^5$K, radiative recombination and thermal bremsstrahlung for $10^5 - 10^6$K, and thermal bremsstrahlung for $\gtrsim 10^6$K, respectively. This can be understood as follows: line-cooling, which is a binding-binding transition of atoms that does not require ionized gas (free electrons), is dominant in the low-temperature region, while cooling by free-free, in which ionized gas is the cooling material, is dominant in the high-temperature region. We note that there are two temperature regions where the cooling function has a negative slope with respect to temperature (near the region where line-cooling is dominant). If the temperature drops in this region, it drops further and the temperature drop is unstoppable. In other words, a thermally unstable region exists.

Molecular cooling process

Figure A.1 shows that the cooling function of atoms (H, He) is effective for $\gtrsim 10^4$K, and that cooling by atoms is almost ineffective at temperatures below that. The cooling mechanism in this $\lesssim 10^4$K is played by molecules and dust. In this section, we focus on molecular cooling processes.

(vi) Hydrogen molecule

Hydrogen molecules are isonuclear molecules and do not have a dipole moment. Therefore, although line emission occurs due to rotational and vibrational transitions of the molecule, the emission probability (Einstein A coefficient) is small. Figure A.2 shows the cooling function due to rotational and vibrational transitions of molecular hydrogen (Susa & Umemura, 2004). It is clear that the effect of cooling by rotational and vibrational transitions of the hydrogen molecule is small.

The cooling function of a molecule due to electronic transitions is also basically expressed in the same form as the equation for the cooling function of an atom (Equation A.1),

$$\Lambda_{\rm H_2} = \sum_{i \geqq 2} \sum_{j<i} n_i A_{ij} h\nu_{ij}. \tag{A.6}$$

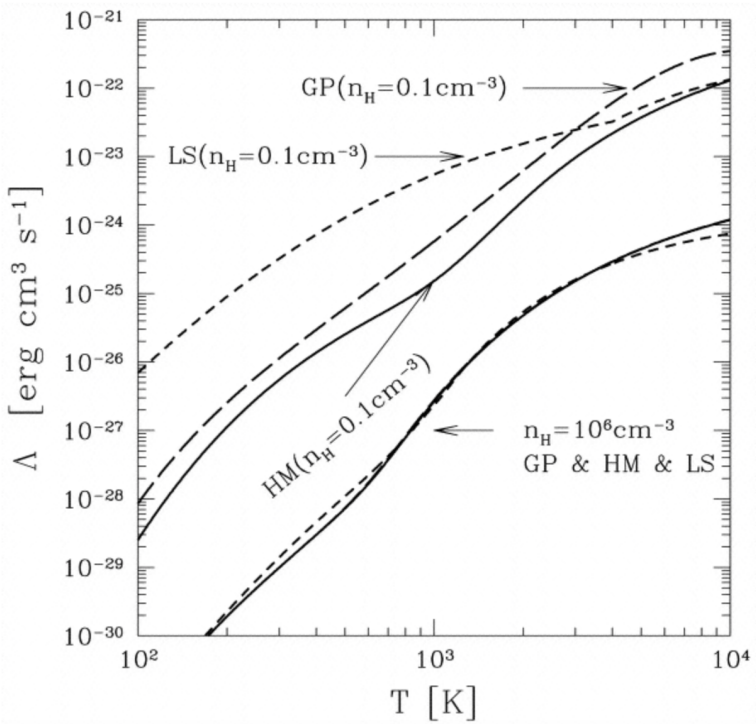

Figure A.2: H_2 cooling functions induced by H-H_2 collision are plotted against the temperature for two different densities. Cited from Susa & Umemura (2004).

However, if the density of the gas is below a certain critical density ($\sim 10^4 \mathrm{cm}^{-3}$ for hydrogen molecular), spontaneous emission is responsible for deexcitation to an energy level, and collisional processes are responsible for excitation. This means that the relation $n_i A_{ij} \sim n_j n_e C_{ij}$ holds, and the cooling function due to molecular emission is

$$\Lambda_{\mathrm{H_2}} \sim \sum_{i \geqq 2} \sum_{j<i} n_e n_j C_{ij} h\nu_{ij}, \tag{A.7}$$

where C_{ij} is Einstein's C coefficient, which represents the transition probability due to the collision process.

Cooling process of heavy elements

Heavy elements occupy only a small fraction of the gas composition compared to hydrogen and helium ($\sim$ 0.01% for the solar composition). However, line-cooling by heavy elements plays an important role in the cooling mechanism because of the large number of bound electrons present compared to hydrogen and helium. The left side of Figure A.3 shows the cooling function including heavy elements (in solar composition) expressed as a function of gas temperature (Sutherland & Dopita, 1993). This figure shows that line-cooling of heavy elements (C,O,Ne,Fe) is the main cooling mechanism at 10^{5-7}K, while free-free cooling is the dominant mechanism at $\gtrsim 10^7$K.

The amount of heavy elements also strongly depends on the cooling function. In the right side of Figure A.3, the cooling function including heavy elements expressed as a function of gas temperature, is shown for varying the ratio of Fe to H in the solar composition from 10^{-3} to $10^{0.5}$ (Sutherland & Dopita, 1993). From this figure, it can be seen that for solar compositions, when the ratio of Fe toH is less than 10^{-3}, the cooling function due to line-cooling including heavy elements matches the cooling function

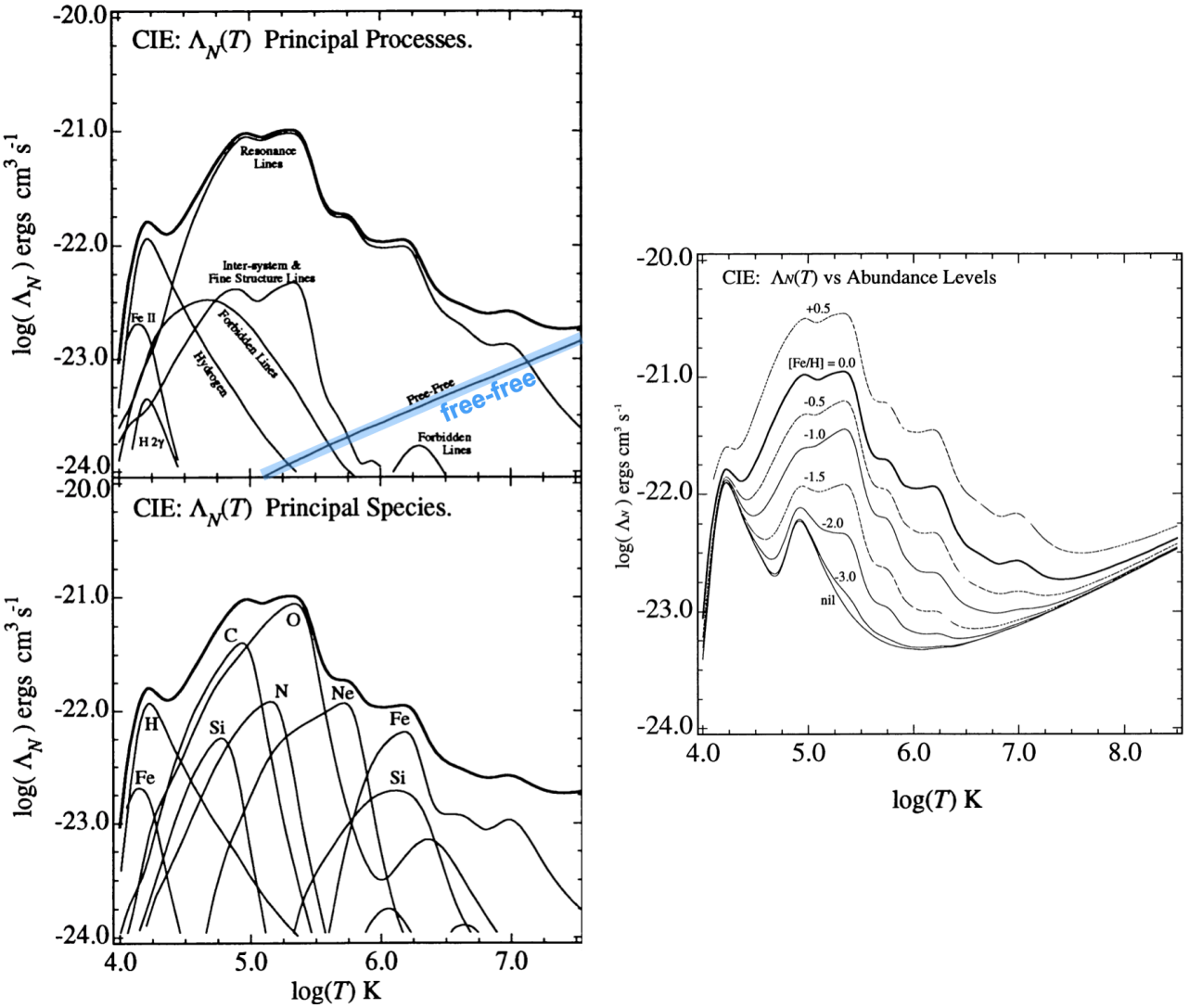

Figure A.3: Left panel: The upper panel shows the cooling function including the heavy elements. The lower panels show the emission by species, selecting only the dominant species for clarity. Right panel: The cooling functions as a function of plasma metallicity. The solid curves represent curve for different metallicities. Cited from Sutherland & Dopita (1993) with some modification.

when only H and He are considered. In other words, below 10^{-3}, line-cooling of heavy elements is hardly effective.

Cooling process of dust thermal emission

At the temperature of $10^1 - 10^2$K, the cooling mechanism by thermal radiation of dust is important. The cooling function by thermal radiation of dust is as follows:

$$\Lambda^{\rm dust} = \int\int \pi B_\nu(a_{\rm d}, T_{\rm d}) 4\pi a_{\rm d}^2 Q(a_{\rm d}, \nu) \frac{dn_{\rm d}}{da_{\rm d}} da_{\rm d} d_\nu, \tag{A.8}$$

where $a_{\rm d}$is the geometric cross section of dust (0.1-1μm), $n_{\rm d}$ is number density of dust grains, $T_{\rm d}$ is dust temperature, $B_\nu(a_{\rm d}, T_{\rm d})$ is Planck distribution function, $Q(a_{\rm d}, \nu)$ is the effective cross-section of the dust.